Dissertation

submitted to the
Combined Faculties of the Natural Sciences and Mathematics
of the Ruperto-Carola-University of Heidelberg, Germany
for the degree of
Doctor of Natural Sciences

Put forward by
Dipl.-Phys. Christian Reinhold Ott
born in: Erlenbach am Main

Oral examination: 04.07.2012

Attosecond multidimensional interferometry of single and two correlated electrons in atoms

Referees: **Dr. Thomas Pfeifer**
Prof. Dr. Marcus Motzkus

Multidimensionale Attosekunden-Interferometrie einzelner und zweier korrelierter Elektronen in Atomen—Innerhalb dieser Arbeit wird die Elektronendynamik in Atomen auf ihrer natürlichen Attosekundenzeitskala sowohl experimentell als auch numerisch untersucht. Für den Zugang zu dieser Dynamik werden ultrakurze Laserpulse moderater Intensität und weniger Zyklen Dauer überlagert mit attosekundengepulster Strahlung im extrem ultravioletten Spektralbereich. Beide Lichtquellen werden in einem von Grund auf geplanten und neu aufgebauten Vakuumapparat kombiniert, welcher auch zur Erzeugung der Attosekundenpulse verwendet wird. Neuartige experimentelle Methoden zur zeitlich und spektral interferometrischen Nutzung beider Lichtquellen werden entwickelt, wobei verschiedene dynamische Parameter in einem mehrdimensionalen Spektroskopieansatz Verwendung finden. Diese Parameter beinhalten sowohl die Intensität und die Träger-zu-Einhüllenden Phase der Laserpulse als auch deren zeitlichen Versatz zu den Attosekundenpulsen. Aus wissenschaftlicher Sicht war sowohl die Beobachtung und Kontrolle der Quantenbewegung gebundener Elektronen als auch die lasergetriebene quasiklassische Bewegung freier Elektronen ein zentrales Ziel dieser Arbeit. Insbesonders wurde ein gebundenes Zweielektronenwellenpaket in Helium auf der Attosekundenzeitskala zum ersten Mal experimentell beobachtet. Ermöglicht wurde dies durch eine bis dato nicht erreichte zugleich hohe zeitliche *und* hohe spektrale Auflösung. Weiterhin wird ein neuartiger Koppelmechanismus mehrerer zweifach angeregter Zustände mit einem effektiven Einelektronenkontinuum identifiziert und analysiert. Sowohl diese Zweielektronenzustände, als auch Einelektronenzustände werden interferometrisch erfasst, mit Zugang zur Phase ihrer quantenmechanischen Wellenfunktion. Dies ermöglicht die in dieser Arbeit demonstrierte Beobachtung und Kontrolle der Quantendynamik zweier korrelierter Elektronen in Atomen auf der Attosekundenzeitskala.

Attosecond multidimensional interferometry of single and two correlated electrons in atoms—Within this work, electron dynamics in atoms are experimentally and numerically investigated on their natural attosecond time scales. To access these dynamics, ultrashort and moderately-intense few-cycle laser pulses are superposed with attosecond pulsed radiation in the extreme-ultraviolet spectral region. Both these sources are combined in a new experimental vacuum setup which was designed and built up from scratch, also in order to generate the attosecond pulses. Novel experimental schemes are developed which involve the temporal and spectral interferometric utilization of both ultrashort light sources and include the multidimensional spectroscopy employing different dynamical parameters. These are the intensity and the carrier-envelope phase of the laser pulses, as well as their temporal delay with respect to the attosecond pulses. Scientifically, the observation and control of the quantum-motion of bound electrons, as well as the laser-driven quasi-classical motion of free electrons was a key goal of this work. In particular, a bound two-electron wave packet in helium on attosecond time scales was experimentally observed for the first time. This was realized by combining unprecedented high temporal *and* spectral resolution. In addition, a new coupling mechanism of several doubly-excited states to an effective single-electron continuum is identified and analyzed. Both these two-electron states as well as single-electron states are interferometrically investigated with access to the phase of their quantum-mechanical wave function. This allows the observation and control of the quantum dynamics of two correlated electrons in atoms on the attosecond time scale which was demonstrated within the scope of this work.

List of Publications

Parts of this work have been published or prepared in the following references:

C. Ott, A. Kaldun, P. Raith, K. Meyer, Y. Zhang, M. Laux, S. Hagstotz, T. Ding, R. Heck, and T. Pfeifer.
Quantum Interferometry and Correlated Two-Electron Wave-Packet Observation in Helium.
submitted to Nature (2012).

C. Ott, M. Schönwald, P. Raith, A. Kaldun, M. Krüger, G. Sansone, P. Hommelhoff, Y. Zhang, K. Meyer, and T. Pfeifer.
Two-Dimensional Spectral Interferometry using the Carrier-Envelope Phase.
submitted to Phys. Rev. Lett. (2012).

C. Ott, P. Raith, and T. Pfeifer.
Sub-cycle strong-field interferometry.
Opt. Express **18** 24307–24315 (2010).

Further publications with own contributions:

K. Meyer, C. Ott, P. Raith, A. Kaldun, Y. Jiang, A. Senftleben, M. Kurka, R. Moshammer, J. Ullrich, and T. Pfeifer.
Noisy Optical Pulses Enhance the Temporal Resolution of Pump–Probe Spectroscopy.
Phys. Rev. Lett. **108**, 098302 (2012).

P. Raith, C. Ott, C. P. Anderson, A. Kaldun, K. Meyer, M. Laux, Y. Zhang, and T. Pfeifer.
Fractional high-order harmonic combs and energy tuning by attosecond-precision split-spectrum pulse control.
Appl. Phys. Lett. **100**, 121104 (2012).

P. Raith, C. Ott, and T. Pfeifer.
Attosecond twin-pulse control by generalized kinetic heterodyne mixing.
Opt. Lett. **36**, 283–285 (2011).

M. C. Kohler, C. Ott, P. Raith, R. Heck, I. Schlegel, C. H. Keitel, and T. Pfeifer.
High Harmonic Generation Via Continuum Wave-Packet Interference.
Phys. Rev. Lett. **105**, 203902 (2010).

R. Spitzenpfeil, S. Eyring, C. Kern, C. Ott, J. Lohbreier, J. Henneberger, N. Franke, S. Jung, D. Walter, M. Weger, C. Winterfeldt, T. Pfeifer, and C. Spielmann.
Enhancing the brilliance of high-harmonic generation.
Appl. Phys. A **96**, 69–81 (2009).

Contents

Chapter 1

Introduction

What is a time-resolved measurement? From our experiences with the macroscopic world, such a measurement can be considered as the detection of any changes in an observed system. It is always implicitly assumed that the observation time is short compared to the time-scale of changes in the system. A popular example are snapshots of a galloping horse taken by Muybridge in the 1870s using triggered short-exposure-time photography. A long-standing question could be resolved, namely that for a certain instant in time, on the order of milliseconds, all four legs of a galloping horse are up in the air.

Things are moving faster in the microscopic world. Dynamics for instance in atoms occur on the order of femtoseconds (1 fs $= 10^{-15}$ s) and below. The time it takes the electron in the hydrogen atom to circle the proton in the lowest $n = 1$ orbit in Bohr's atomic model is only ~ 150 attoseconds (1 as $= 10^{-18}$ s). In order to get information out of any microscopic system, particles have to be detected (photons, electrons, ions, ...), just as in the above macroscopic example where the reflected light off the horse is measured with a camera. Any modern detector is based on electronics where the intrinsic temporal resolution is limited to nanoseconds (1 ns $= 10^{-9}$ s) or possibly, with considerably more effort, to several tens or hundreds of picoseconds (1 ps $= 10^{-12}$ s). This means that the much faster atomic dynamics cannot be directly resolved.

How does a microscopic system evolve in time? In non-relativistic quantum theory, which is exclusively discussed in this thesis, time evolution is governed by the time-dependent Schrödinger equation

$$i\hbar\frac{\partial}{\partial t}|\Psi(t)\rangle = \hat{\mathbf{H}}|\Psi(t)\rangle. \tag{1.1}$$

As a consequence of this equation, in particular due to the appearance of the complex factor "i" on the left hand side, the temporal evolution of the wave function $|\Psi(t)\rangle$—which describes the microscopic system—is encoded in complex phase factors "$\exp[-i(E/\hbar)t]$". These are oscillatory in time with frequency $E/\hbar$, where E is the energy of a quantum state. This could for example be the energy of an electron which is bound to a nucleus.

Measuring time in quantum mechanics is thus intimately related to measuring phases. How can time-information be retrieved from a phase changing with time? Within an

oscillatory motion, time T, frequency ω and energy E are related by

$$T = \frac{2\pi}{\omega} = \frac{2\pi \cdot \hbar}{E}. \tag{1.2}$$

Therefore time is the ratio of phase and energy. As only relative changes of time—in comparison with a ruler—are meaningful, a straightforward definition of temporal changes would be to evaluate the derivative of the phase Φ:

$$\Delta T \equiv \frac{\mathrm{d}\Phi}{\mathrm{d}E}. \tag{1.3}$$

In quantum mechanics a peculiarity arises alongside the notion of these phases. Phases characterize the complex amplitudes in a superposition of separate states of a quantum system, the eigenstates which are labeled by their respective energy. If only one of these states is present—is populated—such as the above mentioned lowest Bohr orbit of an atom, no change with time can be seen by any means, because only the absolute value squared of the wave function $|\Psi|^2$ which describes measurable quantities can be detected. The time-information encoded in the phase drops out. Only when more than one quantum state is populated, i.e. the electron wave function populates more than one Bohr orbital, detectable quantities such as the mean position of the electron relative to the nucleus do change with time and can be measured. An analogy of this peculiarity can be found in acoustics. Imagine the sound of two sine waves with slightly different frequencies. If played separately, a single tone with constant volume will each be heard with no changes in time. However if played together, these two tones interfere—they beat—and a volume oscillating with time will be heard.

This direct measurement of time-dependent phases in quantum mechanics on the electronic attosecond time scale is unfortunately not possible, simply as a detector which could resolve these fast atomic time-scale changes does not (yet) exist. Instead, only the energy of particles leaving the quantum system can be determined. However if their phase as a function of energy can be determined, temporal information is directly gained as outlined above. In order to extract this phase a powerful tool can be employed: **Interferometry**.

If states of different energy are projected onto an equal energy region—e.g. by absorption of photons—their relative phase can be measured out of which temporal information is finally gained. In order to create this overlap, a tool is needed which fully conserves the phase of the quantum states, thus this tool itself needs to have a perfect phase-relationship, in other words a high coherence. This high degree of coherence is realized in lasers. In order to be sensitive to ultrafast dynamics on the atomic time scale, a broad coherent spectrum of different frequencies is needed in order to coherently cover a broad energetic range of quantum states to support these ultrafast dynamics.

The explanation why a broad spectral range is needed in order to access fast time scales goes back to the work of Jean Baptiste Josephe Fourier [1]. With the nowadays well known and further developed mathematical concepts of Fourier analysis, the time and frequency representation of a signal can be mapped into each other. As a consequence, the temporal duration and the frequency bandwidth of a signal—or process—are directly related. In particular their product cannot be smaller than a certain constant. For example,

an infinitely narrow frequency component is only defined when the temporal duration of the process is infinitely long, i.e. a perfect sine wave. In contrast, when a very fast process is happening in time, it must be supported by a broad set of different frequencies. This is closely related to the uncertainty principle of quantum mechanics, where position and momentum cannot be measured simultaneously with arbitrary precision. It should be noted that it is not exactly equivalent, because both position and momentum in non-relativistic quantum mechanics are operators, i.e. observables, which is also true for the energy. In contrast, time cannot be represented as an operator but only enters as a parameter.

From this correspondence of time and energy, temporal information of a quantum system is already encoded in the energy spectrum of the observation. If for instance the superposition of two electronic quantum states is considered, the ground state and an excited state, radiation is emitted from the system due to the oscillating charge distribution until the excited state decays within its life time. Detecting the energy spectrum (in particular its width) of this radiation directly reveals this life time. It is thus important to note that already from a precise measurement in the energy domain, dynamics about the system can be deduced. However this interpretation assumes additional information on the system: Two quantum states are involved. From such a measurement alone it could not be distinguished whether only two states are present with a certain life time, or if many independent states with similar energy positions are present with longer life times where the spectral lines, by incoherently adding at the detector, appear as a single line falsely implying a shorter lived state.

In addition, the interferometric capability of laser pulses comes with another benefit: The degree of control. These pulses can coherently and strongly couple different electronic quantum states which implies the possibility to control their phase. A motivation for this control of electron dynamics is drawn from chemical reactions. Electrons are the fundamental ingredient of any chemical bond. Being in between atoms they typically form the covalent bond involving two electrons. It is the dynamics of these pairs of electrons which are fundamentally responsible for any course of chemical reaction. In addition, these two electrons are correlated. In their quantum-mechanical description, their evolution has to be treated as one whole entity, a two-electron wave function. Accessing and controlling the phase of correlated two-electron states in simpler systems could thus be considered as a first step towards control schemes of such two-electron orbitals in molecules.

The aim of this thesis is to interferometrically measure ultrafast electronic quantum dynamics, its understanding and control by employing the coherence of ultrashort few-cycle laser pulses. Emphasis is put on the attosecond temporal and the extreme ultraviolet (XUV) spectral domain, which is the natural domain of closely-bound atomic electrons in motion. Being the main result of this work, it will be demonstrated how correlated two-electron dynamics in atomic helium can be directly measured, controlled and understood.

Special emphasis will be placed on exploiting several dynamical parameters. Not only the time delay between laser pulses, as utilized in conventional pump–probe measurements, but also the carrier-envelope phase (CEP) and the intensity of ultrashort laser pulses will be utilized as dynamical parameters which allow the temporal control of the investigated processes. In addition, the encoding of dynamics in the spectral line shape which is measured in the energy domain, as outlined above, will be included in the investigation. The

whole temporal evolution of the system, coherently integrated for the detection is to be considered (the spectral line shape), while the control on the much faster dynamics is enabled by the available ultrashort laser sources. In order to analyze the effects of the above-mentioned dynamical parameters, including the detected spectral line shapes, two-dimensional representations of the measured data will be investigated. This involves also concepts from Fourier analysis in order to relate directly comparable domains—temporal or spectral—of these parameters. The motivation for this originates from multidimensional spectroscopy, nowadays mainly applied in the femtosecond temporal and infrared-to-visible spectral domain which correspond to longer time scales as considered here. These spectroscopy techniques are successfully applied to measure and control mainly vibrational dynamics in molecules and slower electronic transition pathways in molecular systems. A direct copy of these concepts is however not yet directly applicable in the natural domain of moving electrons deeply bound in small molecules. The reason is because appropriate and intense enough attosecond laser sources are not yet available in this range, but may become available in the near future.

The thesis is structured as follows: In the following chapter, fundamental theoretical concepts will be introduced with emphasis on the connection between descriptions in the temporal and spectral domain, described by the Fourier transformation, but also to establish a common background of the underlying physical concepts, especially for the description of two-electron systems. In chapter 3 the experimental apparatus will be described in detail as it was designed and built from scratch in order to address the here outlined scientific topics. In chapter 4 a home-built numerical simulation—a computer experiment—is performed which investigates a highly non-linear interferometric scheme solely with intense femtosecond laser pulses to access sub-cycle attosecond dynamics, with prospects of phase-resolved access to a variety of different electron quantum states. Chapter 5 outlines a novel two-dimensional spectroscopic method involving the CEP of one single femtosecond laser pulse to disentangle overlapping temporal contributions of electron quantum paths in strong laser fields. In chapter 6 the main scientific result of this work is presented, which is the phase-resolved measurement of a set of different correlated two-electron quantum states in helium, where a three-dimensional experimental data set is acquired, spanned by the spectral line shape, the femtosecond laser intensity and the temporal delay of this laser pulse to attosecond pulsed light in the extreme ultraviolet. Laser-coupling between discrete and fully-correlated two-electron states and *in addition* simultaneous coupling to an effective single-electron continuum of states is observed and controlled. Understanding of this process is established with a home-built numerical close-coupling simulation. Finally, in section 7 the results of this work will be summarized and an outlook will be given.

Chapter 2

Theoretical background

2.1 Ultrashort laser pulses

This section is devoted to the mathematical description of ultrashort femtosecond laser pulses, as they are ideally suited to demonstrate the connection between time and spectral frequency domain, via the Fourier transformation. Properties such as their carrier-envelope phase will be introduced. Both their generation as well as certain control aspects will be shortly described, as these pulses are nowadays a key tool in ultrafast science for measuring ultrafast dynamics on their natural time scales. They also serve as the driver tool to generate even shorter attosecond pulses which will be described in more detail in section 2.2.2. Nowadays, many aspects of ultrashort laser pulses can be found in textbooks such as [2] which this chapter is mainly referring to.

In the time domain, ultrashort laser pulses are described by a time-dependent electric field $E(t)$. It is a real electromagnetic wave which therefore could in principle be directly measured with an oscilloscope, provided that the electronics were fast enough. In most general terms, it is described as a product of a slowly varying envelope function $\mathscr{E}(t)$, and an oscillatory part defined by the phase $\phi(t)$ as

$$E(t) = \mathscr{E}(t)\cos[\phi(t)], \tag{2.1}$$

where linear polarization is assumed. The envelope $\mathscr{E}(t)$ defines the overall temporal structure of the laser pulse and is mainly characterized by its duration, which is usually defined as the full width at half maximum (FWHM) of the intensity profile, where the intensity $I(t)$ is proportional to the square of the real and positive valued envelope function, $I(t) \propto \mathscr{E}(t)^2$. The pulse profiles are typically described by a Gaussian envelope

$$\mathscr{E}_{\mathrm{G}}(t) = \mathscr{E}_0 \exp\left[-\left(\frac{t}{t_{\mathrm{G}}}\right)^2\right] \tag{2.2}$$

or a cosine squared $\cos^2$ envelope function

$$\mathscr{E}_{\mathrm{C}}(t) = \begin{cases} \mathscr{E}_0 \cos^2\left(\frac{t}{t_{\mathrm{C}}}\right) & \text{for } -\frac{\pi}{2}t_{\mathrm{C}} \leq t \leq \frac{\pi}{2}t_{\mathrm{C}} \\ 0 & \text{otherwise.} \end{cases} \tag{2.3}$$

The corresponding parameters are related to the FWHM pulse duration via

$$t_{\mathrm{G}} = \frac{t_{\mathrm{FWHM}}}{\sqrt{2\ln 2}} \approx 0.849 \cdot t_{\mathrm{FWHM}} \tag{2.4}$$

and

$$t_{\mathrm{C}} = \frac{t_{\mathrm{FWHM}}}{2\arccos\left(2^{-1/4}\right)} \approx 0.874 \cdot t_{\mathrm{FWHM}}. \tag{2.5}$$

The temporal phase $\phi(t)$ can be expanded in a Taylor series and can be written as

$$\phi(t) = \phi_{\mathrm{CEP}} + \omega_{\mathrm{c}} t + \varphi(t), \tag{2.6}$$

where ϕ_{CEP} is the carrier to envelope offset phase, ω_{c} is the central frequency, and $\varphi(t)$ is the phase which contains only higher-order terms in time (t^k with $k \geq 2$). For $\varphi(t) = 0$, a constant oscillation of frequency ω_{c} is imprinted into the envelope, and is thus also called the carrier frequency. The constant offset phase ϕ_{CEP} determines the position of this oscillation with respect to the envelope. The instantaneous frequency $\omega(t)$ is generally defined as the time derivative of the temporal phase

$$\omega(t) = \frac{\mathrm{d}}{\mathrm{d}t}\phi(t) = \omega_c + \frac{\mathrm{d}}{\mathrm{d}t}\varphi(t), \tag{2.7}$$

which is only changing with time if $\varphi(t) \neq 0$, i.e. terms of order $k \geq 2$ have a non-zero contribution to $\phi(t)$. In these cases, the pulses will be called up- or down-chirped, depending on whether $\omega(t)$ is increasing or decreasing with time. If the change in $\omega(t)$ is linear with time, i.e. $\phi(t)$ contains only terms up to 2$^{\mathrm{nd}}$ order in time, the chirp is called linear. Otherwise, the pulse exhibits a non-linear chirp.

For mathematical convenience, the field can also be described in complex form as

$$\tilde{E}(t) = \mathscr{E}(t)\exp[i\phi(t)], \tag{2.8}$$

however its real part is still the only measurable quantity interacting with the physical system. Only when approximations are made (such as the rotating wave approximation as will be shown in section 2.6) its complex representation directly enters the terms which describe the interaction with the system. This is in contrast to the wavefunction $|\psi(t)\rangle$, which is truly a complex quantity and directly enters the description (exact or approximative) of a system.

In the spectral domain (or frequency domain) the field is obtained via the Fourier transform, defined as

$$\tilde{E}^{(\mathrm{s})}(\omega) = \mathscr{F}\left\{\tilde{E}(t)\right\} = \int_{-\infty}^{+\infty} \mathrm{d}t \tilde{E}(t) e^{-i\omega t}, \tag{2.9}$$

and the corresponding inverse transform is given by

$$\tilde{E}(t) = \mathscr{F}^{-1}\left\{\tilde{E}^{(\mathrm{s})}(\omega)\right\} = \frac{1}{2\pi}\int_{-\infty}^{+\infty} \mathrm{d}\omega \tilde{E}^{(\mathrm{s})}(\omega) e^{i\omega t}, \tag{2.10}$$

The complex electric field in the frequency domain can also be expressed with an envelope $\mathscr{E}^{(\mathrm{s})}(\omega)$ and a phase $\phi^{(\mathrm{s})}(\omega)$ as

$$\tilde{E}^{(\mathrm{s})}(\omega) = \mathscr{E}^{(\mathrm{s})}(\omega)\exp[i\phi^{(\mathrm{s})}(\omega)]. \tag{2.11}$$

Related via the Fourier transform, the temporal duration t_{FWHM} and the spectral bandwidth $\Delta\omega_{\mathrm{FWHM}}$ fulfill the uncertainty principle of Fourier analysis [2], which states that their product cannot be smaller than a pulse-shape dependent constant. That is

$$t_{\mathrm{FWHM}} \cdot \Delta\omega_{\mathrm{FWHM}} \geq 2\pi c_{\mathrm{B}}. \tag{2.12}$$

The spectral bandwidth ($\Delta\omega_{\mathrm{FWHM}}$) is defined as the full width at half maximum of the spectral intensity profile $S(\omega)$, where $S(\omega) \propto \mathscr{E}^{(\mathrm{s})}(\omega)^2$. The constant c_{B} depends on the exact shape of the envelope $\mathscr{E}(t)$. For a Gaussian pulse as defined in Eq. (2.2), $c_{\mathrm{B}} = 2\ln 2/\pi \approx 0.441$, while for a cosine squared envelope as given in Eq. (2.3), $c_{\mathrm{B}} \approx 0.262$. The inequality in Eq. (2.12) holds for a non-zero higher order ($k \geq 2$) spectral (or temporal) phase, i.e. when the pulses are chirped. If the equality holds, the pulses are typically unchirped and reach the shortest possible duration (t_{FWHM}) for a given spectral bandwidth $\Delta\omega_{\mathrm{FWHM}}$. In this case, the pulses are also called bandwidth limited.

The spectral phase can also be expanded in a Fourier series and is expressed as

$$\phi^{(\mathrm{s})}(\omega) = \sum_{k=0}^{\infty} \frac{1}{k!} \frac{\partial^k \phi^{(\mathrm{s})}(\omega)}{\partial \omega^k} \cdot \omega^k = \phi_{CEP}^{(\mathrm{s})} + \tau_0 \cdot \omega + \varphi^{(\mathrm{s})}(\omega). \tag{2.13}$$

where $\varphi^{(\mathrm{s})}(\omega)$ now only contains higher-order terms in frequency (ω^k with $k \geq 2$). In analogy to Eq. (2.7), a frequency-dependent temporal delay, called group delay, can be defined as

$$\tau(\omega) = -\frac{\mathrm{d}}{\mathrm{d}\omega}\phi^{(\mathrm{s})}(\omega) = -\tau_0 - \frac{\mathrm{d}}{\mathrm{d}\omega}\varphi^{(\mathrm{s})}(\omega), \tag{2.14}$$

where the delay is only changing with frequency when $\varphi^{(\mathrm{s})}(\omega) \neq 0$. The minus sign results from the definition of the spectral phase in Eq. (2.11) and the Fourier transform performed as given in Eq. (2.10).

According to the shifting theorem of the Fourier transform, linear phase terms, both in the temporal and spectral domain, merely linearly shift the pulse as a whole in the other respective domain without changing their shape. Thus, ω_{c} and $-\tau_0$ can be interpreted as a mean frequency and a mean time delay which the pulses are centered around in the spectral and the temporal domain, respectively. This connection also decouples the carrier frequency ω_c from the given spectral distribution within $\Delta\omega_{\mathrm{FWHM}}$. The carrier frequency does not necessarily need to be part of the spectrum, e.g. for pulses which have a centered gap in the spectral distribution. It is typically defined as the mean of the spectral distribution of frequencies, i.e. the intensity weighted average frequency [2]. For most common cases however (which are also exclusively discussed in this thesis) ω_{c} is found around frequencies ω, where the spectral amplitude $\mathscr{E}^{(\mathrm{s})}(\omega)$ takes its largest values.

This shifting property also nicely illustrates (though not mathematically exact) how the effect of the higher order terms are encoded in $\varphi(t)$ and $\varphi^{(\mathrm{s})}(\omega)$. If the pulses are defined in the spectral domain, these higher order terms result in a true frequency-dependent

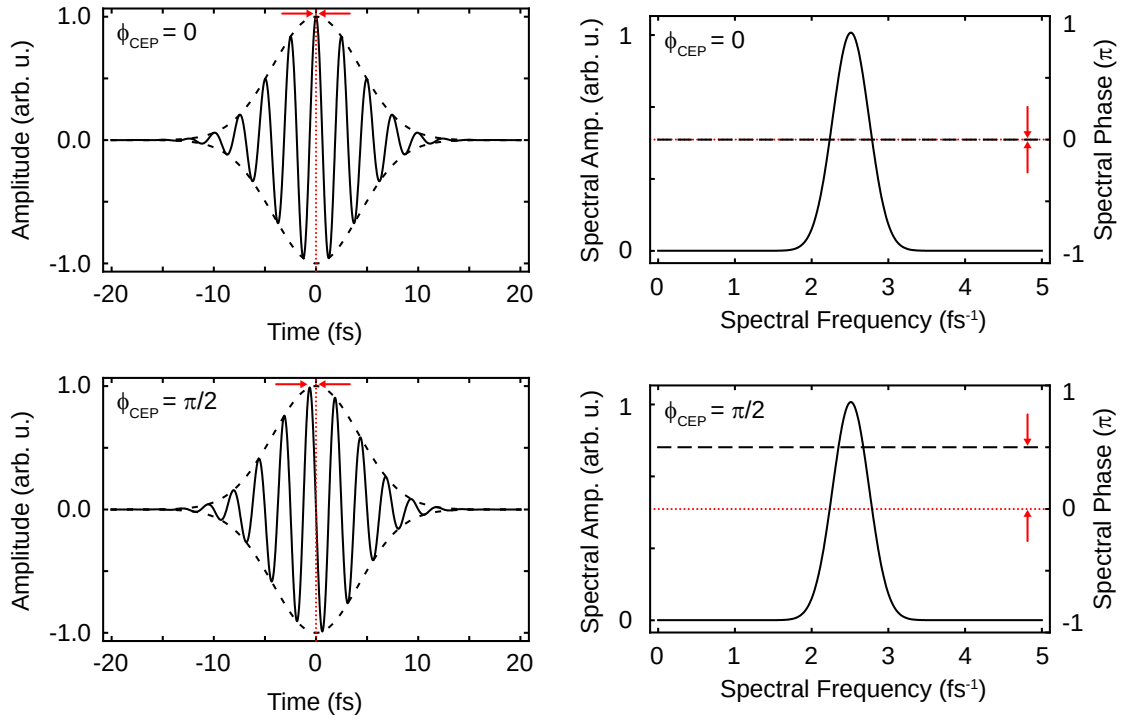

Figure 2.1: Gaussian-shaped laser pulses with 7 fs FWHM duration and 750 nm center wavelength in temporal (left) and spectral (right) representation for $\phi_{\mathrm{CEP}} = 0$ (top) and $\phi_{\mathrm{CEP}} = \pi/2$ (bottom). In the temporal representation, the envelope of the electric field is indicated (dashed line), centered around time zero which is additionally marked with red dotted lines. In the spectral representation (right panels), the spectral envelope is shown (black line) together with the spectral phase (black dashed line) which is flat for the bandwidth limited pulses shown here. Here, the red dotted lines mark zero spectral phase. The red arrows denote the definition of the CEP in each respective domain.

delay $\tau(\omega)$. This means that different spectral parts of the pulse are shifted to different temporal delays. For the case of a linear chirp, higher and lower frequencies are shifted to opposite times of the pulse, causing $\tau(\omega)$ to become both bigger and smaller than the mean temporal delay $-\tau_0$. For non-linearly chirped pulses, $\tau(\omega)$ may be always bigger (or smaller) than the mean delay $-\tau_0$. Thus higher and lower frequencies can be shifted to a single side of the pulse, where they temporally interfere (beat) and consequently can create separate pulses to one side of the original pulse. This explains, how pre- and postpulses are usually connected to higher than 2$^{\mathrm{nd}}$ order dispersion, with the third order dispersion being the leading term.

With the definition of Eqs. (2.6) and (2.13), the constant terms are equal in both representations ($\phi_{\mathrm{CEP}} = \phi^{(\mathrm{s})}_{\mathrm{CEP}}$), and can be placed outside the integrals in Eqs. (2.9) and (2.10). In general their exact value depends on the choice of reference. In the current mathematical definition, ϕ_{CEP}, in the time domain, is the phase slippage of the carrier wave with respect to $t = 0$, which has the same value as the spectral phase $\phi^{(\mathrm{s})}(\omega)$ when extrapolated to $\omega = 0$. Only changes of the CEP are relevant within experimental observations. These changes ($\Delta\phi_{\mathrm{CEP}}$) are equal to both the temporal and spectral domain and allow for example their exact measurement in the spectral domain at any arbitrary (but fixed) spec-

tral component. This implies that the carrier wave in the time domain is shifting by this measured amount. Methods how to measure the CEP will be discussed along with the experimental setup in section 3.2. Fig. (2.1) gives an illustration of the CEP both in the temporal and spectral domain.

The frequency-dependent delay, given by $\tau(\omega)$, for the different spectral parts of a laser pulse is generated by the dispersive character of any medium which the pulse is propagating through. In terms of the superposition principle, a laser pulse can be thought of as the coherent sum (or integral) of a range of monochromatic waves. Assuming plane waves, these are given by

$$a^{(s)}(\omega) \cdot \exp[i(\omega t - k(\omega)z)], \tag{2.15}$$

where $a^{(s)}(\omega)$ is the spectral amplitude and $k(\omega)$ is the wave vector . The sign of the phase terms is chosen such that the waves travel in the $+z$ direction in time. The wave vector is related to the refractive index $n(\omega)$ of a medium via

$$k(\omega) = \frac{\omega}{c} \cdot n(\omega). \tag{2.16}$$

Only conditions where $n(\omega) = const.$ will cause the phase to change linear with frequency as described by Eq. (2.15), resulting in the laser pulse to propagate without distortion. For optical frequencies this is typically only true for propagation in vacuum. Applying Eq. (2.14) to the spectral phase defined in Eqs. (2.15) and (2.16) yields

$$\tau_z(\omega) = -t + \frac{n(\omega)}{c} z + \frac{\omega}{c} \frac{\mathrm{d}n(\omega)}{\mathrm{d}\omega} z \tag{2.17}$$

which is the frequency-dependent delay that the material imparts to the pulse as it propagates in the z direction. In most common materials, both $n(\omega)$ and $\mathrm{d}n(\omega)/\mathrm{d}\omega$ are positive and increase as a function of frequency. Thus, according to Eq. (2.17) within the pulse higher frequencies are delayed to later times. This implies that propagation through normally dispersive material (such as glass or air) will result in more positively chirped (or up-chirped) laser pulses. Methods on how to shape the spectral phase of laser pulses (which directly changes their temporal profile) and especially how to compensate for the propagation-induced chirp are outlined below, but first the effects of a medium on the CEP will be considered.

The CEP constantly changes when pulses propagate in dispersive media. This can be seen by comparing the phase velocity of the carrier wave defined as

$$v_{\mathrm{ph}} = \frac{\omega_{\mathrm{c}}}{k(\omega_{\mathrm{c}})} = \frac{c}{n(\omega_{\mathrm{c}})} \tag{2.18}$$

with the group velocity (v_{g}) of the wave packet centered around the average frequency ω_{c} defined as

$$v_{\mathrm{g}} = \left.\frac{\mathrm{d}\omega}{\mathrm{d}k(\omega)}\right|_{\omega_{\mathrm{c}}} = \left(\left.\frac{\mathrm{d}k(\omega)}{\mathrm{d}\omega}\right|_{\omega_{\mathrm{c}}}\right)^{-1} = \left(\frac{1}{v_{\mathrm{ph}}} + \frac{\omega_{\mathrm{c}}}{c} \cdot \left.\frac{\mathrm{d}n(\omega)}{\mathrm{d}\omega}\right|_{\omega_{\mathrm{c}}}\right)^{-1}. \tag{2.19}$$

For normal dispersion, $v_{\mathrm{g}} < v_{\mathrm{ph}}$, which means that the carrier wave will shift towards the leading edge of the envelope (i.e. to earlier times) in the moving frame of the pulse. The

propagation distance for a phase slippage of one full cycle (i.e. $\Delta\phi_{\mathrm{CEP}} = 2\pi$) can be easily calculated and is given by

$$z_{2\pi}(\omega) = 2\pi \frac{v_{\mathrm{g}}}{v_{\mathrm{ph}} - v_{\mathrm{g}}} \frac{c}{\omega}. \tag{2.20}$$

As an example, for 750 nm light propagating in fused silica this amounts to $z_{2\pi} \approx 74\ \mu$m, and $z_{2\pi} \approx 130$ mm for propagation in air. The dispersion formulas used to calculate these values were taken from [2] for the case of fused silica glass and from [3] for the case of air. The value for air should be considered as an order of magnitude estimation, since the exact value depends on other parameters such as the water content, the ambient pressure, the temperature, etc. [4].

For focused laser beams, the Guoy phase has to be taken into account, which means that the phase fronts of the beam are advanced with respect to the parallel phase fronts of the unfocused plane waves and is given by

$$\Phi_{\mathrm{Guoy}}(z) = \arctan\left(\frac{z}{z_{\mathrm{R}}}\right), \tag{2.21}$$

where z_{R} is the Rayleigh range of a beam with focus position at $z = 0$. This also means that the CEP, within a focused pulse, will undergo a total phase change of π, even without any further dispersion. $\pi/2$ of this phase change will accumulate across the focus confined over $2z_{\mathrm{R}}$. It is necessary to take this into account when accumulating data from different points within the focal region [5]. Further details on that and other issues on spatially-profiled Gaussian beams can be found in [6].

For the case of temporal pulse profiles using Gaussian envelopes (cf. Eq. (2.2)) we now neglect all higher-order ($k \geq 3$) phase terms (i.e. considering only linearly chirped pulses) and can perform further calculations. These allow for first-order estimates on the change of the pulse duration after propagation through dispersive material. The calculations are straightforward and can be found in more detail in [2]. The temporal duration after propagating at a distance z is given by

$$t_{\mathrm{G}}(z) = t_{\mathrm{G},0}\sqrt{1 + \left(\frac{z}{L_d}\right)^2} \tag{2.22}$$

where $t_{\mathrm{G},0}$ is the bandwidth-limited pulse duration and the characteristic length is defined as

$$L_d = \frac{t_{\mathrm{G},0}^2}{2\left|\frac{\mathrm{d}^2 k(\omega)}{\mathrm{d}\omega^2}\Big|_{\omega_{\mathrm{c}}}\right|}. \tag{2.23}$$

To compensate for this pulse stretching, the pulse needs to be negatively chirped, thus the lower frequencies need to be delayed with respect to the higher frequency components. This is achieved for example by using angularly dispersive elements such as prisms or gratings, where the different spectral parts of the pulse are spatially separated. It is then possible to propagate higher frequencies along shorter optical paths as compared to the lower frequencies, which results in a negative chirp. Usually the pulses are

overcompensated so that only when they arrive at the interaction region is the shortest pulse duration achieved. When prisms or gratings are used, only second-order phases can most efficiently be compensated for. The spectrum therefore has to be sufficiently narrow that the change of the refractive index can be considered approximated as constant ($\mathrm{d}n(\omega)/\mathrm{d}\omega$=*const.*). For shorter pulse durations approaching the few-cycle regime, thus where a larger spectral bandwidth needs to be compressed, this is no longer easily possible. A key to enter the few-cycle regime was then the implementation of multilayer mirrors [7]. Their working principle is still based on delaying lower frequencies with respect to the higher ones, but now an almost arbitrary group delay can be compensated. Constructive and destructive interference is caused at different depths below the mirror surface due to a changing thickness of the layers as a function of depth within the mirror. Lower frequencies (i.e. longer wavelengths) are reflected deeper inside the mirror and thus delayed with respect to the higher frequencies, reflected more close to the surface. The phase function imprinted by these mirrors is typically sinusoidally modulated, which introduces satellite pulses in the time domain. To compensate for this, these mirrors are usually fabricated in pairs to induce a π-phase change in the dispersion function in order that the sum effect on the dispersion compensation is approximately flat. Within these constraints, the layer thickness can be designed appropriately so that a certain amount of glass and air, or other components in the experimental beam path, can be compensated for.

2.2 Strong laser fields

The femtosecond laser pulses which are used in the here described experiments yield peak intensities in the 10^{14} to 10^{15} W/cm^2 regime. The corresponding electric field strength is on the order of 10^8 to 10^9 V/cm, thus approaching the atomic unit of field strength, $\mathscr{E}_{\mathrm{a.u.}} = 5.14 \cdot 10^9$ V/cm (see appendix A), the electric field which the electron feels in the first Bohr orbit of the hydrogen atom. Due to this reason, these electric fields (of the laser pulses) cannot be treated perturbatively anymore when interacting with atomic systems. This gives rise to new effects such as high-order harmonic generation (HHG), non-sequential double ionization (NSDI), high-order above threshold ionization (HATI), and many more. It is not the aim here to present a thorough overview over these effects, which can be found in review articles and text books. As an example for further reading, [8] is mentioned, which shall also serve as a reference for related literature.

Here, particular emphasis is placed on HHG because it serves as a tool for the generation of attosecond pulses which are experimentally used in this work. This will be described in section 2.2.2. A prerequisite for this process, and also for many other interactions with strong laser fields, is the strong-field ionization of electrons bound to atoms. Before describing this in detail in section 2.2.1, some more general aspects of strong laser fields shall be summarized in the following.

As it was mentioned above, with laser electric field strengths approaching the atomic unit of field strength, a perturbative approach in order to accurately describe the interaction with for instance atomic systems will fail. In order to have a reference for the strength of the laser electric field, the interaction with free electrons is taken, i.e. the extreme case

where the ionic potential of the atom can be completely neglected.

The motion of a free electron in an oscillating field can be described classically, obeying Newton's equations with

$$a(t) = -\frac{e}{m_\mathrm{e}} E(t) \tag{2.24}$$

$$v(t) = v_0 - \frac{e}{m_\mathrm{e}} \int_{-\infty}^{t} E(t')\mathrm{d}t' = v_0 + A(t) \tag{2.25}$$

$$x(t) = x_0 + v_0 \cdot t + \int_{-\infty}^{t} A(t')\mathrm{d}t', \tag{2.26}$$

assuming a linearly-polarized time-dependent electric field $E(t)$, with $x(t)$, $v(t)$ and $a(t)$ being the time-dependent position, velocity and acceleration of the electron with mass m_e and charge $-e$. The vector potential $A(t)$ of the electric field is identified as

$$A(t) = -\frac{e}{m_\mathrm{e}} \int_{-\infty}^{t} E(t')\mathrm{d}t', \tag{2.27}$$

and the initial position and velocity of the electron are x_0 and v_0, respectively. Assuming a monochromatic wave $E(t) = \mathscr{E}_0 \cos(\omega t + \phi_\mathrm{CEP})$ these equations can be solved analytically. The mean kinetic energy of an electron, initially at rest ($v_0 = 0$), moving in the laser field is referred to as ponderomotive energy, and is given by

$$U_\mathrm{p} = \frac{1}{2} m_\mathrm{e} \overline{v(t)^2} = \frac{e^2 \mathscr{E}_0^2}{4 m_\mathrm{e} \omega^2} \tag{2.28}$$

where the average is performed over one laser cycle. Similarly, with Eq. (2.26), the oscillation amplitude of the electron quiver motion in the monochromatic electric field can be expressed as

$$x_\mathrm{p} = \frac{e\mathscr{E}_0}{m_\mathrm{e}\omega^2} \tag{2.29}$$

which is known as the ponderomotive radius. The here presented scales serve as a reference in order to estimate the strength of the laser fields in use. It should be mentioned that these formulas are only valid for non-relativistic field strengths, i.e. when the magnetic component of the electromagnetic field of the laser can still be neglected and the electron moves with velocities well below the speed of light. This is justified for the here considered field intensities.

An approximation widely used to describe the interaction of strong laser fields with atomic systems is the single active electron (SAE) approximation. In such treatments, an atom with more than one electron is treated in a way that only one effective electron—usually the outermost—is interacting with the laser field, while the remaining electrons merely screen the ionic potential of the nucleus. In such treatments, an effective orbital quantum number n^* is defined, essentially mapping onto "fractional" Bohr orbits, with

$$n^* = \frac{Z}{\sqrt{2I_\mathrm{p}}}, \tag{2.30}$$

where the ionization potential I_p of the outermost electron is expressed in atomic units and Z is the charge of the atomic residue when this outermost electron is removed ($Z = 1$ for neutral atoms). For the mostly considered neutral rare gas atoms in interaction with strong laser fields, both the ionization potentials and the respective effective orbital quantum numbers are listed in Tab. (2.1).

Table 2.1: Ionization potential I_p and effective orbital quantum number n^* for neutral rare gas atoms, calculated with values from [9].

	I_p (eV)	I_p (a.u.)	n^*
helium	24.59	0.9036	0.7439
neon	21.56	0.7925	0.7943
argon	15.76	0.5792	0.9292
krypton	14.00	0.5145	0.9858
xenon	12.13	0.4458	1.0591

The general treatment of such effective single-electron atoms in strong laser fields is semi-classical, where the electron bound in the atomic potential is treated quantum mechanically, while the laser electric field is treated classically. This results in the Schrödinger equation for a single-active electron. In the length gauge it reads

$$i\frac{\partial}{\partial t}|\Psi(\vec{r},t)\rangle = \left(\frac{\hat{\vec{\mathbf{p}}}^2}{2} + V(\hat{\vec{\mathbf{r}}}) + \hat{\mu}\cdot\vec{E}(t)\right)|\Psi(\vec{r},t)\rangle \tag{2.31}$$

where all terms are expressed in atomic units and the interaction with the electric field is assumed in dipole approximation, with the dipole operator $\hat{\mu} = -e\hat{\vec{\mathbf{r}}}$. The ionic potential of the atom is expressed in $V(\hat{\vec{\mathbf{r}}})$. Alternatively, the electric field can also be expressed via the vector potential in the velocity gauge which reads

$$i\frac{\partial}{\partial t}|\Psi(\vec{r},t)\rangle = \left(\frac{[\hat{\vec{\mathbf{p}}} + \vec{A}(t)]^2}{2} + V(\hat{\vec{\mathbf{r}}})\right)|\Psi(\vec{r},t)\rangle. \tag{2.32}$$

The choice of gauge is mainly due to numerical convenience and shall not be discussed here any further. Remarks on this can be found in [8]. When using linearly polarized laser fields, a one-dimensional treatment often gives reasonable results, where the ionic potential is expressed with a smoothed Coulomb potential [10] (see also section 4.3) to avoid divergences across the origin.

If the ionic potential $V(\hat{\vec{\mathbf{r}}})$ is completely neglected the Schrödinger equation can be solved analytically. The solutions are known as Volkov states which are basically expressed as plane waves in the continuum with kinetic momentum $\vec{p}$ and including the characteristic phase factor

$$\exp\left[-i\int_{-\infty}^{t}\frac{[\vec{p}+\vec{A}(t')]^2}{2}\mathrm{d}t'\right]. \tag{2.33}$$

This phase factor, when the $\vec{p}^2/2$ term containing the electron kinetic energy is singled out, is also known as the Volkov phase and it results from solving Eq. (2.32) in the absence of the ionic potential $V(\vec{r})$.

A starting point for many processes in strong laser fields is the ionization of electrons which will be described in more detail in the following section.

2.2.1 Strong field ionization

The mathematical description of ionization in strong electric fields goes back to the 1960s. In the work of Keldysh [11] the process of ionization in alternating electromagnetic fields was investigated and the parameter

$$\gamma = \sqrt{\frac{I_\mathrm{p}}{2U_\mathrm{p}}}, \tag{2.34}$$

later known as the Keldysh parameter, was introduced. It describes the adiabaticity of the atomic response in the laser field. In the limit $\gamma \ll 1$ the electronic response is fast with respect to the oscillating character of the laser field. This is the so-called tunneling regime, where for the instant of ionization the electric field can be assumed static. In the limit $\gamma \gg 1$, the electric field is oscillating much faster than the time scales of the considered electron. This is the limit where the multi-photon description holds and an integer number of photons $n \cdot \hbar\omega$ are absorbed in order to overcome the ionization potential I_p. The ponderomotive energy U_p (see Eq. (2.28)) is a measure for the strength of the electric field and especially leads to a distinction between the two regimes. The theory has been generalized in subsequent work [12] where explicit formulas for the ionization rate are given. All further derived formulas are very closely related to this original work, as can also be found in a more recent review [13] which may serve as an overview of the Keldysh theory of strong-field ionization.

In the tunneling regime ($\gamma \ll 1$) a widely recognized description of the ionization rate is the so-called ADK formula, noted in [14], where the rate of ionization w_ADK is expressed for arbitrary angular and orbital quantum numbers l and m of the ionized electron, respectively. It is expressed in atomic units and given by

$$\begin{aligned} w_\mathrm{ADK}(t) = \left(\frac{2e}{n^*}\right)^{2n^*} \frac{1}{2\pi n^*} \frac{(2l+1)(l+|m|)!}{2^{|m|}(|m|)!(l-|m|)!} I_\mathrm{p} \left(\frac{3\mathscr{E}(t)}{\pi(2I_\mathrm{p})^{3/2}}\right)^{1/2} \times \\ \left(\frac{2(2I_\mathrm{p})^{3/2}}{\mathscr{E}(t)}\right)^{2n^*-|m|-1} \exp\left[-\frac{2(2I_\mathrm{p})^{3/2}}{3\mathscr{E}(t)}\right] \end{aligned} \tag{2.35}$$

where n^* is the previously introduced effective principal quantum number (see Eq. (2.30)), e is Euler's number and $\mathscr{E}(t)$ is the envelope of the electric field. In deviation from the original description in [14], where a constant envelope $\mathscr{E}_0$ was used (i.e. a monochromatic wave), the time-dependent envelope $\mathscr{E}(t)$ results in an explicitly time-dependent ionization rate $w_\mathrm{ADK}(t)$, averaged over one laser cycle. This formula is also frequently used to express the instantaneous ionization rate of the full electric field $E(t)$. Doing so, the factor $(3\mathscr{E}(t)/\pi(2I_\mathrm{p})^{3/2})^{1/2}$ has to be omitted, as it results from the average over one modulation period of the electric field [15]. It should be also noted, although the validity of Eq. (2.35) is explicitly defined in the tunneling regime ($\gamma \ll 1$), it also yields relatively accurate results for $\gamma \simeq 1$ and is therefore widely used.

In a more recent work [16], a generalized formula for the instantaneous ionization rate is given, valid for arbitrary Keldysh parameters γ. It is also known as the Yudin-Ivanov ionization rate, not explicitly shown here due to its lengthy expression. A comparison between this formula and the ADK rate is shown in Fig. 2.2, where the time-dependent ionization rate is calculated for the example of neon and argon both interacting with a 7 fs FWHM laser pulse of 5×10^{14} W/cm^2 peak intensity.

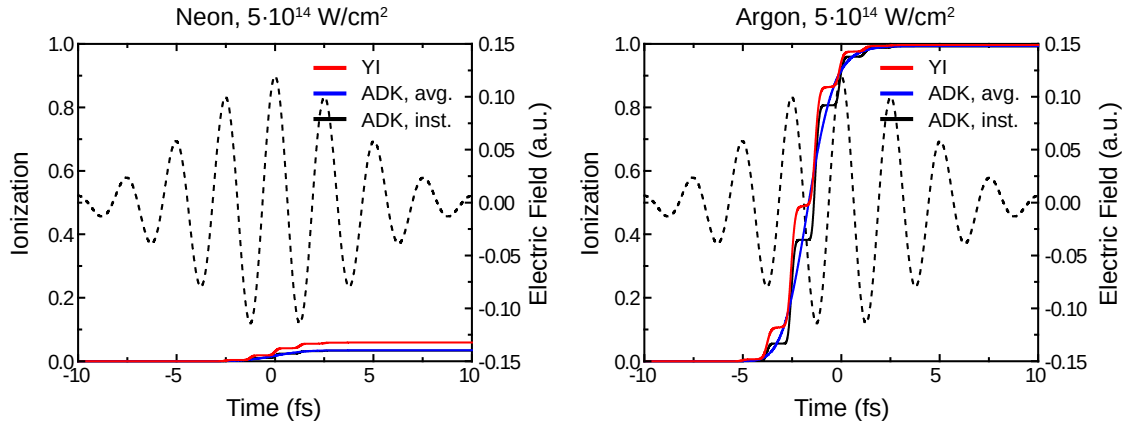

Figure 2.2: Comparison of strong-field ionization from the neon ($I_p = 21.56$ eV) or argon ($I_p = 15.76$ eV) ground state with 7 fs FWHM Gaussian laser pulses at $5 \cdot 10^{14}$ W/cm^2 peak intensity and 760 nm central wavelength. The Yudin-Ivanov (YI) and ADK ionization rates are employed, the latter both with the instantaneous electric field (ADK, inst.) and cycle averaged (ADK, avg.).

As it can be seen in Fig. 2.2, the step-like increase of the instantaneous ionization rate is directly linked to the peaks of the electric field. This implies that strong-field ionization is intrinsically locked to times where the oscillating amplitude exhibits its maximum values. Almost all strong-field processes, as they were shortly outlined at the beginning of this chapter (see also [8]), are described via tunnel ionization as the first step. This temporally well-defined starting point thus explains the underlying sub-cycle nature of many strong-field processes which is a fundamental prerequisite for the results which will be presented in chapter 5.

Another scenario of strong field ionization is an extreme case of tunneling ionization: If the laser field strength is above a critical value $\mathscr{E}_{\text{crit}}$, which in atomic units is defined by

$$\mathscr{E}_{\text{crit}} = \frac{I_p^2}{4Z}, \tag{2.36}$$

the electric field is so strong that the Coulomb barrier is completely suppressed and the bound electron is free to move into the continuum.This is also known as barrier suppression ionization (BSI) [15].

All three mentioned scenarios, multi-photon, tunneling and barrier-suppression ionization are depicted in Fig. 2.3.

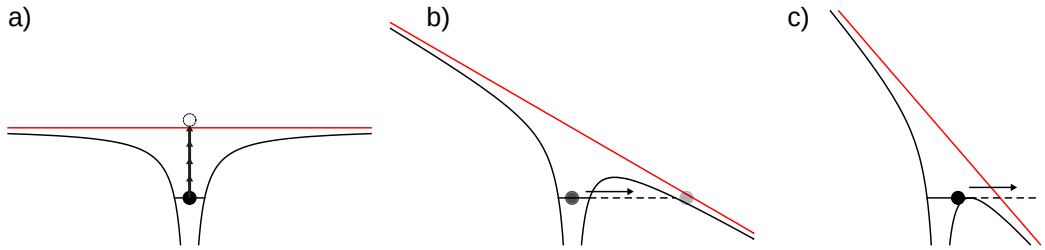

Figure 2.3: Three different scenarios of strong-field ionization in the single-active electron approximation. The atomic potential is shown in black while the laser electric field is shown in red. a) Multi-photon ionization ($\gamma \gg 1$). The electron absorbs many photons (vertical arrows) to overcome the ionization potential. b) Tunneling-ionization. The Coulomb potential is bent and a tunnel-barrier is formed through which part of the electronic wave function can tunnel quantum mechanically. c) Barrier-suppression ionization. The electric field is suppressed below the ionization potential. As a consequence, the bound electron is (classically) free to move into the continuum.

2.2.2 High-order harmonic generation and attosecond pulse production

The aim of this section is to convey some fundamental aspects of high-order harmonic generation (HHG) as it serves as a driver tool for the generation of attosecond pulses used in some of the here presented experiments. While here only a short summary of the most important theoretical aspects is given, a more detailed overview can be found in [8] and also in review articles such as [17, 18]. Being closely related to the investigated experiment in chapter 5, a more detailed overview of attosecond pulse trains will be given in section 5.1. From a more technical point of view, aspects of their generation are also mentioned in section 3.3 in connection to the description of the experimental apparatus.

HHG is an example of strong-field laser–matter interaction which can be understood from a classical perspective [19], where Newton's equations (see Eqs. (2.24)-(2.26)) are able to describe the electron trajectory after the initial tunnel-ionization as it was introduced in the previous section. With these classical equations trajectories can be calculated where the electron is driven away from the ionic core and subsequently may reencounter its parent ion with a certain kinetic energy $E_{\mathrm{kin}}^{(\mathrm{r})}$. At this point the electron may recombine into its original bound state and the difference energy is transferred into a single high-energy photon, with its photon energy given by

$$\hbar\omega_{\mathrm{HHG}} = E_{\mathrm{kin}}^{(\mathrm{r})} + I_{\mathrm{p}}. \tag{2.37}$$

The kinetic energy of such classically calculated recolliding trajectories is depicted in Fig. 2.4. For each kinetic energy, two possible trajectories exist with travel times below one laser cycle. These are known as the short and long trajectories. As this process repeats every half-cycle of the laser field, these half-cycle spaced events interfere. This interference gives rise to harmonic photon energies which are spaced by $2\hbar\omega_{\mathrm{c}}$, where ω_{c} is the fundamental frequency of the laser field. More aspects of this interference will be discussed in chapter 5, where the sub-cycle nature of the harmonic generation process is used to illustrate our novel CEP-resolved spectral interferometry approach. It is this

sub-cycle nature also, which gives rise to attosecond pulses being directly locked to the electric field of the laser pulse. These aspects are also described in section 5.1.

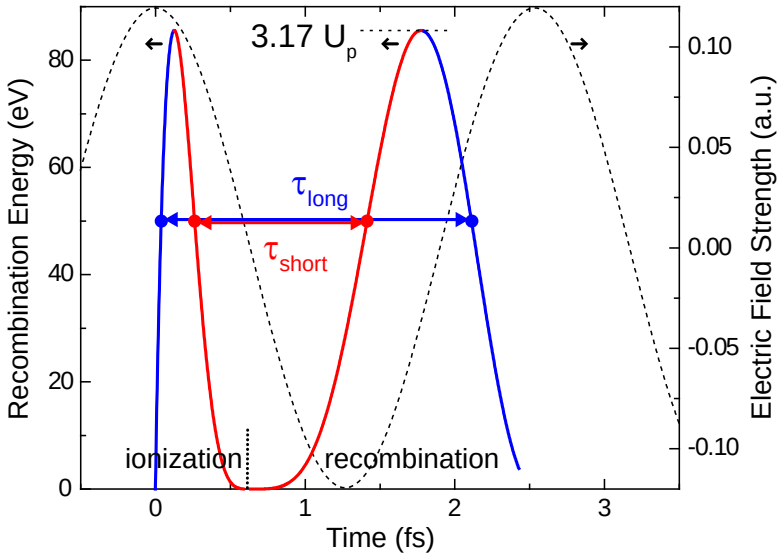

Figure 2.4: Classically calculated kinetic energy of the electrons at recombination, when ionized in a monochromatic electric field (dashed line) of wavelength $\lambda = 760$ nm and strength $\mathscr{E}_0 = 0.12$ a.u. (corresponds to $5 \cdot 10^{14}$ W/cm^2). Both the times of ionization and recombination are shown for each trajectory. A given energy can be reached at two instants of time, corresponding to two electron trajectories. These are categorized by the travel time of the freed electron in the laser field and known as the short (red) and long (blue) trajectories. The highest kinetic energy which can be reached is related to the ponderomotive energy and is given by $\sim 3.17 U_\mathrm{p}$. The vertically dotted line marks the border between ionization and recombination. The small black arrows indicate the scales.

Being an intuitive picture, this classical model of HHG can explain the experimental observation—see e.g. [20] for one of the first experimentally obtained high-harmonic spectra—that a broad range of harmonic photon energies is accessible with relatively equal probability, while a sharp cutoff exists for the highest photon energies. Fig. 2.4 illustrates how this is possible: A broad range of recombination energies is covered by a small window of ionization times ($\lesssim 0.5$ fs). This leads to an extended range of equally probable recombination energies which is also known as the plateau region. Being accelerated in the laser field, the electrons can only acquire kinetic energies up to a certain limit. It is this limit which is responsible for the sharp cutoff in the generated high harmonics, located at ~ 90 eV in Fig. 2.4. As a result, the cutoff law of highest harmonic energies is given by

$$\hbar\omega_{\mathrm{HHG,max}} = 3.17 U_\mathrm{p} + I_\mathrm{p}. \tag{2.38}$$

HHG is also understood within a quantum-mechanical treatment [21] where the laser field is treated classically (see Eq. (2.31)). It employs the strong field approximation (SFA) which also gives name to the model. A detailed description of this quantum-mechanical treatment can also be found in [8]. In conceptual difference to the above-described classical model, the generated harmonic radiation is understood as the quantum-mechanical

interference of different parts of the wave function, i.e. driven by a coherent dipole emission. As such, the tunnel-ionized and "accelerated" part of the electronic wave function interferes with its remaining and still bound part at the ionic core. This gives rise to a rapidly oscillating dipole moment which is the source for the emitted high-harmonic radiation. At this point it shall be mentioned, especially as own work was partly conducted on this [22], that not only the interference of the bound and the continuum part of a wave function gives rise to high-harmonic dipole radiation, as it is commonly understood. In addition, we theoretically demonstrated [22], how the interference of different energetic parts of the continuum wave function, mediated by the fully depleted ionic core, gives rise to coherent high-harmonic dipole emission. A detailed description of this process can be found in [23].

In the quantum-mechanical SFA model the times of ionization and recombination of the electron can be identified in a way which is closely related to the classical model. These times are known as the solutions of a saddle-point analysis. They arise as follows: In the quantum-mechanical model, a highly-oscillating phase term appears, which is given by

$$\exp[-iS(\vec{p}_{\mathrm{can}},t,t')] \tag{2.39}$$

where $S(\vec{p}_{\mathrm{can}},t,t')$ is the quasi-classical action of the electron moving with the canonical momentum $\vec{p}_{\mathrm{can}}$ in the laser field. This action is given by

$$S(\vec{p}_{\mathrm{can}},t,t') = \int_{t'}^{t} \left(\frac{[\vec{p}_{\mathrm{can}} - \vec{A}(t'')]^2}{2} + I_{\mathrm{p}} \right) \mathrm{d}t'', \tag{2.40}$$

where the laser field is expressed via its vector potential $\vec{A}(t)$ (see Eq. (2.27)). To calculate the dipole emission for a given harmonic frequency ω_{HHG}, an integral over all five components—two temporal variables, the time of birth t_{B} and the time of recombination t_{R}, where the latter saddle point results from the Fourier transform into the energy domain as parametrized by ω_{HHG}, and three components of the canonical-momentum vector—of the phase in Eq. (2.39) has to be performed. The action given in Eq. (2.40) varies rapidly as a function of all these variables. Therefore a saddle-point approximation can be performed where the solutions denote configurations of stationary action. The physical picture of this analysis is to identify the set of parameters for an extremal (and thus stationary) phase, which is exactly the definition for the classical path the electron would undergo. Along these lines, the quantum-mechanical treatment of HHG can be understood within Feynman's path integral approach [24]. The solutions for these saddle points are generally complex, which reflects the tunneling nature of the electron path: In order to leave the atom and propagate in the continuum, it first has to tunnel through a potential barrier (see section 2.2.1). With elapsed time below one laser cycle between the ionization and recombination event, also two pairs of saddle points are found for each photon energy, corresponding to the short and the long trajectory. A thorough description of this saddle-point analysis and the related electron quantum paths can be found in [25]. There, the emphasis is on the non-adiabatic nature of few-cycle laser pulses, i.e. that each subsequent half-cycle has to be treated separately.

Fig. 2.5 illustrates these quantum paths for a few-cycle 7 fs FWHM laser pulse of center wavelength 760 nm and peak electric field 0.1033 a.u.—the pulse parameters which

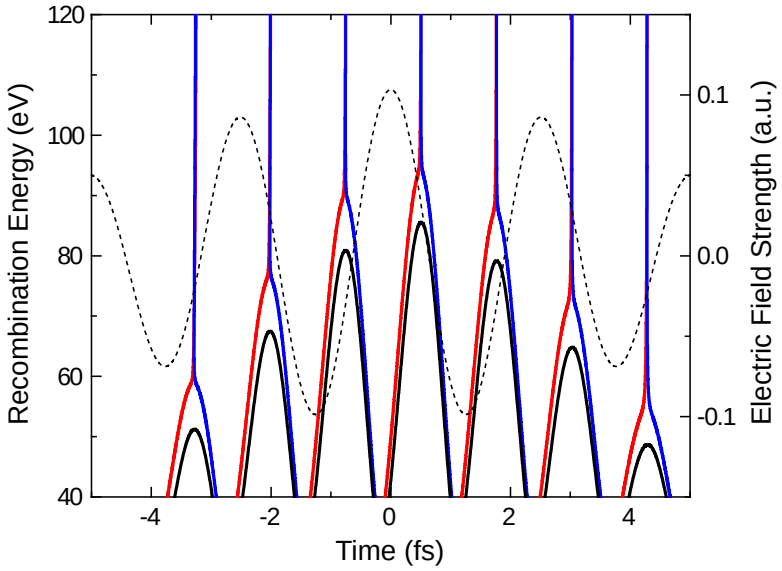

Figure 2.5: The real part of the saddle-point solution which corresponds to the recombination time is shown both for the short (red) and for the long (blue) trajectory. The few-cycle laser field (see text for parameters) is shown as the dashed line. The black lines denote the classically obtained recombination times (compare to Fig. 2.4) both for the short and long trajectory. The solutions of the quantum-mechanical treatment are systematically above the classically-obtained results.

are thoroughly used in section 5.4. It can be seen that the quantum-mechanically obtained solutions acquire systematically higher energies for a given return time than the corresponding classically-obtained solutions. This is known as the quantum-mechanical correction of the cutoff law [21].

2.3 Spectral interferometry and Fourier analysis of spectral patterns

To retrieve the relative amplitude and phase between two laser pulses, the concept of spectral interferometry can be applied. It shares many properties with white-light interferometry [2], where two phase-locked copies of a common light source are created. One copy is sent through a sample from which the linear amplitude and phase response can be retrieved. When applied in a linear way [26], the measurement cannot be sensitive to the spectral phase of the pulses (including their time profile, the reason why the technique is also working with noisy white light), thus only relative quantities can be obtained. Adding however a nonlinear spectral shear across the two pulses, spectral interferometry can also be applied for the direct reconstruction of the spectral phase of ultrashort laser pulses (SPIDER, [27]) up to an arbitrary offset (it is still insensitive to the CEP). In the following, some basic concepts of spectral interferometry including the retrieval procedure of the relative phase will be shortly summarized.

Spectral interferometry can be understood on the basis of a Mach-Zender interferometer (Fig. 2.6). The two pulses propagating along the different arms with a time delay τ can

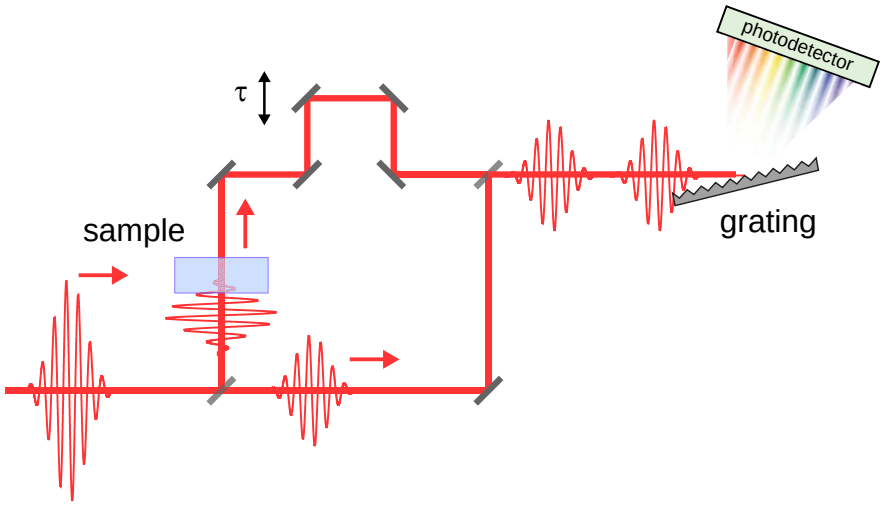

Figure 2.6: Mach-Zender-type illustration for spectral interferometry. A laser pulse is split into two parts which are delayed by τ with respect to each other before being recombined again into a single path. The recombined pulses are spectrally resolved with a grating and measured with a photodetector. The temporal delay induces a sinusoidal modulation pattern $\propto \sin(\omega\tau)$ into the spectrum. Typically a dispersive sample can be put into one arm. The linear response of this sample can be fully—i.e. its amplitude (e.g. absorption) and phase (dispersion)—characterized within this scheme.

be described as two time-dependent electric fields $E_0(t)$ and $E_1(t \quad \tau)$. In the spectral domain, they are given by $E_0^{(s)}(\omega)$ and $E_1^{(s)}(\omega)e^{\ i\omega\tau}$, where $E_n^{(s)}(\omega)$ is the Fourier transform of the time-dependent electric field $E_n(t)$, as defined by Eq. (2.9). The spectral intensity $S(\omega)$ is proportional to $\left|E_0^{(s)}(\omega)+E_1^{(s)}(\omega)e^{\ i\omega\tau}\right|^2$, the coherent sum of the two fields. It is typically detected with the combination of a dispersive element such as a grating and a photon detector, for example a CCD camera. To analyze the recorded signal $S(\omega)$ in more detail, the explicit complex representation $|E_n^{(s)}(\omega)|\exp[i\phi_n(\omega)]$ of the field is considered. The spectral intensity is then proportional to

$$S(\omega) \propto |E_0^{(s)}(\omega)|^2 + |E_1^{(s)}(\omega)|^2 + 2|E_0^{(s)}(\omega)||E_1^{(s)}(\omega)|\cos[\phi_0(\omega) \quad \phi_1(\omega) + \omega\tau], \quad (2.41)$$

Thus, a modulation which depends on the spectral phase difference, $\Delta\phi(\omega) = \phi_0(\omega)$ $\phi_1(\omega)$, is imprinted on the recorded signal. In principle, this difference could be resolved directly from Eq. (2.41) by applying an inverse cosine function and an independent measurement of the power spectrum $|E_n^{(s)}(\omega)|^2$ of each pulse by blocking the other arm of the interferometer. The difficulties using this method are mainly due to experimental noise and divergences of the inverse function. A more elegant method involves the Fourier transform [28] which is often the preferred way of applying spectral interferometry. The time delay τ serves as a carrier "frequency" in the spectral pattern, which contributes to a defined peak in the Fourier transform of the spectral intensity $\mathscr{F}\{S(\omega)\}$. As it is a real function, two peaks appear, both at positive and negative times τ and $\quad\tau$. These correspond to $\exp\{i\Delta\phi(\omega)+i\omega\tau\}$ and $\exp\{\ \ i\Delta\phi(\omega)\quad i\omega\tau\}$, respectively. One of the two peaks can thus be disregarded without loss of information. The time delay τ between

the two pulses has to be large enough so that its Fourier contribution is sufficiently far away from zero, that is where the contribution of the slower varying amplitude functions $|E_n^{(s)}(\omega)|$ can be found. Filtering out the well separated peak at time τ and Fourier transforming back into the frequency domain yields the complex function

$$\begin{aligned}\tilde{S}(\omega) &= \mathscr{F}^{-1}\{\mathscr{F}\{S(\omega)\}\times C(t)\}\\ &= |\tilde{S}(\omega)|\exp[i\Phi(\omega)]\\ &= |E_0^{(s)}(\omega)||E_1^{(s)}(\omega)|\exp\{i[\phi_0(\omega)-\phi_1(\omega)]+i\omega\tau\},\end{aligned} \tag{2.42}$$

with an appropiately chosen filter function $C(t)$. For the work presented here, it is defined piecewise as

$$C(t)=\begin{cases}0 & \text{for } t<t_{\min}-\Delta T\\ \sin^2\left(\frac{t-(t_{\min}-\Delta T)}{\Delta T}\frac{\pi}{2}\right) & \text{for } t_{\min}-\Delta T\le t<t_{\min}\\ 1 & \text{for } t_{\min}\le t\le t_{\max}\\ \cos^2\left(\frac{t-t_{\max}}{\Delta T}\frac{\pi}{2}\right) & \text{for } t_{\max}<t\le t_{\max}+\Delta T\\ 0 & \text{for } t_{\max}+T<t.\end{cases} \tag{2.43}$$

A similar filter can also be used in the spectral domain, replacing all temporal parameters t by the frequency ω or energy E. Such a spectral filter is then applied when analyzing experimental data (in order to avoid discontinuous steps) or when a certain region of interest is selected out of broader spectral range. The phase $\Phi(\omega)$ of the complex function $\tilde{S}(\omega)$ directly incorporates the desired spectral phase difference $\Delta\phi(\omega)$ plus a linear contribution due to the time delay τ. Any linear component of the phase difference $\Delta\phi(\omega)$ can just be considered as an additional time delay and is absorbed in τ. Performing a linear fit to $\Phi(\omega)$ is a way to determine the set time delay and after subtraction from $\Phi(\omega)$, the spectral phase difference $\Delta\phi(\omega)$ is the only remaining quantity. The whole technique is further illustrated in Fig. 2.7, where an up-chirped laser pulse is referenced with a bandwidth-limited pulse of equal spectral distribution. At this point it should be mentioned that the spectral bandwidth of both pulses have to share a common frequency range. Only within this range is the phase difference $\Delta\phi(\omega)$ retrieved, since the modulation amplitude determined by the product $|E_0^{(s)}(\omega)||E_1^{(s)}(\omega)|$ would otherwise be zero. Spectral interferometry can also be applied by directly analyzing the temporal phase of the Fourier-transformed signal in the Fourier-time domain [29, 30], where the temporal filter and the subsequent back transform into the spectral domain are not employed.

Having introduced the concept of spectral interferometry and especially the Fourier analysis applied to it, it is now possible to discuss the Fourier analysis of more general spectral patterns which are created for example by more than two successive temporal events. These events are still defined in the time domain as $E_n(t-t_n)$ and in the spectral domain as $E_n^{(s)}(\omega)e^{-i\omega t_n}$, where again $E_n^{(s)}(\omega)$ is the Fourier transform of $E_n(t)$. The measureable spectral intensity is then given by

$$S(\omega)\propto\sum_n|E_n^{(s)}(\omega)|^2+2\sum_{m>n}|E_n^{(s)}(\omega)||E_m^{(s)}(\omega)|\cos[\Delta\phi_{nm}(\omega)+\omega\tau_{nm}], \tag{2.44}$$

where $\Delta\phi_{nm}(\omega)=\phi_n(\omega)-\phi_m(\omega)$ and $\tau_{nm}=t_n-t_m$ is the spectral phase difference and the relative temporal spacing of the events "n" and "m", respectively. Unfortunately, the direct

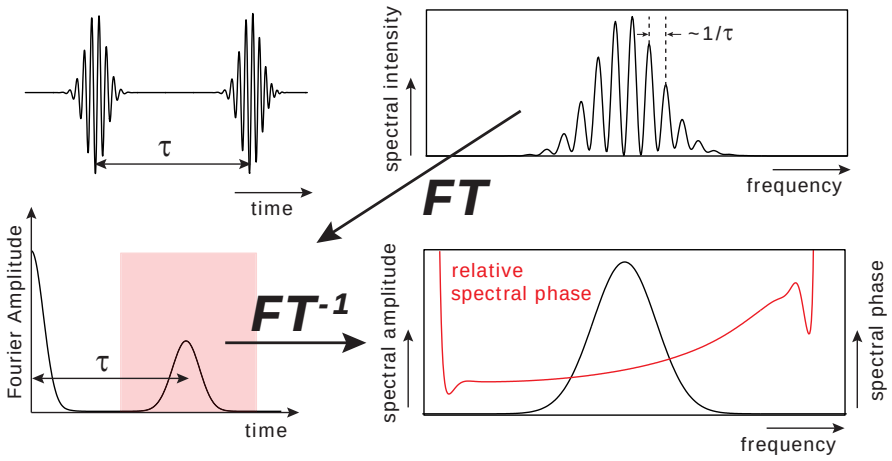

Figure 2.7: Illustration of spectral interferometry. Top left: Two time-delayed (by τ) laser pulses with different phase profiles (the latter pulse is slightly up-chirped). Top right: Spectral interference pattern $S(\omega)$ as recorded with a spectrometer. The fringe spacing corresponds to the time delay τ between the pulses. Bottom left: Fourier transform of the recorded spectrogram. Besides the peak formed at time zero, which corresponds to the summed power spectrum of the two pulses, the separate peak at time τ contains the modulated cross term (see also Eq. (2.41)). Selecting the cross-term contribution with a filter function (red shaded area) and transforming back into the frequency domain yields both the spectral modulation amplitude (black curve) and relative spectral phase (red curve), shown in the bottom right corner. As the linear offset $\omega\tau$ is subtracted, a quadratic increase (corresponding to an up-chirped pulse) is apparent.

retrieval of the relative spectral phase $\Delta\phi_{nm}(\omega)$ is in general no longer unambiguously possible. This is the case whenever temporal spacings τ_{nm} of different pairs of events are equal or overlap within their temporal bandwidth. This is due to the amplitude and phase of the cosine functions in Eq. (2.44) becoming mixed after their summation and cannot be separated in the measured spectra $S(\omega)$. Thus, the corresponding peaks at τ_{nm} in the Fourier representation of the spectral intensity $\mathscr{F}\{S(\omega)\}$ have some overlap.

We can however consider an additional parameter p which enters the spectral intensity $S(\omega, p)$ and influences the relative phases $\Delta\phi_{nm}(\omega, p)$ of the overlapping contributions in a different way. Using this parameter as an additional dimension, its influence on the temporal configuration of the system can be accessed via Fourier analysis and further insight of the underlying physical processes can be gained. This scenario will be discussed in more detail in chapter 5, where the carrier-envelope phase (CEP) of the ultrashort laser pulses plays the role of this additional parameter, by introducing CEP-resolved spectral interferometry (CEPSI).

2.4 Quantum-mechanical wave packets

Quantum wave packets are a direct consequence of the coherent superposition of quantum states. Starting from the time-dependent Schrödinger equation

$$i\hbar\frac{\partial}{\partial t}|\Psi(t)\rangle = \hat{\mathbf{H}}_0|\Psi(t)\rangle \tag{2.45}$$

the Hamilton operator $\hat{\mathbf{H}}_0$ is generating the time-dependence of the wave function $|\Psi(t)\rangle$ which describes the evolution of the quantum system. $|\Psi(t)\rangle$ can be expanded in the eigenstates of the system

$$|\Psi(t)\rangle = \sum_n c_n(t)|\phi_n\rangle + \int \mathrm{d}E\; c(E,t)|\chi_E\rangle\,. \tag{2.46}$$

Here, $|\phi_n\rangle$ represents the discrete (bound) states and $|\chi_E\rangle$ represents the continuous states. The time-dependence is carried by the complex expansion coefficients $c_n(t)$ and $c(E,t)$. Without any external perturbation, $\hat{\mathbf{H}}_0$ is independent of time and its eigenvalues define the energy E_n and E of each discrete and continuous state, respectively. Using Eq. (2.45) the time-dependent expansion coefficients are given by

$$c_n(t) = c_{n,0}\exp\left[-i\frac{E_n}{\hbar}t\right] \tag{2.47}$$

and

$$c(E,t) = c(E,0)\exp\left[-i\frac{E}{\hbar}t\right] \tag{2.48}$$

with their initial values $c_{n,0}$ and $c(E,0)$ at time $t = 0$, when the evolution is considered to begin.

Measureable quantities always involve expectation values of the wave function $|\Psi\rangle$ with respect to some operator. Taking for example the position operator $\hat{\mathbf{r}}$, the quantity $\langle\Psi|\hat{\mathbf{r}}|\Psi\rangle$ is the expectation value for the position of the system. If $|\Psi\rangle$ is an electronic wave function, describing several excited states of an electron bound to an atom then this would be the expectation value of the electron itself. $|\Psi\rangle$ can however also describe any other quantum system such as the vibronic motion of a molecule. Then the above quantity is interpreted as the expectation value of the relative position of the nuclei, i.e. the inter-molecular distance of the two nuclei in a diatomic molecule.

Such an expectation value can be employed to visualize a quantum wave packet, which is defined as a coherent superposition of states as given by Eq. (2.46). Inserting this

superposition into the expectation value yields

$$\begin{aligned}\langle\Psi|\,\hat{\mathbf{r}}\,|\Psi\rangle = \sum_{n,m}\int\int \mathrm{d}E'\mathrm{d}E''\Bigg\{ & c_{n,0}\cdot {c_{m,0}}^{*}\langle\phi_m|\hat{\mathbf{r}}|\phi_n\rangle \exp\left[-i\frac{E_n-E_m}{\hbar}t\right] \\ & + c_{n,0}\cdot c(E'',0)^{*}\langle\chi_{E''}|\hat{\mathbf{r}}|\phi_n\rangle \exp\left[-i\frac{E_n-E''}{\hbar}t\right] \\ & + c(E',0)\cdot {c_{m,0}}^{*}\langle\phi_m|\hat{\mathbf{r}}|\chi_{E'}\rangle \exp\left[-i\frac{E'-E_m}{\hbar}t\right] \\ & + c(E',0)\cdot c(E'',0)^{*}\langle\chi_{E''}|\hat{\mathbf{r}}|\chi_{E'}\rangle \exp\left[-i\frac{E'-E''}{\hbar}t\right]\Bigg\}.\end{aligned} \tag{2.49}$$

From this expansion it can be seen that $\langle\Psi|\,\hat{\mathbf{r}}\,|\Psi\rangle$ is only evolving in time when $|\Psi\rangle$ is a superposition of at least two energetic eigenstates of $\hat{\mathbf{H}}_0$. This is an implicit property of any wave packet, as defined at the beginning of this section. The time evolution is periodic while the cycling period $T_\mathrm{c} = 2\pi\hbar/\Delta E$ is determined by the difference energy ΔE of the involved states. The explicit notation of the complex-valued initial expansion coefficients $c_{n,0}$ and $c(E,0)$ emphasizes the coherent superposition of the involved states. An incoherent superposition cannot be explained using this approach and one must use, for example, the density matrix formalism [31] where dissipative effects (loss of coherence), or incoherent initial conditions, as existing in an ensemble of atoms/molecules, are included. Further theoretical aspects on quantum wave packets, such as the fundamental concepts of quantum theory which were used here, can be found in many text books [32, 33].

2.5 Perturbation theory

The formulation of perturbation theory plays a fundamental role in quantum mechanics and a detailed discussion of this theory can be found in many textbooks. In what follows, the main referencing to the interaction of electromagnetic radiation with atomic and molecular systems was taken from [34]. In general, perturbation theory is useful whenever a quantum system can be described by a Hamiltonian such as

$$\hat{\mathbf{H}} = \hat{\mathbf{H}}_0 + \hat{\mathbf{H}}' \tag{2.50}$$

where $\hat{\mathbf{H}}_0$ is the Hamiltonian of the unperturbed system and $\hat{\mathbf{H}}'$ is a small perturbation to the system. Typically, the unperturbed system can be solved exactly or at least the energy eigenvalues E_n and the eigenstates $|\phi_n\rangle$ are known to an accurate level. For all relevant cases presented in this work, $\hat{\mathbf{H}}'(t)$ will be time dependent and related to the electric field $E(t)$. For completeness, the results up to second order of time-independent perturbation theory (e.g. caused by a weak static field) will first be summarized.

To first order, the energy levels $E_n^{(0)}$ of the unperturbed system $\hat{\mathbf{H}}_0$ will be shifted by the expectation value of the perturbation with the unperturbed states

$$E_n^{(1)} = \left\langle \phi_n^{(0)} \middle| \hat{\mathbf{H}}' \middle| \phi_n^{(0)} \right\rangle \tag{2.51}$$

and to second order, the energy levels are shifted by an amount which is related to the interaction of all unperturbed states of the system

$$E_n^{(2)} = \sum_{m \neq n} \frac{\left| \left\langle \phi_m^{(0)} \right| \hat{\mathbf{H}}' \left| \phi_n^{(0)} \right\rangle \right|^2}{E_n^{(0)} - E_m^{(0)}}. \tag{2.52}$$

These results are valid for the non-degenerate case, i.e. $E_n^{(0)} \neq E_m^{(0)}$, while in the case of degeneracy, where some $E_n^{(0)}$ are equal, the perturbation can lift the degeneracy and can cause a splitting of otherwise equal energy levels. This for example occurs in atoms, where the perturbative coupling of the spin magnetic moment with the angular momentum causes a splitting of energy levels when they have the same principal quantum number n but different angular quantum number l.

For a weak time-dependent perturbation $\hat{\mathbf{H}}'(t)$ transitions can occur between different levels. The natural time evolution of an eigenstate $|\phi_n(t)\rangle$, of the unperturbed system, can be obtained with the time-dependent Schrödinger equation and is given by

$$|\phi_n(t)\rangle = |\phi_n(t=0)\rangle \exp(-iE_n/\hbar t) = |\phi_n\rangle \exp(-i\omega_n t). \tag{2.53}$$

The total wave function $|\Psi(t)\rangle$ can be expanded in this basis and may be expressed via

$$|\Psi(t)\rangle = \sum_n c_n \exp(-i\omega_n t)\,|\phi_n\rangle \tag{2.54}$$

where in the absence of any perturbation the expansion coefficients c_n are constant with time. If $\hat{\mathbf{H}}'(t) \neq 0$ after a time $t = 0$, the coefficients are time dependent ($c_n \equiv c_n(t)$) and to first order are given by

$$c_n^{(1)}(t) = -\frac{i}{\hbar} \int_0^t \mathrm{d}t' \sum_m \langle \phi_n | \hat{\mathbf{H}}'(t) \, |\phi_m\rangle \exp(i\omega_{nm} t) c_m^{(0)}, \tag{2.55}$$

where $\omega_{nm} = \omega_n - \omega_m$ is the difference frequency (or energy, divided by $\hbar$) between the states $|\phi_n\rangle$ and $|\phi_m\rangle$. Eq. (2.55) is very general and can be implemented numerically when an arbitrary time-dependent transition operator $\hat{\mathbf{H}}'(t)$ is perturbatively interacting with a system of states and the time integral cannot be solved analytically.

For a time-dependent electric field $E(t)$, the perturbative interaction with the system in the dipole approximation is given by

$$\hat{\mathbf{H}}'(t) = \hat{\mu} \cdot E(t) = \hat{\mu} \cdot \frac{\mathscr{E}(t)}{2} \cdot (e^{i\omega_c t} + e^{-i\omega_c t}), \tag{2.56}$$

where the pulse here is assumed to be bandwidth limited and $\mathscr{E}(t)$ is the slowly varying temporal envelope of the pulse, and $\hat{\mu}$ is the electric dipole operator $-e\hat{\mathbf{r}}$. Assuming that the system is initially prepared in a state $|\phi_i\rangle$ at $t = 0$, the evaluation of the first-order perturbation is given by

$$c_n^{(1)}(t) = -\frac{i}{\hbar} \mu_{ni} \cdot c_i^{(0)} \int_0^t \mathrm{d}t' \frac{\mathscr{E}(t')}{2} \cdot (\exp[i(\omega_n - \omega_i + \omega_c)t] + \exp[i(\omega_n - \omega_i - \omega_c)t]), \tag{2.57}$$

where $\mu_{ni} = \langle \phi_n | - e\hat{\mathbf{r}}(t) | \phi_i \rangle$ is the dipole matrix element evaluated for the corresponding states. If the pulse is fully contained within the integration limits then Eq. (2.57) is nothing else but the Fourier transform of the time-dependent electric field $E(t)$ to be evaluated at the transition frequency $\omega = \omega_n - \omega_i$. When the interaction with the short laser pulse is over, the first-order expansion coefficients are evaluated to

$$c_n^{(1)} = -\frac{i}{\hbar}\mu_{ni} \cdot c_i^{(0)} \tilde{E}^{(s)*}(\omega_n - \omega_i), \tag{2.58}$$

where $\tilde{E}^{(s)}(\omega) = \mathscr{F}\{E(t)\}$ is the complex Fourier transform of the real electric field as defined by Eq. (2.9) and is the reason for the appearance of the complex conjugate $\tilde{E}^{(s)*}(\omega)$. The explicit notation of the two exponential terms in Eq. (2.57) allows further interpretation because the carrier frequency ω_c of the laser field is always larger than zero. Both the excitation of the system ($\omega_n - \omega_i > 0$), i.e. taking energy from the laser field is described (where the second exponential term is close to resonance), as well as the system's deexcitation ($\omega_n - \omega_i < 0$), which puts energy into the laser field is contained in Eq. (2.57) and corresponds to the first exponential term then being close to resonance. Both cases are naturally contained in the Fourier domain representation in Eq. (2.58) as the Fourier transform of a real function evaluates both at positive and negative frequencies. The two cases also describe nothing else but the stimulated absorption or emission of radiation.

With Eqs. (2.57) and (2.58) two extreme cases of perturbative electric fields can be discussed. An infinitely short pulse, represented by a delta function, and an infinitely long pulse, represented by a monochromatic wave. The first case, an infinitely short excitation or deexcitation, is already described by Eq. (2.58), where the spectral representation of the pulse turns into a proportionality constant, as the spectrum of an infinitely short pulse is equal for all frequencies. It is important to see that the phase factor $-i$ and the dipole factor μ_{ni} still remain, thus the (de-)excited states always evolve with a different phase with respect to the initial state, also after the interaction with an infinitely short pulse.

For a monochromatic wave of frequency ω_c and field strength E_0, the time integral in Eq. (2.57) can be performed analytically. The physical meaning of the result is best analyzed with $|c_n^{(1)}(t)|^2$ which is understood as the probability of finding the system in the state $|\phi_n\rangle$ at time t. It is finally given by

$$|c_n^{(1)}(t)|^2 = \frac{2\pi}{\hbar^2}|\mu_{ni}|^2 \frac{E_0^2}{4} t\, \delta(\omega_n - \omega_i \pm \omega_c) \tag{2.59}$$

for large times t. Division of Eq. (2.59) by the time t then yields the final result of a constant transition rate

$$W_{ni} = \frac{|c_n^{(1)}(t)|^2}{t} = \frac{2\pi}{\hbar^2}|\mu_{ni}|^2 \frac{E_0^2}{4} \delta(\omega_n - \omega_i \pm \omega_c) \tag{2.60}$$

which is also known as Fermi's golden rule, except for the missing density of states, as just one state was considered here. The $\pm$ sign in Eq. (2.59) and (2.60) again corresponds to cases where the transition energy is put into (stimulated emission) or absorbed from (stimulated absorption) the electric field. In both cases, the population of the initial state $|\phi_i\rangle$ was assumed unity ($|c_i^{(0)}|^2 = 1$).

In general, the here presented perturbative treatment is only valid for small changes of the system. For a time-independent perturbation, the shift of energy levels is only described accurately within this treatment if the calculated shift is small enough, or rather, small with respect to the distance to other states which are involved. For a time-dependent perturbation, only a small amount of population is transferred between the states. In particular this means, that the initial state $|\phi_i\rangle$, which is most often the ground state $|g\rangle$ of the system is not depleted, its population remains constant at all times ($\partial_t c_g(t) = 0$). The amount of population $|c_n^{(1)}(t)|^2$ which is transferred into the states $|\phi_n\rangle$ is seen proportional to the intensity E_0^2 of the laser field, which means that the laser intensity needs to be small enough for the validity of the perturbative treatment.

2.6 Two-level system

So far, the interaction of a system of states with an oscillating electric field was only described perturbatively. If the intensity of the oscillating field increases, a higher fraction of the population will transfer between the states which then necessitates a treatment beyond perturbation theory. The new effect which arises from higher field intensities is a significant population transfer between the involved states. The population can also be transferred back and forth between the states and is commonly known as Rabi oscillations [35]. Furthermore, the energy levels are also observed to shift when they are strongly coupled with the laser field, which is known as the Autler Townes effect or AC Stark splitting [36]. All these effects can most easily be described with only two states $|\phi_n\rangle$ and $|\phi_m\rangle$, and the interaction with a monochromatic field whose frequency is close to the transition frequency between the two states ($\omega_\mathrm{c} \approx \omega_{nm}$).

As defined in the previous chapter, the Hamiltonian of the system can be written as

$$\hat{\mathbf{H}} = \hat{\mathbf{H}}_0 + \hat{\mu} \cdot E(t) \tag{2.61}$$

which now only acts on the superposition of two states

$$|\Psi(t)\rangle = c_\mathrm{n}(t)\,|\phi_\mathrm{n}\rangle + c_\mathrm{m}(t)\,|\phi_\mathrm{m}\rangle\,. \tag{2.62}$$

The Schrödinger equation is then transformed into a set of coupled linear differential equations for the time-dependent coefficients $c_{\mathrm{n,m}}(t)$ which can be given in matrix form as

$$i\hbar \frac{\mathrm{d}}{\mathrm{d}t} \begin{pmatrix} c_n(t) \\ c_m(t) \end{pmatrix} = \mathbf{H}_\mathrm{2LS} \cdot \begin{pmatrix} c_n(t) \\ c_m(t) \end{pmatrix} \tag{2.63}$$

with the coupling matrix

$$\mathbf{H}_\mathrm{2LS} = \begin{pmatrix} E_n & \mu_\mathrm{nm} \cdot E(t) \\ \mu_\mathrm{nm}^* \cdot E(t) & E_m \end{pmatrix} \tag{2.64}$$

where E_n and E_m are the energies of the field-free system $\hat{\mathbf{H}}_0$ and μ_nm are the dipole matrix elements as defined just below Eq. (2.57). The matrix in Eq. (2.64) can also be generalized to more than two states. The diagonal elements always contain the energy of the

corresponding state, while the off-diagonal elements describe the interaction (coupling) between the states. The set of equations as given in Eq. (2.63) can also be considered as the most fundamental starting point for a numerical treatment, whenever a finite number of states $|\phi_n\rangle$ is relevant for the physical mechanism to be described. Approximate analytical solutions are only possible for certain specific cases, however they contain further physical insight such as the discussion and understanding of the above mentioned effects.

To solve the system in Eq. (2.63), the coefficients are rotated in phase such that

$$c_{\mathrm{n}}(t) = \tilde{c}_{\mathrm{n}}(t)\exp[-i(\omega_n - \Delta/2)t] \tag{2.65}$$

and

$$c_{\mathrm{m}}(t) = \tilde{c}_{\mathrm{m}}(t)\exp[-i(\omega_m + \Delta/2)t], \tag{2.66}$$

where $\Delta = (\omega_{\mathrm{n}} - \omega_{\mathrm{m}}) - \omega_{\mathrm{c}}$ is the detuning of the laser frequency from the transition frequency between the two levels. Expressing the electric field as

$$E(t) = \mathscr{E}_0 \cos\omega_{\mathrm{c}} t = \frac{\mathscr{E}_0}{2}\left[\exp(i\omega_{\mathrm{c}} t) + \exp(-i\omega_{\mathrm{c}} t)\right] \tag{2.67}$$

and using the rotating wave approximation, which means that rapidly oscillating phase terms with frequency $(\omega_{\mathrm{n}} - \omega_{\mathrm{m}}) + \omega_{\mathrm{c}}$ are neglected, a new set of equations as given in Eq. (2.63) is obtained, but now for the coefficients $\tilde{c}_{\mathrm{n,m}}(t)$ with the corresponding matrix

$$\mathbf{H}_{\mathrm{2LS}}^{(\mathrm{rot})} = \frac{\hbar}{2}\begin{pmatrix} \Delta & \Omega_{\mathrm{R}} \\ \Omega_{\mathrm{R}}^{*} & -\Delta \end{pmatrix} \tag{2.68}$$

in the rotating frame which contains the Rabi frequency $\Omega_{\mathrm{R}} = \mu_{\mathrm{nm}}\mathscr{E}_0/\hbar$. The eigenvalues of this matrix are given by

$$\lambda_{1,2} = \pm\frac{\hbar}{2}\sqrt{\Delta^2 + |\Omega_{\mathrm{R}}|^2}. \tag{2.69}$$

These eigenvalues are the new energies of the system which is time-independent and known as the laser-dressed states. They each appear centered around both energy levels, which were defined in the rotating frame with Eqs. (2.65) and (2.66). Thus the old energy levels E_{n} and E_{m} are now described in the presence of a monochromatic and detuned laser field by

$$E_{\mathrm{n}}^{\pm} = E_{\mathrm{n}} - \frac{\hbar\Delta}{2} \pm \frac{\hbar}{2}\sqrt{\Delta^2 + |\Omega_{\mathrm{R}}|^2} \tag{2.70}$$

and

$$E_{\mathrm{m}}^{\pm} = E_{\mathrm{m}} + \frac{\hbar\Delta}{2} \pm \frac{\hbar}{2}\sqrt{\Delta^2 + |\Omega_{\mathrm{R}}|^2}. \tag{2.71}$$

The repulsion of both energy levels, due to near-resonant coupling with an oscillating field, is commonly known as AC Stark splitting. An illustration of the shifted energy levels is depicted in Fig. (2.8). In the limit of low field intensities or weak coupling ($|\Omega_{\mathrm{R}}|^2 \ll \Delta^2$) both uncoupled energy levels E_{n} and E_{m} are contained in the corresponding dressed system. Due to laser coupling, the other level respectively appears at energetic positions which are determined by the detuning Δ. For high field intensities or strong coupling, Δ^2 can be neglected and the difference between each new pair of energy levels is just proportional to the Rabi frequency $\hbar|\Omega_{\mathrm{R}}|$. These are centered around the mean

value of each pair of dressed states in the low field limit. If an additional weak laser is used to probe the transition from a third level across any of the two coupled states $|\phi_{n,m}\rangle$, then the two absorption lines can be measured according to Eq. (2.70) or (2.70) when the coupling laser is on. This set of two measured absorption lines is known as an Autler-Townes doublet or the observation is often referred as the Autler Townes effect [36].

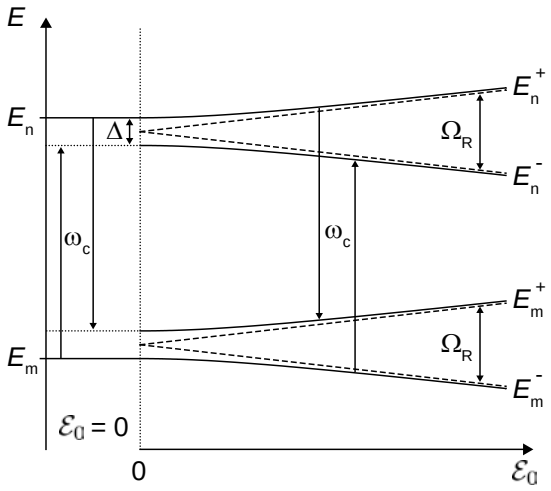

Figure 2.8: Two states $|n\rangle$ and $|m\rangle$ are coupled with a monochromatic field $\mathscr{E}_0\cos(\omega_c t)$. In the laser field, new states are formed which mutually repel each other with increasing field strength, corresponding to Eqs. (2.70) and (2.71). The dashed lines indicate the limit for high laser intensities ($|\Omega_R|^2 \gg \Delta^2$).

To obtain the shifted energy levels of Eqs. (2.70) and (2.71), the diagonalization of the coupling matrix in Eq. (2.68) is required. As a result, these new levels of the constantly driven system are stationary in time with constant population. Looking into the dynamics of the system, the time-dependent solution of the coefficients $\tilde{c}_{n,m}(t)$ needs to be evaluated and will lead to a physical interpretation of the Rabi frequency. The solutions are

$$\tilde{c}_n(t) = -i\frac{\Omega_R}{\Omega'_R}\sin\left(\frac{\Omega'_R}{2}t\right) \tag{2.72}$$

and

$$\tilde{c}_m(t) = \cos\left(\frac{\Omega'_R}{2}t\right) + i\frac{\Delta}{\Omega'_R}\sin\left(\frac{\Omega'_R}{2}t\right) \tag{2.73}$$

with the generalized Rabi frequency given by $\Omega'_R = \sqrt{|\Omega_R|^2 + \Delta^2}$ and the initial condition of all population in the lower state at time zero ($\tilde{c}_n(0) = 0$ and $\tilde{c}_m(0) = 1$). From Eqs. (2.72) and (2.73) it can be seen that the population (i.e. $|\tilde{c}_{n,m}|^2$) oscillates back and forth between the two levels with the Rabi frequency Ω_R or in case of non-zero detuning Δ with the generalized Rabi frequency Ω'_R, completing one full Rabi cycle $2\pi/\Omega'_R$. The complex coefficients also show that their phase jumps by a value of π every other Rabi cycle, so full periodicity in the coefficients themselves is obtained every second Rabi cycle or at a rate half the (generalized) Rabi frequency. The Rabi frequency is therefore also a characteristic measure of the dynamics of the system. When the lifetime of the states (which thus far has been assumed infinitely long) becomes comparable to the Rabi cycle

new effects will arise as will be discussed for autoionizing states in strong fields [37] in chapter 2.7.2.

In most intuitive terms, one can think of changing the line width (i.e. the life time) of a fastly decaying state $|a\rangle$. If such a state is strongly coupled to another state $|b\rangle$ of longer life time, and the coupling laser intensity is chosen such that the Rabi cycle approaches the life time of the fastly decaying state $|a\rangle$, the population can "escape" the fast decay as it is coupled to the longer living state $|b\rangle$ before its natural decay, which effectively extends the life time of state $|a\rangle$. Thus, the laser intensity even of a monochromatic wave can also be considered a dynamical parameter, as it dynamically influences the system in terms of the Rabi frequency.

For short laser pulses with a changing envelope function $\mathscr{E}(t)$ one could in principle also define a time-dependent Rabi frequency $\Omega_{\mathrm{R}}(t) = \mu_{\mathrm{nm}}\mathscr{E}(t)/\hbar$. However, if the envelope of the electric field changes rapidly with time compared to the Rabi cycle, the definition of a time-dependent Rabi frequency does not have an easy interpretation (if at all), and the underlying equations are then better solved numerically.

As a final remark, the "$-i$" factor in Eq. (2.72) of the upper state shows the same phase delay with respect to the lower state as in the case of perturbative excitation given for example in Eq. (2.57). The phase difference between the states is a direct consequence of the Schrödinger equation and thus has to appear in both treatments. The same phase shift is also known from classical mechanics, where the resonantly driven oscillation of a system is $\pi/2$ out of phase with respect to periodic driving force.

2.7 Autoionization

The theory of autoionization is most easily understood with Fano's description of configuration interaction and goes back to the early 1960s [38]. The description can be considered as a rather general formalism which is applicable whenever different pathways are possible and interfere, in particular when these pathways involve both discrete and continuous parts. This is exactly the case in helium when both electrons are excited simultaneously and for which this formalism can be applied.

2.7.1 Fano's original work

Fano's theory of configuration interaction [38] describes a bound state $|\varphi\rangle$ which is embedded within a set of continuum states $|\chi_E\rangle$. In other words, the energy E_φ of the bound state is degenerate with the energetic spectrum E of the continuum states. If both the continuum states and the bound state interact, neither $|\varphi\rangle$ nor $|\chi_E\rangle$ are eigenstates of the complete system. However, these states can be chosen as a full basis set which the new eigenstate $|\Psi_E\rangle$ is expanded into. In Fano's original treatment, the problem is described time-independently and completely expressed in the energy domain. Extensions to this model in order to include strong laser fields and Rabi cycling between autoionizing states will be presented after first introducing Fano's time-independent theory.

First, the system is described in absence of any external field. The Hamiltonian $\hat{\mathbf{H}}$ needs to be diagonalized, where its interaction with the configuration states is given by

$$\begin{aligned} \langle\varphi|\hat{\mathbf{H}}|\varphi\rangle &= E_\varphi \\ \langle\chi_{E'}|\hat{\mathbf{H}}|\varphi\rangle &= V_{E'} \\ \langle\chi_{E''}|\hat{\mathbf{H}}|\chi_{E'}\rangle &= E'\delta(E''-E'). \end{aligned} \tag{2.74}$$

The ground state $|g\rangle$ of the system is neglected in this description which is justified as it can be assumed far away in energy from the states of interest. It will later be introduced when a transition $\hat{\mathbf{T}}$ into these configuration states is described. The off-diagonal term $V_{E'}$ is the configuration-interaction matrix element which describes the interaction of the discrete state at energy E_φ with a continuum state at energy E', therefore it in general depends on E'. The eigenstates $|\Psi_E\rangle$ of the system after diagonalization can be expanded in a complete basis set

$$|\Psi_E\rangle = a_E\,|\varphi\rangle + \int \mathrm{d}E' b_{EE'}\,|\chi_{E'}\rangle\,, \tag{2.75}$$

and the problem now is shifted to the determination of the energy-dependent expansion coefficients a_E and $b_{EE'}$, while the diagonalized eigenstates $|\Psi_E\rangle$ are assumed to fulfill the equation

$$\langle\Psi_E|\hat{\mathbf{H}}|\Psi_E\rangle = E. \tag{2.76}$$

The solution of a_E and $b_{EE'}$ involves some algebra which is described in detail in [38]. The first step is to evaluate Eq. (2.76) with the expansion of Eq. (2.75) and using Eqs. (2.74) to evaluate the matrix elements, which results in a set of two equations relating the two coefficients a_E and $b_{EE'}$. Then one of these two equations can be solved for one coefficient and inserted into the other remaining equation which then cancels one of the two coefficients. The remaining coefficient is then determined by normalization

$$\langle\Psi_E|\,\Psi_{\bar{E}}\rangle = \delta(E-\bar{E}) \tag{2.77}$$

which solves the complete problem. Exactly this was done by Fano in his paper [38], where scattering theory was applied to circumvent some peculiarities of the continuous spectrum like the division by $E-E'$, which is zero for $E=E'$ and has to be treated properly. The final results for the two unknown expansion coefficients are

$$a_E = \frac{\sin\Delta_E}{\pi V_E} \tag{2.78}$$

and

$$b_{EE'} = \frac{V_{E'}}{\pi V_E}\frac{\sin\Delta_E}{E-E'} - \delta(E-E')\cos\Delta_E, \tag{2.79}$$

where Δ_E is given by

$$\Delta_E = -\arctan\frac{\pi\,|V_E|^2}{E-E_\varphi-F(E)} \tag{2.80}$$

and the energy shift $F(E)$ is

$$F(E) = \mathscr{P}\int \mathrm{d}E'\frac{|V_{E'}|^2}{E-E'}. \tag{2.81}$$

The eigenstates are then finally expressed as

$$|\Psi_E\rangle = \frac{\sin\Delta_E}{\pi V_E}|\Phi\rangle - \cos\Delta_E|\chi_E\rangle \tag{2.82}$$

with the *modified* bound state

$$|\Phi\rangle = |\varphi\rangle + \mathscr{P}\int \mathrm{d}E' \frac{V_{E'}}{E-E'}|\chi_{E'}\rangle\,. \tag{2.83}$$

In the above equations, $\mathscr{P}$ denotes the principal value of the integral, i.e. circumventing the pole at $E = E'$ via integration in the complex plane. The argument of the arctan in Eq. (2.80) is a dimensionless number and can be expressed as

$$\varepsilon = \frac{E-(E_\varphi + F(E))}{\Gamma/2} = \frac{E-E_\Phi}{\Gamma/2} \tag{2.84}$$

with

$$\Gamma = 2\pi|V_E|^2\,. \tag{2.85}$$

The appearance of a *modified* bound state $|\Phi\rangle$ means that a set of continuum states $|\chi_{E'}\rangle$ is directly mixed into the original bound state $|\varphi\rangle$ due to the configuration interaction $V_{E'}$. The reduced energy variable ε causes a rapid change in the expansion of the state $|\Psi_E\rangle$ around $E = E_\Phi$ within the energy range Γ. It is thus straightforward to interpret E_Φ as the resonance position of the *modified* bound state $|\Phi\rangle$ and Γ being its width, consequently h/Γ its lifetime due to autoionization into the continuum states $|\chi_E\rangle$. As the sine and cosine functions in Eq. (2.82) are odd and even functions of the reduced energy variable ε, the two configurations $|\Phi\rangle$ and $|\chi_E\rangle$ interfere constructively and destructively on either side of the resonance energy E_Φ which gives rise to an asymmetric line shape. The asymmetry can best be parametrized when the transition $\hat{\mathbf{T}}$ into the state $|\Psi_E\rangle$ is considered. The transition from an initial state (e.g. the ground state $|g\rangle$) is described as $\langle\Psi_E|\hat{\mathbf{T}}|g\rangle$. The probability of transition into $|\Psi_E\rangle$ with respect to the probability of transition $\langle\chi_E|\hat{\mathbf{T}}|g\rangle$ into the undisturbed (usually flat) continuum states $|\chi_E\rangle$ (as if the bound state $|\varphi\rangle$ was not there) can then be parametrized as

$$\frac{\left|\langle\Psi_E|\hat{\mathbf{T}}|g\rangle\right|^2}{\left|\langle\chi_E|\hat{\mathbf{T}}|g\rangle\right|^2} = \frac{|q+\varepsilon|^2}{1+\varepsilon^2}. \tag{2.86}$$

The asymmetry parameter q is expressed as

$$q = \frac{\langle\Phi|\hat{\mathbf{T}}|g\rangle}{\pi V_E^*\langle\chi_E|\hat{\mathbf{T}}|g\rangle} \tag{2.87}$$

which is the ratio of the transition into the *modified* bound state $|\Phi\rangle$ divided by πV_E^* (corresponding to the first term in Eq. (2.82)) and the undisturbed continuum states $|\chi_E\rangle$ (corresponding to the second term in Eq. (2.82)). The complex conjugate of V_E appears in Eq. (2.87) as the final bra state $\langle\Psi_E|$ is used to parametrize the transition.

The term on the right-hand side in Eq. (2.86) is the well known Fano line shape, which can be measured in an experiment. It is proportional to the cross section σ_E appearing

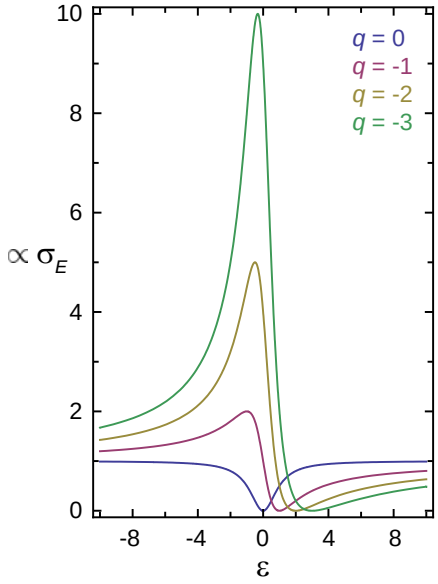

Figure 2.9: The Fano line shape of Eq. (2.86) is shown for different asymmetry parameters as a function of the reduced energy $\varepsilon = (E - E_\Phi)/(\Gamma/2)$. Due to the intrinsic interference among the configuration states, values below 1 are obtained, which is the continuum absorption in the absence of the bound state.

both in the absorption spectrum of the transition $\langle \hat{\mathbf{T}} \rangle_E$, for instance photoabsorption as described in this work, as well as it can appear in the emission spectrum of particles leaving the system and hitting a detector. The above cross section σ_E then denotes the microscopic probability of the process, when an energy E with respect to the ground state $|g\rangle$ is put into the system. For several values of q, Eq. (2.86) is plotted as a function of the reduced energy variable ε in Fig. (2.9). The Fano cross section is taking zero values at different energetic positions (depending on the value of q), which is a direct consequence of the destructive interference of the configuration states. The probability of exciting the state $|\Psi_E\rangle$ around these energy values is lower as if the bound state $|\varphi\rangle$ was not present, thus enhanced transparency is an intrinsic feature of the here presented case of configuration interaction due to destructive interference. In the extreme case of $q = 0$, which means that the direct transition pathway to the state $|\Phi\rangle$ is suppressed, while it is still there and finite configuration interaction V_E with the continuum $|\chi_E\rangle$ occurs, the destructive interference causes the relative transition probability to be always smaller than unity. These cases are thus also termed window resonances. Far from resonance ($|\varepsilon| \gg 1$), the relative transition probability is approaching unity, therefore the bound state $|\varphi\rangle$ can only significantly influence the surrounding continuum states $|\chi_E\rangle$ within the autoionization width Γ.

For fitting the Fano resonance profile to experimentally obtained data, a line profile

$$\sigma_E = a \cdot \frac{|q+\varepsilon|^2}{1+\varepsilon^2} + \sigma_{\mathrm{NR}} \tag{2.88}$$

is commonly used, where a scales the relative strength of the asymmetric profile (also including experimental parameters like the detector efficiency or the target density) with respect to the non-resonant background part σ_{NR} which describes the interaction with

other continua $|\xi_E\rangle$ not taking part in the configuration interaction with the bound state (which are either microscopically suppressed or could also be attributed to a different target species present in the experiment).

2.7.2 Autoionizing states in strong fields

In the previous section, autoionizing states were only considered to be weakly excited within a fully time-independent picture. When stronger fields are used, non-perturbative effects such as Rabi cycling are expected to occur, which however will be different as compared to usual bound states due to the autoionizing nature of the states. This was analyzed in detail by Lambropoulos and Zoller [37] who introduced an analytical framework to describe the interaction of autoionizing states with strong laser fields. In the following, the basic ideas and main results of this work will be summarized in brief.

The basic idea is to use the diagonalized states $|\Psi_E\rangle$ of Eq. (2.82) which Fano obtained and then non-perturbatively describe the coupling between these states and another state $|g\rangle$ which could for example be the ground state. The system is then described as a superposition of these states

$$\left|\tilde{\Psi}(t)\right\rangle = c_g(t)\,|g\rangle + \int \mathrm{d}E' c_{E'}(t)\,|\Psi_{E'}\rangle \tag{2.89}$$

which is subjected to the full Hamiltonian in dipole approximation

$$\hat{\mathbf{H}} = \hat{\mathbf{H}}_0 + \hat{\mu}\cdot E(t). \tag{2.90}$$

Both states $|g\rangle$ and $|\Psi_E\rangle$ are eigenstates of $\hat{\mathbf{H}}_0$ where the configuration interaction was already considered. The time evolution of the coefficients $c_g(t)$ and $c_{E'}(t)$ is therefore determined by the coupling $\hat{\mu}\cdot E(t)$ which is caused by a time-dependent electric field. The coupling can then be solved along the same lines as described for the two level system in section 2.6, which means that the electric field is taken as a monochromatic wave and the rotating wave approximation is applied. Doing so is however far more complicated due to the continuous nature of the autoionizing states $|\Psi_E\rangle$ which involves an energy integration for the expansion coefficient $c_{E'}(t)$.

The main results of [37] are the identification of an effective Rabi frequency

$$\tilde{\Omega}_\mathrm{R} = \langle\Phi_E|\,\hat{\mu}\,|g\rangle\,\mathscr{E}_0/\hbar \tag{2.91}$$

which directly incorporates autoionization because the *modified* bound state $|\Phi_E\rangle$ is used. Interference effects due to the mixing with the continuum $|\chi_E\rangle$ are therefore directly encoded into the Rabi frequency. Furthermore, due to the strong coupling of the bound state $|g\rangle$ directly with the continuum $|\chi_E\rangle$, a so-called radiation-induced shift S_g and width γ_g of the bound state is also present. Finally, the formalism also revealed an additional factor $(1-i/q)$ appearing together with the effective Rabi frequency. The exact definitions of the above quantities can be found in [37] or also in follow-up papers [39–43] which apply the developed formalism in a related context. It is explicitly stated that strong coupling of autoionizing states as described in [37] is not just the coupling of discrete states with finite

lifetime h/Γ. It is important to note that the continuum and especially the accompanying interference effects otherwise would not be present.

Finally, the strong coupling of more than one autoionizing state was also considered and discussed, i.e. adding more autoionizing states $\sum_n \int \mathrm{d}E' c_{E'}^{(n)}(t) \left|\Psi_{E'}^{(n)}\right\rangle$ into the expansion of the wave function in Eq. (2.89). In this case, the basic processes can also be cast into parameters such as effective Rabi frequencies and radiation-induced shifts and widths similar to the ones introduced above. The laser-induced coupling of different continua $\left|\chi_E^{(n,m)}\right\rangle$ (belonging to different autoionizing states $\left|\Psi_{E'}^{(n,m)}\right\rangle$) is now possible in principle. This complication was mentioned in [37] and can be neglected for not too high laser intensities. Significant contributions of this channel where the whole developed model may become unreliable were expected at intensities above maybe 10^{14} W/cm^2 [37]. It can thus be safely neglected in the 10^{12} W/cm^2 intensity regime discussed in this thesis.

Within the developed framework, the line shape of autoionizing resonances coupled by a strong laser field can be described. For example, a weak (perturbative) field is inducing the transition from the ground state to an autoionizing resonance, which in turn is strongly coupled to another autoionizing state. This scenario is also realized in helium where own measurements will be presented in chapter 6. As for the strong coupling of usual bound states, an Autler-Townes doublet is formed. Due to the interference effects of configuration interaction, it is possible that the line shape and especially the width of the two lines appearing within the doublet are changing differently as a function of the coupling laser electric field strength. This would not be the case for strongly coupled incoherently decaying bound states, where the shape of the splitted lines is equal, even for unequal (incoherent) life times.

A summarizing review for two-electron atoms in strong laser fields can be found in [44].

2.8 The theory of linear absorption

Absorption of classical electric fields after transmission through macroscopic media is most straightforwardly described via the dielectric susceptibility $\chi(\omega)$ which connects the electric field $E^{(\mathrm{s})}(\omega)$ to the macroscopic polarization $P^{(\mathrm{s})}(\omega)$ of the medium:

$$P^{(\mathrm{s})}(\omega) = \varepsilon_0 \chi(\omega) \cdot E^{(\mathrm{s})}(\omega), \tag{2.92}$$

where only the linear response is considered. A detailed description of absorption and coherence effects also connected to nonlinear orders $\chi^{(i)}(\omega)$ can be found in [45, 46], which shall serve as references for the linear case discussed here.

The refractive index $n(\omega) = \sqrt{1+\chi(\omega)}$ connects the wave vector

$$k(\omega) = \frac{\omega}{c} \cdot \sqrt{1+\chi(\omega)} \approx \frac{\omega}{c} \cdot \left(1 + \frac{\chi'(\omega)}{2} + i \cdot \frac{\chi''(\omega)}{2}\right) \tag{2.93}$$

with the real and imaginary part of the dielectric susceptibility which is assumed to be small. Otherwise the full propagation obeying Maxwell's equations would need to be

solved as then dispersion and absorption can no longer be decoupled which is the essence of the approximation in Eq. (2.93). The imaginary part of Eq. (2.93) is identified as the absorption coefficient

$$\alpha(\omega) = \frac{\omega}{c} \cdot \chi''(\omega) \tag{2.94}$$

which according to Beer–Lambert's law

$$I(\omega, z) = I_0(\omega) \exp[-\alpha(\omega) \cdot z] \tag{2.95}$$

describes the attenuation of the incident light intensity $I_0(\omega)$ after propagating a distance l. The connection to microscopic quantities is found with the atomic number density ρ_N which yields

$$\alpha(\omega) = \rho_N \cdot \sigma(\omega). \tag{2.96}$$

and

$$P^{(\mathrm{s})}(\omega) = \rho_N \cdot \mu(\omega), \tag{2.97}$$

where $\mu(\omega)$ is the dipole expectation value of the system. With these relations, the microscopic cross section is found to be

$$\sigma(\omega) = \frac{1}{\rho_N} \frac{\omega}{c} \mathrm{Im}\,(\chi) = \frac{\omega}{\varepsilon_0 c} \mathrm{Im}\left(\frac{\mu(\omega)}{E^{(\mathrm{s})}(\omega)} \right). \tag{2.98}$$

In the following, the microscopic calculation of the susceptibility of a bound state $|\phi\rangle$ with finite lifetime $1/\Gamma$ (e.g. due to spontaneous decay) is shortly outlined. After the perturbative excitation from the initial state $|0\rangle$ at $t = 0$, the time evolution of the state with energy position E_r (E_0 of the initial state $|0\rangle$ is set to zero) is given by

$$c_\phi(t) = -\frac{i}{\hbar} \mu_{\phi,0} \exp[-i \frac{E_\mathrm{r}}{\hbar} t] \exp[-\frac{\Gamma}{2} t] \tag{2.99}$$

for times $t \geq 0$, and $\mu_{\phi,0} = \langle \phi | \hat{\mu} | 0 \rangle$ is the dipole matrix element connection both states. In the energy domain (connected via the Fourier transform) the expansion coefficient of the bound state is then given by

$$\tilde{c}_\phi(E) \propto \frac{i\mu_{\phi,0}}{\frac{\hbar\Gamma}{2} - i(E - E_\mathrm{r})}. \tag{2.100}$$

With this expansion coefficient, the dipole expectation value of the superposition of both $|\phi\rangle$ and $|0\rangle$ finally leads to the dielectric susceptibility

$$\chi(E) \propto \frac{i|\mu_{\phi,0}|^2}{\frac{\hbar\Gamma}{2} - i(E - E_\mathrm{r})} \propto -\frac{E - E_\mathrm{r}}{\frac{\hbar^2\Gamma^2}{4} + (E - E_\mathrm{r})^2} + i \frac{\frac{\hbar\Gamma}{2}}{\frac{\hbar^2\Gamma^2}{4} + (E - E_\mathrm{r})^2} \tag{2.101}$$

where the real and imaginary part respectively describe dispersion and absorption across the resonant transition at energy E_r and width Γ. The last term in Eq. (2.101) corresponds to the well-known Breit-Wigner absorption line shape and both terms are illustrated in Fig. (2.10).

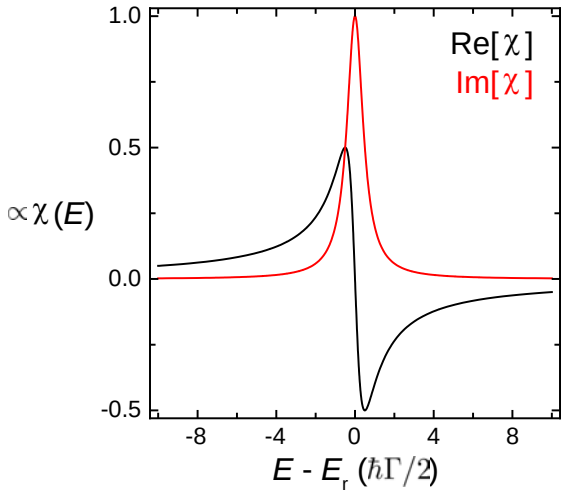

Figure 2.10: Real (black line) and imaginary part (red line) of the dielectric susceptibility for a incoherently decaying (Lorentzian) bound state using Eq. (2.101).

2.9 Two-electron states and electron correlation in helium

In this work, doubly excited states (DES) in helium are investigated which involve two electrons. Electrons are indistinguishable particles which means that their total wave function $\Psi(e_1,e_2)$ has to obey certain symmetry properties which is already a manifestation of correlation. The wave function can be written as (see e.g. [34])

$$\Psi^{(2)}(\vec{\mathbf{r}}_1,\vec{\mathbf{r}}_2)\cdot\chi(S_1,S_2) \tag{2.102}$$

where the first term describes the spatial degrees of freedom with the particle coordinates $\vec{\mathbf{r}}_n$, and the second term describes the spin of both particles. The spin degree of freedom is decoupled and will play no role for the discussion of this work.

The spectroscopic notation for such two electron states is

$$^{2S+1}L^{\pi} \tag{2.103}$$

where L is the total angular momentum quantum number and S is the quantum number for the total spin. The greek letter π takes values "o" (odd) and "e" (even) which are added for convenience to clarify the parity of L. The considered DES in helium are spin singlet states ($S=0$) with an antisymmetric spin wave function $\chi(1,2)$. The spatial wave function thus must be symmetric obeying Pauli's principle for fermions. The L quantum number is usually given in letter notation with $L=$ S, P, D, F, ... denoting the sum angular momentum of the single-electron orbitals. With laser interaction in dipole approximation, only transitions among different-parity states are allowed. With this classification, the ground state of helium is a $^1S^e$ state from which $^1P^o$ states can be reached with single-photon (or perturbative) excitation.

The spatial wavefunction $\Psi^{(2)}(\vec{\mathbf{r}}_1,\vec{\mathbf{r}}_2)$ can in general not be written as a product of two single-electron wavefunctions

$$\Psi^{(2)}(\vec{\mathbf{r}}_1,\vec{\mathbf{r}}_2)\neq\Psi^{(1)}(\vec{\mathbf{r}}_1)\cdot\Psi^{(1)}(\vec{\mathbf{r}}_2). \tag{2.104}$$

which is due to the interaction between the two particles, the Coulomb force

$$\vec{F}_{\mathrm{c}} = -\frac{1}{4\pi\varepsilon_0}\frac{e^2}{|\vec{\mathbf{r}}_1 - \vec{\mathbf{r}}_2|}. \tag{2.105}$$

This notion can most generally be understood as electron correlation mediated by the Coulomb repulsion, i.e. the particles interact with each other. Taking the Coulomb interaction into account is the starting point for many approximate theories [34] when describing the correlated interaction of these two particles with a third partner such as a nucleus (e.g. the helium atom) but also within covalent bonding orbitals in molecules. Approximation methods have to be applied as the full Coulomb interaction between three particles cannot be solved analytically, neither in a classical nor in a quantum treatment.

For the case of autoionizing states in a helium atom, the concept of configuration interaction (see section 2.7) is an approach to describe such correlations (see e.g. [47] as a review), as different single-electron configuration states are allowed to mix due to their interaction. In this treatment, the interaction matrix element V_E essentially is the Coulomb repulsion.

The DES in helium can be intuitively classified along their inner and outer quantum number N and n, respectively, resembling the uncorrelated product of single-electron orbitals. The excitation of the first DES series in helium with $N = 2$ and $^1\mathrm{P^o}$ symmetry would mean that three series (2snp, 2pns and 2pnd) should be allowed [48], all converging to the $N = 2$ ionization threshold (see also Fig. 2.11). Excitation of the first two series involving the s orbital should be more probable than the latter one, involving no s orbital. This distinction is explained as only one electron has to absorb angular momentum from the radiation field for the first two cases, while both electrons have to exchange angular momentum with the radiation field in the third case, with excitation from the $1\mathrm{s}^2$ ground state. However only one strong and one weak series was initially detected [49]. This lead to the description of superposition states [50] where the linear combination

$$\frac{1}{\sqrt{2}}(2\mathrm{s}n\mathrm{p} \pm 2\mathrm{p}n\mathrm{s}) \tag{2.106}$$

is considered to describe the observed strong "+" and weak "-" series, while the third "pd" series being even weaker in strength was not yet detected. The identification of these superposition states is thus an early indication for the correlated (entangled) nature of these two-electron states. The two series are abbreviated throughout as

$$\mathrm{sp}_{2,n+} \quad \text{and} \quad \mathrm{sp}_{2,n-} \tag{2.107}$$

where the 2s2p configuration trivially belongs to the "+" series [50]. The weakest "pd" series was experimentally found more than 30 years later within high-resolution synchrotron studies [51, 52], where these measurements also serve as a reference for the position and line shape of the here considered $\mathrm{sp}_{2,n+}$ series (see Fig. 2.11). The $N = 2$ ionization threshold at 65.40 eV denotes the energy above which one electron is ionized and the other electron is remaining in an excited $N = 2$ Bohr orbit. Slightly above this ionization threshold, the ionized electron is moving with relatively low kinetic energy (the difference to the 65.40 eV threshold energy), in contrast to the degenerate $N = 1$ continuum

where the (auto-)ionized electron is moving with much higher kinetic energy (the difference to the single-electron ionization threshold at 24.59 eV). The autoionization life times range between 17 fs for the lowest 2s2p state up to several 100 fs for the higher $sp_{2,n+}$ states, i.e. having energetic widths between 38 meV down to few meV. Table 2.2 shows parameters for the three lowest states.

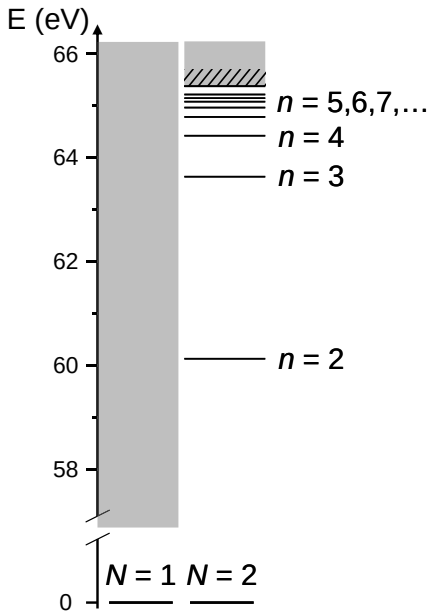

Figure 2.11: Energy level scheme of doubly-excited states in helium with $^1P^o$ symmetry converging to the $N = 2$ threshold at 65.40 eV. These states can be reached via single-photon excitation from the $1s^2$ ($^1S^e$) ground state. The level positions are obtained from [51,52]. Only the strongest $sp_{2,n+}$ series is shown. The mixing of these states with the energetically degenerate $N = 1$ continuum is the essence of Fano-type autoionization and quantum interference apparent in absorption spectra.

Table 2.2: Line shape parameters (cf. Eq. (2.88) in section 2.7) for the three lowest doubly excited states belonging to the $sp_{2,n+}$ ($^1P^o$) series. Values are taken from [51]. See [51, 52] for more parameters of other $^1P^o$ states.

	E_r (eV)	Γ (meV)	q
2s2p	60.1503±0.0040	37.6±0.2	-2.74±0.04
$sp_{2,3+}$	63.6575±0.0030	8.3±0.5	-2.53±0.04
$sp_{2,4+}$	64.4655±0.0020	3.4±0.7	-2.58±0.05

Within a group-theoretical approach, symmetry properties of these states could be identified which yielded a more rigorous classification system [53,54] (see e.g. [55,56] for reviews) along the hyperspherical coordinate approach. This approach is basically treating the distance r_{12} between the two electrons as a parameter, similar to the nuclear distance R in molecules. The interpretation of the helium atom as a "molecule" with two light nuclei (the electrons) and one surrounding particle (the nucleus) shall however be nothing more than an intuitive picture of this scheme. The hyperspherical coordinate approach becomes

increasingly important for higher DES (high N Bohr orbitals of the inner electron). In the here considered work, the older but more intuitive (at first sight) $sp_{2,n\pm}$ classification is used throughout.

The classification (or symmetry properties) of two-electron states become more and more complex with higher quantum number N. This can be understood intuitively as 1) an increasing number of overlapping two-electron Rydberg series are possible, and 2) more than one degenerate continuum is open for the autoionization channel. An overview over more recent studies on two-electron atoms can be found in [57] which may serve as a review. Nowadays it is possible to approach the Coulombic three-body problem with *ab initio* models [58, 59], taking correlation effects from the lowest to the highest excited states into account.

From an experimental point of view, these highly excited autoionizing Rydberg states are more easily accessible, as their dynamics (due to a closer level spacing) happen on longer time scales (on the order of picoseconds and beyond), where doubly excited Rydberg wave packets are more easily accessed. Typically alkaline earth atoms are investigated as helium-like systems (two electrons in the outermost S shell). As an example, the non-exponential decay of an autoionizing shock wave packet [60] was measured, which is evolving after the Rydberg wave packet is suddenly excited into a different ionic potential (shake up). A manifestation of the classical dynamics across these highly excited states was the experimental observation [61] that autoionization can be understood as a single collision event between the two excited electrons.

All this mentioned theoretical and experimental work are examples for the investigation of electron correlation and their dynamics. In parallel, with the advent of strong laser fields, a different category of electron correlation was and is investigated, such as the interaction of two electrons with strong laser fields. Traditionally, the single active electron (SAE) approximation was and is widely applied for theoretical models because the interaction even of single-electron atoms with strong laser fields is a field of extensive research (see section 2.2). Thus electron correlation can be identified as the breakdown of the SAE approximation. As such, an increased double-ionization yield was found in helium [62, 63], the well-known 'knee structure' which was higher than expected from sequential ionization of both electrons. It can be understood in terms of the rescattering model [19] (see also section 2.2.2) and is termed non-sequential double ionization [64]. Non-sequential in that sense that the electrons are not ionized independently in a sequential way. This interpretation was experimentally confirmed in [65] where the angular-resolved detection of neon ions in strong fields could be explained with this model. In a sense, this "non-sequential" process can still be understood "sequentially" with the first electron ionized and recolliding shortly later to kick out the second electron in a correlated manner.

It was also proposed in [66] how two electrons are cooperatively tunnel-ionized in strong laser fields, being an example for strong-field-induced electron correlation without rescattering. In a recent experiment [67] where circularly polarized light was used which effectively rules out rescattering, data was obtained which could not be explained with the assumption of the sequential ionization of single active electrons. These observations are thus in favour of such and other models (e.g. [62]).

Finally to close this overview and introduction into electron-correlation effects, approx-

imation methods to describe more than two electrons are shortly outlined. Traditionally the Hartree-Fock (HF) method is often used [34], which involves the antisymmetric linear combination of all involved single-electron orbitals including their spin, the so-called Slater determinant. In that sense, electron correlation (exchange correlation, but not Coulomb correlation) is taken into account with regard to the mixing of different single-electron orbital product wave functions. Extensions of this approach involving time-dependent treatments (TDHF) and further mixing of multi-configuration states (MCTDH, MCTDHF) to account for inclusion of electron-electron interaction are just a few examples how electron correlation can be systematically (but still in an approximate way) be taken into account. For a recent review on these methods, see e.g. [68]. Also density functional theories (DFT) and its time-dependent variant (TDDFT) are used to approximatively describe and calculate many-electron effects and to some extent also electron correlation, where e.g. [69] may serve as a review.

Chapter 3

Design and construction of the experimental apparatus

For the interferometric experiments as they are described in this work, a whole new beamline was designed and set up. This shall be described in the following, also highlighting some typical challenges accompanying these kind of experiments. It shall also serve as a reference for future experiments performed with this setup.

3.1 The femtosecond laser system

Writing about LASERs (**L**ight **A**mplification by **S**timulated **E**mission of **R**adiation), it is very easy to summarize its fundamental working principle in just one sentence: "An energetically pumped and population inverted gain medium is enclosed in a resonator to repetitively amplify propagating radiation via stimulated emission." Of course there is much more to say since the early developments in the 1960s [70, 71], both from a physics as well as from a technological point of view. Details on lasers in general can nowadays be found in many textbooks such as [6]. Emphasis on ultrashort laser pulses and the techniques for creating them (such as mode locking, dispersion control, self phase modulation, etc.) can be found in newer textbooks such as [2, 46].

We use a commercially available amplified laser system, the Femtopower compact Pro CEP by Femtolasers [72] which delivers CEP-stabilized sub-30 fs laser pulses with high pulse energies in the 1 mJ range at 4 kHz repetion rate. When focused down to typical spot sizes around 50 μm as in our experiments, peak intensities in the 10^{14} to 10^{15} W/cm^2 regime can be accessed. These intensities are needed for the experiments performed in this work. The laser system basically consists of the laser oscillator itself which delivers sub-10 fs CEP-stabilized laser pulses at high repetition rates (typically 80 MHz) however with low pulse energies of only a few nJ. These pulses are subsequently amplified up to ~ 0.8 mJ using chirped pulse amplification (CPA) [73] in a multipass configuration.

To describe CPA in simple words, the sub-10 fs pulses from the oscillator are stretched (chirped) in time up to the order of picoseconds. This is done to avoid any damage during amplification due to the high peak powers (at 10 fs duration even nJ pulses yield peak

powers in the MW range). Then they are propagated several times (9 times in our setup) through an amplifying gain medium which is strongly pumped using a high power Q-switched pump laser (DM-30, Photoncis Industries). After that, the amplified and chirped pulses are recompressed down to their bandwidth limit with sub-30 fs duration, after gain narrowing has occurred in the amplifier. This means that only the centermost spectral parts of the laser pulses are most efficiently amplified, thus the spectral bandwidth of the amplified laser pulses has decreased. At the cost of a lower repetition rate (from 80 MHz down to 4 kHz, mainly limited due to the average heat consumption at higher repetition rates, i.e. there is a limited availability of high pulse energy *and* high rep. rate pump lasers) the pulse energy is increased from the nJ to the mJ regime.

The gain medium both of the oscillator as well as the amplifier system is a titanium-doped sapphire crystal (Ti:Al_2O_3, or Ti:Sa) which exhibits a spectrally broad amplification band (almost octave-spanning, centered around 800 nm, the typical center wavelength of these lasers, thus having photon energies around 1.55 eV), being a prerequisite for the generation of ultrashort-duration laser pulses. Dispersion in these laser systems is a severe issue and has to be compensated for. It is mainly caused by propagation through the optical elements (fused silica glass) or the laser crystal itself but also through air. Compensation is achieved with negative dispersive elements where multilayer mirrors (such as third-order-dispersion (TOD) mirrors and chirped mirrors (CMs)) are used to efficiently compensate especially for the higher-order dispersion terms which would otherwise prevent pulse compression down to the bandwidth limit of few-cycle pulses. These elements (TOD mirrors and CMs) are both parts of the laser oscillator itself (intra cavity) as well as at the various stages during stretching, amplification and recompression of the pulses (extra cavity). The high chirps necessary for CPA are realized via propagation through a thick sample of fused silica glass while recompression is achieved using prisms to introduce negative dispersion, in addition to TOD mirrors and CMs which are mainly responsible for efficient compensation of the higher-order terms.

All these optical elements need to be perfectly aligned as even small deviations may have tremendous effects on the overall performance. Due to environmental conditions (thermal or humidity drifts, as well as dust particles), these systems typically have to be maintained and aligned on a daily basis, i.e. far from turn-key operation. An efficient monitoring and control system was set up in order to measure and keep track of salient performance parameters such as the pump laser power along with its focal spot profile, the spectrum of the oscillator pulses, environmental conditions (temperature and humidity) around the laser, etc..

To shorten the pulse duration from sub-30 fs down to the few-cycle regime, their spectral profile again has to be broadened. This is achieved using the hollow-core-fiber compression technique [74], where the laser pulses are focused into the center hole of a glass capillary in order to propagate high peak powers in the focal spot over a long distance (roughly 70 cm for our system). The fiber is filled with rare gas at high pressure (we use neon at 1.5 bar absolute stagnation pressure). Exhibiting high peak intensities ($\sim 10^{14}$ W/cm^2) throughout the propagation in the fiber, the laser pulses interact nonlinearly with the gas atoms. Due to the intensity-change across the temporal pulse envelope, more frequencies are coherently added to either side of the pulse spectrum. A more detailed description of this process, also called self-phase modulation (SPM), can be found in [2]. Subsequently

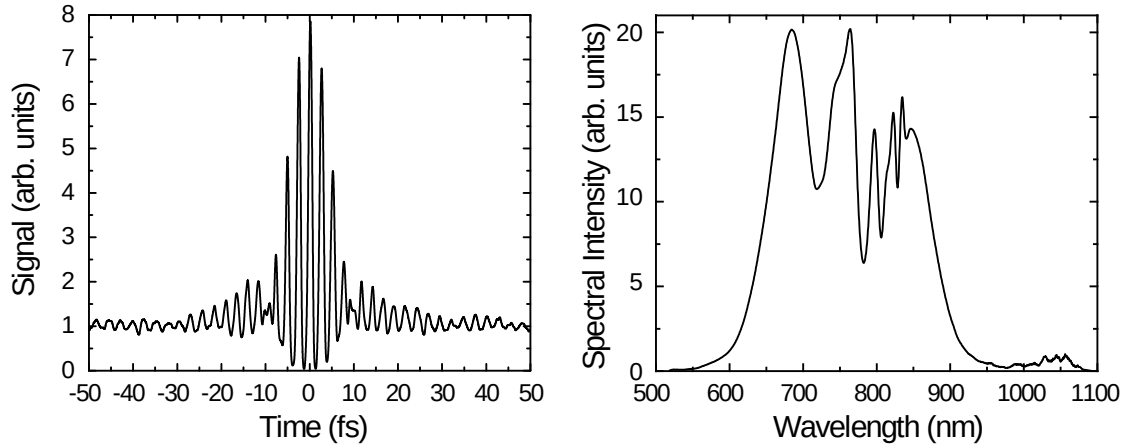

Figure 3.1: Interferometric autocorrelation of the laser pulses after transmission through the hollow-core fiber filled with 1.5 bar neon and subsequent compression with chirped mirrors. This measurement yields a pulse duration of 6.2 fs FWHM where the laser spectrum is centered around 756 nm. The wings at ± 15 fs hint on a weak pre-/post-pulse.

this broadened spectrum (almost octave spanning) is compressed again by using chirped mirrors which are specifically designed for such broad spectra. Finally, ~ 7 fs duration laser pulses at typical energies around 0.3 mJ (mainly due to losses during propagation in the hollow-core fiber and the subsequent CM compressor as well as reflection losses from the silver mirrors) are available and ready for use in following experiments. Due to the high density of free electrons in the ionized gas medium, plasma-induced spectral blue-shifting occurs [75] which means that the laser pulse spectrum is shifted to smaller wavelengths. This is the reason for the typical center wavelengths around 750 nm or lower of few-cycle laser pulses.

The duration of these pulses was measured using second-order interferometric autocorrelation [2] where a typical trace is shown in Fig. 3.1 and yielded a FWHM duration of 6.2 fs. The side-peaks accompanying the center-most main peak hint on the presence of additional pre- or post-pulses which are typical for chirped mirror compressors as used in our setup. However, most of the energy is still contained in one short pulse. The possibility of pre-/post-pulses are explained by residual spectral-phase modulations in the dispersion curves of chirped mirrors. The main limitation for obtaining shorter pulses is the limited spectral bandwidth for which phase compensation is achieved by a set of chirped mirrors. Just recently it was demonstrated how even shorter so-called "sub-cycle" optical pulses with a measured FWHM duration ~ 2.1 fs could be achieved [76]. The key idea there was to compress different parts of the octave-spanning spectrum (after SPM) with different and specifically customized chirped mirrors and beam splitters.

3.2 Carrier-envelope-phase stabilization

In this section, some general aspects on CEP stabilization will be discussed with emphasis on how it is implemented in our experimental setup. Our commercial laser system was delivered and installed fully equipped with CEP control [72]. It was then custom enhanced

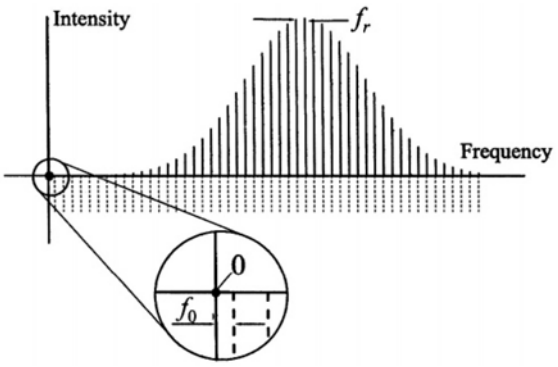

Figure 3.2: Taken from [78]. Within the gain bandwidth, the laser spectrum consists of frequencies spaced exactly by the MHz repetition rate f_r. The offset frequency f_CEO (f_0 in the figure) as defined by Eq. (3.1) corresponds to the CEP slippage from pulse to pulse. It can be identified as the offset of the frequency comb when extended down to zero.

by ourselves with additional equipment where more details are presented in [77]. A good general reference for CEP control and the closely connected field of frequency metrology can be found in [78].

CEP control in the laser oscillator is based on the fact that mode-locked laser cavities deliver identical pulses (except their CEP) spaced by the round-trip time in the cavity. This yields frequency combs in the near-infrared (NIR) to visible spectral range [79, 80] consisting of optical frequencies (the amplified laser modes) which are spaced evenly, exactly by the repetition rate of the laser oscillator (experimentally confirmed with accuracy better than 10^{-15} [79]). As this scheme connects radio frequencies (i.e. the MHz repetition rate) to the optical domain it has also many applications in frequency metrology [78] for high-precision measurements.

In the time domain, the CEP shift of propagating laser pulses is explained due to mismatching group and phase velocities (see Eq. (2.20) in section 2.1). Connecting this to one round trip of a propagating pulse in the mode-locked laser cavity, it is straightforward to define the carrier-envelope offset (CEO) frequency [78]

$$f_\mathrm{CEO} = \frac{\Delta\phi_\mathrm{CEP}}{2\pi} f_\mathrm{r}, \tag{3.1}$$

where $\Delta\phi_\mathrm{CEP}$ is the accumulated phase mismatch according to Eq. (2.20) and f_r is the MHz repetition rate of the oscillator. Both frequencies f_CEO and f_r are illustrated in Fig. 3.2, where f_CEO is identified as the offset of the frequency comb when extrapolated down to zero frequency. Running freely without any stabilization and in the presence of any source of noise (typically present in the pump laser light), f_CEO jitters arbitrarily between zero and f_r as a function of time, i.e. the CEP changes randomly from shot to shot coming out of the laser oscillator. If however f_CEO can be kept fixed at an integer multiple of the repetition rate (i.e. $f_\mathrm{CEO} = f_\mathrm{f}/n$) then every n^th shot coming out of the laser cavity shows the same CEP.

Being in the radio frequency range, both f_f and f_CEO can in principle be measured electronically, however both have to be deduced from the optical pulses. By measuring the train of pulses with a fastly responding (ns time scale) photo diode, the repetition rate f_r

can be determined directly. The trick for directly measuring f_{CEO} is based on nonlinearly mixing frequencies of an octave-spanning frequency comb, either by second harmonic generation (SHG) or difference frequency generation (DFG). Either of these mixing process will project frequency components from one end of the spectrum onto the other one, interfere with the fundamental frequency there, and cause a beating in time where the beating frequency can be identified as f_{CEO}. The beating can then also be measured directly with a fastly responding photo diode.

In our setup, both DFG and SPM (to create an octave spanning spectrum) are realized in one single element, a periodically poled lithium niobate crystal (pp:$LiNbO_3$ or ppLN) [72] which is making use of an *in situ* implementation of CEP control within the emitted laser pulses from the oscillator, yielding phase stabilities on the order of 100 mrad [81]. The beat note is then measured with a photo diode after selecting the relevant spectral range around 1300 nm (where fundamental and DFG light spectrally overlap) with an interference filter [72].

The main mechanism behind fluctuations of f_{CEO} are changes of the refractive index especially in the Ti:Sa crystal, where due to the optical Kerr effect changes in the laser intensity may also have a severe effect on f_{CEO} [78]. For CEP stabilization, the pump laser intensity can be finely tuned with an acousto-optic modulator (AOM), closing the loop in order to keep f_{CEO} at a fixed fractional integer of f_{r}. In our setup with enabled phase lock $f_{\mathrm{CEO}} = f_{\mathrm{r}}/4$, and thus every 4^{th} pulse leaving the oscillator is equal in CEP. Picking out only one of these pulses for amplification, which is realized with an electro-optical Pockel's cell, only pulses of equal CEP leave the amplifier.

In order to both compensate for slow CEP drifts within the CPA stage, which are mainly caused by thermal effects, and to experimentally use the CEP as a control knob, a second nonlinear measurement of the CEP has to be realized. The measurement needs to determine the CEP within one and the same pulse (i.e. single shot). This is achieved in an f-$2f$-interferometer based on SHG. The working principle is to let interfere the highest frequencies of the fundamental spectral profile (the "blue" part) with the frequency-doubled region of the lower side of the fundamental spectrum (the "red" part). The pulse spectrum then of course has to span at least one octave. In the spectral overlap region, a sinusoidal modulation appears whose period corresponds to the inverse temporal spacing between the blue and red spectral parts of the pulse. This means the pulses have to be chirped. The phase of this modulation pattern then corresponds to the relative phase between the blue and red spectral parts of the pulse. Due to the involved frequency doubling, that in fact not only doubles the frequency but the entire phase (including the CEP) of the pulse, this relative phase exactly corresponds to ϕ_{CEP} of the pulse. Performing a Fourier analysis on the modulation pattern (cf. section 2.3) the CEP can be retrieved on a single shot basis.

In our setup this is realized with the commercial f-$2f$-interferometer APS800 from Menlo Systems [82], where the spectrum is octave-broadened in a sapphire plate and SHG is realized with a nonlinear beta barium borate crystal (β-$Ba(BO_2)_2$ or BBO). The pulses are spectrally detected with a compact Czerny-Turner spectrometer (Thorlabs SP1-USB), triggered by the amplifier and set to exposure times ~ 250 μs (corresponding to the 4 kHz repetion rate) thus measuring single shots. The CEP is retrieved by software and a

feedback control signal is generated. This signal controls the CEP by piezo-translating the amount of glass (a prism) which is used for pulse stretching. Within this configuration, a CEP stabilization on the order of 100 to 200 mrad phase noise is realized. It should be noted that the feedback response time of the piezo control is on the order of 10 to 100 ms. Therefore, even though the CEP is measured with single shots, it cannot be controlled on a shot-to-shot basis. Only slower thermal drifts can therefore be compensated for. Shot-to-shot based measurements of the CEP can be realized for example with so-called stereo ATI setups [83, 84]. In this case, the laser oscillator can even be set to freely run (no CEP stabilization), as every single shot is measured (CEP tagged) and can be connected to experimentally measured data. However this scheme is not feasible for the here presented experiments, as XUV high-harmonic spectra typically have to be integrated over several shots (on the order of 1000 to 10000) to get a reasonable signal with good signal-to-noise ratio (SNR).

Along the experimental design, a second f-$2f$-interferometer was set up [77] after the SPM hollow-core fiber in order to check for CEP fluctuations of the pulses on the way to the experiment (predominantly induced by the nonlinear refractive index change during SPM). A whole new measurement and feedback software was also developed, especially as the commercial software turned out to be incompatible with the LabVIEW-based data acquisition system for the main experiment. Indeed it turned out that the SPM spectral-broadening stage introduced both a higher phase noise (on the order of 500 mrad) as well as additional fluctuations on longer time scales which were not present before the SPM stage (see [77] for further details). Unfortunately, the higher phase noise (mainly shot-to-shot noise) after the SPM spectral broadening stage could not be compensated for with the relatively slow piezo-based system. Besides, random (of course within a certain range) shot-to-shot fluctuations can never be compensated for with such kind of measurement, as the feedback loop can at best influence the subsequently generated laser shot. In this case, *in situ* measurements such as [84] should be the method of choice. In order to avoid introducing the higher phase noise into the feedback loop, we decided to stabilize the CEP before the SPM stage with lower noise contributions. In order to rule out additionally introduced CEP fluctuations of the pulses on their way to the experiment, experimental data was always acquired for several CEP cycles. This way, via comparison of the different cycles, real microscopic effects in the experiment can be disentangled from unwanted CEP fluctuations (see also section 5.3).

3.3 Generation of attosecond pulses

In order to perform the aforementioned experiments, a new source for the generation of attosecond pulses, or in general, *coherent* broad-band radiation in the extreme ultraviolet (XUV) spectral range (from below 20 eV up to as high as 150 eV photon energies) had to be designed and set up. Conceptually, this is very simple: Just focus intense laser pulses into some gaseous medium. However, as presented in the introductory overview of high-harmonic generation and attosecond pulse production given in section 2.2.2, and as it will be presented in the following, it is much more than that and still challenging, both from a theoretical as well as from a technological point of view.

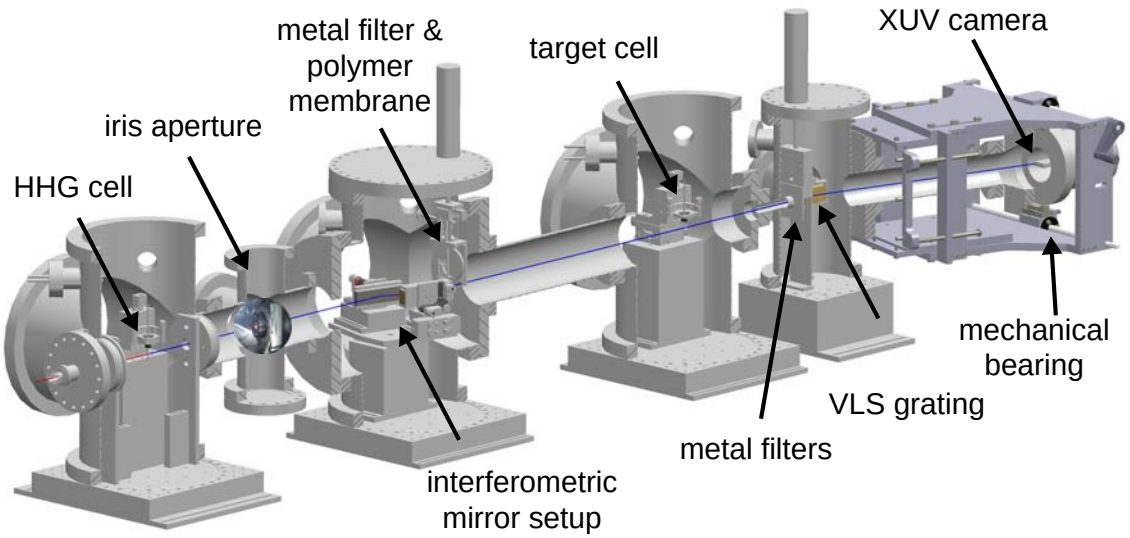

Figure 3.3: Schematic overview over the complete vacuum setup for attosecond pulse generation and interferometric experiments. The different parts are further described in this and the following sections. HHG cell and target cell: see Fig. 3.4 in section 3.3, interferometric mirror setup: see Figs. 3.5 and 3.6 in section 3.4, metal filter & polymer membrane: see Fig. 3.9 in section 3.4, metal filters, VLS grating, mechanical bearing and XUV camera: see Figs. 3.12 and 3.11 in section 3.5.

Parts of the experimental setup and design are also described in [85], where a more detailed and specific description of the setup can be found. Here, the main goal is to present the fully established beamline as a whole while putting emphasis on the technical and physical parameters in order to understand the design and operation of such a beamline. A schematic overview of the complete vacuum setup for attosecond pulse generation and subsequent experiments can be seen in Fig. 3.3.

HHG and attosecond pulse production has to take place under vacuum conditions, simply as the generated XUV photons would knock out valence electrons from any atom or molecule along their propagation and thus be absorbed. The generated XUV radiation is well above any ionization potential, where the highest values (i.e. for rare gas atoms) are on the order of 10 to 20 eV [9]. As an example, the absorption length through air at atmospheric pressures for radiation between 20 and 150 eV is just 1 mm or less [86]. Under vacuum conditions, already for vacuum pressures around 10^{-1} mbar the absorption length is on the order of 1 m and more. Requirements on the vacuum design are therefore relatively loose for HHG. As a rule of thumb, if a vacuum pressure around 10^{-3} mbar in the generation chamber is maintained, reabsorption of the generated XUV radiation can be completely neglected.

In the herein described setup, rare gas atoms are used as the conversion medium. They are favourable for attosecond pulse production simply due to their high ionization potential as then ionization/depletion on the leading edge is suppressed and HHG can occur across the centermost part of the driving laser pulses with the highest field strengths (see also Fig. 2.2 in section 2.2.1). We used neon with ionization potential $I_p = 21.6$ eV [9].

Optimizing the conditions for neon, a $f = 500$ mm silver-coated[1] spherical mirror is used

[1]The preferred coating-material for steering few-cycle laser pulses is protected silver. It supports high

to focus the ~ 0.3 mJ laser pulses into the gas target. With this geometry, peak intensities in the mid 10^{14} W/cm^2 range can be expected with focal spot sizes ~ 50 μm. A mirror is used in favor of a lens primarily to avoid unnecessary dispersion for the 7 fs duration laser pulses during propagation through the lens material, but also to avoid chromatic aberrations of the broad band spectrum [2]. To avoid astigmatism, the mirror has to be used under as normal angle of incidence as geometrically possible. In the setup, an apparent astigmatism across the spatial beam profile *before* the spherical mirror could be compensated for by increasing the angle of incidence to $\sim 15°$. The reason for this apparent astigmatism might be a deformed output window of the vacuum tubing containing the SPM hollow-core fiber. This rather technical issue was however not further pursued.

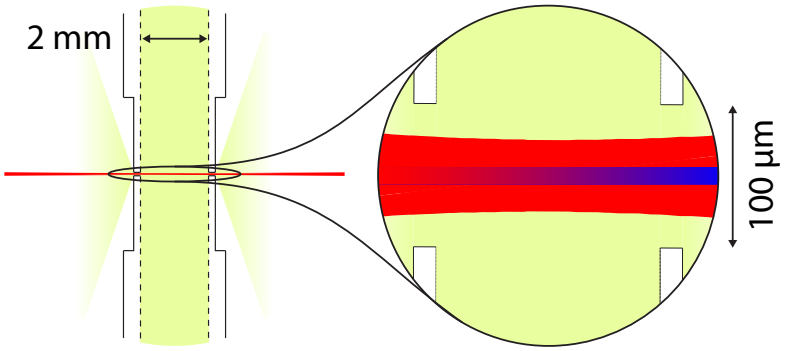

Figure 3.4: Schematic illustration of the HHG source cell which is used for the generation of attosecond pulses. A magnified view of the interaction volume is shown, where the coherent buildup of XUV radiation (blue) is cartooned. The target cell is an exact copy of this HHG source cell.

The neon generation medium inside the first vacuum chamber is contained in a 2 mm inner diameter (3 mm outer diameter) stainless-steel tube with machine-drilled 100 μm diameter holes in the cladding in order to let the focused laser beam pass through. For technical convenience, the cladding was reduced to about 200 μm thickness around the machine-drilled holes. A schematic picture of the generation cell is depicted in Fig. 3.4. This yields a conversion length of about 2.5 to 3 mm, taking into account the cladding and higher gas densities in the exit flow along the laser beam. For efficient generation in neon, relatively high gas densities in the interaction volume are needed, translating into backing pressures around 100 mbar and above within the neon-filled gas cell. This corresponds to at least ~ 0.2 mbar l/s of neon leaking into the generation chamber under full operation [89], where the leak rate was calculated assuming two 100 μm holes and 100 mbar backing pressure. In order to maintain an overall pressure of 10 ^{3} mbar inside the vacuum chamber, a pumping speed >200 l/s is needed. In the current setup, a 2000 l/s turbomolecular pump is used to allow for safe operation also under non-optimal conditions (e.g. enlarged aperture due to laser ablation). To carefully optimize for phase-matching conditions, the conversion cell is mounted on an XYZ linear-positioning stage equipped with picomotors [90] to allow for steering under vacuum conditions during operation.

reflectivity over a broad spectral range and introduces minimal group delay distortions which would otherwise influence the temporal pulse structure (see e.g. [87, 88]).

3.4 The interferometric mirror setup

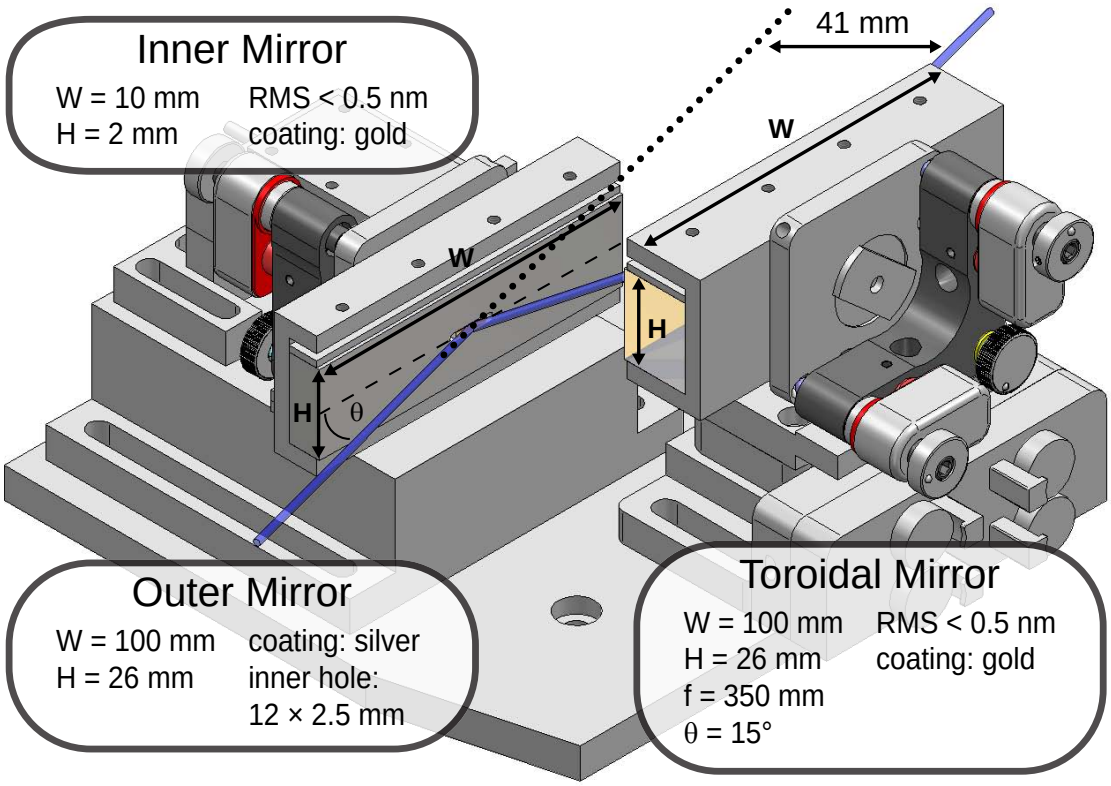

Figure 3.5: Schematic illustration of the all-grazing-incidence interferometric mirror setup. The beams reflect off both mirrors with grazing angle $\theta = 15°$. The incoming and exiting beams propagate parallely offset. Technical details such as the width (W), the height (H) or the focal length (f) of the optics are given in the figure.

In combination with the high-resolution flat-field spectrometer which is described in the next section, the interferometric mirror setup can be considered the heart of the newly designed and built beamline. It consists of two grazing-incidence mirror arrays: One pair of flat mirrors to spatially and temporally separate the attosecond-pulsed XUV radiation from the driving laser pulses, and another toroidal-shaped mirror to refocus both spectral parts into the experimental target. A schematic image of the mirror system is depicted in Fig. 3.5. More details on the mirror setup with emphasis on the toroidal mirror and its alignment procedure can be found in [91] and also in [85] for a more general overview. Utilizing a toroidal mirror was also part of own prior work for a similar setup [92] which may also serve as a reference.

The idea of the grazing-incidence split-mirror setup was to use both the broad spectral-range reflectivity of grazing-incidence optics together with the highest possible interferometric stabilities within a monolithic setup, where both interferometric parts propagate along the same path. So far, the monolithic design was only used with (close to) normal incidence optics (see e.g. [93]) where multilayer coatings are incorporated in order to have reasonable reflectivity of the XUV radiation. Multilayer coatings have the disadvantage (in terms of flexibility) that they need to be designed for a specific spectral range.

This of course can also be an advantage if a certain spectral region is of exceptional interest. Typically, a spectral range of 30 eV can be realized at best (see e.g. [94]), which is then of course fixed for each specific mirror. In contrast, using metallic surfaces in grazing incidence geometry, high reflectivities over the whole XUV spectral range can be achieved [95]. Due to increased aberrations of conventional spherical optics operated in grazing-incidence geometry [6], where the astigmatism is the leading order, mirrors with a toroidal surface are usually incorporated [96]. They can be designed for imaging with zero astigmatism for a specific (grazing) angle of incidence. The 1:1 imaging geometry then introduces the least additional aberrations, while using (de-)magnifying geometries, a substantial coma aberration will be unavoidable [91, 95]. In the latter case, when for example demagnification is needed in order to achieve higher XUV intensities in the focus, ellipsoidal mirrors [97] have to be used. The choice of the grazing angle of incidence (measured with respect to the surface) is in any case a trade-off between higher reflectivities [86] (for smaller angles) and higher tolerances for possible misalignment [95] (for larger angles). In general, imaging aberrations within an attosecond-pulsed beam of light should be avoided as much as possible as these aberrations also influence their temporal structure [98].

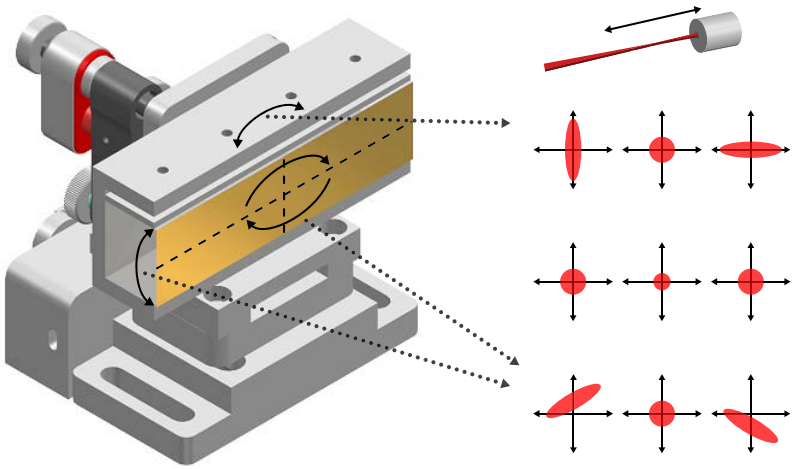

Figure 3.6: Alignment of toroidal mirror. The arrows on the mirror assembly denote the crucial degrees of freedom for the alignment of a toroidal mirror, where any misalignment results in astigmatic beam profiles when measuring across the focal spot. The tip/tilt in the sagittal plane and the rotation in the mirror plane compensate a vertical displacement from the optical axis and a tilted astigmatism (lower set of images), respectively. Both degrees of freedom are usually coupled including also the absolute height positioning of the mirror. The tip/tilt in the tangential plane of the mirror compensate purely horizontal astigmatism (upper set of images). When perfectly aligned, the beam profile is symmetric across the focal spot (middle set of images), yielding the smallest spot sizes and highest peak intensities. A detailed description of the alignment procedure can be found in [91].

In the setup, a gold-coated toroidal mirror with $\theta = 15^\circ$ grazing angle of incidence and 350 mm focal length operated in 1:1 imaging geometry is used. The angle of incidence was chosen rather high in order to allow for reasonable imaging also for the driving NIR laser pulses. Due to their higher wavelength, they posses intrinsically higher divergences (~ 15 mrad in the current focusing geometry). In addition, the demands on mirror align-

ment for the lower divergent (~ 1 mrad) attosecond pulses are more relaxed. The reflectivity for the XUV radiation (between 30 and 130 eV) is expected to be above 40% [86]. The focal length was chosen large enough in order to have geometrical space for intensity control of the laser pulses (as will be described below). In addition it was chosen to allow for differential pumping [89] to stepwise decrease the vacuum pressure from 10^{-3} mbar in the generation chamber down to below 10^{-9} mbar in the experimental interaction region to optionally operate the beamline with coincidence electron/ion detection techniques [99], where these low pressures are prerequisites. The toroidal mirror is equipped with a picomotor-controlled 4-axis tilt-aligner stage in addition to a picomotor-controlled two-axis mirror mount (details can be found in [91]) in order to allow for precision alignment of the toroidal mirror under vacuum conditions. To shortly summarize, the degrees of freedom which are substantial for aligning a toroidal mirror are depicted in Fig. 3.6.

In order to decouple the precise alignment demands of a toroidal mirror from the split-mirror setup, we decided to use an additional plane-mirror assembly to achieve the temporal separation of the attosecond pulses from the driving laser pulse. The arrangement is similar to normal-incidence split-mirror configurations [93], where the inner mirror can be moved with respect to the outer one with a high-precision (nanometer positioning) piezoelectric stage. These setups make use of the intrinsically lower divergence (see above) of the attosecond pulses. Therefore both spectral parts are spatially separated and can be accessed independently with the two mirrors. In our setup, both mirrors are flat and are coated with gold and silver for optimized reflection of the attosecond pulses and the driver laser pulses, respectively. Full separation is achieved when in addition appropriate spectral filters are used as described below. Further details on the geometrical mirror dimensions and their assembly are depicted in Fig. 3.5 and can be found in [85, 91].

The reflectivity of gold decreases for optical wavelengths below ~ 600 nm [100], thus the toroidal mirror might also affect the temporal structure of the driving laser pulses as it is used to focus both spectral parts. This implicates only minor limitations for the current setup, as the spectral bandwidth for 7-fs-duration laser pulses falls just within this restriction. Besides, the currently used set of chirped mirrors for pulse compression after the SPM fiber only support spectra above this limit [72]. These issues should however be considered when shorter pulses with broader spectra are to be used in the future.

The interferometric stability was experimentally determined to be on the order of 10 as rms-noise during operation of all vacuum pumps connected to the setup. The value was obtained via measuring the intensity-modulation of a HeNe laser reflected off the split-mirror assembly (see [91] for a similar measurement). This value is close to the minimal "theoretical" value as the typical 1 nm accuracy of the piezo-positioning device [101] translates into 2 as accuracy when taking into account the $\theta = 15^\circ$ grazing angle of incidence. Along this measurement, the mirror movement could also be calibrated to the temporal delay which yielded

$$1\ \mu\text{m} \equiv 1.7115\ \text{fs} \tag{3.2}$$

A minor drawback of the grazing-incidence split-mirror setup shall finally be given. As the time-delay is realized along the geometrical displacement of the inner mirror (Eq. (3.2)), a slight walk-off is induced on the XUV beam which can be deduced from geometrical considerations (see Fig. 3.7). The displacement Δw is related to the mirror

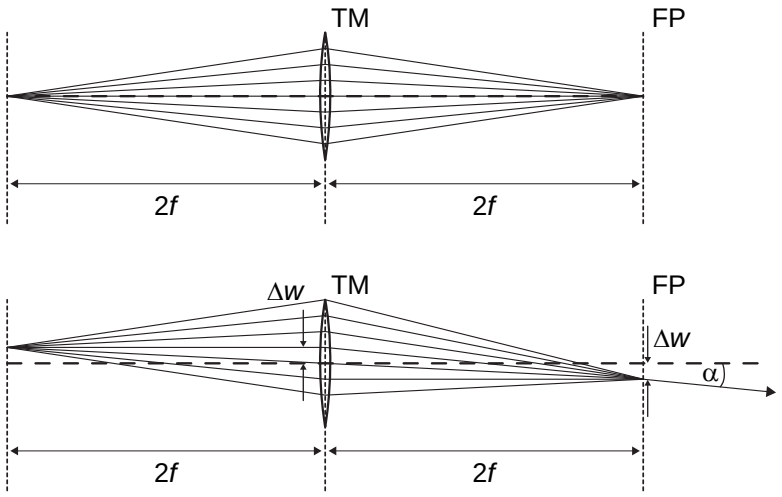

Figure 3.7: Walk-off induced by the grazing-incidence split-mirror setup. The toroidal mirror (TM) can be illustrated as a lens with 1:1 imaging geometry. A parallel shift Δw is induced on the XUV beam by the geometrical movement of the inner mirror. This shift corresponds to a displacement of the focal spot in the imaging plane of the setup. In addition, the wave front of the beam is tilted by the angle $\alpha = \arctan(\Delta w/f)$ with respect to no displacement (upper panel) which corresponds to the IR beam path of the outer mirror. f is the focal length.

movement d via

$$\Delta w = d \cdot \frac{\sin 2\theta}{\sin \theta} \tag{3.3}$$

where θ is the grazing angle of incidence. For the given setup, changing the time delay by $\Delta t = 1$ fs implies a transverse displacement $\Delta w = 1.13$ μm and wave-front tilt $\alpha = 3.22$ μrad of the XUV beam with respect to the IR beam. The tilted wave front implies a temporal averaging over $2.15 \cdot 10^{-4}$ as (assuming an XUV focal spot size on the order of 20 μm) which is thus completely negligible. The displacement Δw however implies that the geometrical overlap between the XUV and IR foci is lost with increasing time delay. For this reason, the accessible time-delay region is limited to ~ 50 fs in total in the current setup. To compensate for this walk-off, a two-point piezo stage with translation and tilt properties could be used. A small wave-front tilt however would still remain ($\alpha/2$ under optimal conditions) which is unavoidable in grazing-incidence geometry but can be safely neglected as argued above.

To fully separate the attosecond pulses from the driving laser pulses after reflection off the split-mirror assembly, additional spectral filters were inserted into the combined beam path. An uncoated 2 μm-thin nitrocellulose membrane is transparent for visible light and due to its minimal thickness introduces only minor dispersion on the laser pulses. In contrast, it is thick enough to completely absorb (with transmission on the order of 10^{-5} [86]) the XUV spectral range of the attosecond pulses. For the latter spectral range, 200 nm thin metal foils show reasonable transmission above 50% ([86], see also Fig. 3.8) where both aluminium (for transmission between ~ 20 to 70 eV) and zirconium (for transmission between ~ 60 to 200 eV) is installed and can be interchanged during vacuum operation. In turn, these metals show almost zero transmission for the NIR spectral range with penetration depths on the order of 10 nm [3]. Remaining transmission is then only caused

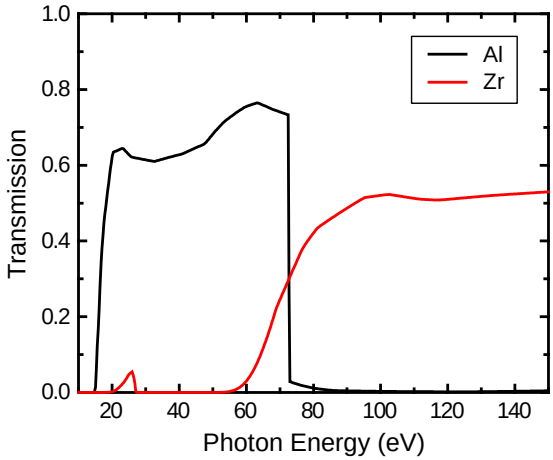

Figure 3.8: XUV photon transmission for 200 nm thin metal filters, for aluminium (Al) and zirconium (Zr). Data from [86].

by microholes in the foil surface with diameters on the order of 1 μm or less which is unavoidable during the fabrication process [102]. Both polymer membrane and metal filters are geometrically arranged in order to filter out only the attosecond pulses from the inner mirror, and the laser pulses from the outer mirror. Precise *in-situ*-positioning under vacuum operation is achieved with a mechanical feedthrough (selection of aluminium or zirconium and coarse adjustment along the vertical direction) in combination with a picomotor-controlled translation stage for fine adjustments along the horizontal. Further details on the technical realization are depicted in Fig. 3.9 and can be found in [85].

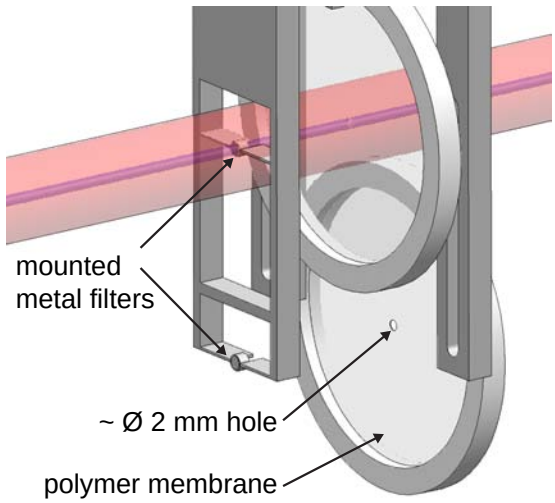

Figure 3.9: Separation of the XUV (blue) and IR (red) spectral parts using a metal filter and a polymer membrane. Both aluminium (Al) and zirconium (Zr) can be selected without opening the vacuum chamber.

To control the intensity of the NIR laser pulses for interferometric experiments, a motorized zero-aperture iris is concentrically mounted along the combined beam path after the attosecond pulses were generated. The opening of the aperture can be finely con-

trolled during vacuum operation with a picomotor-equipped rotation mount. With this arrangement, the amount of NIR light impinging on the outer mirror can be flexibly chosen, thus also the intensity of the laser pulses in the experimental interaction region is finely controlled. The set laser intensity in the interaction region is a monotonic function of the opening of the aperture. The calibration can then be yielded *in situ* and is further discussed in section 6.4. A photographic picture of the arrangement is shown in Fig. 3.10.

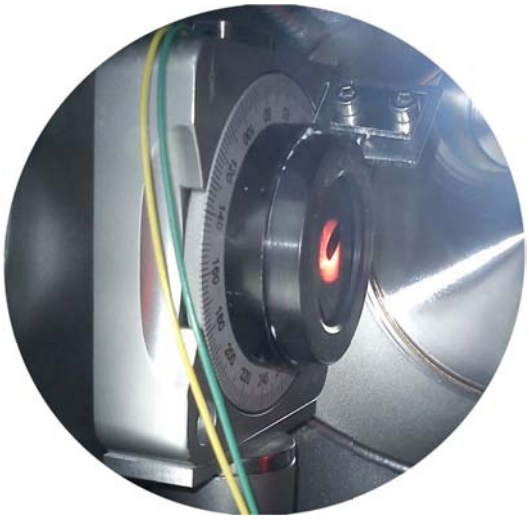

Figure 3.10: Photographic picture of the iris aperture mounted on the motorized translation stage to finely control the transmitted laser intensity.

3.5 The high-resolution flat-field XUV spectrometer

An integral part of the newly constructed beamline for interferometric experiments is a high-resolution spectrometer for the XUV spectral range. This is realized with a so-called flat-field spectrograph [103] which is operated in grazing-incidence geometry. The key element of such a spectrograph is an aberration-corrected concave grating with a variable groove density (variable line spacing, VLS) [104]. This grazing-incidence reflection grating disperses the entrance slit onto a flat spectral plane. In other words, the entrance slit is spectrally resolved and imaged onto a flat exit plane. The imaging geometry of such gratings is depicted in Fig. 3.12 with specifications added for the grating in use. It is due to the VLS properties of the grating that spectral imaging is now realized in a single plane, as opposed to conventional concave gratings with fixed line spacing, where the exit slit is imaged onto the so-called Rowland circle [105, 106]. With these conventional spectrographs, a high spectral resolution can only be achieved when the exit slit is scanned over the Rowland circle (or more commonly the grating is rotated, keeping the position of the exit slit fixed) and the transmitted light intensity is measured as a function of the slit position (or the grating position). By replacing the exit slit with a CCD camera it is possible to detect a broad spectral range at high spectral resolution within a single measurement. The flat-field imaging of the VLS grating then guarantees an equally high spectral resolution as with a conventionally scanned exit slit, now without moving any mechanical parts.

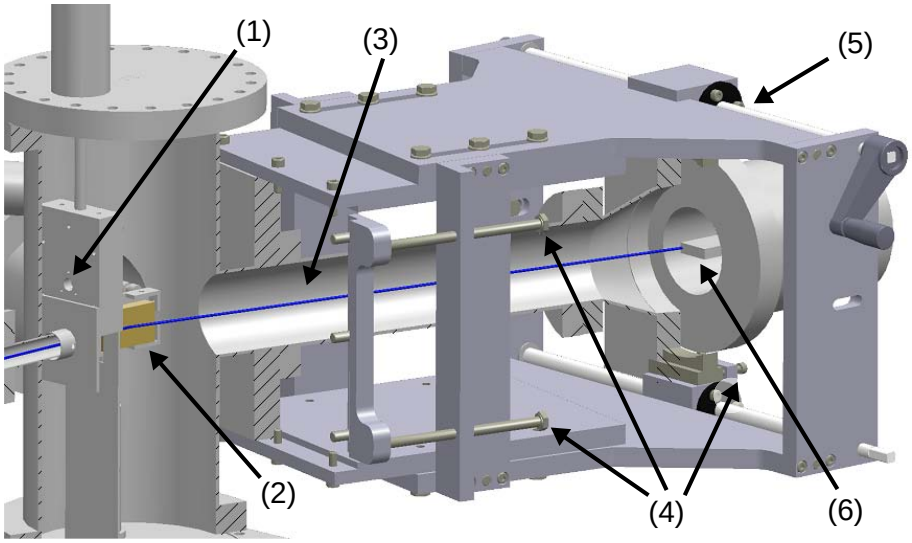

Figure 3.11: Schematic assembly of the customized flat-field high-resolution spectrometer. (1) Metal filters to shield against visible stray light, (2) VLS grating, (3) flexible membrane bellow, (4) set screws for coarse and fine positioning, (5) bearing for precise positioning along spectral plane, (6) CCD chip of XUV camera.

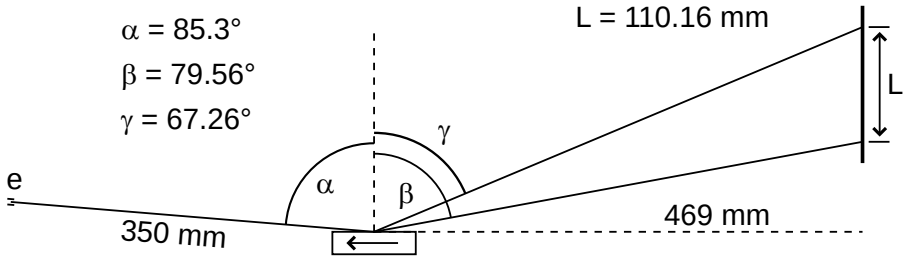

Figure 3.12: Imaging geometry of the used VLS grating which spectrally disperses the entrance slit (e) onto the flat imaging plane across the distance L. Technical details are taken from [107].

The VLS grating in use disperses the wavelength range between ~ 11 and 62 nm (corresponding to ~ 20 to 110 eV) onto a flat ~ 110 mm wide image plane. The average groove density is 1200 mm ^{1}. Further specification details are indicated in Fig. 3.12 and can also be found in [107]. For the detection, a back-illuminated thermo-electrically cooled CCD camera is used [108], which is sensitive for the XUV spectral region of interest. Both low thermal and readout noise and high dynamic range allows for efficient and fast (typically hundreds of milliseconds up to a few seconds) detection also of a low XUV photon flux.

The CCD chip contains 1340×400 pixels, each of size 20×20 μm^2. In the spectral direction, a region of 26.8 mm can thus be covered with the chip. The camera therefore has to be moved along the flat spectral plane in order to cover the whole energetic range. This is realized with a home-built (machine shop at MPIK) mechanical bearing including a flexible membrane bellow and set screws. The flexible design allows for fine adjustments in order to exactly position the camera chip into the imaged spectral plane. During operation, the camera can be freely moved along the spectral plane while its relative position can be read out with ~ 0.1 mm precision. Further technical details on the mechanical

bearing and the spectrometer design in general are depicted in Fig. 3.11. The entrance slit of the spectrometer is defined by the focal spot of the XUV light which is created by the toroidal focusing mirror (see section 3.4) inside the target cell. Its size can be estimated from the focused laser spot and is expected to be on the same order as the size of a single CCD pixel.

Assuming an evenly spaced dispersion of the specified wavelength range along the full spectral plane, a mapping of $\sim 9.3 \cdot 10^{-2}$ Å per CCD pixel can be expected. With this first estimation, for 60 eV XUV energy, a theoretically achievable resolution of ~ 27 meV can be expected, assuming the size of the camera pixel as the limiting element. The convolution of an experimentally measured spectral line shape (see section 6.2) with a Gaussian point spread function yielded a resolution of ~ 47 meV FWHM at 60 eV which is very close to the theoretically estimated value and was sufficient for the first performed experiments as presented in chapter 6. Further improvements are still possible within the capabilities of the spectrometer design and subject of future alignment work.

Chapter 4

Sub-cycle strong field interferometry

This chapter is devoted to the sub-fs motion of an electron bound to an atom – an attosecond electron wave packet. The processes that occur when atoms are interferometrically exposed both to strong (on the order of 10^{14} W/cm^2) and ultrashort few-cycle laser pulses were analyzed. It is numerically shown, by utilizing a computer experiment, how characteristic time scales can be accessed that are much shorter than the duration of the laser pulses which are used. The observed time period is also shorter than the cycle duration of the laser pulses. In addition, the energy spacing ΔE which corresponds to the observed wave-packet motion (cf. section 2.4) is not contained within the bandwidth of the laser pulses. While these results may seem unexpected at first glance, it is a natural consequence of the well-defined coherence of the laser pulses and it shows that the time scale of their duration (both envelope and cycle) is not imposing any fundamental limit to the time-scale of observation in such fully coherent interferometric experiments. The presented scheme is very similar to Fourier transform spectroscopy, where limitations are only of technical nature (detector resolution, stability, etc.) as they are a result of Fourier analysis (Nyquist's criterion).

The strong-field interferometric scheme is possible with the availability of CEP-stable laser pulses [109], which perfectly define the electric field evolution of the pulses with sub-fs precision. This means that not just the *envelope* of a laser pulse, but more precisely its well-defined electric *field* interacts with a system. More aspects of the CEP within this scheme can be found in section 4.5. The remainder of this chapter is based on our already published work [110], where the scheme was already introduced and the key findings were described.

The introduced strong-field interferometric scheme creates and measures an electron wave packet. In the following, a short overview of similar experimental configurations will be given where also wave packets (both electronic and vibronic) were interferometrically observed directly in the time domain.

4.1 Quantum wave-packet interferometry

As introduced in section 2.4, quantum wave packets evolve on time scales which correspond to the inverse spacing of the involved energy levels. Rotational wave packets in molecules were observed earliest (see e.g. [111] and references therein) as their characteristic time scale is on the order of picoseconds (the typical energy level spacing is on the order of few to sub-meV) which was most easily accessible along the development of ultrafast tools. Employing pairs of femtosecond laser pulses in an interferometric configuration, vibrational wave packets could be directly observed in the time domain [111, 112], where the vibrational period of an electronically excited iodine molecule was determined to about 300 fs, and the vibrational level structure could be retrieved from the time-resolved measurement via Fourier analysis [112]. Moving to shorter time scales, the vibrational level structure of the D_2^+ molecular deuterium ion was experimentally analyzed more recently [113, 114] and opened a route towards the full determination of the combined rotational and vibrational motion of small molecules [115]. In these latest experiments, intense ($5 \cdot 10^{14}$ W/cm^2) few-cycle (7 fs) laser pulses were used to tunnel-ionize neutral D_2 into D_2^+ and coherently prepare a vibrational wave packet. This excitation step was later replaced by an isolated attosecond pulse [116] where a vibrational wave packet was prepared and measured in an H_2^+ molecular ion. Within this scheme, the authors could also demonstrate a measurement of the combined nuclear and electronic motion [117], pointing towards dynamics beyond the Born-Oppenheimer approximation, in which electronic rearrangement is assumed instantaneous on the time scale of nuclear motion.

For the electronic degree of freedom only, bound wave packets were observed in Rydberg states of a potassium atom [118] on time scales of few hundred femtoseconds. About ten years later it was shown [119] that free electron wave packets (on their way to the detector) interfere in response to two time-delayed non-linear two-photon interactions again with a potassium atom. As a consequence of the involved two-photon interferometric scheme, a modulation frequency of twice the laser central frequency ($2\omega_c$, i.e. a modulation period corresponding to half the laser cycle) was imprinted into the measured photoelectron spectra. This finding already points out how sub-cycle dynamics can be accessed, namely via nonlinear interferometric interaction of the involved laser pulses. Very recently, an interferometric experiment was performed in singly excited helium using an isolated attosecond pulse and a time-delayed few-cycle femtosecond pulse [120]. The experimentally measured photoelectron spectrum contained a signature of both bound and continuum electron wave packets beating on an sub-femtosecond time scale. The broad energy spectrum of the attosecond pulse allowed the simultaneous excitation of several bound (and continuum) electronic states which formed an attosecond electron wave packet. Finally, we could recently realize the excitation and measurement of a two-electron wave packet evolving on attosecond time scales which involves doubly-excited states in an helium atom. This will be described in more detail in chapter 6.

All these experiments show that the direct time-resolved measurement of quantum wave packets is a very active field. Based on the nonlinear interferometric approach in [119] we now further investigate this approach for the case of both strong and ultrashort laser pulses, involving higher nonlinearities with spectrally broader few-cycle pulses. Within

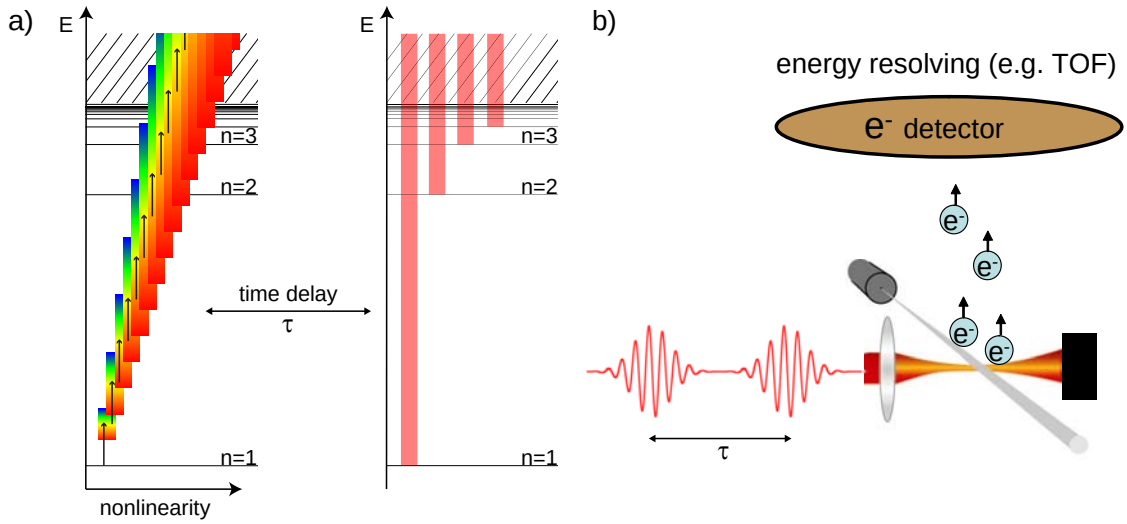

Figure 4.1: Basic experimental scheme of the nonlinear pump–probe scenario. a) Model electronic level scheme of an atom, where for simplicity only the principle quantum levels of hydrogen are shown. The typical energy spacing extends over the order of 10 eV, with photon energies on the order of 1.6 eV. Due to the large spectral width of the few-cycle laser pulses (indicated by the rainbow colors) the excited states ($n \geq 2$) can be reached via combination of different numbers of photons with increasing nonlinearity. The multi-photon picture is used for illustration while the whole process is better understood in the tunneling regime (see text). The indicated spectral width is used only for illustrative purposes and may not reflect the actual broadness, however this does not affect the argument of overlapping orders for the highest excited states (as also justified by our simulation). After a time delay τ all bound states are projected into common continuum states with a second strong laser pulse (vertical red bars). The nonlinear steps there are not shown for simplicity. b) Schematic of the experiment. Two time-delayed laser pulses are focused into an atomic gas jet. The released electrons encode the interferometric signal and are energy resolved e.g. with a time-of-flight (TOF) detector.

this scheme we can access both bound and continuum electron wave packets on attosecond time scales where neither attosecond pulses nor ultraviolet or shorter-wavelength fields are required for excitation, and in addition a vast range of energy levels, both dipole-allowed and non-dipole allowed, can be reached, going beyond linear two-pulse interferometry.

4.2 The basic experimental scheme

The basic scheme of our numerical experiment is depicted in Fig. (4.1). An atom is exposed to an intense laser pulse which partly excites an electron from the ground state both into higher lying electronic states as well as into continuum states (i.e. ionization). Due to the fully coherent interaction of the laser pulse with the atom, an electronic wave packet is formed which evolves freely after the atom-laser interaction. After the time delay τ, a second laser pulse, an exact copy of the first pulse, again interacts with the atom and can project different spectral parts of the excited wave packet onto each other in the continuum where an energy-dependent interference pattern is formed. This scheme

can also be understood in the traditional pump (first laser pulse) and probe (second laser pulse) scenario which will subsequently be used for simplified reading.

A crucial prerequisite of this scheme to work is of course the first step, that it is possible to excite various electronic energy levels of an atom after the interaction with an intense laser pulse. For strong fields in the tunneling regime this was recently demonstrated in an experiment [121]. It can be understood in terms of frustrated tunneling ionization, where a part of the electron is initially tunnel-ionized within a fraction of the laser field (see also section 2.2.1). If the ionic Coulomb potential is fully considered for the subsequent laser-driven electron motion (which is usually neglected in SFA), it was shown [121] that the electron can be recaptured into higher-lying excited states. We also considered this scenario for different pulse durations down to the few-cycle regime, where more details can be found in [122]. The name "frustrated tunneling ionization" thus stems from the fact that the electron, though tunnel-ionized at first, never really leaves the atom which means that the ionization channel is partly suppressed. This effect has also been theoretically discussed earlier in the multi-photon picture [123, 124], where due to the resonant coupling of many Rydberg states with the continuum a destructive interference sufficiently suppresses the ionization channel in favour of excitation.

The basic selection rules known from single photon excitation [34] can be considered broken which means that electronic states of any parity can in principle be excited. This is explained with the broad-band multi-photon excitation scheme as illustrated in Fig. (4.1). In our scheme we consider single-electron excitations only i.e. using intensities only slightly above the onset of strong-field single ionization.

4.3 Analytical and numerical framework

After the first pump pulse a coherent wave packet is formed similar to Eq. (2.49) in section 2.4, where the position expectation value evidences the wave packet. The excitation step with the pump pulse from the ground state $|g\rangle$ can be formally expressed as

$$\langle \Psi(t=0)|\hat{L}_{\mathrm{pu}}|g\rangle, \tag{4.1}$$

where $\hat{L}_{\mathrm{pu}}$ describes the full coupling with the pump laser pulse $\tilde{E}_{\mathrm{pu}}(t)$ (e.g. by means of frustrated tunneling ionization). The excited final state $|\Psi(t=0)\rangle$ is a superposition of both bound states $|\phi_n\rangle$ and continuum (momentum) states $|\vec{k}\rangle$. The excitation step can be expressed by the complex expansion coefficients b_n and $c(\vec{k})$ of the bound and continuum states, respectively. After the pump-pulse excitation, the electronic wave function of the atom can therefore be written in most general terms as

$$|\Psi(t)\rangle = \sum_n b_n e^{-iE_n t}|\phi_n\rangle + \int_{\vec{k}} d^3k\, c(\vec{k}) e^{-\frac{i}{2}k^2 t}|\vec{k}\rangle \tag{4.2}$$

where atomic units $\hbar = e = m_e = 1$ are used throughout. The now following derivation of the final continuum states after the probe-pulse interaction, which eventually leads to the detectable photoelectron momentum spectrum $S(\vec{k})$, follows our work which we already described in [110]. The superposition state as given in Eq. (4.2) evolves freely for a time

τ given by the delay between the pump and the probe pulses. After the probe laser pulse, the evolved initial superposition state is modified and its continuum portion can be written as

$$\begin{aligned} |\tilde{\Psi}_c(t)\rangle &= \int_{\vec{k}} d^3k \, |\vec{k}\rangle \langle \vec{k}|\hat{L}_{\mathrm{pr}}|\Psi(\tau)\rangle e^{-\frac{i}{2}k^2(t-\tau)} \\ &= \int_{\vec{k}} d^3k \, \tilde{c}(\vec{k}) e^{-\frac{i}{2}k^2(t-\tau)}|\vec{k}\rangle \end{aligned} \tag{4.3}$$

where $\hat{L}_{\mathrm{pr}}$ describes the full coupling of the atom with the intense probe laser pulse $\tilde{E}_{\mathrm{pr}}(t)$. The $\tilde{c}(\vec{k})$ represent the amplitudes of the continuum wave function after the probe laser pulse:

$$\tilde{c}(\vec{k}) = \sum_n c'_n(\vec{k}) e^{-iE_n\tau} + c''(\vec{k}) e^{-\frac{i}{2}k^2\tau} \tag{4.4}$$

with

$$\begin{aligned} c'_n(\vec{k}) &= L_{\mathrm{pr}}^{\vec{k}n} b_n \\ c''(\vec{k}) &= c(\vec{k}) e^{-\frac{i}{2}\int_{t_1}^{t_2} \vec{A}(t)^2 dt}, \end{aligned}$$

in which $L_{\mathrm{pr}}^{\vec{k}n} = \langle \vec{k}|\hat{L}_{\mathrm{pr}}|\phi_n\rangle$ stands for the matrix element of $\hat{L}_{\mathrm{pr}}$ connecting bound state $|\phi_n\rangle$ with the momentum state $|\vec{k}\rangle$ due to the probe pulse. Times t_1 and t_2 are chosen such that the probe laser pulse is fully contained in the interval $[t_1, t_2]$ before and after the pulse, respectively, and the vector potential $\vec{A}(t)$ is defined in the Coulomb gauge with $\lim_{t\to\pm\infty}|\vec{A}(t)| = 0$. For the formulation of $c''(\vec{k})$ we consider only the Volkov phase, which is justified for the probe pulse arriving after some time when the pump-ionized electron is already far away from its parent ion. The photoelectron momentum spectrum obtained for the combined interaction of both pulses thus reads:

$$\begin{aligned} S(\vec{k}) &= |\tilde{c}(\vec{k})|^2 \propto \sum_n |c'_n(\vec{k})|^2 + |c''(\vec{k})|^2 \\ &+ \Bigg[\sum_{n,m<n} c'_n(\vec{k}) c'^*_m(\vec{k}) e^{-i(E_n - E_m)\tau} \\ &+ \sum_n c'_n(\vec{k}) c''^*(\vec{k}) e^{-i(E_n - \frac{1}{2}k^2)\tau} + c.c. \Bigg]. \end{aligned} \tag{4.5}$$

The terms in brackets are responsible for τ-dependent oscillations of the photoemission probability with frequencies $E_n - E_m$ and $E_n - \frac{1}{2}k^2$. Note that these interference terms appear *regardless* of the nature or complexity of the pump and probe interaction. For few-cycle pulse excitation as considered here, the CEP enters the complex-valued wave-function coefficients $c'_n(\vec{k})$ and $c''(\vec{k})$ such that for non-CEP stable pulses the interference patterns are generally washed out. This will be discussed in more detail in section 4.5. Even though both the pump and the probe step are nonlinear and can be complex, the evolution of the states proceeds in the field-free temporal window between the two pulses. Signatures of the field-free electron wave packet during this time window are thus encoded in the detectable photoelectron spectrum.

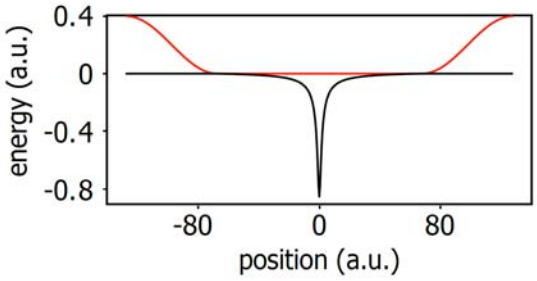

Figure 4.2: The black line shows the 1D soft-core potential for the model argon atom along the simulated spatial grid. The imaginary boundary potential in order to absorb the ionized electron wave packet is shown in red. Recolliding trajectories of the electron in the laser field are fully contained because $\omega_c = 0.057$ a.u. and $\mathscr{E}_0 = 0.08$ a.u. correspond to a ponderomotive radius $r_p \sim$ 25 a.u. (see Eq. (2.29) in section 2.2.2).

The numerical framework of the computer experiment is now described in detail, which was performed in order to confirm above theoretical considerations. We assume linear polarization of both laser fields pointing into the same direction. This is most of the times also realized in experiments. In order to enhance the computation time (the system has to be evaluated for a large set of different temporal delays τ), a one-dimensional solution of the time-dependent Schrödinger equation (1dTDSE) is implemented.

An atom with a single active electron is considered here, using the soft-core binding potential $V(x) = -(x^2+a^2)^{-1/2}$ introduced in [10] which has since then become a routine approach to study the interaction of atoms with strong laser fields. The parameter a is chosen to match the ground state energy $E_0 = -15.7596$ eV ($a \approx 1.154$) of argon [9] as an example target. The non-relativistic, dipole-approximation Hamiltonian with the laser field present thus reads

$$\hat{H} = \frac{(\hat{p}+A(t))^2}{2} - \frac{1}{\sqrt{\hat{x}^2+a^2}} \tag{4.6}$$

with the vector potential $A(t)$ defined in the Coulomb gauge. The split-operator technique (see for instance [125–127]) is employed for the numerical evolution of the 1dTDSE. It employs the separate evolution of the wave function in real space ("$\hat{x}$") and in momentum space ("$\hat{p}$") for each single time step Δt, where the two domains are connected via Fourier transform. The advantage of this technique is that the temporal evolution of the wave function $|\Psi(t)\rangle$ within each time step Δt is merely the multiplication of a phase factor $\exp[-iH_{x,p}\Delta t]$, where the split Hamiltonian $H_{x,p}$ in each domain is just a function of x or p rather than an operator. The ground state of the system is obtained by field-free evolution in imaginary time ($\Delta t \to -i\Delta t$) starting from a completely random wave function. In that case, the phase factor turns into an exponentially decaying function which, when renormalizing $|\Psi(t)\rangle$ after every imaginary time step, eventually leads to the ground state $|\phi_0\rangle$ with the smallest (least decaying) energy E_0.

Gaussian laser pulses with a FWHM duration of 6 fs, a carrier wavelength of 800 nm ($\omega_c = 1.55$ eV) and $\phi_{CEP} = \pi/2$ are used in the simulation. The peak of the electric-field envelope is $\mathscr{E}_0 = 0.08$ a.u., corresponding to a peak intensity of $2.2 \cdot 10^{14}$ W/cm^2. Two equal pulses of this kind are temporally delayed for a range of τ between 1000

and 2998 atomic units of time. For each delay, the wave function is evolved for a total time $T = 4000$ a.u. with a step size $\Delta t = 0.1$ a.u.. The parameters of the space grid ($N = 512$, $\Delta x = 0.5$ a.u., which yields ± 128 a.u. spatial extension) are chosen such that recolliding electron trajectories (propagating in the strong laser field) are fully contained (see also Fig. (4.2)). An imaginary absorbing potential is used to collect the outgoing electrons in order to obtain the photoelectron spectra.

When entering the imaginary boundary region at positive x, the absorbed electron wave function is transferred to a new "detector grid" of 8192 sampling points and spatial resolution $\Delta x' = 1.5$ a.u.. This resampling is done for several reasons. The maximum kinetic energy of interest is the first ATI cutoff at $2U_\mathrm{p} = 0.7553$ a.u. in our case. This corresponds to a momentum $p_\mathrm{max} = 1.23$ a.u. which is still well below the Nyquist limit $p_\mathrm{Ny} = 2.09$ a.u. of the detector grid. Furthermore, this grid has a momentum resolution $\Delta p = 5.11 \times 10^{-4}$ a.u.. To resolve the modulation $\Delta E \sim 2\pi/\tau$ at the maximum time delay $\tau = 2998$ a.u., $\Delta p = \Delta E / p_\mathrm{max} = 1.7 \times 10^{-3}$ a.u. is needed, which is also fulfilled by the parameters of the detector grid. Finally, the spatial dimension of the grid are large enough to avoid unphysical interferences due to periodicity, as the time it takes for the fastest electrons to cross half the grid is about 5000 a.u., which is still larger than the total simulation time T.

The interferometric step size $\Delta\tau$ to sample the pump–probe delay is directly connected to the maximum resolvable energy E_{max} via Nyquist's theorem reading $\Delta\tau = \pi/\Delta E_\mathrm{max}$. As an example, to probe the beating between the ground and highest bound electronic states of argon, separated by ~ 15.8 eV, the time resolution should be at least set to $\Delta\tau = 130$ as. We chose an interferometric step size $\Delta\tau = 2$ a.u. corresponding to about 50 as. In turn, the total interferometric time span which is scanned directly influences the energy resolution of the simulated level scheme. We scanned in total over 2000 a.u. (i.e. 50 fs) which yields an energy resolution $\delta E = 1.6 \cdot 10^{-3}$ a.u. (i.e. 40 meV). These considerations show that within this interferometric scheme, there is no fundamental limit in resolution. Limits are only of a technical nature (stability, time of data acquisition, statistics, detector resolution) which of course most of the times are quite challenging. An ultimate resolution limit is then of course given by the life time of the excited states just as in any other spectroscopic approach [34, 46], including line-shape broadening and related effects. The travel time to the detector (on the order of nanoseconds) is usually not an issue for the here considered time scales.

4.4 Demonstration of the strong-field-interferometry scheme

In order to demonstrate the excitation of the wave packet after the interaction of the atom with the pump pulse, both the dipole $\langle\Psi|\hat{\mathbf{r}}|\Psi\rangle$ and quadrupole $\langle\Psi|\hat{\mathbf{r}}^2|\Psi\rangle$ expectation values are shown in Fig. (4.3). These correspond to an electronic wave-packet beating among odd and even parity states, respectively. For three dimensions this implicates that both dipole-allowed and dipole-forbidden states were excited and are coherently beating. This proofs that within our strong-field excitation scheme more than single-photon

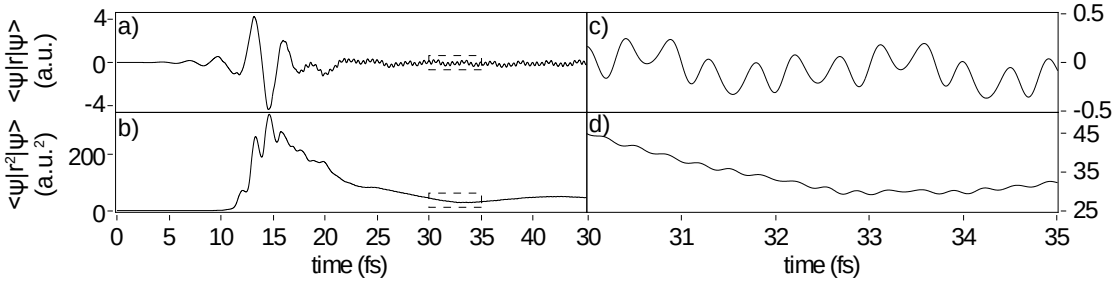

Figure 4.3: Coherent wave-function beating after the interaction with the first pump pulse which arrives at $t \approx 14$ fs. Both the position a) and position squared b) expectation values are evaluated where c,d) are magnified views. A sub-fs-timescale oscillation occurs after the pump pulse which indicates the coherently excited wave packet. Both odd (a,c) and even (b,d) parity states are excited which corresponds in 3D to the excitation of both dipole-allowed and dipole-forbidden states.

dipole-allowed states can be accessed. A Fourier transform of this modulation is shown in Fig. (4.7) and will be discussed at the end of this section. Before that, the experimentally accessible photoelectron spectra are now presented and discussed.

In Fig. (4.4) the obtained photoelectron momentum spectra are plotted both for a single pump pulse (which was also used to show the beating in Fig. (4.3)) as well as for two pump–probe cases at different time delays $\tau_{1,2}$ which are indicated in the figure. Spectral modulations that are enveloped by the single pulse spectrum are observed. This modulation is time-delay dependent as predicted by Eq. (4.5). The entire set of photoelectron spectra between τ_1 and τ_2 are shown in Fig. (4.5). Even though both pump and probe pulses are significantly longer than 1 fs, as is the optical cycle of 2.7 fs, pronounced non-trivially structured sub-femtosecond beating patterns are observable as a function of time delay. This sub-cycle beating is due to the time-dependent complex electronic wave packet as shown in Fig. (4.3). As motivated in the introductory section of this chapter, it is created by and synchronized to the CEP-stable strong electric *field* of the pump pulse that gets projected into the continuum by the probe field. Importantly, this is in contrast to the temporally less well-defined excitation and probing by the longer pulse *envelope* as for single-photon excitation or schemes using non-CEP-stabilized strong-field excitation that tend to wash out such sub-cycle beating patterns. More considerations on CEP- and intensity-effects will be discussed in the following (section 4.5).

To reveal the beating frequencies within the time-delay modulations in Fig. (4.5b), the photoelectron momentum spectra are Fourier transformed with respect to the time delay τ. The result is shown in Fig. (4.6), exhibiting the entire set of beating frequencies predicted by Eq. (4.5). The modulation $|E_n - \frac{1}{2}k^2|$ (with negative binding energies E_n) is given by the parabola-shaped features which start at the corresponding energy level $|E_n|$ at zero photoelectron momentum. The strongest contribution to the modulation is observed in the parabola starting at the ground-state ionization potential energy $I_p = 0.58$ a.u. ($E_0 = -15.76$ eV for argon). This corresponds to an interference of free electron wave packets ionized by the pump pulse and the probe pulse out of the ground state, as first measured in [119] for a two-photon step. The momentum-independent vertical lines can be assigned to $E_n - E_m$ (see Eq. (4.5)) and therefore refer to the attosecond

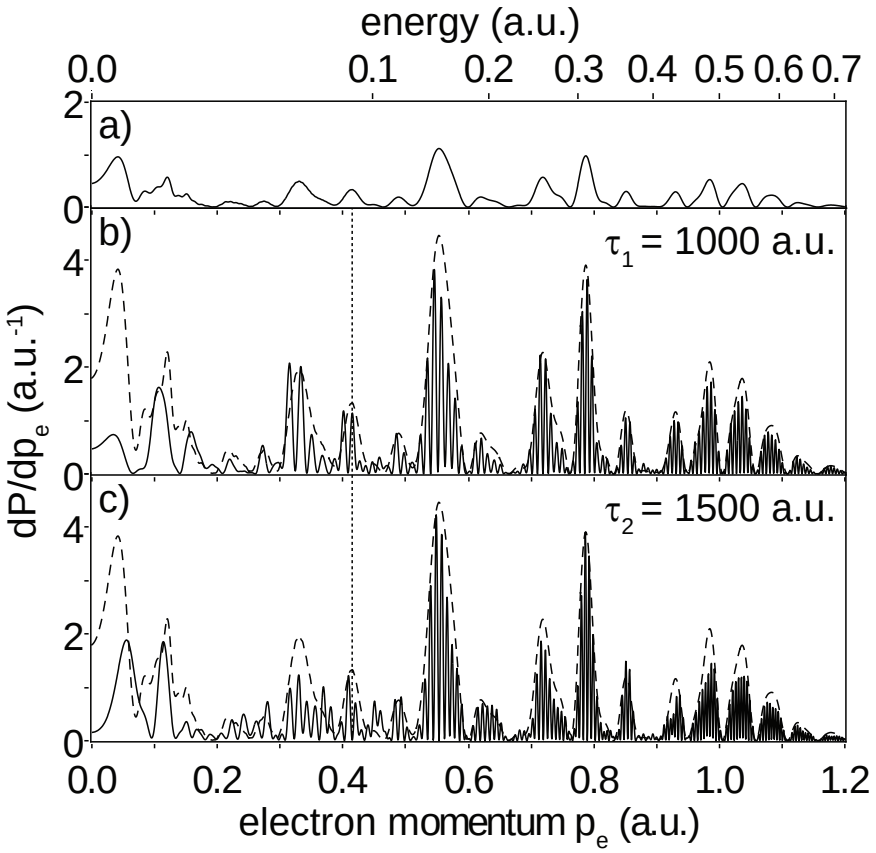

Figure 4.4: Taken from [110]. Photoelectron momentum spectra a) for one single pump pulse, b) and c) for two identical pump–probe pulses at two different time delays $\tau_{1,2}$ as indicated in the figure (solid lines). In b) and c), the rescaled (times four) single-pulse spectrum of a) is also shown (dashed line). A vertical dashed line at an electron momentum $p_e = 0.415$ a.u. is drawn to highlight the time-delay-dependent modulation.

quantum beating between different bound electronic states of the atom which recently has been measured in helium [120] but with a single-photon excitation scheme using an attosecond pulse for the pump.

In our situation, for strong driving fields slightly above the onset of single-electron ionization, the ground state remains the most populated bound state in the system ($\approx 93\%$ of the bound electron wave packet) after the interaction with both laser pulses. Therefore, the strongest vertical lines refer to electron wave-function beating between the ground state and the higher excited states. The ground state population thus plays a role similar to a strong local oscillator in a heterodyne detection scheme, leading to large observable beating amplitudes of weak signals (the small populations of the excited states in this case). Wave-function beating among the higher excited states themselves results in the weaker vertical lines at low energies up to $E = 0.24$ a.u. (the energy for ionization out of the first excited state). As can be seen from the two single-momentum and integrated-momentum lineouts in Fig. (4.6a,d), it is necessary to observe the time-dependent modulation resolved for a certain range of electron momenta or at least for two separated electron momenta in order to distinguish between bound and continuum electron wave packets.

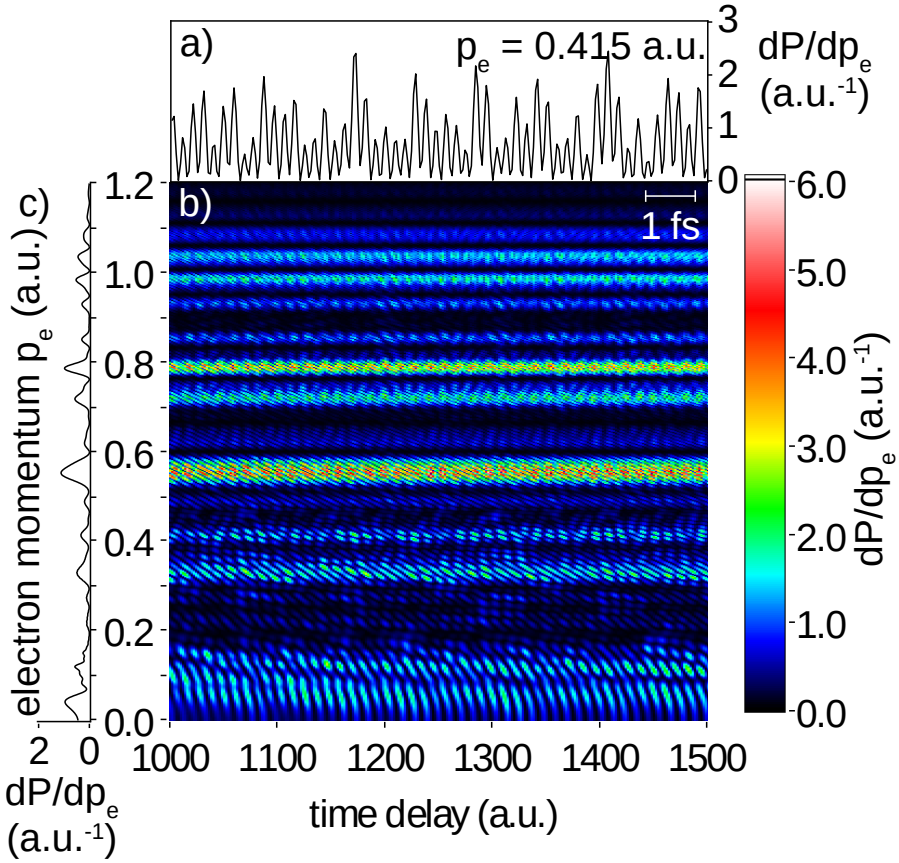

Figure 4.5: Taken from [110]. Time-delay dependent photoelectron spectrum a) at the selected photoelectron momentum $p_e = 0.415$ a.u. (dotted line in Fig. (4.4)), b) for a broad range of photoelectron momenta. The single-pulse spectrum from Fig. (4.4a) is additionally shown in c). Attosecond time-scale beatings are clearly observable as a function of time delay. Note the momentum-dependent visibility of the modulation in b) is corresponding to the peaks and dips of the single-pulse photoelectron spectrum in c).

Fig. (4.7) finally shows the dipole and quadrupole beating spectra obtained via Fourier transform of the expectation values presented earlier in Fig. (4.3). For comparison, the momentum-integrated pump–probe spectrum from Fig. (4.6d) is also shown. The position of the spectral lines obtained from the pump–probe data in Fig. (4.7a) agrees perfectly with the electron wave-function beating in Fig. (4.7b,c), proving that both dipole-allowed and dipole-forbidden transition energies among states are accessible within this approach, a qualitative augmentation compared to the single-photon pumping schemes such as [120].

As mentioned at the end of section 4.3, the spectral resolution of this method is limited solely by the inverse of the pump–probe scanning period as in earlier interferometry approaches [112, 118]. The spectral resolution $\delta E = 40$ meV is much less than the bandwidth of the individual femtosecond pulses (~ 0.3 eV) and certainly much less than the entire spectral range of accessible beating frequencies (> 16 eV). This proves that the spectral and temporal structure of the pulses in such schemes are decoupled from the accessible spectral and temporal resolution in experiments.

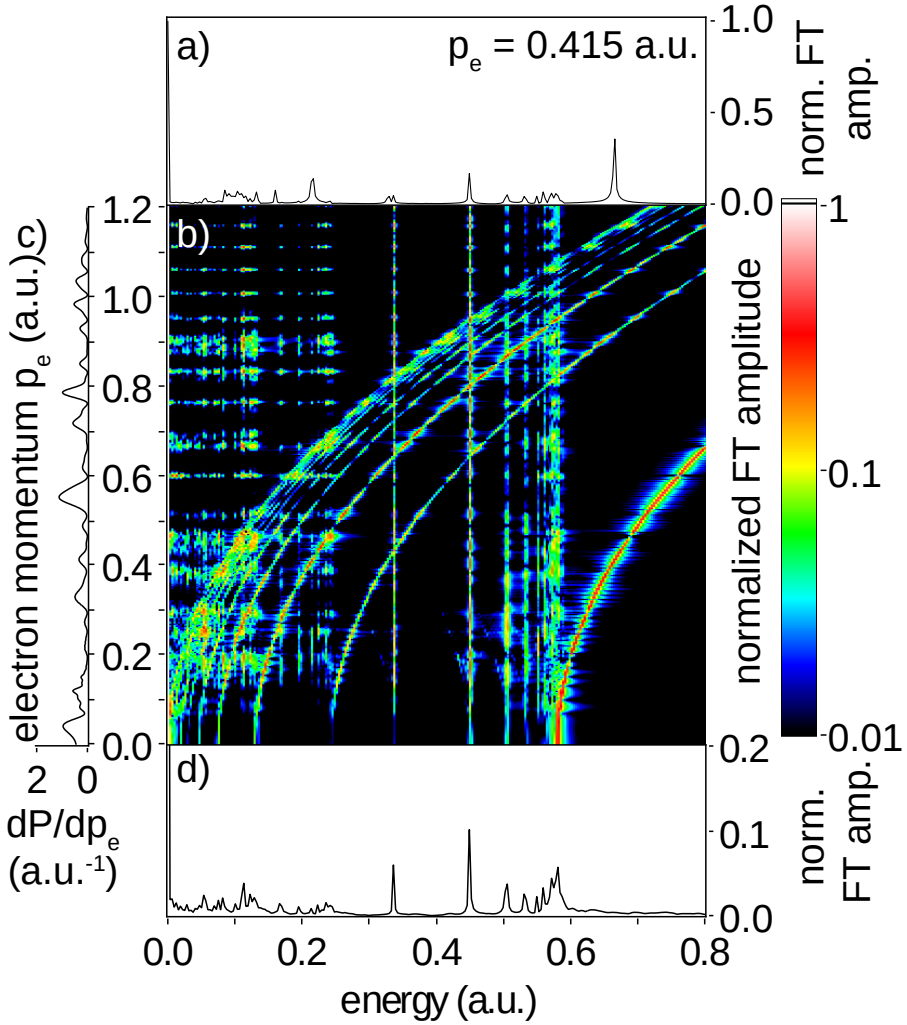

Figure 4.6: Taken from [110]. Beating frequencies of electronic bound and continuum states after Fourier transformation of the data in Fig. (4.5b), a) for a lineout at momentum $p_e = 0.415$ a.u., b) for all photoelectron momenta. Each Fourier-transformed spectrum is normalized to its zero-frequency component, thus numerical noise along the minima in the photoelectron spectrum is artificially enhanced (the horizontal features). c) The single-pulse photoelectron spectrum from Fig. (4.4a). d) Momentum-integrated frequency spectrum. See also text for further explanations and interpretation of the features. When comparing the single-momentum lineout in a) with the integrated-momentum lineout in d), the contribution from the bound states (the vertical lines in b)) are present in both lineouts, while the contributions from free wave-packet interferences (the parabolas in b)) are only present in the single lineout and are washed out in the integration.

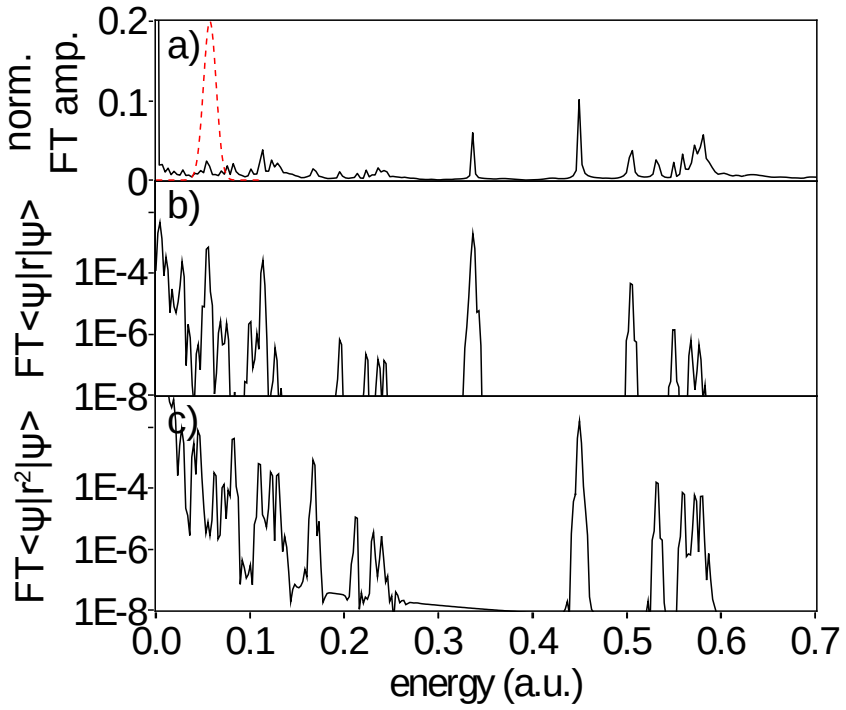

Figure 4.7: Taken from [110]. a) Momentum-integrated frequency spectrum of the electron beating signal (from Fig. 4.6d). The dashed red line shows the laser-pulse spectrum. b,c) Fourier transform of the position (b) and position-squared (c) expectation value of the electronic wave function as shown in Fig. (4.3) after the interaction with the pump pulse. The agreement of the spectral positions of the wave-packet beatings in b) and c) with the experimentally observable data from a) is excellent and predicts that both dipole-allowed and dipole-forbidden excitations can be experimentally measured. The laser pulse spectrum (dashed red line in a)) illustrates that the accessed levels are well outside the linear-excitation spectrum.

4.5 Effects of the intensity and the carrier-envelope phase

Fig. (4.8) shows the time-delay-dependent modulation pattern across the photoelectron momentum spectrum as a function of the electric field strength and the CEP. Especially for the variation of the electric field strength, a strong shift of the modulation peaks is apparent. Using Fourier analysis, the modulation repeats roughly 12 times across the shown range $\Delta\mathscr{E} = 0.02$ a.u., which can also be confirmed by counting the interference maxima along a fixed momentum value (e.g. $p_e = 0.415$ a.u.). This is also the case for higher electron momenta (not shown). An absolute change $\delta\mathscr{E} \approx 2 \cdot 10^{-3}$ a.u. of the electric field strength would therefore shift subsequent fringes into each other, corresponding to 2.5% relative change at $\mathscr{E}_0 = 0.08$ a.u., which corresponds to an intensity variation of 5%. The laser intensity has to be kept fixed below this value in order to reveal the interferometric modulation pattern. This might be technically challenging but is within reach of currently available intense laser sources in the few-cycle regime, which typically can be kept stable with shot-to-shot noise on the order of 1% rms.

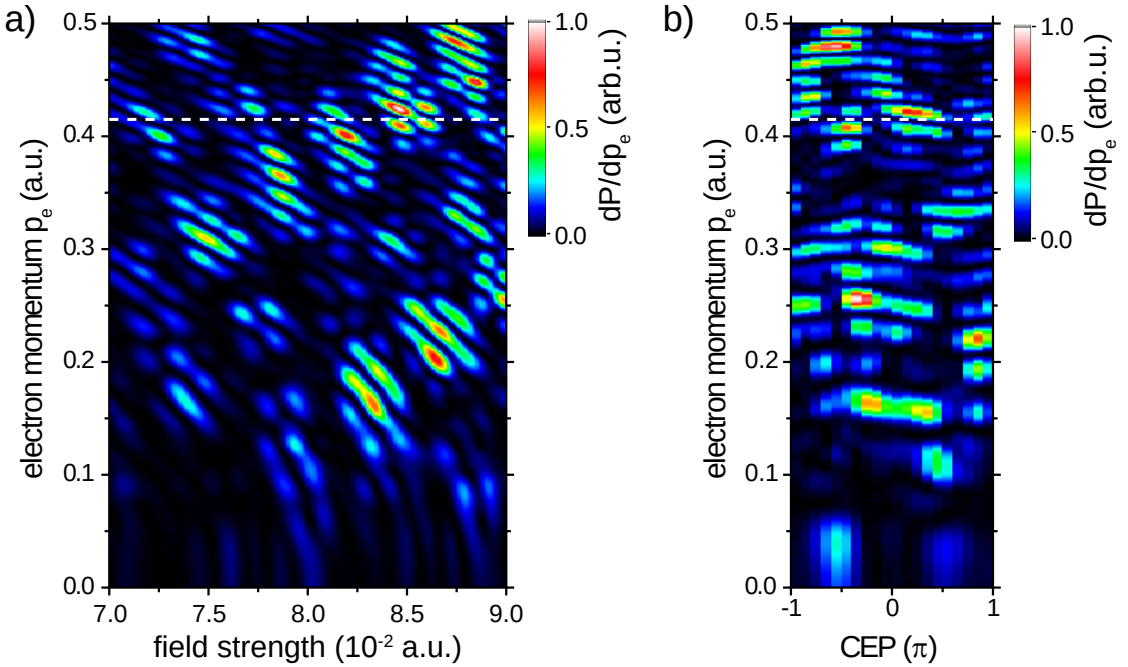

Figure 4.8: Pump–probe-induced modulation pattern across the photoelectron momentum spectrum as a function of the electric field strength (a) and the CEP (b). The time delay was set to $\tau = 1000$ a.u.. The CEP was fixed at $\phi_{\mathrm{CEP}} = \pi/2$ in (a), and the electric field strength was set to $\mathscr{E}_0 = 0.08$ a.u. in (b). The remaining pulse parameters are unchanged and defined in section 4.3. The dashed white lines outline the electron momentum $p_{\mathrm{e}} = 0.415$ a.u..

The impact of the CEP on the interference pattern can be quantified to a shift of modulation maxima into their neighbouring minima within $\Delta\phi_{\mathrm{CEP}} \approx \pi$. Currently available shot-to-shot stabilities of the CEP are on the order of 500 mrad and better. These stabilities are therefore sufficient in order to resolve the pump–probe-induced modulation pattern. Besides, measuring the photoelectron spectra separately for every single shot, much higher laser stabilities can be reached as nowadays few-cycle laser pulses can be characterized on a shot-to-shot basis [83]. Appropriate focusing conditions have to be used in an experimental realization, both to avoid focal volume averaging and rapid changes of the Gouy phase along the focused beam [5]. This has to be done in order to avoid further intensity and CEP averaging.

Fig. (4.8) also shows that additional changes in the photoelectron spectra are induced by a variation of the electric field strength or the CEP which originate from each single laser pulse. They can be explained with quantum orbits [128, 129] where electron emission is timed with attosecond sub-cycle resolution also within one laser field. It is based on the interpretation of the electron emission as a temporal-slit-interference experiment [130], which can be influenced both by the laser intensity and the CEP. These parameters thus also encode changes in the emission dynamics in strong-field ionization which can be experimentally resolved when exploring these parameters in multidimensional data sets. In the remaining chapters this is realized for different experimental configurations.

4.6 Concluding remarks on sub-cycle strong field interferometry

In conclusion for this chapter, a new interferometric scheme was proposed and demonstrated with a computer experiment. It involves a highly nonlinear interferometric detection scheme inducing sub-cycle attosecond wave-packet beating. The highly nonlinear interaction of few-cycle laser pulses with a medium (which itself also generates attosecond pulses, see section 2.2.2) can be utilized *directly* in order to access these sub-fs time scales, or equivalently for a description in the energy domain to coherently excite and probe a multitude of quantum states, spanning over several eV.

A crucial point of this work was to demonstrate that using the interferometric approach the only limitations in temporal or spectral resolution are of technical nature. Besides the stability issues, the achievable resolution can be determined from considerations of Fourier analysis as described at the end of section 4.3. It should however also be mentioned that a high-resolution electron-detection (on the order of 40 meV or better, depending on the investigated process) is needed to resolve the interferometric modulation in the photoelectron momentum spectra.

In principle, using linear polarization only as it was considered here, certain electronic orbitals might not be accessible or be suppressed as compared to others (obeying a non-accessible symmetry). One could therefore think of replacing at least the first pump pulse with arbitrary elliptical polarization, or using polarization-shaped laser fields [131] to selectively excite a certain range of states. This might especially prove advantageous when using molecules as target species. However, the key point of the here described scheme is that no matter how complex the excitation step might be, after the interaction, the system evolves in a *field-free* environment. As the second laser pulse is interferometrically phase-locked to the first pulse, this evolution can subsequently be measured. In order to fully reconstruct the three-dimensional wave packet, coincidence measurement techniques [99] can be applied, especially when more than one electron is involved, or other electron/ion-imaging techniques like velocity map imaging [132] could be used. Both techniques allow to access the electron momentum differentially across the full 4π solid angle.

Usually spatial interferometers are applied to precisely measure small changes along the interferometric paths. Applying this idea to the time domain as it was presented in this chapter (and as it was already applied in [112, 118] and certainly in many more related work which is not mentioned here), it is possible to use a third laser pulse to disturb the field-free system. This way, the coupling among various excited states can be analyzed. Transferring the scheme to molecules, the excitation might also involve metastable transition states which influence the outcome of chemical reactions. In that case, it is finally crucial that the duration of the coupling laser pulse is on the time scale of the transition process, where the temporal structure of the pulses is ultimately needed. However, as it should have become clear from this chapter, there is no fundamental limitation for the interferometric detection and only broad-band excitation spectra (which here are achieved in a nonlinear way) are needed to reach the states of interest. A realization might for example involve the tracking of an ultrafast charge migration in glycine molecules [133].

When using a weak attosecond pulse for a perturbative coupling of the excited states, it needs to be further investigated if this is sufficient for such a scheme. On the other hand, also stronger few-cycle femtosecond pulses could be used to couple the excited states, already yielding a temporal resolution of few femtoseconds, which is most of the times sufficient even for many ultrafast electronical rearrangements in chemistry.

It turns out that this proposed scheme is very similar to the experiment which we performed for doubly-excited autoionizing states in helium, where we could measure how metastable states can be disturbed from their field-free evolution. This is described in more detail in chapter 6, where the interferometric detection scheme is realized with attosecond pulses and the interferometric nature of the spectral line shape itself, while the coupling is achieved with a few-cycle femtosecond laser pulse.

Finally, with the intra-pulse CEP and intensity effects mentioned in section 4.5, a highly multidimensional interferometric scheme can be constructed, involving not only the time delay but also both the CEP and the pulse intensity as dynamical parameters. All this is possible with the ultimate control over the electric field of the pulses itself. It is needless to say that much further effort is needed in order to fully analyze all these parameters and their influence on possible experimental realizations, while even more parameters could be constructed like the chirp of the laser pulses, their duration or even other more complex degrees of freedom of shaped laser fields. The topmost questions which further conceptual work should address are (i) how linearly independent are all these parameters in the constructed multi-dimensional space and (ii) what is the structure of this space and how is it changing across specific time-dependent problems which are under investigation. The answers should then finally lead to optimally constructed schemes for experimental realizations and to extracting a maximum amount of information about the physical processes at work.

For the remainder of this thesis, two further experimental approaches are investigated, where in both cases the multidimensionality in terms of the dynamical parameters is particularly emphasized. In the following chapter 5, the role of the CEP is particularly addressed with the concept of spectral interferometry, while in the last chapter 6, the laser intensity will play a major role.

Chapter 5

CEP-resolved spectral interferometry

In conventional multi-dimensional (mainly two-dimensional) spectroscopy, more than one spectral parameter is used in order to reveal couplings between different energy states. The basic idea is to use multiple-pulse configurations in time which create spectral interference patterns. These patterns can be analyzed with Fourier techniques employing spectral interferometry (SI) which reveals both amplitude and phase response of the system. This complex information can be represented along an additional spectral axis to result in an effective emission vs. excitation spectrum where characteristic diagonal and off-diagonal contributions reveal the couplings between different quantum states of the system (see e.g. [134, 135] for reviews). The field originated from multidimensional NMR spectroscopy [136], where a sequence of radio-frequency pulses are applied and couplings of nuclear spins can be analyzed with temporal resolution (typically microseconds). Moving to the infrared spectral domain, these principles were theoretically described (e.g. [137, 138]) and experimentally realized (e.g. [139, 140]), where vibrational excitation dynamics in molecules could be traced at femtosecond to picosecond time scales. It was further applied in the optical domain [141] where couplings of electronic (excitonic) excitations were followed in photosynthetic systems with femtosecond time resolutions, which also revealed quantum coherence in the energy transfer of these systems [142]. A realization in the x-ray domain was proposed [143] but is not yet experimentally realized due to the historic lack of intense coherent pulses in this frequency range, because nonlinear excitations are needed. This situation is about to change with the intense free-electron laser (FEL) pulses that have now been demonstrated at several large-scale facilities around the world. In all these examples, SI is a key tool to create a link between the temporal and spectral domain and to access both amplitude and phase information of the system. The interacting laser fields are typically considered in the perturbative regime.

By contrast, when *intense* laser pulses interact with an electronic system, the *highly nonlinear response* leads to non-perturbative effects, typically resulting in repetitive events in time spaced by the laser half-cycle (in the case of inversion symmetry). In a most simplified manner this can be classically understood because strong-field ionization is intrinsically locked to regions where the electric field is near its maximum values (see section 2.2.1). It was early realized, that high-harmonic generation interpreted in this way must lead to trains of attosecond pulses [144], which was subsequently also demon-

strated in an experiment [145]. The quantum-mechanical interpretation of these processes is based on the identification of few quantum orbits (typically two, the so-called short and long trajectory) per laser cycle which dominantly contribute to the observable signals [24]. Directly applying spectral interferometry to attosecond pulse trains generated from multiple-cycle laser fields most likely would not lead to substantially more information, simply as many equally-spaced contributions overlap in time. It could only yield an estimate on how many attosecond pulses are in the train [146, 147].

For few-cycle laser pulses, CEP effects are now frequently observed in interaction with all kinds of media. Attosecond timed electron emission from atoms can be interpreted as a temporal double slit experiment [130]. Asymmetric electron emission from simple diatomic molecules [148] in few-cycle laser pulses reveal interference patterns originating from few quantum paths. Few-cycle laser interaction with nano-scale metal tips [149] yielded collective electron emission which also encodes interference signatures originating from one or two emission events. Just recently, collective electron emission was also gained from plasmas in interaction with few-cycle extreme intense ($\sim 10^{18}$ W/cm^2) laser pulses [150], where temporally interfering signatures were observed in the XUV high-harmonic emission from this process. All these experimental schemes incorporated CEP-stable laser pulses where strong dependencies on the CEP were observed in the recorded data. Even for a multiple-cycle (20 fs duration) laser field in interaction with an argon gas target [151], CEP effects could be observed in the generated high-harmonic signal, which is due to the different impact of the CEP on the involved long and short quantum paths.

As CEP dependence is present in so many different scenarios, we can now introduce the idea of CEP-resolved spectral interferometry (CEPSI). It uses the power of SI to access relative amplitudes and phases of the interfering contributions within one and the same few-cycle pulse on attosecond time scales. For few-cycle pulses, naturally only few contributions are expected which makes data obtained from SI more easy to interpret, but this does not represent a strict limitation of the method. In addition, we can make use of the CEP as an additional parameter which sensitively influences these different interfering contributions. Therefore, the CEP will also influence the additional phase-information which SI can convey. As the CEP is directly related to the temporal domain—it is a parameter which shifts the laser cycles along the time axis, which is defined/fixed by the envelope peak of the pulse—it is more straightforward to directly interpret the phase signature obtained from SI in the Fourier-time domain, i.e. skipping the temporal filtering and subsequent back-transformation (see section 2.3). Already the direct Fourier transform then yields both relative amplitude and phase information as it was for example employed in [29, 30]. Conceptually this scheme is of course different from conventional two-dimensional spectroscopy methods as introduced above. In the same manner, however, multi-dimensionality again allows to disentangle otherwise inseparable interfering contributions. While in the latter case, typically spectral vs. spectral data is shown and individual quantum state contributions are separated, here the data is analyzed in two quasi-temporal domains—the CEP and the Fourier time—and temporal quantum pathway information is separated. In both schemes, spectral interferometry (based on Fourier analysis) is employed to access the phase contributions.

Before further introducing the CEPSI framework in section 5.2, the generation and characterization of attosecond pulse trains will be shortly introduced in the following section,

as our scheme is exemplary applied to the observed interference of few attosecond pulses which is then finally presented in section 5.3.

5.1 Attosecond pulse trains

Attosecond pulse trains (APTs) were theoretically described in [144] shortly after the experimental demonstration of high-harmonic generation (HHG, see also section 2.2.2). Actually APTs were even considered before [152, 153], however at that time, the high-harmonic generation process was not yet fully understood and confusion was caused by rapid "unpredictable" phase changes across the harmonics obtained from a numerical solution of the time-dependent Schrödinger equation [153, 154]. This confusion was resolved when later a fully quantum-mechanical description of the process was achieved [21], employing the strong-field approximation (SFA) and based on the classical three-step model [19]. Within this quantum-picture of HHG, the interference of different quantum paths per laser half-cycle is responsible for the seemingly "unpredictable" phase changes which was resolved in [144].

The first direct experimental demonstration of APTs [145] also involved a new characterization technique using a two-colour cross-correlation of the generated APTs with its driving near-infrared (NIR) laser pulse. The method of data analysis was subsequently termed RABBITT (resolution of attosecond beating by interference of two-photon transitions) [155]. Its basic working principle is the absorption or emission of one additional NIR photon during photoionization of atoms with high harmonics. This NIR interaction appears in between two neighbouring high harmonics (sidebands) which modulate as a function of the time-delay between the generated APT and the NIR pulse. With this, the relative phase of adjacent harmonics can be retrieved. This allowed the temporal characterization of APTs and was applied in many subsequent experiments.

A simplified train of attosecond pulses generated from a monochromatic laser field is illustrated in Fig. (5.1). The different recombination times and kinetic energy of the tunnel-ionized electron explains why the generated attosecond pulses are chirped, resulting from the classical three step model [19]. This is the so-called attochirp [157] which was experimentally confirmed with RABBITT [158]. In [157] it was also shown how the slow variation of the APT across the femtosecond envelope can be determined, making use of the laser-intensity dependence of the harmonic phase [159], by varying the intensity of the whole laser pulse and still assuming that the attosecond pulses within the train only change slowly from pulse to pulse, i.e. the adiabatic assumption of infinitely long driver pulses is still valid.

With shorter driver-pulse durations approaching the few-cycle regime, non-adiabatic effects have to be taken into account [160], where the trajectories (or quantum orbits) belonging to every subsequent laser half-cycle have to be treated separately [25]. In this regime, the CEP also strongly influences the generation of APTs from few-cylce laser pulses [161].

For the few-cycle domain, an iterative algorithm based on frequency-resolved optical gating (FROG), the complete reconstruction of attosecond bursts (CRAB) [162] is applied to

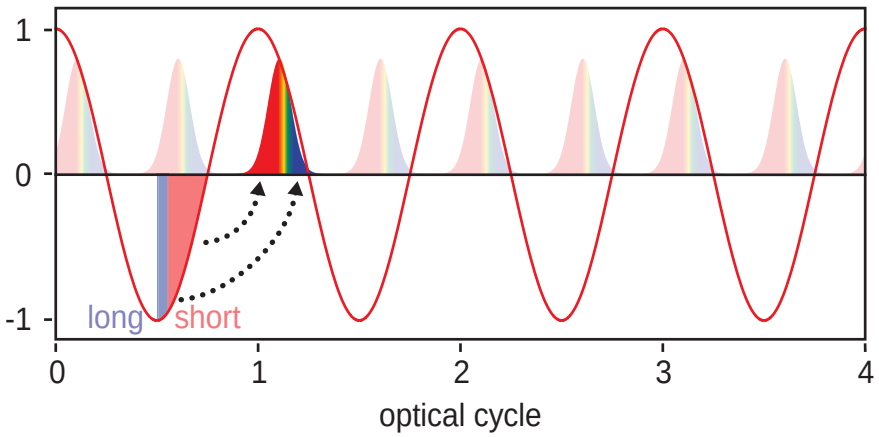

Figure 5.1: Schematic illustration of an APT, shown for long driver pulses (approximated as a monochromatic wave, solid red line). Two attosecond pulses are generated per laser cycle. The blue and red shaded areas denote the birth time of the tunnel-ionized electron within the three step model [19] which eventually will reencounter the ionic core (see also section 2.2.2), where the colour encodes long (blue) and short (red) travel times with equal kinetic energy at recombination. Considering only short trajectories (red, experimentally selected e.g. via phase matching [144, 156]), the energy depends on their time of birth and is converted into the instantaneous frequency of the attosecond pulses (illustrated by the arrows and with rainbow-coloured pulses). This explains why the attosecond pulses are chirped.

the obtained photoelectron spectra from cross-correlation XUV/NIR measurements. This algorithm allows both the reconstruction of the attosecond-pulse structure as well as the electric field of the driving femtosecond pulse. As it is not assuming infinitely long driver pulses as opposed to RABBITT, it is explicitly non-adiabatic and more suited for the few-cycle regime. It is most easily applied to the temporal reconstruction of isolated attosecond pulses [163,164], where the experimental scheme can be more easily understood as attosecond streaking [165–167]. Recently the CRAB algorithm was also successfully applied to the reconstruction of an APT [168] from 30-fs-duration multiple-cycle laser pulses.

Signatures of few interfering attosecond pulses were also directly identified in the high-harmonic spectrum [146, 147], generated from CEP-stabilized laser fields. Such spectra are perfectly suited for applying spectral interferometry techniques in order to additionally access the relative phase of the interfering pulses, thus gaining comprehensive access to the individual quantum paths directly from the optical response. This is where our general two-dimensional CEPSI analysis method will now be described and demonstrated, namely for the example of few interfering attosecond pulses. It allows the experimental separation of the phase contributions of individual pulses in a few-cycle APT only by measuring its optical spectrum, which directly connects to its temporal profile when phase information is included.

5.2 Illustration of the CEPSI framework for three attosecond pulses

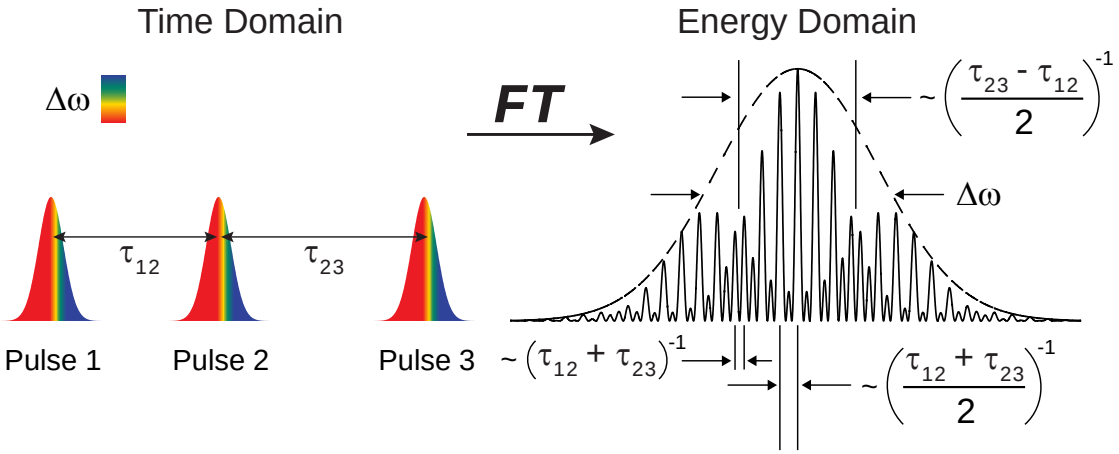

Figure 5.2: Illustration of an asymmetrically-spaced temporal triple slit. The three pulses are non-equally spaced by τ_{12} and τ_{23}. Their spectral bandwidth is contained within $\Delta\omega$ where the spectral phase of all three pulses is assumed equal ($\tilde{\Phi}_1(\omega) = \tilde{\Phi}_2(\omega) = \tilde{\Phi}_3(\omega)$). In the energy (Fourier) domain, an interference pattern $S(\omega)$ is formed with major and minor peaks, resembling the pattern of a spatial triple slit. The pattern encodes the different temporal spacings as marked. A slow spectral beating is formed due to a small non-zero difference $\tau_{23} - \tau_{12}$ in the asymmetric pulse spacing. A characteristic of this beating is a transition from major to minor diffraction maxima.

To illustrate the CEPSI framework for interfering attosecond pulses, we add one more degree of complexity as to the two-pulse case introduced in section 2.3. Thus, three temporal events (pulse 1,2,3) are interfering (with overlapping spectral components), which have close, but not necessarily equal temporal spacing τ_{12} and τ_{23}. Following Eq. (2.44) from section 2.3, their spectral intensity modulation can generally be described as

$$\begin{aligned} S(\omega) \propto & \tilde{A}_1(\omega)\tilde{A}_2(\omega)\cos[\tilde{\Phi}_1(\omega) - \tilde{\Phi}_2(\omega) + \omega\tau_{12}] + \\ & \tilde{A}_2(\omega)\tilde{A}_3(\omega)\cos[\tilde{\Phi}_2(\omega) - \tilde{\Phi}_3(\omega) + \omega\tau_{23}] + \\ & \tilde{A}_1(\omega)\tilde{A}_3(\omega)\cos[\tilde{\Phi}_1(\omega) - \tilde{\Phi}_3(\omega) + \omega\tau_{13}], \end{aligned} \tag{5.1}$$

where here $\tilde{A}_n(\omega)$ and $\tilde{\Phi}_n(\omega)$ respectively denote the spectral envelope and the spectral phase of pulse n. Fig. 5.3 illustrates the spectral interference which can be expected from such a configuration which can essentially be interpreted as an asymmetric temporal triple slit. In the spectral (energy) domain, every signature can be attributed to the different pulse spacings τ_{nm}. Especially a slow spectral beating occurs due to the close temporal spacings $\tau_{12} \approx \tau_{23}$, with a π-phase jump of consecutive major interference peaks identified as a significant spectral feature.

The small spectral features (minor peaks) might be harder to detect experimentally due to their smallness and a limited spectral resolution, in contrast to the more easily visible

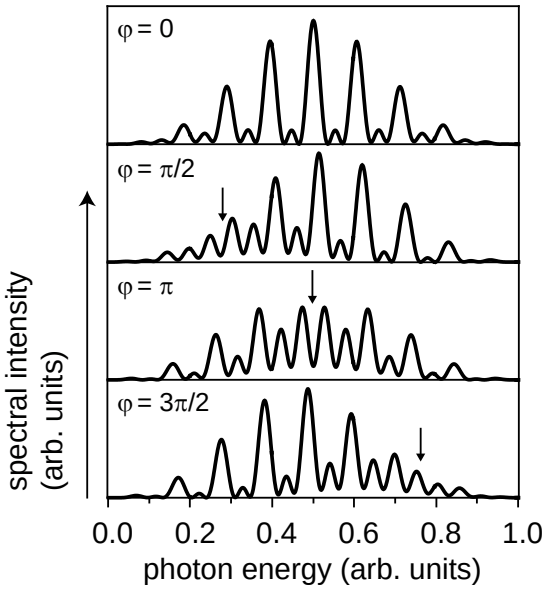

Figure 5.3: Spectral interference pattern for three asymmetrically spaced pulses where the observed spectral bandwidth is smaller than the beating period ($2/[\tau_{23}-\tau_{12}] \gtrsim \Delta\omega/2\pi$). The spectral phases of the three pulses are defined as $\tilde{\Phi}_1(\omega) = \tilde{\Phi}_2(\omega) = \tilde{\Phi}_3(\omega) + \varphi$. Depending on φ, the characteristic π-phase jump (where all interference peaks are equally high and thus swapping between minor and main peaks occurs) of the temporally asymmetric configuration is rapidly sweeping through the observed spectra as a function of φ, indicated by the small arrows.

π-phase jumps which could be identified as an anomaly. In particular when the separation-difference $\Delta = \tau_{23} - \tau_{12}$ approaches a fraction of the pulse duration, the beating frequency can become larger than the (detected) spectral bandwidth ($2/[\tau_{23}-\tau_{12}] \gtrsim \Delta\omega/2\pi$), which would move these π-phase jumps out of the detected range. This case is illustrated in Fig. 5.3. In addition however, consider the spectral phase $\tilde{\Phi}_3(\omega)$ of the third pulse can be changed by a constant offset φ relative to the phases of pulse 1&2. An intrinsic feature of such a change in φ can be identified as the rapid movement of the beating-induced π-phase jump across the detected spectral range.

As it is clear from the previous two sections on attosecond pulse generation, the CEP influences the individual attosecond pulses produced in each half cycle differently, when the driving pulse is few-cycle in nature. Thus, φ can later be identified as the CEP. In order to show how the different phase contributions $\tilde{\Phi}_n(\omega)$ can be directly retrieved from the spectral intensity modulation $S(\omega)$, the phase φ is continuously scanned between 0 and 2π, creating a two-dimensional data set which is subsequently Fourier analyzed both in amplitude and phase (Fig. 5.4). In this analysis, the previously defined relative pulse characteristics can be separated by recording a φ-dependent amplitude and phase structure, which would not have been possible for a single value of φ or a φ-averaged one-dimensional spectrum. The amplitude peak appearing at τ_{13} (which corresponds to the interference of pulse 1&3) exhibits the linear phase difference of φ between the two pulses. The amplitude peaks at τ_{12} and τ_{23} (which corresponds to the interference of pulse 1&2 and pulse 2&3, respectively) appear very close to each other within their temporal bandwidth where $\tau_{23} \approx 1.1 \times \tau_{12}$ was chosen. For a single value of φ, e.g. at $\varphi \approx n \cdot 2\pi$, where n is an

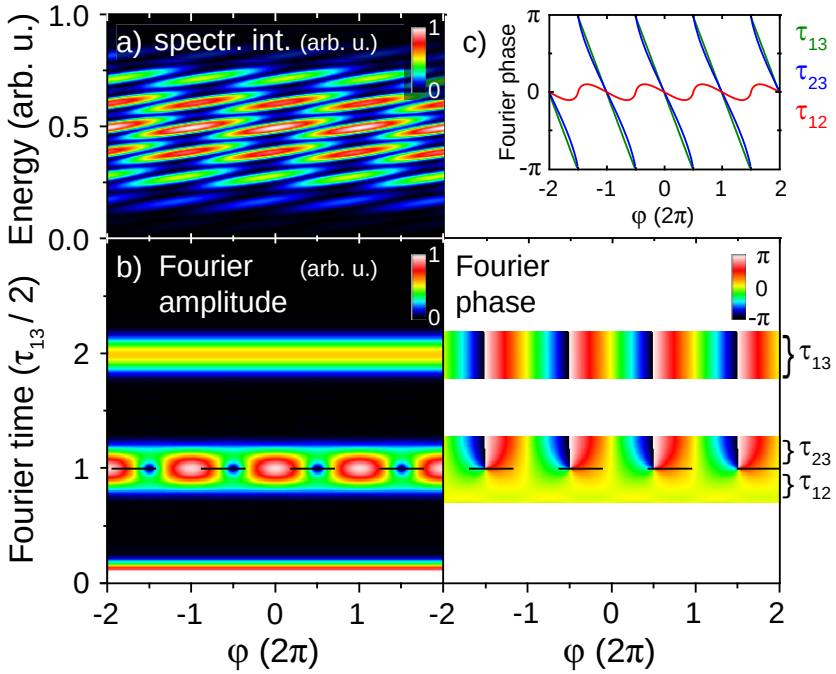

Figure 5.4: Spectral interference generated by all three pulses with phases $\tilde{\Phi}_1(\omega) = \tilde{\Phi}_2(\omega) = \tilde{\Phi}_3(\omega) + \varphi$ and $\tau_{23} \approx 1.1 \times \tau_{12}$. a) Two-dimensional spectroscopic data as a continuous function of energy and the relative phase φ, b) Fourier analysis of a) both in amplitude (left) and phase (right) where the correspondence to the different temporal components τ_{12}, τ_{23} and $\tau_{13} = \tau_{12} + \tau_{23}$ is indicated. c) averaged Fourier phase as a function of φ for each temporal contribution shown in b). In analogy to the experimentally obtained data four equal cycles of φ are shown.

integer number, the superposition of these two contributions exhibits one single peak in the Fourier amplitude while the phase is equal across this peak. However due to their different φ-dependence which is perfectly revealed in the two-dimensional plot, a minimum appears in the temporal overlap region at $\varphi = (2n+1)\cdot\pi$. The two-dimensional representation of the Fourier phase thus directly reveals the relative phase contributions from all three pulses. This is further illustrated in Fig. 5.4c where the Fourier phase is temporally averaged in order to create Fourier-phase lineouts, separately for each interfering contribution. While both τ_{13} and τ_{23} contributions clearly show a nearly-linear φ-dependence with slope 1, the contribution averaged over τ_{12} is only slightly changing with φ and is, most importantly, not changing from one into the next cycle. Deviations from a "perfectly" linear (which is only realized for the separated τ_{13} contribution) and "perfectly" flat φ-dependence across the overlapping τ_{12} and τ_{23} contributions are of course due a continuous transition between the two partly overlapping contributions. Nevertheless, the here presented Fourier analysis shows how the initially chosen phase behaviour for the three pulses can clearly and straightforwardly be disentangled.

For the here presented simplified and well-behaved toy model the above-defined relative-phase dependence could in principle also be read out directly from the spectral interference pattern which is shown in Fig. 5.4a. This of course then necessitates the understanding of the rapidly sweeping beating-signature which was presented along the discussion of the asymmetric triple slit. In contrast, the Fourier analysis directly reveals this

phase behaviour, thus a direct access to the relative pulse configurations can be gained. This motivates the power of the two-dimensional CEPSI method: First being "blind" to any measured (and potentially complicated) CEP-dependent spectral pattern, the complex Fourier analysis directly reveals and disentangles the different relative contributions, which are well localized in time, whereas delocalized in the spectral domain (broad harmonic spectrum). This will become even more clear after presenting the experimentally obtained data and the comparison to numerical simulations based on the non-adiabatic saddle-point approximation, both analyzed within the CEPSI framework.

5.3 Experimentally observed interference of few attosecond pulses

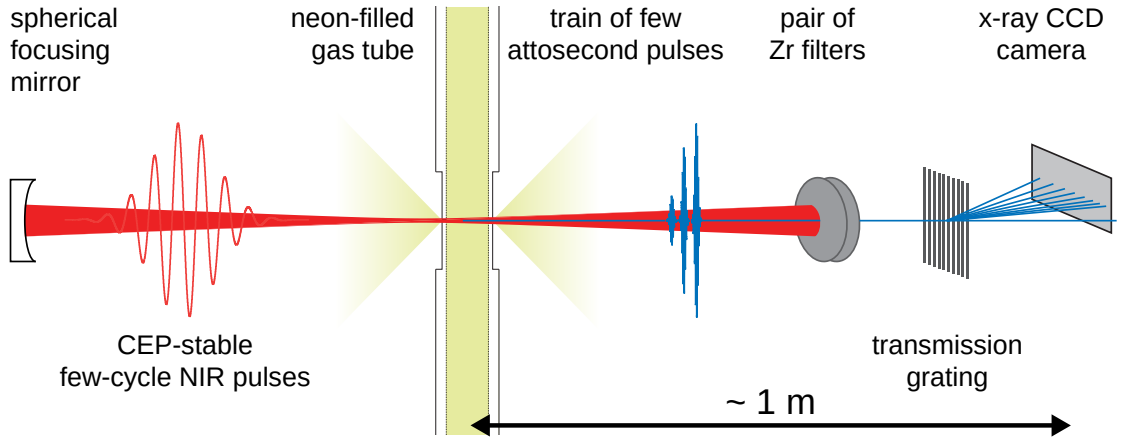

Figure 5.5: Schematic illustration of the experimental setup for the measurement of interference spectra generated from a train of few attosecond pulses. The individual setup components are described in the text.

The experiment was carried out at the beam line which is described in detail in section 3. Deviating from this beam line, the refocusing interferometric mirror setup and the high-resolution VLS grating were not yet implemented. Further details on the differing setup can be found in [85]. It should also be noted that a broad range of different high-harmonic generation parameters were used along these CEP-resolved experiments: Spatially resolved spectra in the far field were recorded for various gas pressures ranging between 0 and 150 mbar and cell positions varying by ~ 8 mm around the laser focus. All these macroscopic parameters are known to influence the relative-phase dynamics of the generated attosecond pulses [8, 169]. In order to illustrate the power of the CEPSI framework as it is applied to experimentally obtained data, only a single set of experimental parameters will be presented. A more detailed overview can also be found in [85], with emphasis on the observation of isolated half-cycle cutoffs [170]. In the following, the most important parameters of the setup are shortly summarized.

Few-cycle (~ 7 fs) laser pulses at ~ 760 nm central wavelength with stable CEP down to ~ 200 mrad are focused, with an $f = 500$ mm spherical mirror, into a ~ 3 mm long

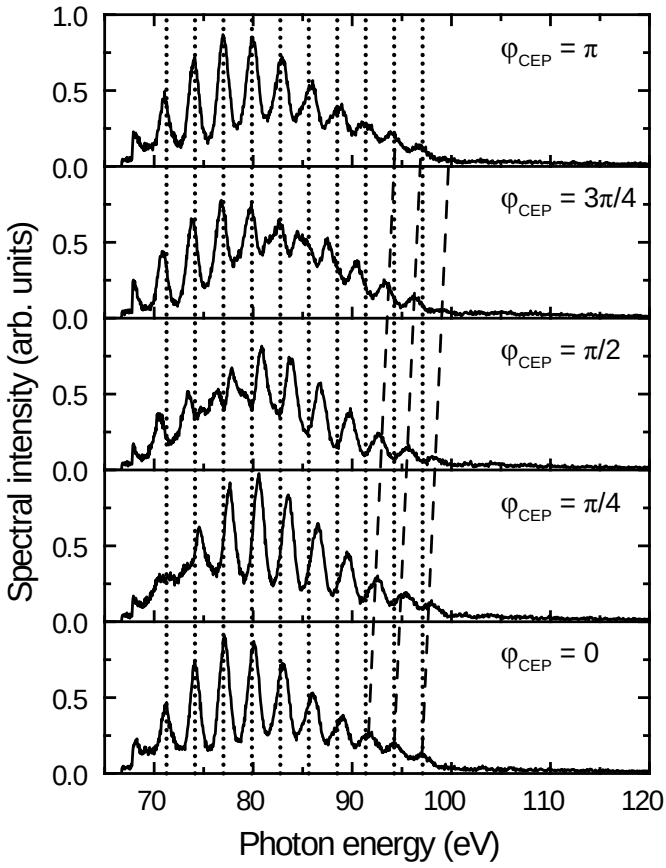

Figure 5.6: Spatially integrated high-harmonic spectra measured with ~ 7 fs CEP-stable laser pulses focused in ~ 100 mbar neon. The vertical dotted lines mark positions of constant photon energy in order to compare the different spectra. For the lowest energies the harmonic peaks stay close to these reference lines across the different CEP values. For the highest energies the harmonic peaks linearly shift into the neighbouring higher order as the CEP is varied from 0 to π (indicated with the tilted dashed lines). See also text for further discussions.

cell filled with neon gas at ~ 100 mbar backing pressure. To preferentially phase match short trajectories, the gas cell was placed just after the laser focus [144], on the order of 5 mm. The generated attosecond pulses are transmitted through a pair of 200 nm thin zirconium metal foils to remove direct and indirect fundamental stray light. Spectral dispersion is achieved with a 100 nm period free-standing Si_3N_4 transmission grating, and the separated spectrum is detected with a back-illuminated x-ray CCD camera. The setup scheme is also illustrated in Fig. 5.5. The spectrometer was calibrated with the identification of the Al $L_{II,III}$ absorption edge at 72.7 eV [86] of an optionally inserted Al filter, and the Si $L_{II,III}$ absorption edge at 99.7 eV [86] imprinted by the transmission grating. The spectrometer resolution is estimated to ~ 0.8 eV FWHM of a Gaussian point spread function at ~ 70 eV. With this resolution, interference signatures from up to two full-cycle spaced (i.e. 5.4 fs) attosecond pulses can be resolved, which correspond to a fringe spacing ~ 0.75 eV.

Fig. 5.6 shows experimentally-obtained high-harmonic spectra for five different CEP values between 0 and π. The interference fringes are spaced by ~ 3 eV, the well-known odd-

harmonic spacing, which corresponds to half-cycle spaced emission times of attosecond pulses. A region of low fringe visibility between 70 and 90 eV can be seen at intermediate CEP values. With the observed cutoff around 90 to 100 eV, a peak electric field strength on the order of 0.10 a.u. can be estimated ($\sim 3.5 \cdot 10^{14}$ W/cm^2). The interference peaks at the highest energies above ~ 90 eV appear to linearly shift as a function of the CEP, in agreement with earlier findings in the harmonic cutoff region [161]. It can be explained by the non-adiabatic saddle point approximation [25], identifying few interfering quantum paths.

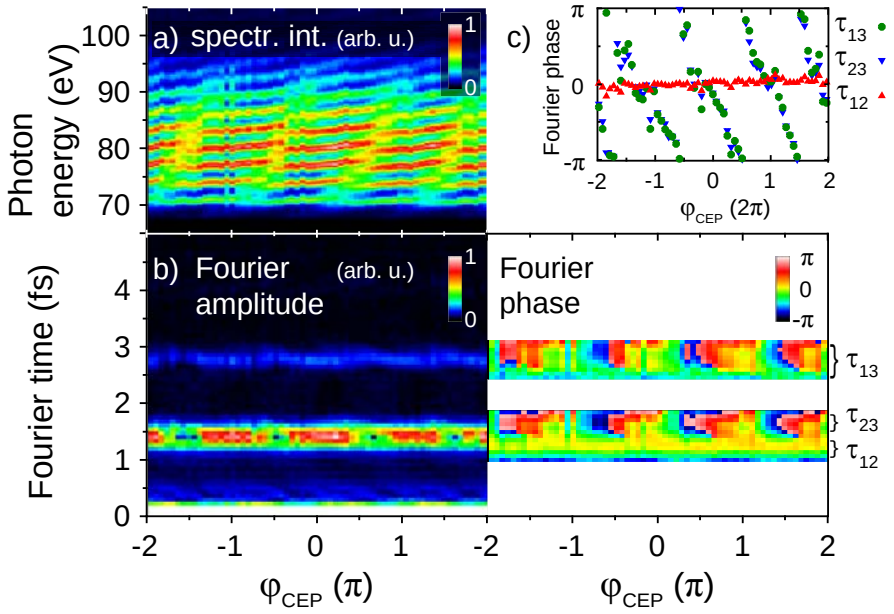

Figure 5.7: CEPSI analysis of experimentally obtained interference spectra from few attosecond pulses. a) Spectral interference pattern recorded as a function of the CEP. At energies below ~ 90 eV a splitting of the interference structures (harmonics) occurs as discussed in the previous section introducing the toy model of an asymmetric triple slit (compare to Fig. 5.4). b) Fourier analysis of a) with spectral filter parameters $E_{\min} = 71$ eV, $E_{\max} = 116$ eV, $\Delta E = 4$ eV (see text). A splitting of the amplitude peak as well as a bimodal phase behaviour is observed as the CEP is varied, as in the toy-model presented before (Fig. 5.4). c) The phase averaged over the marked temporal regions for τ_{12} (red triangle up), τ_{23} (blue triangle down) and $\tau_{13} = \tau_{12} + \tau_{23}$ (circle, green) is shown to clarify the qualitatively different CEP dependences.

To further analyze the CEP-dependent changes in preparation for the CEPSI method, the spectra are again represented two-dimensionally as a continuous function of the photon energy and the CEP in Fig. 5.7a. The experimental data is shown in a range of $\Delta\varphi_{\mathrm{CEP}} = 4\pi$ which corresponds to 4 periodic cycles in order to distinguish experimental noise from true CEP-dependent behaviour. Any real effect must therefore repeat periodically. For photon energies above 90 eV the harmonic interference structures shift linearly from one order to the next within one CEP as discussed along Fig. 5.6. Interestingly, in the energy region just below the cutoff ($\lesssim 90$ eV), a switching between different harmonic peaks occurs with a change in CEP. Repeating the previously illustrated Fourier analysis on these experimental data (Fig. 5.7b) results in a close agreement to the previous asymmetric three-pulse toy model. For the analysis, a spectral filter $C(E)$ along Eq. (2.43) was applied

where the parameters are noted in the figure caption. The CEP now takes the role of the general phase φ as introduced before, with $\Delta\varphi = 2\Delta\varphi_{\mathrm{CEP}}$ which is due to half-cycle periodic harmonic emission in the inversion-symmetric atomic conversion medium. Both for the full-cycle Fourier peak at τ_{13} as well as for the upper temporal part of the half-cycle Fourier peak at τ_{23}, the Fourier phase shows a linear CEP-dependence with slope 2. This slope corresponds to a completed full cycle (2π) every $\Delta\varphi_{\mathrm{CEP}} = \pi$. In contrast, the lower temporal part of the half-cycle peak at τ_{12} shows a constant Fourier phase as a function of the CEP. This observation also corresponds to the $\Delta\varphi_{\mathrm{CEP}} = \pi$-periodic occurence of a local minimum within the Fourier amplitude of the half-cycle peak. To better compare the different phase evolutions, the Fourier phase is integrated for the different τ_{nm} components and shown in Fig. 5.7c.

In direct comparison with the previously introduced toy model we can conclude that three attosecond pulses are most dominantly present, where the CEP only affects the phase of one of these pulses (pulse 3), while it has no influence on the remaining two pulses (pulse 1&2). In addition, the three attosecond pulses appear to be unevenly spaced. To confirm these findings revealed by the CEPSI analysis, a quasi-classical strong-field approximation of HHG [21] based on the three-step model [19] was carried out by using the non-adiabatic saddle point approximation [25] (see also section 2.2.2). This is the standard theoretical approach for calculating such CEP-dependent harmonic spectra. A direct comparison with the experimental observations can be performed by again analyzing the so calculated interference spectra with CEPSI. In addition, more physical insight is gained as the non-adiabatic treatment of every single quantum path allows to separately study the contribution of each attosecond pulse directly in the real-time (rather than Fourier time) domain and thus to confirm the validity of the CEPSI approach.

5.4 Quantum path analysis

The non-adiabatic saddle point calculations were performed for neon ($I_{\mathrm{p}} = 0.7416$ a.u.) with a 7 fs FWHM $\cos^2$ laser pulse (cf. Eq. (2.3)) centered around 760 nm and peak electric field strength 0.1033 a.u.. Only the short trajectories were considered. The quantum paths were calculated for 8 evenly spaced CEP values ranging between 0 and $7\pi/8$ in steps of $\pi/8$. These calculations were performed by [171]. A careful analysis of this data is performed within the CEPSI framework and presented in the following.

The resulting harmonic spectra are shown in Fig. 5.8a, where the same spectral filter $C(E)$ was applied as for the experimentally obtained data in Fig. 5.7. A first explanation for the asymmetric temporal spacing can be found in Fig. 5.8c. In the here discussed non-adiabatic case the cutoffs of each subsequent attosecond pulse (i.e. the half-cycle cutoffs) are located at different energies from pulse to pulse, spanning over ~ 20 eV which is much more than the harmonic spacing. In addition, the attosecond pulses posses an intrinsic chirp which is encoded in the electron recombination times (the red lines). These two effects give rise to an asymmetric pulse spacing within a fixed energy window: Different characteristic regions (i.e. half-cycle-plateau and half-cycle-cutoff regions) of neighbouring attosecond pulses may interfere. The exact recombination dynamics of neighbouring electron quantum paths thus give rise to the asymmetric temporal spacing of subsequent

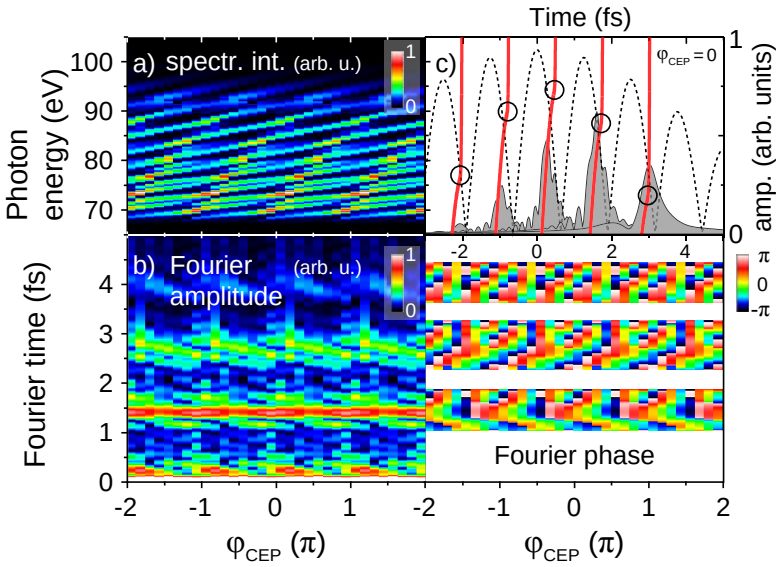

Figure 5.8: Simulation results from the non-adiabatic saddle-point approximation. The laser pulse parameters are $t_{\mathrm{FWHM}} = 7$ fs, $\lambda_c = 760$ nm, $\mathscr{E}_0 = 0.1033$ a.u., $\cos^2$ envelope function as defined in Eq. (2.3), bandwidth limited, with $I_p = 0.7416$ a.u. for neon. The CEP was ranging between 0 and $7\pi/8$ in $\pi/8$ steps. a) spectral intensity for all simulated CEP values, repeated over four cycles to allow an easier comparison with the experiment. A spectral filter $C(E)$ (cf. Eq. (2.43)) was applied with $E_{\mathrm{min}} = 71$ eV, $E_{\mathrm{max}} = 116$ eV, $\Delta E = 4$ eV. b) Fourier analysis of a) both in amplitude and phase. c) time-domain representation of the attosecond pulses for $\varphi_{\mathrm{CEP}} = 0$. Both the amplitude (grey shaded areas) as well as the recombination times (red solid lines) are shown, together with the absolute value of the electric field (black dashed line). The amplitude envelopes were obtained after applying the $C(E)$ spectral filter function. The black circles denote the beginning of the half-cycle-cutoff region of each pulse (where the slope of the red curves bend to infinity). Below this region, each pulse smoothly transits into its half-cycle-plateau region. See text for further discussion.

attosecond pulses.

The Fourier analysis in Fig. 5.8b reveals a more complicated structure as for the analyzed experimental data in Fig. 5.7b. Contributions of a 3rd Fourier peak (around 4 fs) which corresponds to a temporal spacing of three half-cycles can be seen. One further peak (above 5 fs, not shown in scale) is also present for certain CEP values. A comparison with Fig. 5.8c explains this observation, as mainly four attosecond pulses have non-zero amplitude, and for certain CEP values (e.g. $\varphi_{\mathrm{CEP}} = \pi/4$, not shown), even five attosecond pulses significantly contribute. The Fourier phase (right panel in Fig. 5.8b) also shows a seemingly complicated structure as many contributions are overlapping. A rapid phase slope of a least 2 along the CEP (see discussion of experimental results for a definition of this slope) is apparent across all Fourier peaks. In addition, the phase fronts are nearly flat (vertical) across the half-cycle Fourier peak, but they are more tilted in time across the full-cycle Fourier peak. Recalling that a linear phase slope in the Fourier (time) domain is caused by a shift/translation in the original (energy) domain (see section 2.1) this indicates that the contributions for the different Fourier peaks originate from different energy regions. With the previously identified relevance of the half-cycle-cutoff region for

the asymmetric temporal spacing, these regions may also cause the energetically shifted contributions to the different Fourier peaks. Indeed, within the analyzed energy region (between 71 and 116 eV), more than one attosecond pulse shows contributions from its own half-cycle-cutoff region. Especially around 70 eV and around 90 eV groups of different half-cycle cutoffs are located as can be seen in Fig. 5.8c. The analyzed region of interest thus contains many overlapping contributions from different energy regions, while this is most interestingly not the case for the experimental data shown in Fig. 5.7, which however spans over the same energetic range.

To analyze the different contributions in more detail, it appears useful to employ separate and smaller spectral filters within the analysis of the calculated data. This is shown in Fig. 5.9 for the higher energy region between 80 and 100 eV, and in Fig. 5.10 for the lower energy region between 60 and 80 eV.

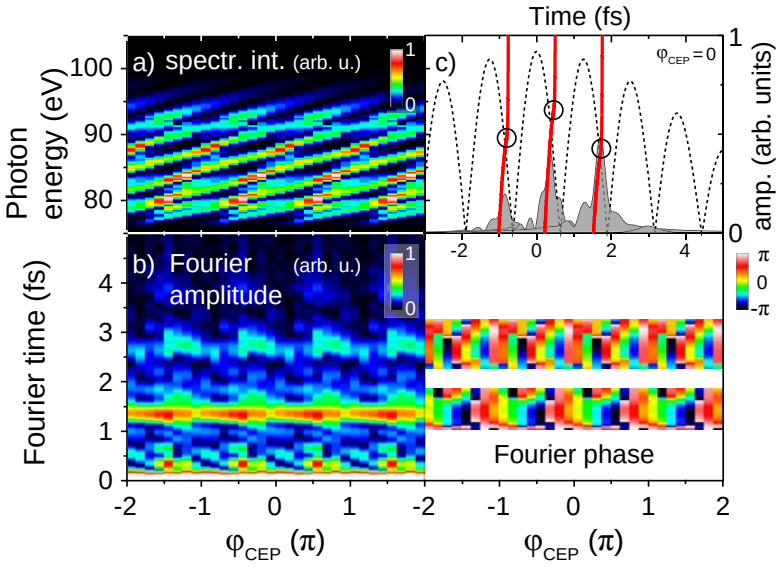

Figure 5.9: Same parameters as in Fig. 5.8 a) spectral intensity, b) Fourier analysis of a), c) attosecond pulses in time-domain representation. See Fig. 5.8 for further explanations. In deviation, $C(E)$ was applied with $E_{\min} = 80$ eV, $E_{\max} = 100$ eV, $\Delta E = 5$ eV for the calculation of b) and c). In the highest energy part, only three attosecond pulses are mainly dominating. The relevant contributions are further discussed in the text.

For the higher energy region in Fig. 5.9, only three attosecond pulses are significantly contributing as can be seen in c). However, the bimodal phase behaviour is absent from the Fourier analysis in b). Instead, the Fourier phase shows a CEP-dependent slope 2 for the half-cycle peak and a slope 4 for the full-cycle peak. The reason for the absence of the bimodal phase behaviour can be found in the more regular temporal distribution of the attosecond pulses in c): The half-cycle-cutoff regions of the three pulses are distributed within a relatively small energy region within $\lesssim 8$ eV. Therefore, the subsequent electron trajectories appear similar to each other, meaning that similarly chirped attosecond pulses interfere. The different CEP-dependent slopes of the Fourier phase (2 and 4) will be explained below, after first discussing the lower energetic region between 60 and 80 eV in Fig. 5.10.

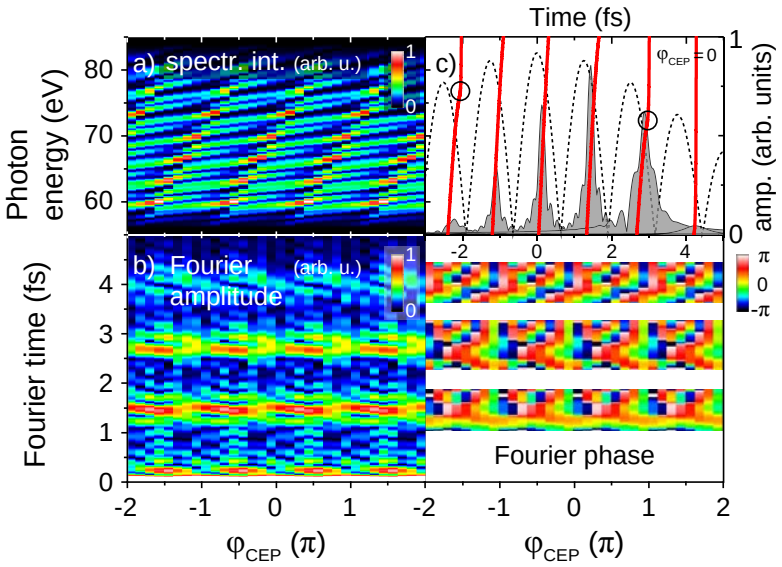

Figure 5.10: Same parameters as in Fig. 5.8 a) spectral intensity, b) Fourier analysis of a), c) attosecond pulses in time-domain representation. See Fig. 5.8 for further explanations. In deviation, $C(E)$ was applied with $E_{\min} = 60$ eV, $E_{\max} = 80$ eV, $\Delta E = 5$ eV for the calculation of b) and c). In the lower energetic region, more than four pulses are contributing. See text for further discussion.

Despite the fact that now more than four attosecond pulses are contributing to the data shown in Fig. 5.10, the Fourier analysis in b) also shows a more regular CEP-dependent Fourier phase which is due to the lower spectral bandwidth used for the analysis. Even a first hint for a bimodal structure across the half-cycle Fourier peak can be identified: The contribution at the lowest Fourier time slightly above 1 fs shows a nearly constant Fourier phase, while the contribution at a higher Fourier time ~ 1.5 fs clearly shows a CEP-dependent Fourier phase with slope 2. These two contributions are separated with local minima in the Fourier amplitude appearing around $\varphi_{\mathrm{CEP}} = \pi/8$ and Fourier time ~ 1.3 fs. In addition, the most intense contribution across the full-cycle Fourier peak clearly shows a CEP-dependent slope 2 across the Fourier phase. This behaviour closely resembles the experimental observation and the toy model of an asymmetric triple slit as discussed in the previous sections. Comparing with the temporal distribution shown in c), only one half-cycle-cutoff region can be identified with the most intense pulses. One could therefore attribute the above discussed bimodal-phase behaviour to the three most intense pulses in the 60 to 80 eV energy region. All other contributions to the Fourier analysis (e.g. a splitting of the full-cycle peak, a complicated structure across a further Fourier peak at ~ 4 fs...) can then be attributed an interference with the remaining pulses in this energy region. In order to prove this assumption, we can make use of the separately calculated quantum paths and eliminate all but the three most intense pulses before calculating the spectrum which is shown in Fig. 5.11.

The Fourier analysis in Fig. 5.11b confirms the above assumption. Indeed the outermost three attosecond pulses with only pulse 3 being in its half-cycle cutoff region seem to be responsible for the bimodal phase behaviour as observed in the experiment and as modeled with an asymmetric triple slit. While the lower temporal region of the half-cycle Fourier peak at τ_{12} now shows nearly no change in the Fourier phase as a function of the

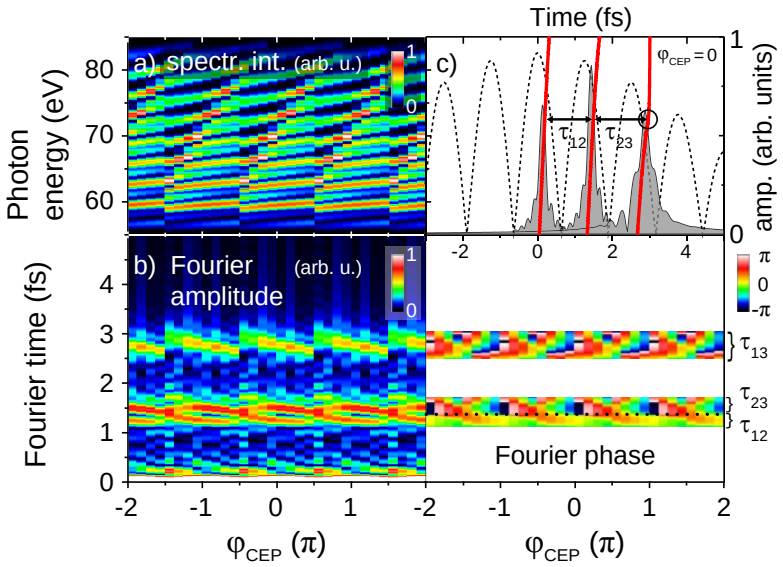

Figure 5.11: Same parameters as in Fig. 5.10, including the spectral filter from 60 to 80 eV. a) spectral intensity, b) Fourier analysis of a), c) attosecond pulses in time-domain representation. See Fig. 5.8 for further explanations. In this spectral region, only the three most intense attosecond pulses are selected and used (to mimic additional temporal filtering e.g. by phase matching) for the Fourier analysis in b). The different temporal contributions are marked both in the Fourier analysis in b) and they are denoted by the arrows in c). The dotted line in b) marks the separation across the half-cycle Fourier peak. See text for further discussion.

CEP, both the upper part of the half-cycle peak at τ_{23} as well as the full-cycle Fourier peak at τ_{13} change with slope 2 as a function of φ_{CEP}.

The explanation why the half-cycle-cutoff region of pulse 3 seems to imprint this CEP-dependent phase with respect to the remaining two pulses, being more in their half-cycle-plateau region is as follows: From Eq. (2.39) in section 2.2.2 it is known that the phase accumulated by the electron during propagation in the continuum is proportional to the quasi-classical action accumulated along its path times the time τ_s spent in the continuum [24, 159]. Therefore, due to the shorter excursion times of the electron for the half-cycle plateau regions, an intensity change of the laser field during its path in the continuum has a smaller effect on the phase. In contrast, a changing laser intensity is more affecting the phase for the half-cycle cutoff regions with longer excursion times. These considerations yield a roughly intensity-independent phase for the plateau region, while the intensity-dependence is roughly linear for the cutoff region [25]. We now can attribute these effects to every single generated attosecond pulse, thus identifying half-cycle-plateaus and half-cycle-cutoff regions as thoroughly done above. The connection between the intensity and the CEP can be argued as follows: The CEP shifts the half-cycles up and down the envelope of the driver pulse, thus also the instantaneous laser intensity acting during the continuum propagation of the electrons is changed as a function of the CEP which in consequence, by the intensity-dependence or independence of dipole phases for the different trajectories, explains the observed effects.

In order to demonstrate that the retrieved relative phase from the Fourier analysis in Fig. 5.11 is caused by the above-mentioned three-pulse behaviour, each pulse pair is con-

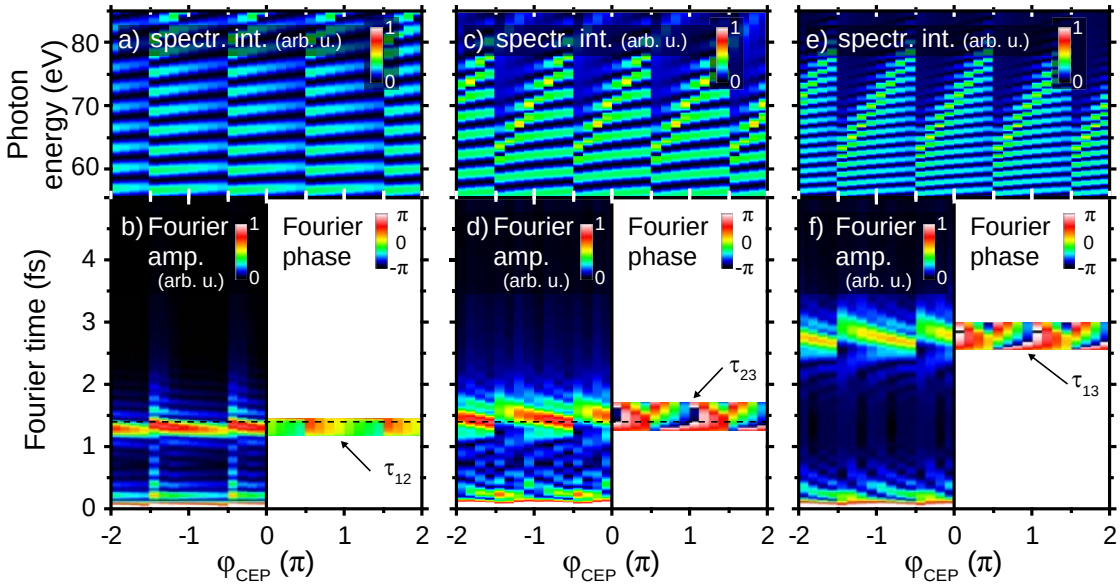

Figure 5.12: Selection of the different pulse pairs from the three-pulse scenario in Fig. 5.11 with the two half-cycle-plateau pulses 1&2 and the half-cycle-cutoff pulse 3. Both the spectral intensity (a) and the Fourier analysis (b) is shown for pulse pair 1&2 corresponding to τ_{12}. The contributions of pulse pair 2&3 (τ_{23}) and pulse pair 1&3 (τ_{13}) is shown in c,d) and e,f), respectively. The above considered configuration is clearly identified with nearly constant CEP-dependence of the Fourier phase at τ_{12}, and a linear CEP-dependence of the Fourier phase with slope 2 at τ_{23} and τ_{13}. The phase slope is also reflected in the shift of the harmonic interference patterns in a,c and e.

sidered separately which is shown in Fig. 5.12. The disentangled contributions clearly show the behavior as it was discussed above. The pulse pair 1&2, which corresponds to both pulses in the half-cycle-plateau region shows a nearly constant CEP dependence. This is reflected in almost horizontal harmonic interference fringes when only the two half-cycle-plateau pulses are selected as seen in a). It is confirmed in the Fourier analysis as the relative phase is only slightly modulated and is not shifting into subsequent cycles which is seen in b). In contrast, the other configurations in c) - f) always involve the half-cycle-cutoff pulse 3. As a consequence a clear CEP dependence is observed. The harmonic fringes shift into the next order as a function of the CEP as well as the relative phase is fully modulated by 2π per π phase change in the CEP.

The CEPSI analysis also reveals that the temporal modulation in the Fourier amplitude is directly connected to the modulation of the relative phase (or Fourier phase). This emphasizes the sensitivity to the non-adiabatic sub-cycle dynamics of the process: As pulse 3, the half-cycle-cutoff-dominated pulse, moves up the envelope of the driver pulse as a function of increasing CEP, the half-cycle-cutoff energies naturally increase in photon energy. This in turn means that within the analyzed range of photon energies, which of course always remains fixed, pulse 3 is beginning to cross over into its own half-cycle-plateau region which naturally needs to be a smooth transition. It is this cross-over which finally leads to a decreasing pulse spacing with increasing CEP. This is also visible in the entangled spectra (all pulses are present) as the contribution of the Fourier amplitude modulates in time as a function of the CEP, both in the calculations (see e.g. the full-

cycle Fourier peak in Fig 5.11b) as well as in the experiment (seen as a modulation of the full-cycle peak in Fig. 5.7b). The experimentally observed feature of splitting harmonic interference structure which rapidly sweeps through the spectral range is thus very closely connected to the observation of isolated half-cycle cutoffs [170].

With this understanding of the sub-cycle dynamics, the Fourier phase behaviour in Fig. 5.9b for the highest energy region between 80 and 100 eV can finally be explained. The slope 2 of the relative phase for both half-cycle contributions is caused by the half-cycle cutoff region of both outermost pulses: While the latest attosecond pulse experiences an increasing intensity as a function of the CEP as it is situated on the trailing edge of the laser pulse, the earliest attosecond pulse feels a decreasing intensity for an equal CEP change as it situated on the leading edge of the pulse. The center pulse instead has the highest half-cycle-cutoff region, thus it is contributing more with its half-cycle plateau region when interfering with the two adjacent pulses. The relative phase between the outermost pulses shows the sum of both half-cycle contributions to the phase, i.e. the phase-contribution of the full-cycle Fourier peak is modulated with slope 4. This observation can be identified as an intrinsic feature of the highest energetic region when mainly three attosecond pulses are interfering in the observed spectral region.

In the experimentally obtained spectra (Fig. 5.7) this feature is absent. The retrieved phase behaviour better fits to the case of attosecond pulses which are generated exclusively on the trailing edge of the laser pulse as illustrated in Fig. 5.11. The reason for this must be attributed to the exact pulse shape of the driving laser, which most likely is not perfectly Gaussian as assumed in the calculations. In addition, macroscopic phase-matching effects were not accounted for in the calculations, which might be responsible for the selective enhancement or suppression of different quantum paths on a sub-cycle basis [169].

Leaving this discrepancy open, it especially illustrates the power of the CEPSI analysis. It allows to carefully distinguish between different cases when comparing experimentally obtained spectra with theoretical calculations. While a direct comparison of the CEP-resolved spectral patterns for instance across Figs. 5.8 to 5.11 shows only little change, a presentation in the Fourier domain leads to the identification of characteristic changes which can be attributed to their respective origin as presented above. This is enabled as two similar domains (Fourier time vs. “CEP-time”) are jointly presented in a fully two-dimensional way.

5.5 Experimental reconstruction of relative phases

In the previous sections, the CEPSI analysis was introduced and applied, resulting in a deeper qualitative understanding of the sub-cycle-emission dynamics of the here discussed example of few attosecond pulses. Based on this understanding, we can now go one step further and retrieve quantitative temporal information from the experiment. In addition the final step of spectral interferometry will be performed and the relative phase of two attosecond pulses for different CEPs can be experimentally retrieved.

The full-cycle Fourier peak corresponding to $\tau_{13} = \tau_{12} + \tau_{23}$ in Fig. 5.7b is fitted with a Gaussian function to determine its central position at each value of the CEP. The result is

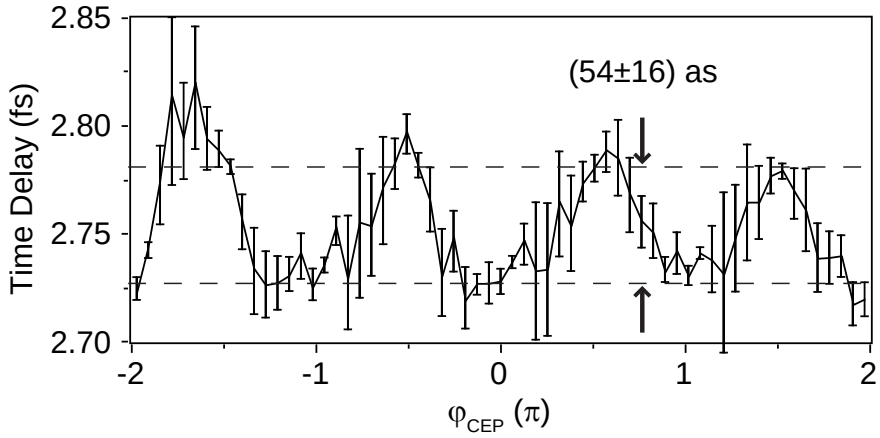

Figure 5.13: Experimentally retrieved mean time delay $\tau_{13} = \tau_{12} + \tau_{23}$ of the two outermost pulses in the attosecond-pulse triplet as a function of φ_{CEP}, extracted from the experimental results in Fig. 5.7b. The error bars denote the standard deviation of the Gaussian fits to the π-periodic data sets. A fit to the systematic variation in time delay results in (54 ± 16) attoseconds (horizontal dashed lines) as the third pulse moves into and out of its half-cycle-cutoff region in the spectral range considered here (70-90 eV).

shown in Fig. 5.13, where a periodic modulation in time delay of (54 ± 16) attoseconds can be observed. The minima appear at CEP values where all three pulses are approximately equal in phase, whereas the maxima correspond to CEP values where phase-jumps occur across the half-cycle Fourier peak (compare to Fig. 5.7b). An explanation for this modulation is as follows: For minimal group delays, the corresponding CEP values belong to situations where all three pulses contribute with their half-cycle-plateau regions. In contrast, when the group delay is at its maximum, the corresponding attosecond pulse configurations consist of only two pulses (1&2) within their plateau region, while the third pulse on the trailing edge contributes with its own cutoff region as discussed along Fig. 5.12 in the previous section. This results in a larger spacing τ_{13} between pulses 1 and 3.

A Gaussian fit to the full-cycle Fourier peak only results in an averaged group delay over the analyzed spectral region because the phase information is not used in such a fit. Using instead the full spectral-interferometry toolkit, the full-cycle Fourier peak can be temporally filtered both in amplitude and phase and back-transformed into the spectral domain (cf. section 2.3). This is done in Fig. 5.14 where two different characteristic CEP values were considered. The parameters for the filter function are denoted in the caption. Now the energy-dependent group delay between the corresponding attosecond pulses is fully revealed.

The determined group delay was averaged over similar CEP values corresponding to $\varphi_{\mathrm{CEP}} = n \cdot \pi$ (left panel), where the splitting of the half-cycle Fourier peak is absent, and to $\varphi_{\mathrm{CEP}} = (n + 1/2) \cdot \pi$ (right panel), where the splitting of the half-cycle Fourier peak is observed. Averaging over several spectra (12 each) yielded an error estimation by means of the standard deviation. A clear difference between the two CEP values can be observed. The $\varphi_{\mathrm{CEP}} \sim \pi$ case (left panel) shows one maximum in the amplitude and a flat but slightly decreasing group delay. A linear fit to this decrease yields $\Delta m = -(2.62 \pm 0.05)$ as/eV

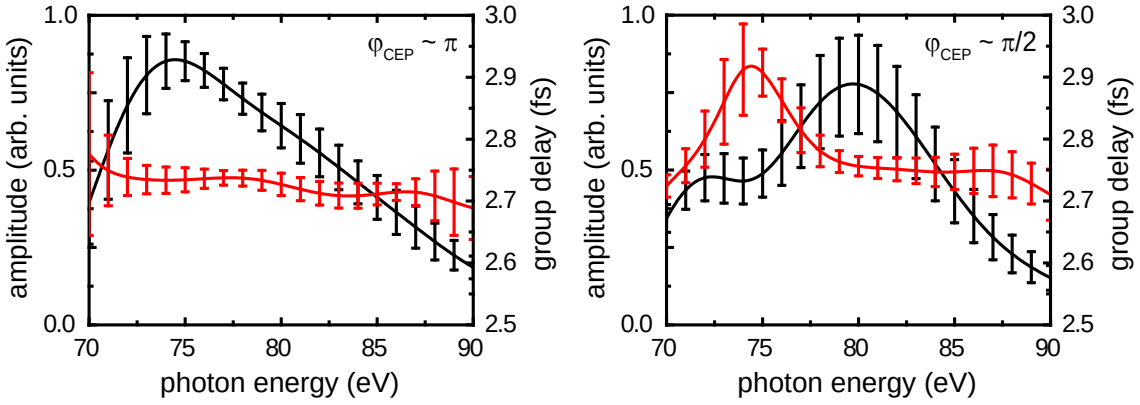

Figure 5.14: Reconstructed group delay for two different φ_{CEP} of the full-cycle Fourier peak at τ_{13}, extracted from the experimental spectra in Fig. 5.7. The temporal filter $C(t)$ (cf. Eq. (2.43) in section 2.3) was set to $t_{\mathrm{min}} = 2.41$ fs, $t_{\mathrm{max}} = 3.10$ fs and $\Delta T = 0.34$ fs. Each curve was retrieved from 12 different experimental spectra, where the error bars denote the standard deviation. The black curves show the spectral-amplitude product of the interfering pulses 1&3. The red curves show the derivative of their relative phase, i.e. the group delay between the two pulses (cf. Eq. (2.14) in section 2.1). See text for further discussion.

where the error denotes the standard error of the fit. Taking the error bars of Fig. 5.14 into account the error would of course be higher, being on the same order as the fitted value for the decreasing slope Δm. Therefore the value should only be considered a first estimate. An explanation of the decrease in group delay could be as follows: With all three pulses contributing with their half-cycle-plateau region, a decrease in group delay means that pulse 1 is closer to its half-cycle-cutoff region than pulse 3. This implicates that pulse 1 should be situated on the leading edge of the driver pulse, while pulse 3 is on the trailing edge. This however seems to be in contradiction to the qualitative observation of the Fourier phase as discussed in the previous section. A clear answer to this question can not be found at the moment and has to be left for further investigations (e.g. to check if it is possible whether certain phase-matching conditions can inhibit the formation of a half-cycle-cutoff on the leading edge of the pulse, while its lower-energy half-cycle-plateau region still remains [169]).

The $\varphi_{\mathrm{CEP}} \sim \pi/2$ case (right panel) shows a different behaviour with a peak in the group delay at ~ 74 eV photon energy, while also the amplitude shows a two-peaked behaviour. In this case, the half-cycle-cutoff region of pulse 3 is within the analyzed energy range. The peak in the group delay can be roughly connected to the location of the half-cycle-cutoff region of pulse 3. This explains the rapid increase in group delay (by ~ 150 as) below ~ 74 eV. For higher photon energies, the group delay is again decreasing. This can only be explained if another pulse prior to pulse 1 now more dominantly takes over the role of pulse 3, as above its half-cycle-cutoff region, pulse 3 is decreasing in amplitude. Indeed in the Fourier analysis of Fig. 5.7, a small indication of a 3$^{\mathrm{rd}}$ Fourier peak is present (not clearly visible on shown scale), which periodically appears for $\varphi_{\mathrm{CEP}} \sim \pi/2$. This additional attosecond pulse is then also located on the leading edge of the laser pulse as the group delay in the right panel of Fig. 5.14 is systematically decreasing. A more detailed analysis should however also include the 3$^{\mathrm{rd}}$ Fourier peak which is left for

further investigations.

5.6 Conclusion on CEP-resolved spectral interferometry

In conclusion, the combination of CEP sweeping and spectral interferometry methods (CEPSI) was introduced. The interpretation of the data was mainly performed in Fourier space, plotting the Fourier time vs. the CEP in a fully two-dimensional way both in amplitude and phase. This combined plot yields an intuitive access to the temporally localized sub-cycle dynamics of the analyzed strong-field process, resulting in a better qualitative understanding. The method is related to conventional two-dimensional spectroscopy methods, where typically two energy domains (also retrieved via Fourier techniques) are jointly shown with the full complex information (real and imaginary part) which reveals *energy*-level couplings and excitation pathways. In analogy, for the case discussed here, the complex plot of two related temporal domains (Fourier-time-delay and "CEP time") gives direct access to the underlying *temporal* dynamics.

Along the application on few (mainly three) interfering attosecond pulses it was applied to experimentally measured data. It was shown in detail how the CEPSI method is able to gain access to the sub-cycle emission dynamics of the attosecond pulses. With the asymmetric temporal triple slit an intuitive model was found to qualitatively explain the experimental data. This model showed how CEPSI is applied in a fully two-dimensional way in order to directly access the relative phase. Connecting the model to other few-cycle strong-field processes, access to the phase in similar ways is typically feasible as the CEP directly enters the relative phase of subsequent temporal events.

A thorough analysis of the calculated quantum paths with the non-adiabatic saddle point approximation allowed to connect the observed effects to known sub-cycle dynamics, identifying interfering half-cycle-plateau and half-cycle-cutoff regions of subsequent attosecond pulses as being responsible for the observed effects. In particular it could be demonstrated how the CEPSI analysis applied on these calculated spectra allowed to disentangle these different contributions. By means of the CEP-resolved Fourier analysis similar spectral modulation patterns can be distinguished, making the method very powerful in order to discriminate between different theoretical models and/or different experimental configurations. In both cases, the influence of different experimental or numerical parameters can be carefully categorized. As such, the effect of different phase-matching parameters on the sub-cycle emission dynamics could be further investigated. Especially in such cases the method may be preferred against conventional characterization techniques on attosecond pulses, as the time for data acquisition can be very fast with the involved all-optical detection. This allows a faster access to a vast range of other (phase-matching) parameters, ensuring the laser stays consistently stable during the required acquisition time while varying the parameters.

It was also shown how a full application of spectral interferometry finally yielded quantitative information on the group delay between interfering (in our case full-cycle spaced) attosecond pulses. The temporal information could be quantified with precision of few tens of attoseconds. A systematic deviation might still remain which however can be

resolved either by a direct comparison with theoretical models or by a simultaneous measurement of the pulses with conventional photoelectron characterization techniques.

The ability of disentangling overlapping contributions on a sub-cycle basis can finally be applied to all kinds of CEP-dependent strong-field processes as mentioned in the introductory part of this chapter. To point out a few examples, ATI electron emission from atoms, molecules and solids or few-cycle harmonic generation from plasma all generate CEP dependent spectra [130,148–150] which exhibit spectral interference structures from few emission events. A careful analysis along the here proposed scheme can thus create a deeper insight into the sub-cycle (attosecond) dynamics at work in these processes.

Finally, the concept of CEP-resolved Fourier analysis and spectral interferometry can also be transferred to transient-absorption measurements, creating a transient-dispersion-spectroscopy scheme [172]. Upon transmission of such interfering attosecond pulses through macroscopic media, not only the absorption but also (due to the interferometric access to both real and imaginary part) the dispersion properties of the medium can be accessed. With the combined nonlinear action of another ultrashort event (such as a time-delayed moderately intense few-cycle laser pulse) these properties can be mapped with high temporal resolution. Considerations on the group delay as presented at the end of this chapter would then be the starting point of the analysis. In such experimental schemes the above mentioned systematic errors are expected to play only a minor role. This is because the underlying dynamics of interest are encoded in the *relative* change of the group delay as a function of another dynamical parameter (e.g. the time delay of another few-cycle pulse), which cancels such systematic deviations. This indicates that within such techniques a temporal resolution of few attoseconds can be achieved. The duration of the interfering attosecond pules would then not limit the temporal resolution, which is only determined by the CEP stability. From the standard deviation error bars in the preceding section it was experimentally confirmed that ~ 200 mrad CEP stabilities already lead to a temporal resolution on the order of few tens of attoseconds.

In the following final chapter of this work, a transient-absorption measurement on atomic helium with attosecond temporal resolution will be presented. It does not yet employ the here proposed analysis of interfering attosecond pulses. However by using the natural interference of different quantum channels at work in the process of autoionization, access to the coupling dynamics of the metastable autoionizing states can be gained.

Chapter 6

Quantum interferometry and correlated wave-packet observation in helium

In the preceding two chapters the concept of interferometry was considered in time-resolved measurements, both with regard to the interference of free electron wave packets (chapter 4) as well as for the interference of strong-field-induced quantum state populations (chapter 5). In the following, the concept of interferometry is identified and instrumentalized in a very natural way within the process of autoionization, considering only one single quantum state naturally interfering with a continuum of states. The concept could thus be termed quantum-state interferometry. In particular, the considered autoionizing states are correlated two-electron states in helium (see sections 2.7 and 2.9) which means that this natural and fundamental process is described by the intrinsic interference of a correlated two-particle quantum state.

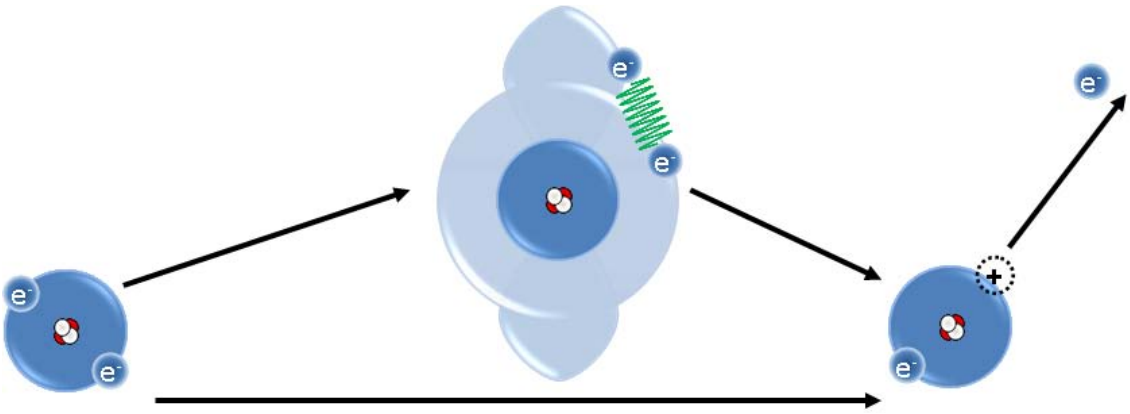

Figure 6.1: Illustrating the interferometric nature of the process of autoionization in helium. Upon interaction with a single photon, the helium ground state (initial state, left) is ionized into a singly-charged helium ion with an electron in the continuum leaving the ion (final state, right). The final state can be reached via two quantum-mechanically interfering pathways: along the direct path (lower) and via an intermediate doubly-excited state (upper path).

The interferometric aspect of autoionization is illustrated in Fig. 6.1 for the case of helium as it will be studied here experimentally, the most simple natural two-electron system.

The final state is a helium ion with one electron in the ground state ($N = 1$) and the other electron leaving the ion with non-zero kinetic energy (see section 2.9). The final state can be reached via two quantum-mechanically interfering pathways. The direct ionization is an effective single-electron process, where only one of the two electrons is ionized while the other electron remains untouched. In contrast, the other pathway involves the fully correlated two-electron state (excitation of both electrons into a doubly excited state), which has a finite life time and eventually "decays" into the same final state (see also sections 2.7 and 2.9).

The crucial idea behind this time-domain interpretation is the possibility to initiate the process with a short pulse, where the duration of the pulse has to be a fraction of the life time of the doubly excited state. Based on the considerations given in section 2.8, the time evolution of the whole process is encoded in the absorption line shape and imprinted onto the spectral profile of this excitation pulse. In the case of autoionization, the asymmetric line shape (see section 2.7) encodes both interferometric pathways, thus also the relative phase is encoded. The excitation with broad-band attosecond pulses and subsequent energy-resolved detection of the absorption line-shape thus serves as a natural pump–probe scenario in analogy to the two-pulse scheme discussed in chapter 4, giving access to the phase of transiently bound two-electron states.

This interferometric pump–probe scheme is possible solely by using the broad-band excitation of attosecond pulses (see section 3.3) together with their detection in high resolution (see section 3.5). The not yet used interferometrically-linked few-cycle femtosecond pulse (see section 3.4) can then be used *in addition* to couple the transiently bound states and influence their temporal evolution. From a technical point of view, the implementation and demonstration of this measurement scheme can be considered one of the main results of this work. Its feasibility will be demonstrated and discussed in more detail in the remainder of this chapter, leading to the most important physical results, the phase-resolved coupling of different correlated two-electron states.

The motivation behind the time-resolved study of such two-electron states can be drawn from chemical reactions. The covalent bond [173] which is formed in between neutral atoms involves two interacting electrons. The formation or breaking of such bonds, or in general also the nuclear rearrangement in more complex molecules is fundamentally connected to (or initiated by) the correlated motion of at least two electrons. Having a profound understanding of such motion from fundamental principles could then finally serve as an input for the more complex study of ultrafast electronic rearrangement in intermediate transition states [174] and the investigation of electron correlation in molecules [175].

Such ultrafast effects in molecules which happen on or are influenced by the electronic time-scale are deeply connected with the Born-Oppenheimer approximation [176] or better said its breakdown, when nuclear and electronic motion cannot be decoupled. Such effects become apparent for example through conical intersections [177], where different electronic potential-energy surfaces cross or intersect. A recent experiment [178] also showed, how non-Born-Oppenheimer dynamics are at play in highly-excited molecular ions.

In the following section a short overview of closely related earlier experiments and theoretical treatments is given. They are outlined in order to establish a basic background

knowledge prior to the presentation of own results.

6.1 Related experimental and theoretical work

The earliest related experiment is [179] which was done in transient absorption geometry. There, electromagnetically induced transparency (EIT, see e.g. [180] for a review) was investigated across the 2s2p autoionizing resonance due to laser-coupling to another doubly-excited state. This additional state is termed $2p^2$ ($^1S^e$) and found at 62.06 eV [181, 182] (see also Fig. 6.11 in section 6.4.1, as it will also play an important role for the explanation of the own results). In that work [179], the formation of an Autler-Townes doublet was described, which was explained using the theory of autoionizing states in strong fields as presented in section 2.7.2. Notably the experimental data could only be explained if single-electron tunnel ionization (see section 2.2) of the doubly excited states into the $N = 2$ continuum (see Fig. 2.11 in section 2.9) was taken into account. Very recently, a direct solution of the time-dependent Schrödinger equation [183] yielded a confirmation of the experimental observation of EIT and the formation of an Autler-Townes doublet between the 2s2p and the $2p^2$ doubly excited states.

Recently, an experiment on the same doubly-excited states in helium was performed with attosecond streaking [184], where the autoionization decay life time of the 2s2p state was directly measured in the time domain and confirmed to 17 fs as it can be deduced from line width measurements [52]. The experiment roots on earlier developed theory on laser-assisted autoionization [185], describing these doubly-excited states in the presence of strong laser fields, within the strong field approximation (SFA, see section 2.2). Such a scheme was also described in [186, 187], investigating the theoretical aspects of time-resolved autoionization. A model was also presented [188] which involved the solution of the time-dependent Schrödinger equation in hyperspherical coordinates (see section 2.9) of doubly-excited states in strong laser fields. All these time-resolved descriptions of ionization dynamics in strong fields were motivated by the first time-resolved measurement with attosecond pulses, the direct life-time measurement of an Auger electron emitted from a krypton atom [189] which was explained within the streaking model [190]. A direct description of the formation and time-evolution of an autoionizing state excited with a short attosecond pulse was also developed in [191, 192]. All these theoretical descriptions however are focusing on the calculation of photoelectron spectra. More recently, the detailed experimental results of [184] were also discussed in [193], where in addition the strong coupling of autoionizing states similar to the experiment in [179] was taken into account.

For all-optical gas-phase experiments in transient absorption geometry, the first demonstration of XUV transient absorption with femtosecond time-resolution was presented in [194], where quantum-state resolved access to core-hole spin-orbit dynamics was measured in strong-field ionized xenon atoms. This was subsequently done with attosecond resolution [195] in strong-field ionized krypton atoms. There, the induced spin-orbit wave packet was explained in detail with a density-matrix approach [196]. As a result, the degree of coherence of this wave packet could be traced in time with a period of 6.3 fs.

For autoionizing states, attosecond transient absorption was also applied in argon [197] where control over the autoionization dynamics was demonstrated with state life times between 10 to 20 fs. Very recently, this experiment and the above discussed transient-absorption experiment on doubly-excited states in helium [179] was jointly described in theory [198] where the time-resolved formation and coupling of different autoionizing states was taken into account.

For singly-excited states in helium, a transient absorption experiment employing an attosecond pulse train [199] was performed, where a sub-fs modulation was observed on different harmonics. This indicated a coupling between different singly-excited states, i.e. a bound electron wave-packet evolving on an attosecond time scale. On the theoretical site, transient absorption was considered across these singly-excited states in helium [200] in the presence of a laser field. It was pointed out, how the dispersion characteristics of the transmitted XUV light can be transiently shaped.

A wave packet across doubly-excited states in helium was recently also described theoretically [201], especially between the two lowest-lying 2s2p and $sp_{2,3+}$ states. Within this analysis, the breathing of this excited wave packet was analyzed in detail and it was found, that the leaving electron (after autoionization) is periodically released in correlation with the breathing, in particular when the breathing wave packet is mostly contracted. These findings are in analogy to [61] with autoionization as a result of an electron-electron collision (see section 2.9), but now described deeply in the quantum regime. A coherent coupling, i.e. the observation of a wave packet formed by the coherent superposition of the same two described states is observed in own measurements as described in section 6.7.

In the following, own measurements will be presented on doubly-excited states in helium ranging between the 2s2p up to the $sp_{2,7+}$ states which were measured in transient absorption geometry. However the measurement can be more intuitively understood as a transient coupling scheme as it will be introduced in the following section and as it was already motivated along the concept of quantum interferometry at the beginning of this chapter.

6.2 Fano interferometry with autoionizing states

As it was introduced in the beginning of this chapter, attosecond (XUV) excitation and subsequent detection with a high-resolution spectrometer is exploited as an interferometric pump–probe scenario. In addition, a time-delayed moderately intense (on the order of 10^{12} W/cm^2 or lower) few-cycle laser pulse (duration ~ 7 fs) (NIR) is used to influence and couple the transiently excited states *after* their excitation by the attosecond pulses. The experimental setup can thus be rather understood as a transient-coupling scheme in contrast to the conventional transient-absorption interpretation, even though the basic pulse arrangement and detection is equal. The traditional scenario of transient absorption spectroscopy is more applicable in cases such as [195] (see previous section) when the intense NIR laser pulse initiates some dynamics, which are subsequently probed by the absorption of the transmitted XUV pulse. It is a configuration where the spectral part which carries the absorption information (the XUV) is interacting with the target at later

times.

The transient-coupling scheme instead is interpreted vice versa, where the XUV pulse initiates temporal dynamics first, while the induced coherent dipole emission (see section 2.8) is imprinted on the collected absorption signal. The dipole emission is present until all induced dynamics have naturally decayed (natural life-time limited). If the system is weakly or strongly perturbed during this decay (e.g. by the time-delayed NIR pulse) this influence is then also imprinted on the measured absorption signal. This is the case even though the absorbed pulse was coming first, being counterintuitive at first glance when not thinking of the coherent dipole emission. This "peculiarity" must of course also happen in the conventional transient-absorption arrangement. Otherwise no sharp features (spectral lines) could be detected in the absorption signal if it was only generated during the short interaction of the attosecond pulse with the system (which is due to the time-bandwidth uncertainty, see section 2.1).

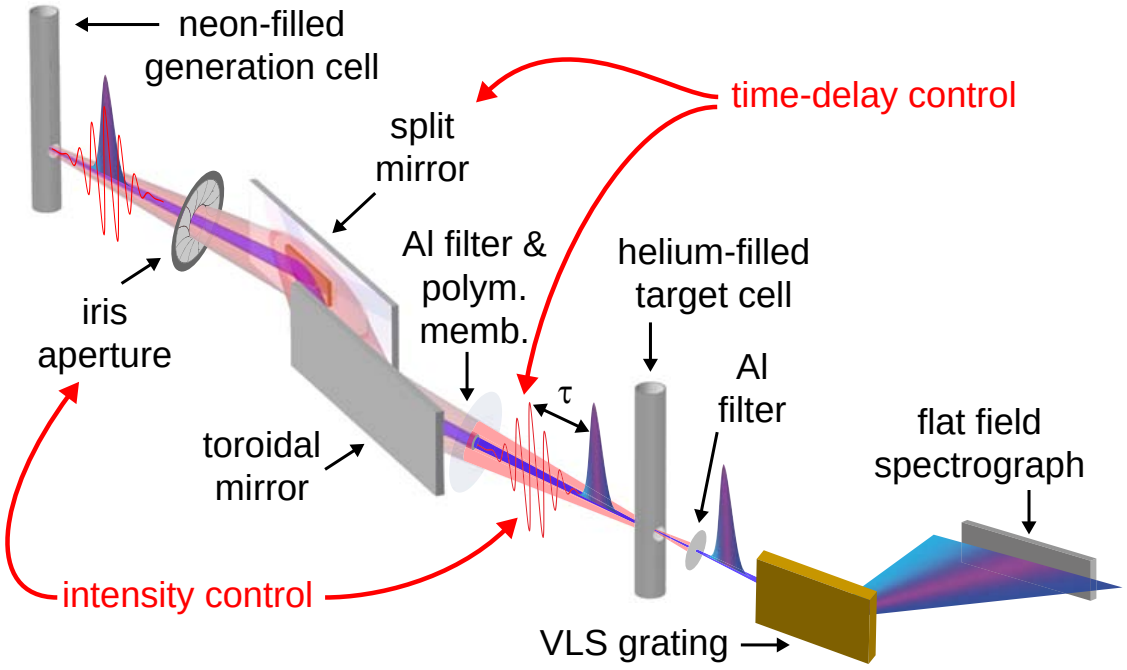

Figure 6.2: Illustration of the transient-coupling scheme as it is experimentally implemented. The different parts are also described in chapter 3 in conjunction with Fig. 3.3. The intensity- and time-delay-controlled NIR pulses are interacting with the transiently-excited helium target. The induced dynamics are imprinted on the transmitted XUV signal by means of the coherent dipole response of the helium atoms.

A schematic picture of the setup which employs the transient-coupling scheme is illustrated in Fig. 6.2, where the previously described (see Fig. 3.3 in chapter 3) home-built vacuum system is used. Both the time-delay and the laser intensity of the NIR pulse can be changed, collecting the interferometric absorption line shape two-dimensionally as a function of dynamical parameters. The polarization of both NIR and XUV spectral parts is linear and pointing into the same direction. XUV spectra are obtained via integration over the full spatial beam profile in the far field.

Fig. 6.3 shows measured absorption spectra with maximally closed iris aperture (no NIR)

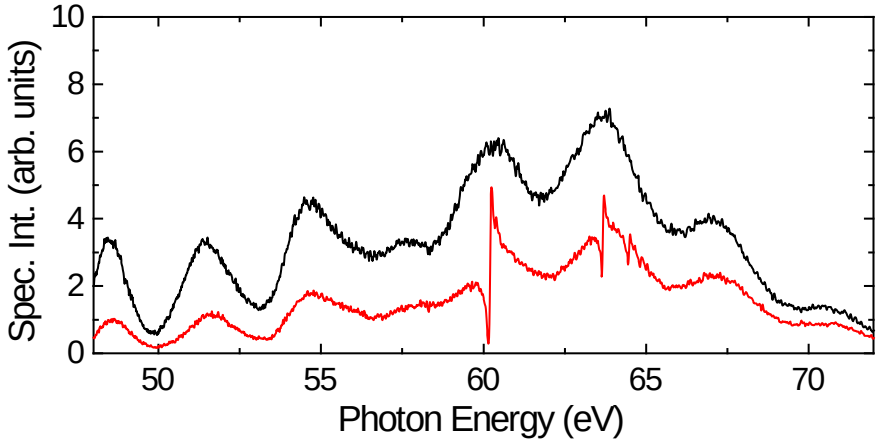

Figure 6.3: Raw XUV-only spectra as measured with our home-built high-resolution flat-field spectrometer. Black line: no helium in target cell. Red line: $\sim$100 mbar helium in target cell. Each spectrum was averaged over $\sim$3200 single laser shots. The statistical noise is visible and on the order of the line thickness. The intensity fluctuation of successively acquired such spectra is on the order of 10%. The odd-harmonic modulation ($\sim$3 eV) is imprinted on both continuous spectra.

in order to obtain XUV-only spectra. Asymmetric features of several absorption lines are clearly visible and correspond to the $sp_{2,n+}$ ($^1P^o$) series in helium (see sections 2.7 and 2.9). The energy calibration was performed via comparison with benchmark synchrotron data [51, 52]. The parameters of the 2s2p absorption line (see Table 2.2 in section 2.9) were used to obtain the spectrometer resolution (see section 3.5).

The parameters for attosecond pulse generation (see section 3.3) were optimized for continuous XUV spectra in the considered energy region (between 59 and 66 eV), with neon backing pressure $\sim$100 mbar and the cell position close to the NIR laser focus. The CEP was not stabilized but averaged over to reduce the fluctuations in the XUV spectra. Both CEP averaging and the excitation with more than one attosecond pulse (apparent from the residual harmonic modulation in Fig. 6.3) do not wash out the observed attosecond dynamics which is due to the intrinsic phase-lock of each attosecond pulse to the laser half-cycle (see section 2.2.2). This is also confirmed in the simulations which are shown in section 6.4. From a technical point of view this makes the interferometric pump–probe scheme also very robust and relatively easy to implement. Both a high temporal resolution of 10 as (see section 3.4) and high spectral resolution of 47 meV (see section 3.5) are available for the interferometric transient-coupling scheme as it is introduced here. This enables us to access the state-selective coupling dynamics with high temporal *and* spectral resolution.

In the following section the processing of the absorption profiles from the measured data is described in detail. The reconstruction involves a Fourier filtering technique to compensate for the 10% intensity fluctuations between successive spectrum acquisitions mostly due to laser beam pointing instabilities and the highly nonlinear harmonic generation process.

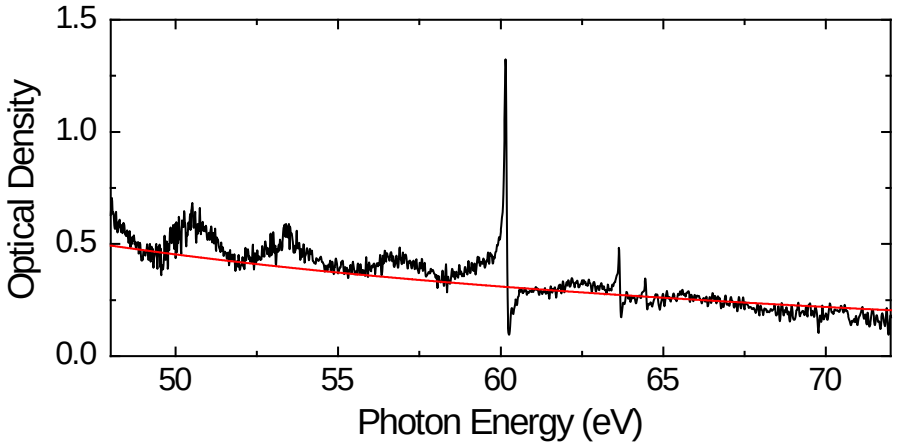

Figure 6.4: Calculated optical density (see Eq. (6.1)) from the measured spectra shown in Fig. 6.3 in section 6.2 (black line). The cross section $\sigma_{\mathrm{PCS}}(\omega)$ of the non-resonant background [202] is scaled with the fitted path-length-density product (red line).

6.3 Data analysis

The standard procedure of data analysis in transient-absorption spectroscopy is the calculation of the optical density (*OD*) from the signal (SIG, XUV-spectra *with* helium target gas) and the reference (REF, XUV-spectra *without* helium target gas) spectral intensity I_{SIG} and I_{REF}. According to Beer–Lambert's law (cf. Eq. (2.95) in section 2.8) it is given by

$$OD(\omega) = -\log_{10}\left[\frac{I_{\mathrm{SIG}}(\omega)}{I_{\mathrm{REF}}(\omega)}\right] = \frac{\rho \cdot l \cdot \sigma(\omega)}{\ln 10} \tag{6.1}$$

which is directly proportional to the photo-absorption cross section $\sigma(\omega)$ as given in Eq. (2.88) in section 2.7. The path-length-density product $\rho \cdot l$ is a measure for the optical thickness of the target gas. $OD = 2$ thus corresponds to 1% transmission. The global maximum of the OD, governed by the helium backing pressure, was experimentally fixed below this value to avoid significant dispersion effects in too dense materials ([196], see also section 2.8).

Eq. (6.1) is applied to the measured spectra in Fig. 6.3 in the previous section and the resulting OD is shown in Fig. 6.4. A residual harmonic modulation is apparent which is due to the intrinsic intensity fluctuations of the recorded spectra, as they cannot be measured simultaneously. This is also apparent from Fig. 6.5 where the OD is shown for different time delays, not affecting the absorption properties in the "no-NIR" configuration. The residual fluctuations on the order of 15% are due to the two independently measured $I_{\mathrm{SIG}}(\omega)$ and $I_{\mathrm{REF}}(\omega)$ spectra.

The asymmetric absorption line shapes and their changes as a function of time delay and NIR intensity are of exclusive interest in this analysis. Making use of them being sharp and imprinted onto a more slowly modulating harmonic background, reference spectra can be reconstructed *in situ* from each obtained $I_{\mathrm{SIG}}(\omega)$ spectrum. Using a low-pass Fourier filter, the harmonic modulation $I_{\mathrm{f}}(\omega)$ can be directly retrieved from each measured signal without the sharp asymmetric absorption features (see Fig. 6.6). This *in-situ* filtered

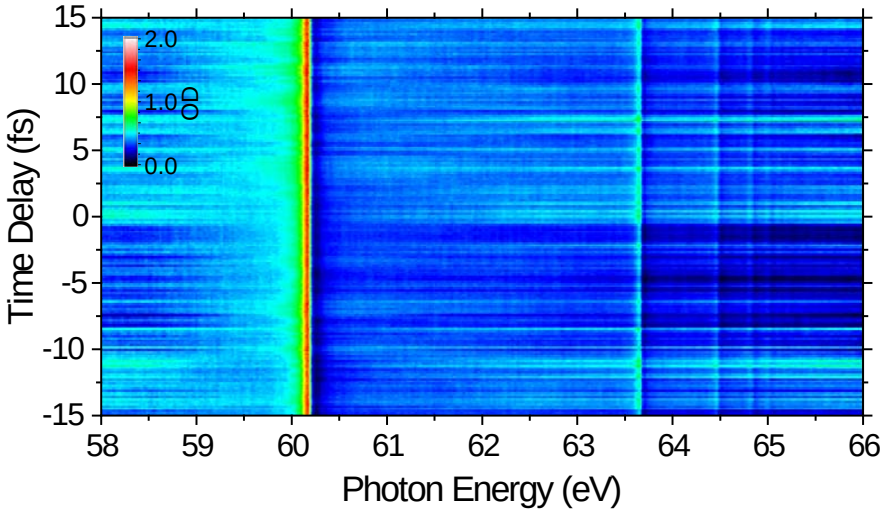

Figure 6.5: *OD* spectra as a function of time delay (showing no expected changes with delay as the iris aperture was maximally closed, so NIR light was absent). Each single spectrum is determined from measured reference spectra (see Fig. 6.3 in section 6.2). The irregularities are due intensity fluctuations of two independently recorded spectra (on the order of 15%).

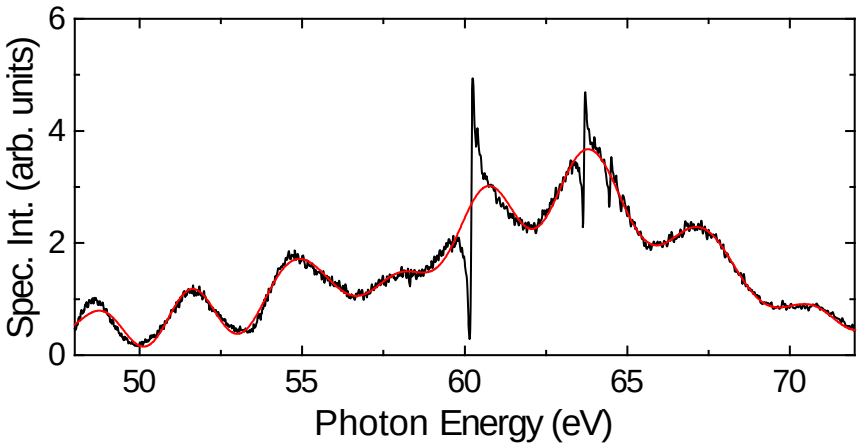

Figure 6.6: *In-situ* calculation of the harmonic modulation spectrum $I_{\mathrm{f}}(\omega)$ employing a low-pass Fourier filter (red line) from the measured absorption spectrum $I_{\mathrm{SIG}}(\omega)$ (black line).

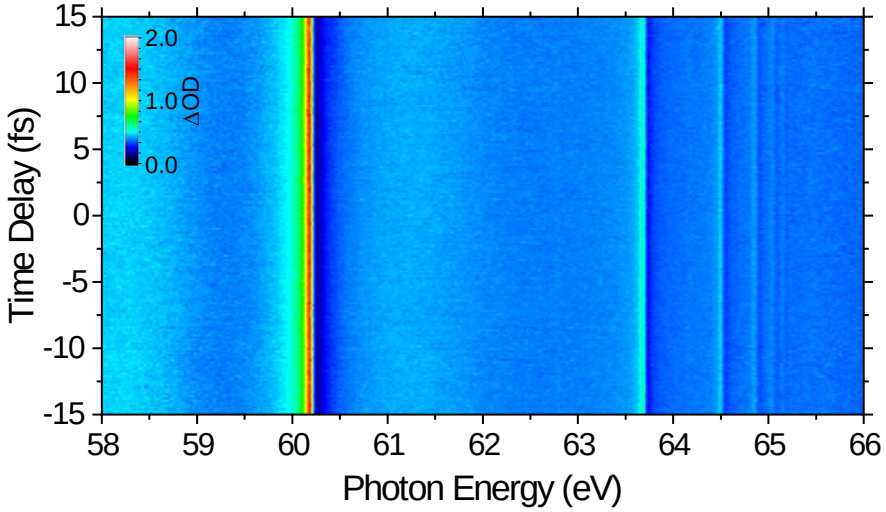

Figure 6.7: *OD* spectra as a function of time delay (showing no changes as the iris aperture was maximally closed). Each single spectrum is calculated with its *in-situ* reconstructed reference spectrum. As a result, only the much lower statistical noise is remaining.

spectrum $I_{\mathrm{f}}(\omega)$ is scaled to obtain a reconstructed reference spectrum

$$I_{\mathrm{REF,rc}}(\omega) = I_{\mathrm{f}}(\omega) \cdot \exp[\sigma_{\mathrm{PCS}}(\omega) \cdot \rho \cdot l] \tag{6.2}$$

with the known non-resonant photo-absorption cross-section $\sigma_{\mathrm{PCS}}(\omega)$ of helium [202]. The path-length-density product $\rho \cdot l$ was fitted to match the non-resonant *OD* as calculated with Eq. (6.1) (see Fig. 6.4) with

$$\rho \cdot l = (0.52 \pm 0.08) \cdot 10^{-18}\ \mathrm{cm}^{-2}. \tag{6.3}$$

The value was obtained from the different OD spectra shown in Fig. 6.5, therefore the error reflects the $\sim 15\%$ intensity fluctuations. As a result of this reference-reconstruction method, the noise of the two-dimensional OD plot is significantly reduced as can be seen in Fig. 6.7. These processed plots are then used throughout as they accurately reproduce the sharp absorption features which are of interest. As the plots are insensitive to the non-resonant background absorption, ΔOD is shown instead of the absolute OD.

With these processed spectra, an overview of the accessed absorption features is given in Fig. 6.8 which reveals $\mathrm{sp}_{2,n+}$ states up to $n = 8$ and $\mathrm{sp}_{2,n-}$ states up to $n = 5$. The state-resolved access to a wide range of strong but also weak contributions is demonstrated with this approach. The spectral resolution does not compete with state-of-the-art synchrotron sources [51,52]. However now, a fully time-resolved access (with 10 attoseconds resolution) to these states is guaranteed within the presented scheme, in contrast to time-independent synchrotron studies.

A comparison between Figs. 6.9 and 6.10 illustrates the here presented reconstruction method for an open iris aperture with non-zero NIR-pulse interaction. It is important to note that all significant features which are discussed and interpreted in the remainder of this chapter are present in both data sets. This confirms the Fourier-filtering technique

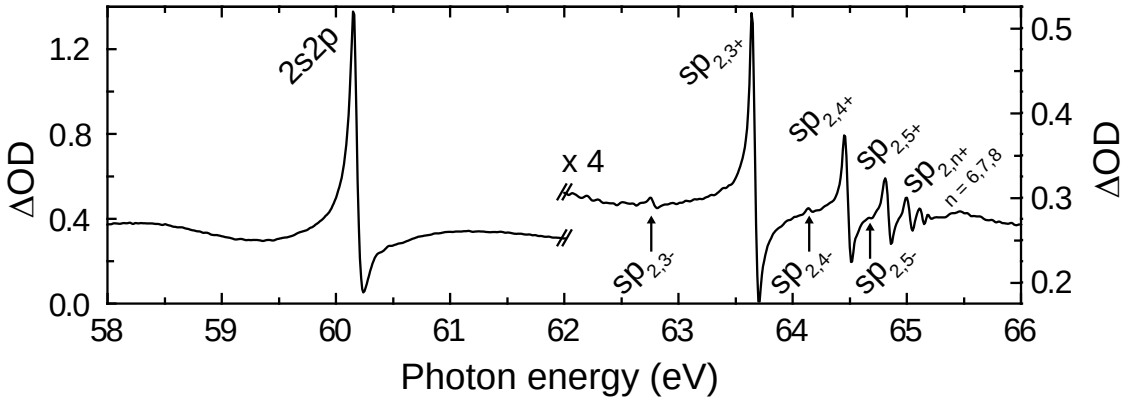

Figure 6.8: The average over all spectra as shown in Fig. 6.7. A magnified vertical scale is employed between 62 and 66 eV. Absorption lines corresponding to $sp_{2,n+}$ states up to $n = 8$ and $sp_{2,n-}$ states up to $n = 5$ are visible from the reconstructed ΔOD spectra.

in order to decrease the noise contributions to be valid. The low-pass filter works because all resonance line shapes exhibit finer spectral structures than the ~ 3 eV harmonic background.

6.4 The numerical framework for the coupling of autoionizing states

From Fig. 6.10 it is apparent that especially the two strongest absorption lines which correspond to the 2s2p and the $sp_{2,3+}$ states are strongly modulated as a function of time delay. The observed features are due to a coherent coupling between these two states which also evidences a two-electron wave packet. The details will be discussed in section 6.7. In order to understand the weak and strong coupling of these two states a numerical simulation was performed. As it was explained in section 6.1, especially from [179] it is evident that the $2p^2$ ($^1S^e$) state has to be considered as it is close to resonant to the 2s2p ($^1P^o$) state with NIR laser coupling present. The parameters of the three considered states which were used in the simulation are summarized in Tab. 6.1.

Table 6.1: Parameters of the 2s2p and $sp_{2,3+}$ ($^1P^o$) and $2p^2$ ($^1S^e$) states as they were considered for the simulation. The values are obtained from [52] for the $^1P^o$ states and from [181,182] for the $^1S^e$ state.

	E_r (eV)	Γ (meV)	q
2s2p	60.15	37	-2.75
$2p^2$	62.06	6	
$sp_{2,3+}$	63.66	10	-2.53

The basic theory for autoionizing states coupled to strong laser fields is introduced in section 2.7.2 with an overview over existing theoretical approaches. A direct application

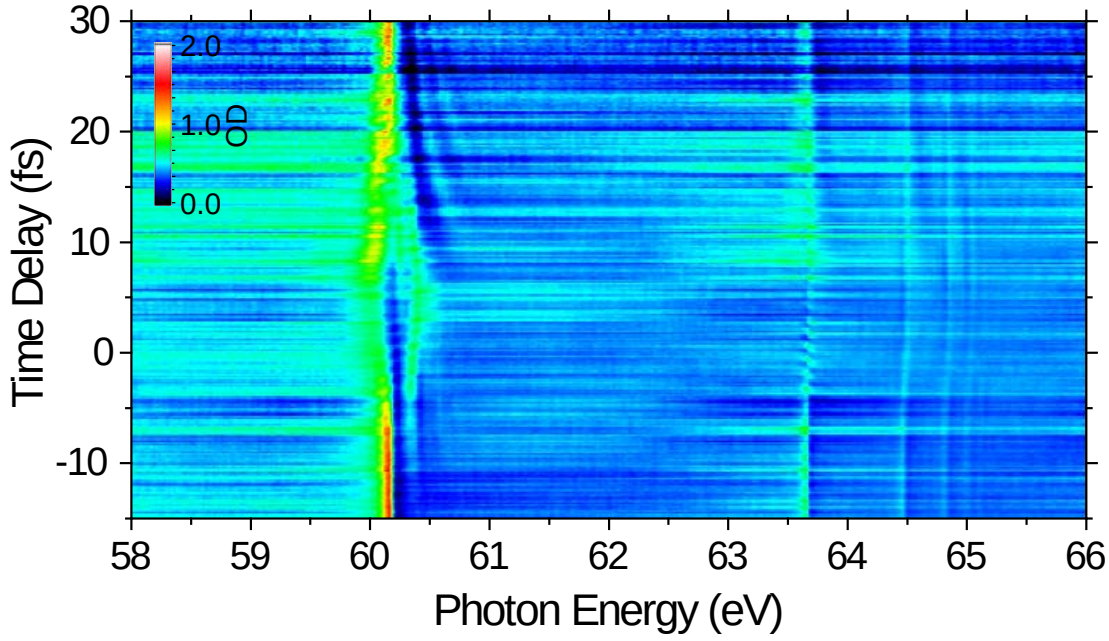

Figure 6.9: OD spectra as a function of time delay for open iris aperture (NIR pulse present). The NIR peak intensity is $3.3 \cdot 10^{12}$ W/cm^2 (see section 6.6). The spectra were obtained from independently measured $I_{\mathrm{SIG}}(\omega)$ and $I_{\mathrm{REF}}(\omega)$.

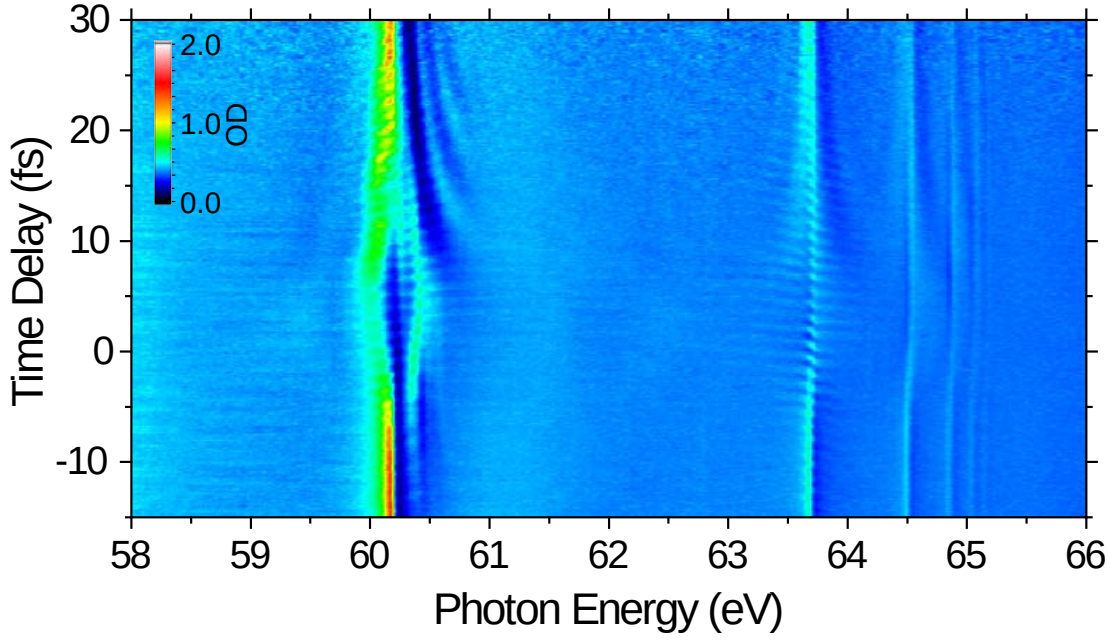

Figure 6.10: ΔOD spectra as a function of time delay for an opend iris aperture (NIR pulse present). The NIR peak intensity is $3.3 \cdot 10^{12}$ W/cm^2 (see section 6.6). The spectra were obtained from the measured $I_{\mathrm{SIG}}(\omega)$ and the *in-situ* reconstructed $I_{\mathrm{REF,rc}}(\omega)$.

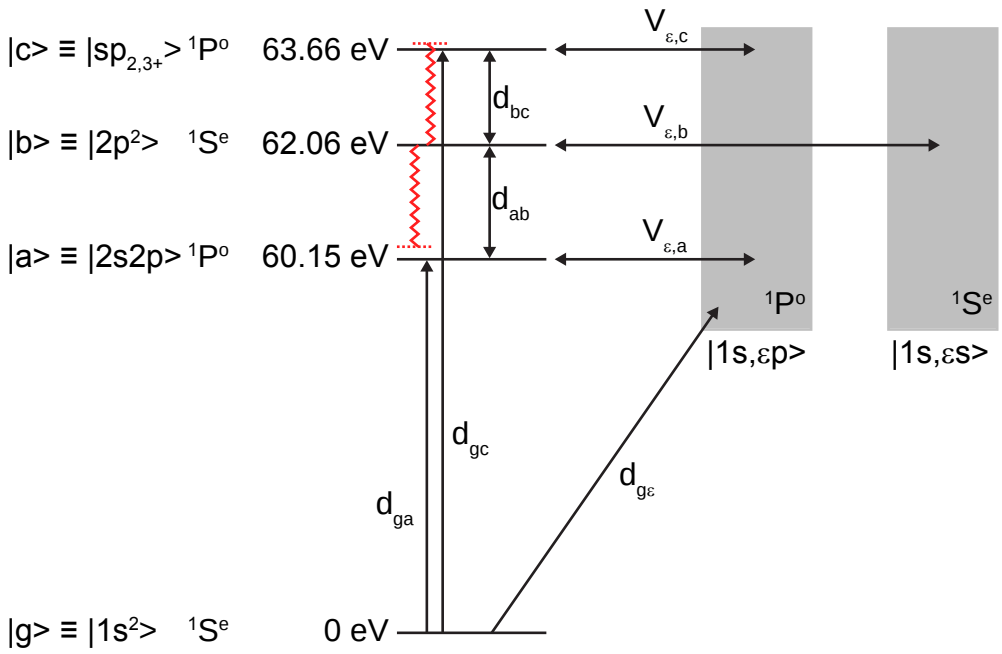

Figure 6.11: Level scheme of the simulated subsystem. The ground state $|\mathrm{g}\rangle \equiv |1s^2\rangle$, the autoionizing bound states $|\mathrm{a}\rangle \equiv |2s2p\rangle$, $|\mathrm{b}\rangle \equiv |2p^2\rangle$ and $|\mathrm{c}\rangle \equiv |sp_{2,3+}\rangle$, and the continua $|1s,\varepsilon p\rangle$ and $|1s,\varepsilon s\rangle$ are coupled via the dipole matrix elements d_{nm} as depicted. The configuration-interaction matrix elements $V_{\varepsilon,n}$ couple the excited states with their corresponding (symmetry $^1\mathrm{P^o}$ or $^1\mathrm{S^e}$) continua. A single-photon transition in a 730 nm (1.7 eV) field is depicted in red.

of these theories to the case considered here seemed problematic due to the very short ($\sim$7 fs) duration of the NIR laser pulses used in our experiments. This means that the instantaneously-defined Rabi frequency (see remarks at the end of section 2.6) changes rapidly on the order of its own time scale, i.e. the whole time-independent concept may become unsuitable. In addition, the introduced interferometric pump–probe scheme suggests that all parameters should be described in the time domain (including the autoionization process). In order to circumvent these difficulties, a time-dependent close-coupling simulation for autoionizing states was numerically implemented. The treatment thus also contains the explicit numerical description of autoionization, expressed by off-diagonal elements in the Hamiltonian which describe the coupling V_E to the continuum (see section 2.7). The scheme is in part also described in [203]. Some details which are presented in the following are also contained in [204].

6.4.1 General considerations

The simulation is based on the coupling of few discrete states as introduced in section 2.6 where the Schrödinger equation is solved (see Eq. (2.63)). The involved continua due to autoionization will be discretized as shown below. The system of interest (see Fig. 6.11) consists of four discrete states (the ground state $|\mathrm{g}\rangle$ and the three autoionizing bound states $|\mathrm{a}\rangle \equiv |2s2p\rangle$, $|\mathrm{b}\rangle \equiv |2p^2\rangle$ and $|\mathrm{c}\rangle \equiv |sp_{2,3+}\rangle$) and two separate continua $|1s,\varepsilon p\rangle$ and $|1s,\varepsilon s\rangle$, into which the two $^1\mathrm{P^o}$ bound states and the one $^1\mathrm{S^e}$ bound state autoionize, respectively. All other states including ionization or coupling to the $N = 2$ continuum are neglected

in this treatment in order keep the degree of complexity at the lowest possible level. As it will be shown below, these states are sufficient to generate absorption spectra which closely resemble the experimentally measured spectra.

The states are coupled via the dipole matrix elements d_{nm} and the configuration interaction matrix elements $V_{\varepsilon,n}$. The laser (NIR)-induced couplings between each discrete state and the other respective continuum is neglected. This is motivated by a similar system [43], from which the corresponding couplings can be deduced small. Also the laser coupling between the two continua can be safely neglected in our intensity regime [37] (see also section 2.7). The full time-dependent Hamiltonian $\mathbf{H}(t)$ of the system in dipole approximation then reads

$$\mathbf{H}(t) = \begin{pmatrix} E_\mathrm{g} & 0 & 0 & 0 & 0 & 0 \\ d^*_\mathrm{ga}\cdot\tilde{F}^*_\mathrm{XUV}(t) & E_\mathrm{a} & d_\mathrm{ab}\cdot F_\mathrm{NIR}(t) & 0 & V_{\varepsilon,\mathrm{a}} & 0 \\ 0 & d^*_\mathrm{ab}\cdot F_\mathrm{NIR}(t) & E_\mathrm{b} & d_\mathrm{bc}\cdot F_\mathrm{NIR}(t) & 0 & V_{\varepsilon,\mathrm{b}} \\ d^*_\mathrm{gc}\cdot\tilde{F}^*_\mathrm{XUV}(t) & 0 & d^*_\mathrm{bc}\cdot F_\mathrm{NIR}(t) & E_\mathrm{c} & V_{\varepsilon,\mathrm{c}} & 0 \\ d^*_{\mathrm{g}\varepsilon}\cdot\tilde{F}^*_\mathrm{XUV}(t) & V^*_{\varepsilon,\mathrm{a}} & 0 & V^*_{\varepsilon,\mathrm{c}} & \frac{[p+A_\mathrm{NIR}(t)]^2-i\kappa}{2} & 0 \\ 0 & 0 & V^*_{\varepsilon,\mathrm{b}} & 0 & 0 & \frac{[p+A_\mathrm{NIR}(t)]^2-i\kappa}{2} \end{pmatrix} \tag{6.4}$$

which couples the states of interest via Schrödinger's equation (see Eq. (2.63) in section 2.6)

$$i\partial_t \begin{pmatrix} c_\mathrm{g}(t) \\ c_\mathrm{a}(t) \\ c_\mathrm{b}(t) \\ c_\mathrm{c}(t) \\ c_{\varepsilon\mathrm{p}}(t) \\ c_{\varepsilon\mathrm{s}}(t) \end{pmatrix} = \mathbf{H}(t) \begin{pmatrix} c_\mathrm{g}(t) \\ c_\mathrm{a}(t) \\ c_\mathrm{b}(t) \\ c_\mathrm{c}(t) \\ c_{\varepsilon\mathrm{p}}(t) \\ c_{\varepsilon\mathrm{s}}(t) \end{pmatrix}, \tag{6.5}$$

with the complex expansion coefficients $c_n(t)$. Atomic units (a.u.) are used throughout this section. The broad-band XUV field F_XUV(t) is treated perturbatively, thus only the resonant part leading to excitation with the XUV field in its complex representation ($\tilde{F}_\mathrm{XUV}$) is kept in the Hamiltonian (cf. Eq. (2.58) in section 2.5). This leads to a constant ground-state population ($\partial_t c_\mathrm{g}(t) = 0$, with $E_\mathrm{g} = 0$). The coupling between the bound states is realized in the full time-dependent representation of the real-valued NIR field $F_\mathrm{NIR}(t)$ (cf. Eq. (2.64) in section 2.6). The continua are treated in strong-field approximation as Volkov states (see section 2.2) with the vector potential $A_\mathrm{NIR}(t) = -\int_{-\infty}^{t} F_\mathrm{NIR}(t')\mathrm{d}t'$ and are parameterized with their kinetic momentum p. A one-dimensional treatment is justified due to the linear polarization of the electric fields. The continuum states are described as quasi-discrete non-interacting states with spacing Δp. Each of these quasi-discrete states can thus be treated separately. To suppress continuum revivals which are an artifact of discretization, a constant decay rate κ is added which broadens the quasi-discrete states to a mutual overlap. The configuration-interaction matrix elements $V_{\varepsilon,n} = \langle 1\mathrm{s},\varepsilon\mathrm{p/s}|\,\mathbf{H}\,|n\rangle \equiv V_n$, which describe autoionization, are taken to be constant (i.e. energy independent) in the vicinity of each configuration state, in accordance with Fano's original theory [38] (see also section 2.7.1).

6.4.2 Numerical calculation of the absorption parameters

Direct numerical integration of the time-dependent complex expansion coefficients $c_n(t)$ is performed with a split-step-like approach, where for each time step Δt, different sub-systems of $\mathbf{H}(t)$ are evaluated separately. The corresponding steps are:

1. The perturbative excitation of states $|\mathrm{a}\rangle$, $|\mathrm{c}\rangle$, and the set of $|1\mathrm{s},\varepsilon\mathrm{p}\rangle$ continuum states in the XUV laser field.
2. The coupling of the three bound states $|\mathrm{a}\rangle$, $|\mathrm{b}\rangle$ and $|\mathrm{c}\rangle$ in the NIR laser field.
3. The coupling of the three bound states $|n\rangle$ with their corresponding continuum states $|1\mathrm{s},\varepsilon\mathrm{p/s}\rangle$ due to configuration interaction.
4. The field-free evolution of the three bound states with eigenenergies E_n.
5. The NIR laser-dressed evolution of the quasi-discrete continuum states.

For each step, the corresponding sub-system is diagonalized, thus temporal evolution corresponds to the multiplication of a complex phase factor "$\exp(-i\lambda_j \cdot \Delta t)$" with λ_j being the eigenvalues of the diagonalized sub-system after a unitary transformation.

Finally, for each time step, the time-dependent dipole moment $D(t)$ between the ground state and the dipole-allowed $|\mathrm{a/c}\rangle$ states as well as the $|1\mathrm{s},\varepsilon\mathrm{p}\rangle$ continuum states is evaluated:

$$D(t) = d_{\mathrm{ga}} \cdot c_{\mathrm{a}}(t) + d_{\mathrm{gc}} \cdot c_{\mathrm{c}}(t) + d_{\mathrm{g}} \sum_{\varepsilon} c_{\varepsilon\mathrm{p}}(t), \tag{6.6}$$

where the ground-continuum dipole matrix element $d_{\mathrm{g}} \equiv d_{\mathrm{g}\varepsilon}$ is assumed independent of energy. With Eq. (2.98) from section 2.8 the ratio of the frequency-dependent dipole moment $\tilde{D}^{\mathrm{s}}(\omega)$ and the XUV laser spectrum $\tilde{E}^{\mathrm{s}}(\omega)$ is directly proportional to the experimentally obtained optical density as discussed previously, in our limit of low absorption and thus negligible propagation/dispersion effects. The Fourier transform is applied to obtain the corresponding values $\mathscr{F}\{D(t)\} = \tilde{D}^{\mathrm{s}}(\omega)$ and $\mathscr{F}\left\{\tilde{F}_{\mathrm{XUV}}\right\} = \tilde{E}^{\mathrm{s}}(\omega)$.

6.4.3 Simulation parameters

The free parameters of the simulation are:

- the time step size Δt and the total time of simulation T,
- the momentum density Δp of the discretized continuum, its range between p_{min} and p_{max} and its decay constant κ,
- the configuration-interaction matrix elements V_n
- the dipole matrix elements coupling the ground state to the excited states $d_{\mathrm{g}n}$ and to the continuum states $d_{\mathrm{g}\varepsilon} \equiv d_{\mathrm{g}}$,

- and the dipole matrix elements d_{ab} and d_{bc} for the allowed optical transitions between the excited states with the VIS laser field.

We used $\Delta t = 1$ a.u. (0.0242 fs) and $T = 32000$ a.u. (774 fs) to accurately sample all the involved dynamics (compare with the NIR laser cycle, typically ~ 2.5 fs) and to cover the full natural autoionizing decay of the states ($\Gamma_b = 6$ meV corresponds to an exponential decay time ~ 220 fs), maintaining a reasonable amount of computation time.

The continuum was sampled with $\Delta p = 0.0145$ a.u. in 100 steps from $p_{min} = 1.35$ a.u. (i.e. $E_{min} = 24.8$ eV) to $p_{max} = 2.80$ a.u. (i.e. $E_{max} = 106.7$ eV), while both positive and negative momenta (in a one-dimensional treatment) were considered. In total this leads to 400 discrete quasi-continuum states, 100 positive and negative momentum states for each $|1s,\varepsilon p\rangle$ and $|1s,\varepsilon s\rangle$ set of states, respectively. The decay rate $\kappa = 0.2$ a.u. broadens these discrete states to a mutual overlap, thus approximating a continuous spectrum. Within the exponential decay time $2/\kappa$ of the population amplitude, the corresponding continuum electrons travel ~ 16 Bohr radii a_0, thus they are maintained in the simulation long enough to interact with the bound states close to the nucleus.

The remaining parameters of configuration-interaction matrix elements V_n and dipole matrix elements d_{gn} and d_g were then chosen for the simulated absorption lines to match known experimental and theoretical line-shape parameters (see Tab. 6.1). The dipole matrix elements between the 2s2p and the $2p^2$ autoionizing states is taken from literature [179] with $d_{ab} = 2.17$ a.u., whereas the dipole matrix element between the $2p^2$ and the $sp_{2,3+}$ autoionizing states was calculated to $d_{bc} = 0.81$ a.u. [205].

The electric fields are defined with Gaussian envelopes (cf. Eq. (2.2) in section 2.1) and bandwith-limited phase.

6.5 Simulation results of coupled autoionizing states

In the preceding section the numerical framework of coupled discrete and quasi-continuum states was introduced in detail. It can be used to calculate time-delay-dependent absorption spectra containing the 2s2p and $sp_{2,3+}$ states in order to compare them with experimental results. In the following, simulated absorption spectra are shown for various pulse parameters (both XUV and NIR). They are shown in order to illustrate the numerical framework and to connect it to the measured absorption line shapes.

6.5.1 The evolution of the bound states

As a result of the above described numerical treatment, the full time evolution of the complex state amplitude is accessible, separately for each of the three considered states. For different XUV/NIR pulse configurations this is shown in Fig. 6.12. In the absence of the NIR laser field, both XUV-populated 2s2p and $sp_{2,3+}$ ($^1P^o$) states decay exponentially due to autoionization into the $1s,\varepsilon p$ continuum, while the $2p^2$ ($^1S^e$) state remains unpopulated (dipole forbidden from the He $1s^2$ ground state). This is also the case for the NIR laser pulse interacting with the system sufficiently early (compared to its duration) before the

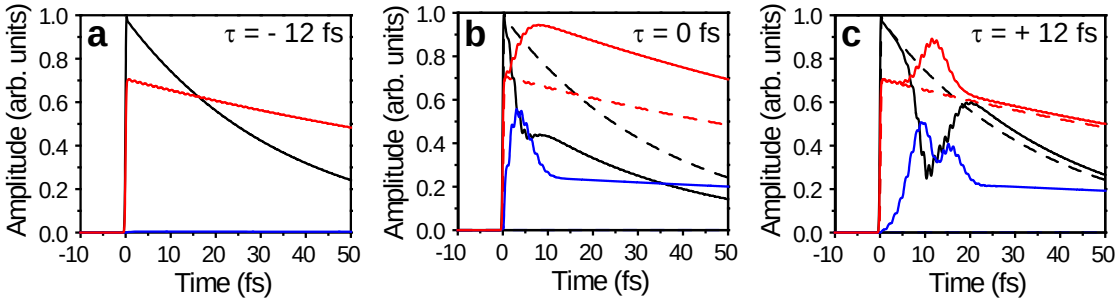

Figure 6.12: Time evolution of the state amplitude for the three simulated 2s2p ($^1P^o$), $2p^2$ ($^1S^e$) and $sp_{2,3+}$ ($^1P^o$) autoionizing resonances for different XUV/NIR temporal configurations. Both $^1P^o$ states (2s2p: black lines, $sp_{2,3+}$: red lines) are perturbatively populated by an XUV attosecond pulse (duration 250 as FWHM, centered around 64 eV) at time 0 fs. The NIR field couples these states to the $^1S^e$ $2p^2$ state (blue lines). The NIR pulse duration is 7 fs FWHM with 3.3×10^{12} W/cm^2 peak intensity and 730 nm central wavelength. The center of NIR pulse appears at times -12 fs (a), 0 fs (b), and +12 fs (c). The dashed curves show the state evolution in the absence of the NIR field.

XUV attosecond pulse arrives, as shown in Fig. 6.12a. If the NIR laser pulse arrives together (b) or shortly after (c) the populating XUV attosecond pulse, but still within the decay time of the states, it can significantly rearrange the population among all three states (i.e. Rabi cycling occurs, see section 2.6). This rearrangement occurs on a time scale on the order of the NIR pulse duration, which justifies the numerical treatment. The faster (1-fs time scale) modulation on both $^1P^o$ decaying amplitudes even in the absence of the NIR pulse is due to their coherent coupling with the same 1s,εp continuum via autoionization. This period exactly corresponds to the energy difference ΔE between the two 2s2p and $sp_{2,3+}$ states (see also section 6.7) and is due to their coherent excitation, i.e. a wave packet is formed (see section 2.4). In any case, after the NIR laser pulse is over, all three states decay exponentially according to their width Γ as given in Tab. 6.1, where the simulation parameters were set accordingly (see section 6.4.3).

Comparing all three panels illustrates the significant influence that the XUV/NIR time-delay configuration has on the induced repopulation of the states (also on a sub-cycle basis, not shown). It is this repopulation of states which significantly changes the coherent dipole emission $D(t)$ with respect to the ground state and which is measured in the absorption signal (see above). This explains how the 1-fs time-scale beating, evidencing the wave-packet motion, finds its way into the measured absorption line shape.

Fig. 6.13 shows a comparision between the experimentally obtained absorption profile (as described in Fig. 6.4) and the calculated profile (as described in section 6.4.2). The pulse parameters for the calculated absorption are that of Fig. 6.12a. The numerical simulation can reproduce the experimentally obtained asymmetric absorption profiles in good agreement.

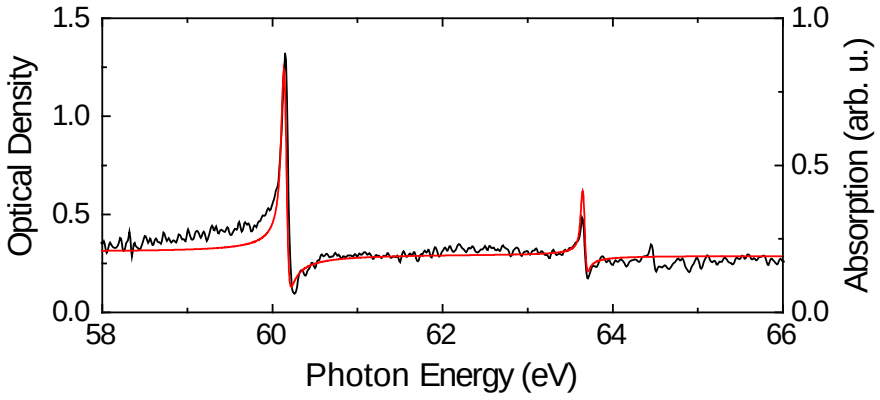

Figure 6.13: Comparison between experimentally measured (black line, see Fig. 6.4) and numerically calculated (red line) absorption spectra showing good agreement. The calculated spectra are convoluted with the experimental detector resolution (47 meV FWHM Gaussian point spread function). The simulated pulse configurations correspond to Fig. 6.12a.

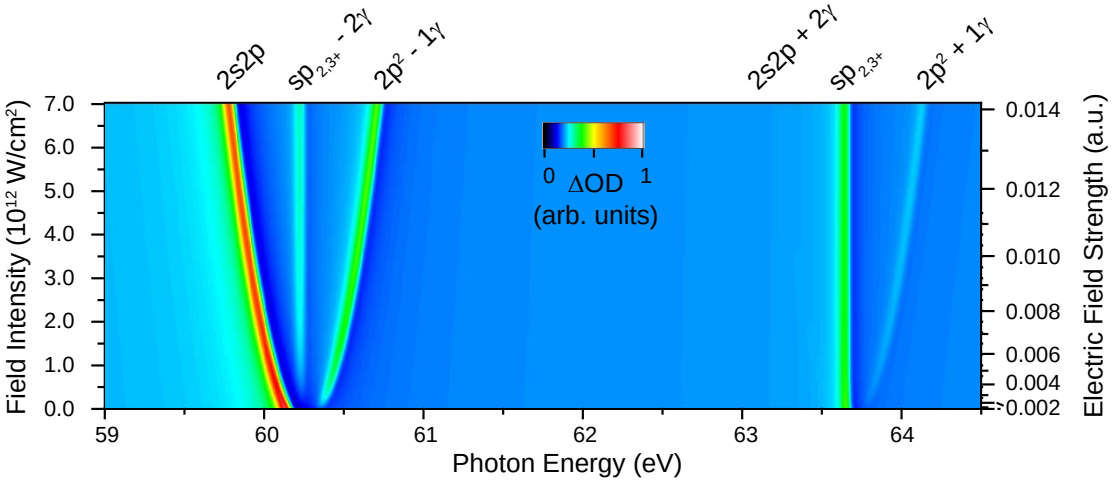

Figure 6.14: Simulated two-dimensional absorption spectra of the three-level system as a function of the photon energy and the NIR field intensity in a monochromatic field (730 nm). The absorption spectra were averaged over one NIR laser cycle of time delay. The spectra are convoluted with the experimental detector resolution (47 meV FWHM). An Autler-Townes splitting of the three mutually repelling states is observed.

6.5.2 Autler-Townes splitting of autoionizing states

To check the performance of the numerical simulation, the XUV-excited autoionizing states were dressed with a monochromatic NIR field (730 nm). The simulated absorption spectra are shown in Fig. 6.14 for a continuous range of different field strengths. In total three states are involved and coupled in the NIR field (730 nm, i.e. 1.7 eV photon energy). The mutually repelling absorption lines are labeled according to their origin, where γ here denotes an NIR photon. The appearance of the additional absorption lines next to the main lines for smallest field strength corresponds to their detuning (see also Fig. 6.11 in section 6.4.1, where the general scheme is depicted in Fig. 2.8 of section 2.6). The 730 nm center wavelength in the experiment was deduced from the experimentally observed detuning (see Fig. 6.17 in section 6.6). The "2s2p+2γ" absorption line is weakest and not visible in the shown scale. According to section 2.6, the Rabi frequency at for instance 4×10^{12} W/cm^2 field intensity evaluates to $\Omega_R = 0.63$ eV$/\hbar$ for the two coupled 2s2p–2p^2 states ($d_{ab} = 2.17$ a.u.). This is in agreement with the observed splitting at this field intensity, with the detuning $\Delta = 0.21$ eV. The sp$_{2,3+}$ state is only slightly shifting which is i) due to a weaker coupling to the 2p^2 state ($d_{bc} = 0.81$ a.u.) and ii) due to an additional 2γ-coupling with the 2s2p state which counteracts the 2p^2–sp$_{2,3+}$-repulsion. This qualitative description shall suffice at this stage and it is only pointed out that the exact energy shifts of all three absorption lines could be computed via diagonalization of the 3×3 coupling matrix, in analogy to the diagonalization procedure of Eq. (2.68) carried out for the two level system in section 2.6. A change in the absorption line shape as a function of the field intensity is not observed (see remarks in section 2.7.2). This is explained as the NIR-induced coupling of the bound states with the autoionizing continua are neglected in this simulation.

The results in this and the preceding section confirm the validity of the simulation framework which can further be applied to simulate and reproduce the experimentally observed absorption spectra. Fig. 6.15 shows calculated absorption spectra as a function of time delay τ between the XUV excitation and the NIR laser pulse of duration 7 fs FWHM. Further pulse parameters are noted in the caption. The definition of time delay zero is also depicted. This definition is motivated with the intrinsic phase-lock of the generated attosecond pulses with the NIR driver field (see also section 2.2.2). It is set to a configuration where the most intense XUV pulse coincides with the first zero-crossing after the most intense half-cycle of the NIR pulse. A fast modulation on a 1 fs time scale is observed across both absorption lines. This and also the overall structure is in good agreement with the experimentally obtained data (compare with Fig. 6.10 in section 6.3). A more detailed comparison and discussion of these features will be given in section 6.7.

An indication of an Autler-Townes splitting and a coupling of all three involved states can also be deduced from the calculated absorption spectra in Fig. 6.15. Between $\tau = 0$ and $\tau = 5$ fs, the absorption maximum of the 2s2p line shifts to lower energies, while at photon energy $E \approx 60.4$ eV (which corresponds to the detuning), a second absorption maximum appears (i.e. "2p^2-γ") which shifts to higher energies in this considered region of time delay. In addition, a third absorption peak (i.e. "sp$_{2,3+}$-2γ") appears in between these two shifted peaks. This is in agreement with the observation in Fig. 6.14 for a monochromatic NIR field. Deviations for a 7 fs NIR pulse are obvious, as the electric

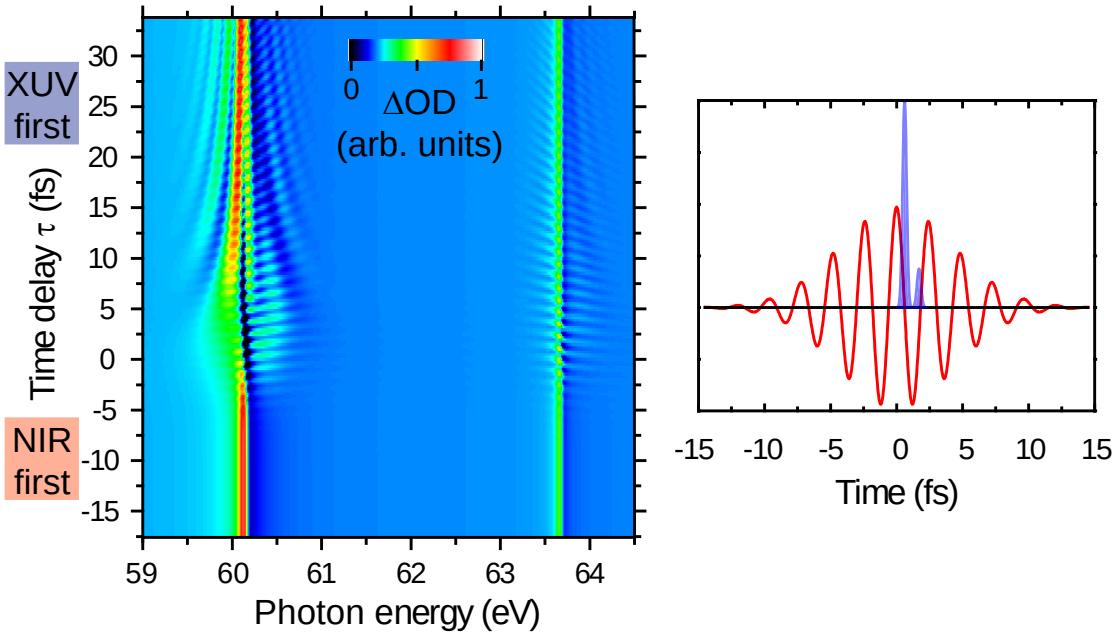

Figure 6.15: Simulated absorption spectra as a function of time delay τ. The NIR pulse was centered around 730 nm with 7 fs FWHM duration and peak intensity $3.3 \cdot 10^{12}$ W/cm^2. The CEP was set to zero. For the excitation, two subsequent attosecond XUV pulses were used to resemble the experimentally observed harmonic modulation (see Fig. 6.3 in section 6.2). The parameters are $t_{\mathrm{FWHM}}^{(XUV)} = 250$ as for each pulse, with relative strength 0.187 and relative phase 5 rad. Both XUV and NIR pulses are shown in the right panel which depicts the definition of time delay zero. The spectra are convoluted with the experimental detector resolution.

field now only couples the three states for a fraction of their life time (see also Fig. 6.12 in section 6.5.1) and in addition the envelope of the electric field is changing on the order of the Rabi frequency. In other words, the larger bandwidth of the 7 fs pulse precludes the observation of spectrally well-defined dressed absorption lines. It should be noted that maximum Autler-Townes splitting is observed for a positive time delay and not for time delay zero. For a positive time delay, the initially excited states are subject to the full NIR pulse and not only to a fraction of it as is the case when attosecond pulse and NIR pulse arrive on top of each other and only the trailing edge of the NIR pulse leads to population transfer among the strongly-coupled states.

6.5.3 Effects of multiple-pulse configuration and the CEP

In order to confirm that neither the CEP nor the excitation with more than one attosecond pulse significantly influences the experimental observation, different configurations were simulated and are shown in Fig. 6.16. As the horizontal line indicates, the 1 fs time-scale modulation is not shifted in phase across the three considered cases. Only the slowly-changing structure below this fast modulation is slightly shifted (almost not notably) on a sub-cycle time scale. This is insignificant as all other dynamics occur on a longer time scale, according to the NIR pulse duration and the life time of the excited states.

These findings illustrate that i) the absorption spectra are not significantly influenced by

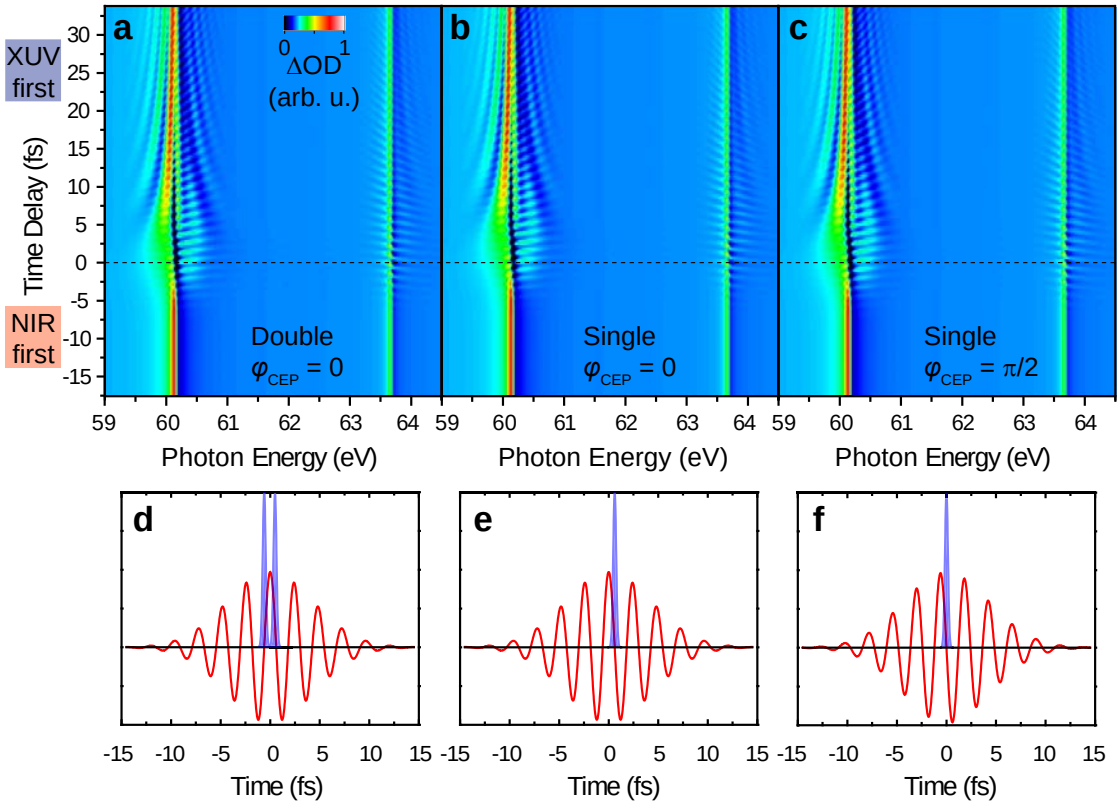

Figure 6.16: Simulated absorption spectra as a function of time delay and energy for different pulse configurations. The general pulse parameters are that of Fig. 6.15, except a) two attosecond pulses of equal strength are used with $\varphi_{\mathrm{CEP}} = 0$ for the NIR laser pulse, b) one attosecond pulse with $\varphi_{\mathrm{CEP}} = 0$ for the NIR laser pulse, and c) one attosecond pulse with $\varphi_{\mathrm{CEP}} = \pi/2$ for the NIR laser pulse is used. The lower panels (d,e,f) illustrate the respective definition of zero time delay. The dashed line connects the three cases to compare the 1 fs time-scale modulation.

multiple-pulse contributions and ii) averaging over the CEP does not wash out the 1 fs modulation. The only necessary ingredients are i) a continuous broad-band XUV excitation spectrum with light across the observed states and ii) a high interferometric stability of the relative timing between the attosecond pulses and the time-delayed NIR pulse. Both requirements are fulfilled in the performed experiment. These observations also explain how such fast modulations can be observed even when using an attosecond pulse train for the excitation [199], in that case of one-electron excited states in helium. Thus, any attosecond-pulsed configuration can be used for such experiments as long as the total temporal window of excitation (be it in form of a single attosecond pulse or a pulse train) is shorter than the life time of the considered states.

6.6 *In-situ* calibration of the NIR intensity

In the previous section, the results of the numerical simulation were presented in detail and, in the case of the Autler-Townes splitting, also compared with experimentally mea-

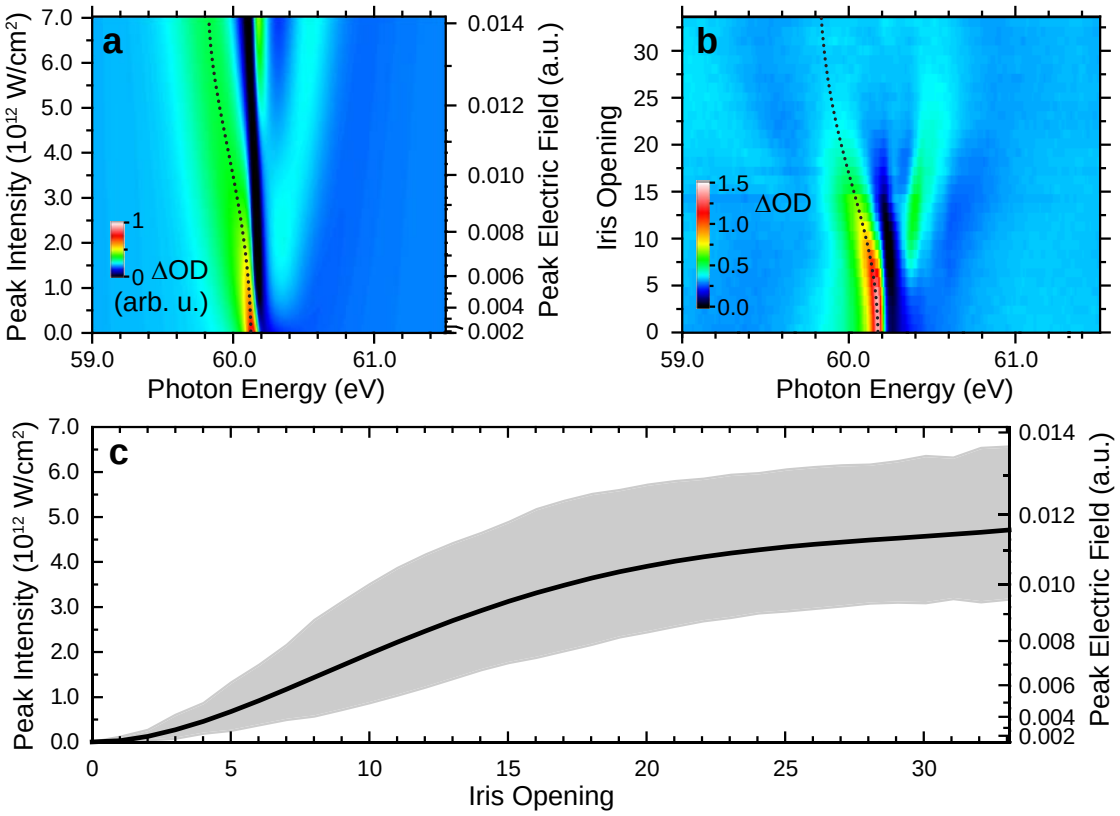

Figure 6.17: Intensity calibration of the experimental data. a) Simulated absorption spectra for a 7 fs FWHM Gaussian NIR laser pulse at varying intensities, centered around 730 nm. b) Experimentally measured OD for different openings of the iris aperture, leading to a systematic increase in the NIR laser intensity. For a) and b), the time delay was set to where the Autler-Townes splitting is at maximum, averaged over two modulation periods. c) The comparison of maximum absorption of the left-shifting 2s2p line (starting from 60.15 eV, marked by the dotted line in a) and b) between numerical and experimental results yields an *in-situ* mapping between the NIR laser peak intensity and the iris opening in the experiment (black line). The grey-shaded area denotes a systematic error, taking into account different simulated pulse durations and an additional comparison near 0 fs time delay (see text for details).

sured data. In particular, the observed splitting of the coupled 2s2p and $2p^2$ states is experimentally confirmed, where the dipole matrix element $d_{ab} = 2.17$ a.u. yielded calculated spectra which could explain the experimental observation [179][1]. This well-understood feature appears both in the simulated as well as in the measured spectra, where the level splitting is directly proportional to the laser intensity and the dipole matrix element. It can therefore be used to perform an *in-situ* calibration of the NIR intensity which was present in the experiment.

Fig. 6.17 shows a comparison of the 2s2p–$2p^2$ Autler-Townes splitting for the simulated absorption spectra in a) (pulse configuration as in Fig. 6.15, convoluted with the exper-

[1] As a side remark, in a very recent theoretical treatment considering this observed coupling, the dipole matrix element was evaluated to $d_{ab} = 2.11$ a.u. [183], and another independent calculation yielded $d_{ab} = 2.16$ a.u. [205]. Future measurements with a more precise and independent intensity calibration in our setup could thus even be used to provide benchmarks for testing atomic structure theories.

imental detector resolution) and the experimentally observed splitting in b). The data is shown for a continuous range of peak intensities (simulated spectra) and for various iris-aperture openings which were recorded experimentally. As discussed in the previous section, (see Fig. 6.15 in section 6.5.2 and Fig. 6.10 in section 6.3), the Autler-Townes splitting is a function of the XUV/NIR time-delay. The data shown in Fig. 6.17 is averaged over two modulation periods (~ 2.5 fs) centered around a temporal region, where the splitting is strongest. This was ~ 5 fs for the experimental results, and ~ 3 fs for the numerical results. The deviation between these two values can be explained with the exact NIR pulse shape in the experiment, which may be not exactly Gaussian with 7 fs FWHM duration. In addition, the position of the generated attosecond pulses with respect to the NIR driver pulse may deviate from the configuration which was assumed for the simulation (see Fig. 6.15 in section 6.5.2).

For both data sets, the shifting of the 2s2p absorption maximum was followed as indicated by the dotted lines in Fig. 6.17a) and b). The comparison between these two positions then yields a mapping of peak intensity vs. iris-aperture opening. In order to estimate the systematic uncertainty due to differently set temporal delays as outlined above, the shift of the absorption maximum was also quantified for zero time delay in both cases. In addition, to account for the effect of a >7 fs pedestal in the NIR pulse (which is typical of the hollow-fiber/chirped-mirror pulse compression method employed, see e.g. Fig. 3.1 in section 3.1) various simulated NIR pulse durations (ranging from 5 to 30 fs) were also considered. The mean value of the peak-intensity/iris-opening mapping for all these configurations is shown in Fig. 6.17c), where the grey-shaded area denotes the standard deviation, giving an estimate of the systematic uncertainty.

It should be noted that the relatively large systematic error in the *in-situ* intensity calibration is only due to uncertainties in the exact pulse configuration as outlined above. In any case, the experimental data was recorded as a function of systematically increasing NIR intensity (as the iris aperture was opened stepwise). This means that the intrinsic statistical fluctations of the intensity are much lower. This is confirmed in Fig. 6.17b), where the absorption maxima are clearly observed shifting monotonically. Larger deviations might only occur above an iris opening ~ 25, where the absorption line disappears due to ionization. All these considerations however confirm, that the discussed experimental data was taken as a function of increasing NIR peak intensity in the 10^{12} W/cm^2 regime.

6.7 Experimental observation of a two-electron wave packet in helium

The general aspects of quantum wave packets were introduced in section 2.4. Typically, a wave packet is formed whenever more than one state quantum state is coherently excited. Thus also for the case considered here, where several correlated two-electron states are coherently excited, a wave packet which is beating on the time scale of the respective energy difference ΔE of the levels is formed. This well-defined excitation can be observed experimentally by means of an interference signal between the considered states.

In a recent theoretical treatment [201], the coherent excitation of the $sp_{2,n+}$ series in he-

lium with a single XUV attosecond pulse was considered. Tracing the autoionized electrons in time, it was shown that they appear periodically in the continuum, in bursts separated by ~ 1.2 fs, which exactly corresponds to the energy level spacing $\Delta E = 3.51$ eV between the two most dominantly populated states 2s2p and $sp_{2,3+}$. It was proposed that this beating in time can be observed with a time-delayed NIR pulse (similar to the one used in our absorption measurement), where the yield of excited ($N = 2$) ions is measured.

Within our measured absorption spectra (shown e.g. in Fig. 6.10 in section 6.3) it is evident that across both the 2s2p as well as the $sp_{2,3+}$ states a fast ~ 1.2 fs modulation appears as a function of the NIR time delay. This observation suggest that also in our case, a well-defined coherent wave packet is formed after the XUV excitation.

One could argue that the excitation with more than one attosecond pulse, as well as an averaging over the CEP would smear out the excitation and observation of such well-defined wave packets as they are theoretically described in [201]. This is however not the case as discussed previously for the multiple-pulse and CEP effects in section 6.5.3. More intuitively said, the attosecond-pulsed excitation is also appearing in bursts (in form of an attosecond pulse train, see section 5.1). The temporal spacing between the attosecond pulses is very close (within their temporal bandwidth even exactly in resonance) to the time period of the considered wave packet (the half-cycle period of 730 nm corresponds to $\Delta\tau = 1.2$ fs). Thus, exciting the above mentioned wave packet is just like resonantly driving a pendulum by periodically applying a force at the right instant of time. The phase-locked interaction with a time-delayed NIR pulse then fixes the "ruler" in order to observe the "excited pendulum". Within this analogy of a mechanical pendulum, the relative phase between two attosecond pulses corresponds to the relative direction of the applied force. This is further illustrated in Fig. 6.18, where the connection between the temporal and spectral domain is stressed. Whenever the excitation bandwidth includes both states, and this is the case in our experimental data, a "net force" remains and a periodic motion is initiated.

In the following, the interfering pathways within the experimentally observed spectra are analyzed in more detail. This allows for an interpretation of the observed features across the absorption line shape as a function of the XUV/NIR time delay. Motivated from the previous discussion of the wave packet and its periodic motion corresponding to the energy difference $\Delta\tau = h/\Delta E$, it is straightforward to transform the time delay into the Fourier energy domain. This is shown in Fig. 6.19 both for the experimentally obtained absorption spectra (which are also shown in Fig. 6.10 in section 6.3) and the numerically simulated spectra (also shown in Fig. 6.15 in section 6.5.2).

The two-dimensional representation in the Fourier domain yields characteristic diagonal lines with slope ± 1 which originate from the energy position $E_1 = 60.15$ eV and $E_2 = 63.66$ eV of the 2s2p and $sp_{2,3+}$ states, respectively. These lines indicate a coherent coupling between the two states along different transition pathways which are further illustrated in Fig. 6.20. Each contribution in the two-dimensional Fourier representation can be connected to a two-photon coupling as outline by the numbers. The two contributions close to 3.5 eV Fourier energy (1,2) both involve a two-photon up- or downward transition connecting both 2s2p and $sp_{2,3+}$ states. These transitions therefore experimentally evidence the two-electron wave packet as the two involved states interfere. As a conse-

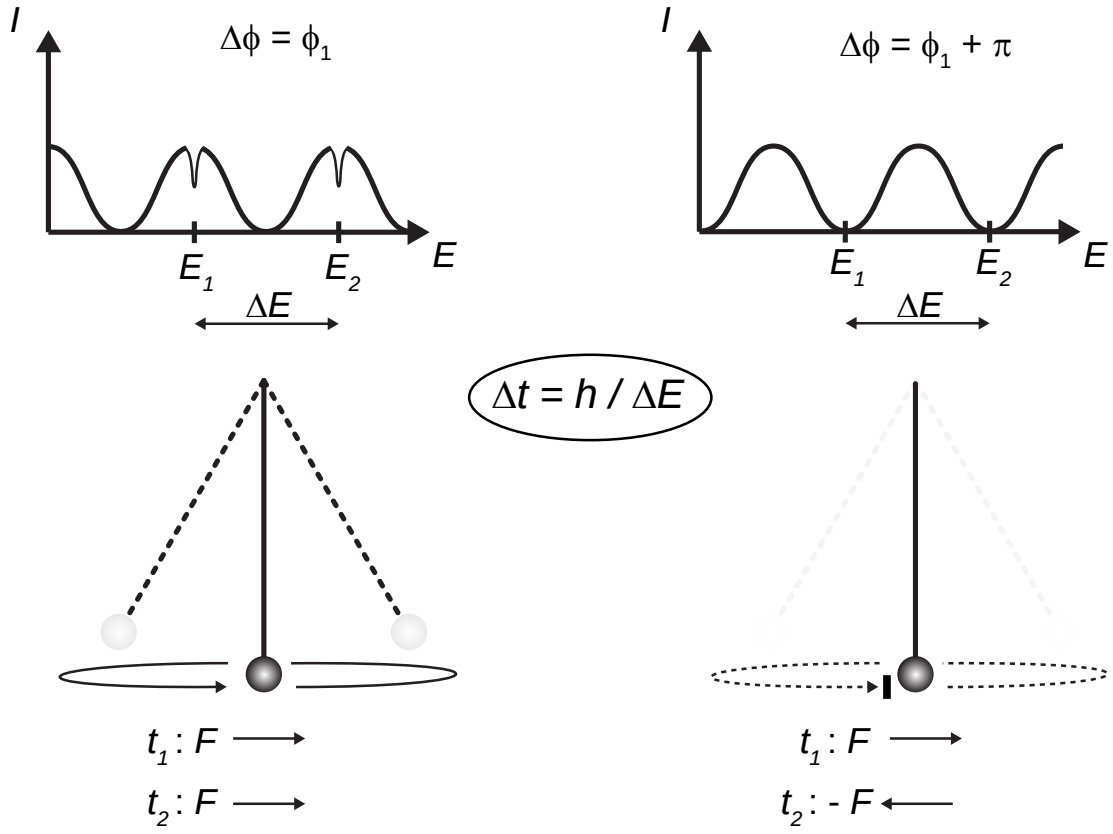

Figure 6.18: Illustrative analogy of a driven pendulum for excitation with more than one attosecond pulse: The pulses are spaced by $\Delta t = h/\Delta E$ and are represented by a sinusoidal modulation of the spectral intensity (top panels). This energy difference also corresponds to the eigenfrequency $\nu = \Delta E/h$ of an oscillating pendulum in the time domain (bottom panels). If the relative phase $\Delta\phi$ is such (ϕ_1, top left) that the spectral intensity is non-zero across both considered levels at energies E_1 and E_2, both states are coherently excited and a periodic motion remains. In the time domain, the pendulum is kicked twice with a force F, thus a periodic motion remains, decaying with the natural life time of the pendulum (bottom left). If by contrast the two pulses are π out of phase, no spectral intensity is available across the states (top right). The pendulum picture in that case is a driving force with opposite direction for the subsequent times t_1 and t_2, resulting a zero net force, i.e. the periodic motion stops after one round-trip as if it never had happened (bottom right). The two cases can thus be interpreted as the constructive or destructive interference of both excitation pathways (note that this is *not* a two-photon process). If the pulse arrangement is such that there is spectral intensity across both states, a net force remains and the pendulum oscillates periodically after the excitation.

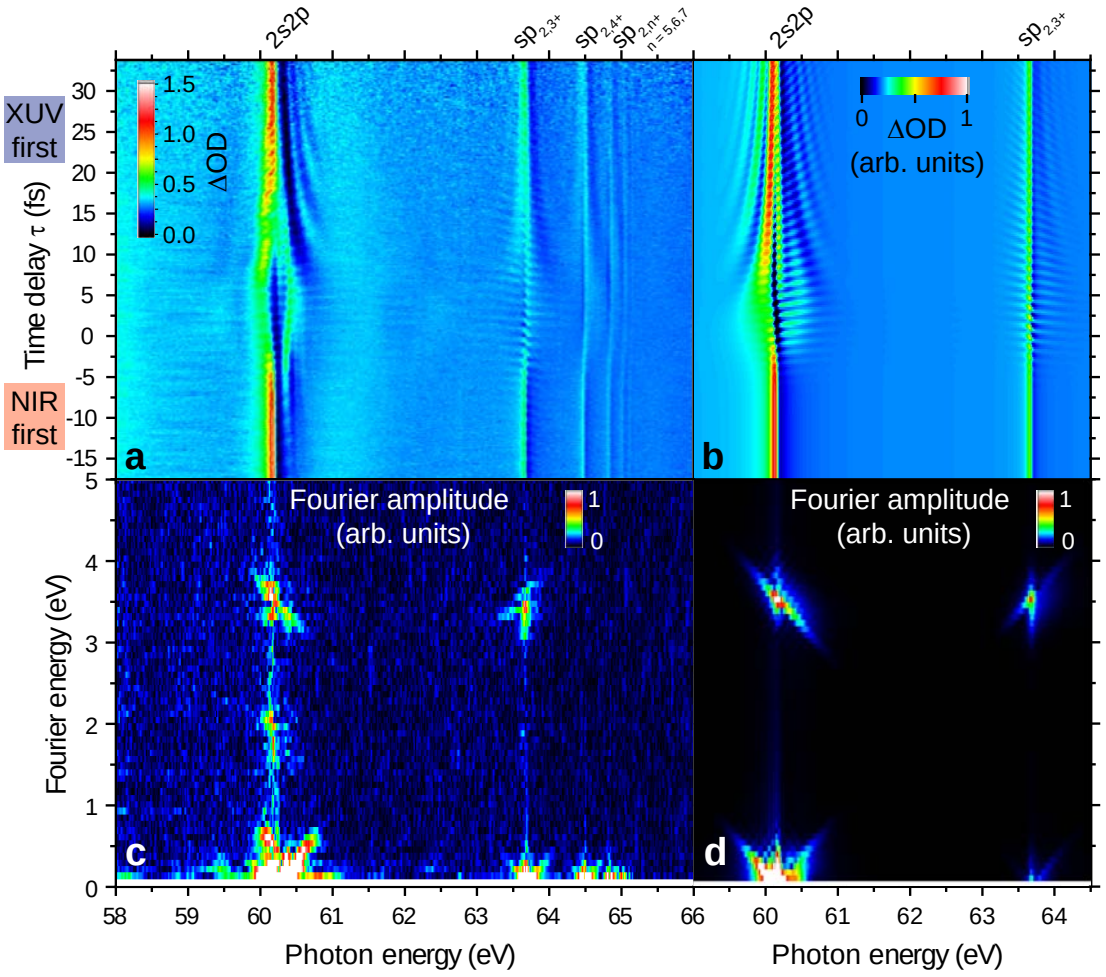

Figure 6.19: Comparison of experimentally measured (a,c) and numerically simulated (b,d) absorption spectra. The peak intensity of the NIR pulse was $3.3 \cdot 10^{12}$ W/cm^2 in both cases. Further parameters are discussed in the previous sections describing Figs. 6.10 and 6.15. The visualization in the Fourier domain (c,d) reveals the coherent coupling between the two considered two-electron states 2s2p and $sp_{2,3+}$ which is discussed in more detail in the text and in Fig. 6.20.

quence, the 1.2 fs modulation as a function of time-delay arises, as seen in Fig. 6.19a,b).

The remaining two contributions close to 0 eV Fourier energy (3,4) involve a Raman-like transition of each 2s2p and $sp_{2,3+}$ state separately. Both these "single-state" cases involve the simultaneous absorption and emission of one NIR photon, i.e. a net interaction with zero NIR photons. The corresponding illustration as a function of time-delay in Fig. 6.19a,b) is the appearance of a slow hyperbolic modulation which converges to the energy position of each state, respectively, for increasing time delay.

All transitions (1-4) are resonantly enhanced by the intermediate $2p^2$ state. It is the spectral broadness of the 7 fs NIR photons (bandwidth $\hbar\Delta\omega \sim 0.7$ eV) which fully explains the diagonal structures, as different "coulored" photons can interact in all four above-mentioned two-photon transition steps.

It is interesting to note that within pathway 3, a difference occurs in comparison between the experimental and simulated data. Along the Fourier analysis of the experimental data

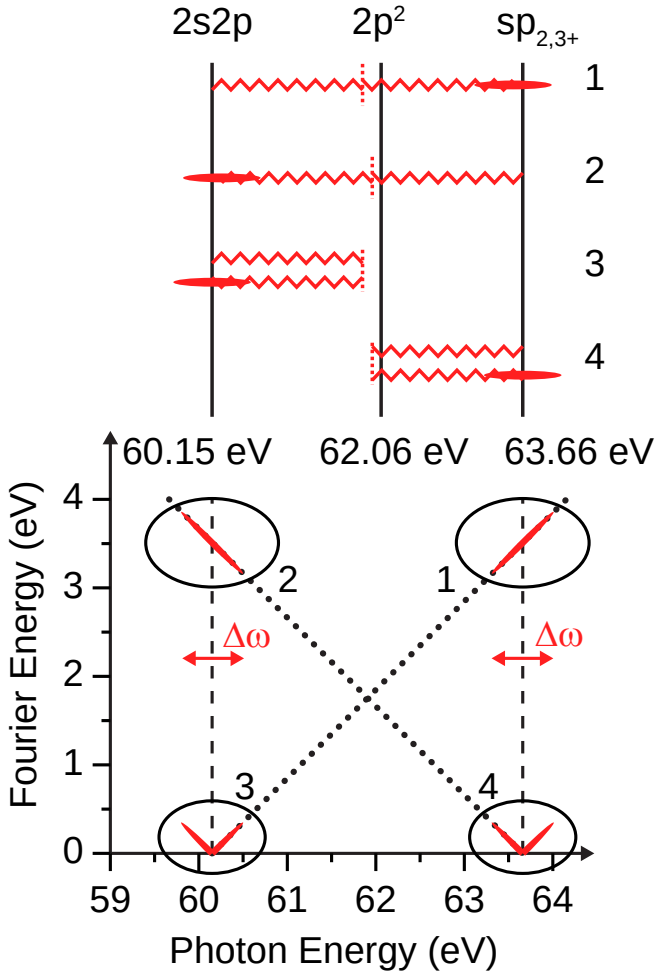

Figure 6.20: Illustration of the different transition pathways—qualitatively very similar to two-dimensional spectroscopy methods—which are revealed by the Fourier analysis of the time-delay dependent spectra shown in Fig. 6.19. The Fourier contributions of both the experimentally recorded and numerically simulated absorption spectra are schematically shown below, indicating the diagonal lines of slope ± 1. Four different transition pathways can be identified as illustrated on top, all resonantly enhanced via the nearby intermediate $2p^2$ state. The NIR photons are depicted as zig-zag lines. The NIR spectral bandwidth $\Delta\omega$ of the ~ 7 fs pulses is indicated by the horizontal arrows and the cigar-shaped structures in the coupling illustration on top.

in Fig. 6.19c), no diagonal line seems to originate from the 2s2p state towards lower energies, in contrast to its appearance in the simulated data in d). This is also reflected in Fig. 6.19a), as no hyperbolic structures are apparent to the left of the 2s2p absorption line as opposed to the simulated data in b). The reason for this is not yet fully understood. It is possible that other $^1S^e$ or $^1D^e$ states influence the Raman-like transition across the 2s2p state. Candidates for such states might be the $2s^2$ ($^1S^e$) at 57.82 eV, or the $2p^2$ ($^1D^e$) at 59.89 eV [181]. However these states are further off resonance as compared to the 1.7 eV NIR photon energy. An inclusion of both states within a full theoretical analysis is needed in order to further clarify this issue.

In Fig. 6.19c), the Fourier amplitude also reveals a contribution close to 2 eV especially across the 2s2p state. Its position in Fourier energy corresponds to the energy difference between the 2s2p ($^1P^o$) and $2p^2$ ($^1S^e$) states (which is 1.91 eV), thus it belongs to a "diagonal transition" emitting one photon into the NIR field, with the $2p^2$ state as the origin. This state, however, is dipole forbidden to the helium $1s^2$ ($^1S^e$) ground state and cannot be directly excited with the XUV pulse. It can, however, be accessed with an NIR photon present during the initial XUV excitation. This is an experimental artifact and due to a small leakage of NIR light transmitted through the thin metal foils which are used to separate the XUV from the NIR beam (see Fig. 3.9 in section 3.4).

All these considerations nicely illustrate, how the Fourier analysis of the time-delayed configuration reveals the different couplings among the involved states. The detailed and seemingly complicated structures across the absorption line shape get disentangled and can be attributed to their different origin. This approach can also explain so far not interpreted hyperbolic features which appear in a very recent theoretical analysis of a similar measurement [198].

Looking closely at the higher-excited states $sp_{2,n+}$ ($n \geq 4$) in Fig. 6.19a), intrinsic features within each asymmetric line shape are present. In addition, Fig. 6.19c) also reveals diagonal contributions for these states near zero Fourier energy which indicate a Raman-like coupling mediated by a different state. This state is the $N = 2$ continuum above 65.40 eV. A closer analysis of this coupling finally reveals the Fano quantum-interferometry scheme as mentioned in the introduction of this chapter. This is subject of the subsequent section.

6.8 Quantum interferometry with autoionizing states

It was mentioned in the introductory part of this chapter how the asymmetric line shape itself serves as a phase-sensitive interferometric probe for the induced dynamics (see also section 6.2). This scheme is now first exploited for the coupling of the 2s2p and the $sp_{2,3+}$ states, which was explained in detail in the previous section. In the second part of this section, the additional coupling of the $sp_{2,3+}$ and all higher states to the $N = 2$ continuum will be discussed.

The two states (2s2p and $sp_{2,3+}$) are coupled by the NIR field at a controlled time delay τ after their initial XUV excitation. As a function of τ, the two states acquire a relative phase

$$\Delta\Phi = \Delta E \cdot \tau/\hbar \tag{6.7}$$

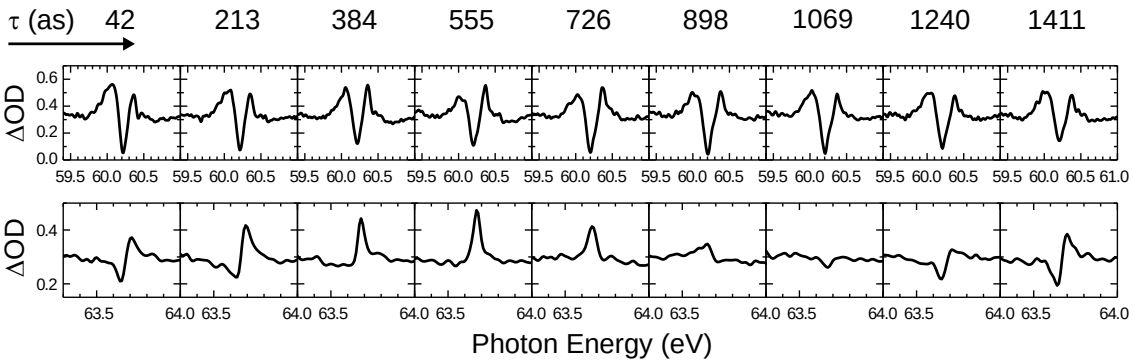

Figure 6.21: Absorption spectra for various time delays τ (top numbers) for both the 2s2p state (top row) and the $sp_{2,3+}$ state (bottom row). The NIR intensity was $3.3 \cdot 10^{12}$ W/cm^2 (see also Fig. 6.19 in the previous section). A significant change of the $sp_{2,3+}$ absorption line shape is observed.

according to their energy difference ΔE (see section 2.4). It is this phase difference which gives rise to the fast ~ 1.2 fs modulation in the absorption spectra (Fig. 6.19), as discussed in the previous section. In addition, this phase difference is also reflected in the modified asymmetric line shape of the absorption spectra.

In order to demonstrate this, Fig. 6.21 shows the measured absorption line shape across both the 2s2p and the $sp_{2,3+}$ state for a series of time delays τ, spaced by ~ 170 as. Especially across the $sp_{2,3+}$ state, a dramatic change of the line shape is observed. The initially asymmetric line shape turns over into a Lorentzian shape close to $\tau \approx 550$ as, reverses its shape close to $\tau \approx 890$ as and even resembles a window resonance (see section 2.7.1) close to $\tau \approx 1070$ as. Within the parameterization of the Fano formalism (see section 2.7.1), a continuous range of q-asymmetry parameter could be attributed to these line shapes.

This asymmtery parameter is given by (see Eq. 2.87)

$$q = \frac{\langle \mathrm{sp}_{2,3+} | \hat{\mathbf{T}} | 1\mathrm{s}^2 \rangle}{\pi V_E^* \langle 1\mathrm{s}\varepsilon\mathrm{p} | \hat{\mathbf{T}} | 1\mathrm{s}^2 \rangle}, \tag{6.8}$$

where $\hat{\mathbf{T}}$ now denotes the perturbative coupling with the XUV. In the following, a qualitative discussion is given how a change in the absorption line shape (i.e. the asymmetry parameter) can be connected to the above mentioned relative phase $\Delta\Phi$.

The considered coupling with the NIR in Fig. 6.21 occurs simultaneously or right after the excitation of the $sp_{2,3+}$ state. The absorption line in contrast retains its sharp features across all shown cases (variation of τ). Thus it can be deduced that the natural life time of the state is not significantly altered, which is ~ 80 fs (deduced from its width $\Gamma = 8.3$ meV [51]). Therefore, the laser pulse with duration 7 fs ($\ll 80$ fs) cannot influence the entire coarse of autoionization which is expressed by V_E. The direct continuum pathway, expressed by $\langle 1\mathrm{s}\varepsilon\mathrm{p} | \hat{\mathbf{T}} | 1\mathrm{s}^2 \rangle$, is happening on the time scale of the XUV excitation. Having ~ 40 eV kinetic energy (the $N = 1$ threshold is located at 24.6 eV) the direct electron is leaving the atom with relatively high momentum (crossing the $\sim 2 \cdot 3^2 = 18$ Bohr diameter of the $n = 3$ shell in ~ 250 as) and can thus also not effectively influence the whole

coarse of autoionization which is expressed in Eq. (2.87). The only remaining matrix element involves the decaying bound state $sp_{2,3+}$. It can thus be deduced that a time-delay dependent NIR-induced modification of the population amplitude or phase of this state does affect the asymmetry of the absorption line shape. It is the coherent dipole emission (characterized by its amplitude, phase and life time) of the bound state with respect to the ground state which gives rise to the sharp feature in the absorption spectrum—in analogy to the Lorentzian line shape of a decaying bound state without a continuum as discussed in section 2.8.

Now how can the bound state $sp_{2,3+}$ acquire this phase $\Delta\Phi$? For the cases shown in Fig. 6.21, the NIR laser pulse couples the two 2s2p and $sp_{2,3+}$ states right after their excitation. Originating from the strongest 2s2p, a significant amount of population is transfered into the $sp_{2,3+}$ due to strong coupling (evidenced by the Autler-Townes splitting, i.e. Rabi cycling occurs). Being more weakly excited, it is now assumed that this transferred population dominates the dynamics of the $sp_{2,3+}$ state. The phase of the state is changed by $\Delta\Phi$ as compared to its initial excitation with the XUV, which is imprinted into the interfering dipole emission during the whole natural decay within ~ 80 fs.

With these considerations, for instance a relative phase $\Delta\Phi = \pi$ would negate q in Eq. 6.8. Considering the parametrization of the absorption line shape (see Eq. 2.86 in section 2.7.1)

$$\frac{\left|q + \frac{E-E_\mathrm{r}}{\Gamma/2}\right|^2}{1 + \left(\frac{E-E_\mathrm{r}}{\Gamma/2}\right)^2}, \tag{6.9}$$

a negation of q would mirror the line shape with respect to the resonance energy E_r. This is however not exactly the case in Fig. 6.7, where a mirrored line shape can be connected to a relative phase $\Delta\Phi \gtrsim \pi$. Note that the shown progression of equidistant $\Delta\tau \approx 170$ as in delay is directly proportional to the relative phase $\Delta\Phi$ (see Eq. 6.7). The reason for this is rooted in the inapplicability of the q-parameter as given in Eq. 6.8, because it was derived within a completely time-independent treatment (see section 2.7.1) which does not distinguish between the excitation step and the subsequent dipole emission, as it is however the case in the here presented experiments.

A rigorous treatment of the time-dependent evolution of such a resonance can unfortunately not be given at the moment. Available time-dependent theories (see section 6.1) so far only employ the process of autoionization to calculate photo-electron spectra [192] or give scattering amplitudes [185]. Theories on absorption [198] appeared very recently, however could not yet be applied within the scope of this work. At the current stage, the experimental observation of significant changes across the absorption profile alone shall serve as a motivation to interpret the process of autoionization as an intrinsic quantum interferometer, while it is left for future work to present an analytical connection between the imprinted phase $\Delta\Phi$ on the state, and the corresponding change in the absorption line shape.

Looking closely at Fig. 6.21 another peculiarity can be found. The periodicity in the changing $sp_{2,3+}$ absorption line shape seems to be in between 1.20 and 1.37 fs. The energy difference $\Delta E = 3.51$ eV between the two states exactly corresponds to 1.18 fs. Indeed, also in Fig. 6.19c) in the previous section, the Fourier amplitude of the two-photon

coupling appears slightly but observably below the diagonal contribution. This is not observed in the simulated spectra in subfigure d), where the maximum is appearing exactly on the diagonal. In contrast, the two-photon contribution across the 2s2p state is appearing exactly on the diagonal of slope -1, both in the experiment and in the simulation. Also in Fig. 6.21, the periodicity of the changing 2s2p profile can be more closely related to 1.18 fs, in deviation to the $sp_{2,3+}$ periodicity below. A Gaussian fit to the two-photon contributions in the Fourier amplitude in Fig. 6.19c) yields

$$\hbar\Delta\omega_a = (3.51 \pm 0.18)\ \text{eV} \tag{6.10}$$

for the 2s2p, and

$$\hbar\Delta\omega_c = (3.36 \pm 0.18)\ \text{eV} \tag{6.11}$$

for the $sp_{2,3+}$ state. The error denotes the standard deviation. Only $\hbar\Delta\omega_a$ perfectly agrees with the energy difference ΔE between the two states. $\hbar\Delta\omega_c$ still agrees within the Gaussian standard deviation but appears systematically lower. The value of $\hbar\Delta\omega_c$ corresponds to a periodicity of 1.23 fs.

The reason for this deviation can be found in Fig. 6.19a) in the previous section. In addition to the fast two-photon modulation, the line shape of the $sp_{2,3+}$ state seems inverted. This is also the case for the higher excited states $sp_{2,n+}$ ($n \geq 4$). Also in Fig. 6.21 the asymmetry profile of the $sp_{2,3+}$ seems reversed when e.g. comparing the $\tau \approx 210$ as to the undisturbed profile of Fig. 6.8 in section 6.3. The closest agreement with the natural profile occurs at $\tau \approx 900$ as, which is however strongly suppressed.

To further investigate this phenomenon, the NIR intensity, which thus far was fixed at $3.3 \cdot 10^{12}$ W/cm^2, is now continuously changed using the iris aperture (see section 6.2). In total 33 different NIR intensities were set, where also the time-delay was scanned each over the full range, thus creating a full three-dimensional data set. The *in situ* calibration of the NIR intensity was discussed in section 6.6.

Fig. 6.22 shows a selection of different absorption spectra for NIR peak intensities ranging between 0.0 and $4.5{\cdot}10^{12}$ W/cm^2. A significant change in the absorption line shape for all states can be observed. The structure across the lowest 2s2p state is the formation of an Autler-Townes doublet (involving the 2s2p and the "$2p^2 - \gamma$") and even the appearance of the "$sp_{2,3+} - 2\gamma$" for higher intensities $\gtrsim 3.0 \cdot 10^{12}$ W/cm^2. This has been explained previously (see sections 6.3 and 6.6). In [179], the formation of the 2s2p–$2p^2$ Autler-Townes doublet alone was discussed along with the effect of electromagnetically induced transparency (EIT, see e.g. [180] for a review, where reduced absorption is achieved due to destructive interference of different transitions). A small hint for this effect is also present in the here observed spectra, as the absorption minimum, which is formed between the Autler-Townes doublet, is clearly decreasing between intensities 1.0 and $2.0{\cdot}10^{12}$ W/cm^2. A more detailed investigation on the systematics of the low-pass Fourier data analysis (see section 6.3) are however needed in order to justify this observation. This is the reason why ΔOD is shown rather than OD.

The absorption line shape across the higher excited $sp_{2,n+}$ ($n \geq 3$) states also changes as the NIR intensity is varied. They do not move in energy position as in the case of an Autler-Townes effect. Instead, their asymmetry parameter q changes as discussed above for the sub-cycle time-delay dependent absorption profiles in Fig. 6.21. Between NIR

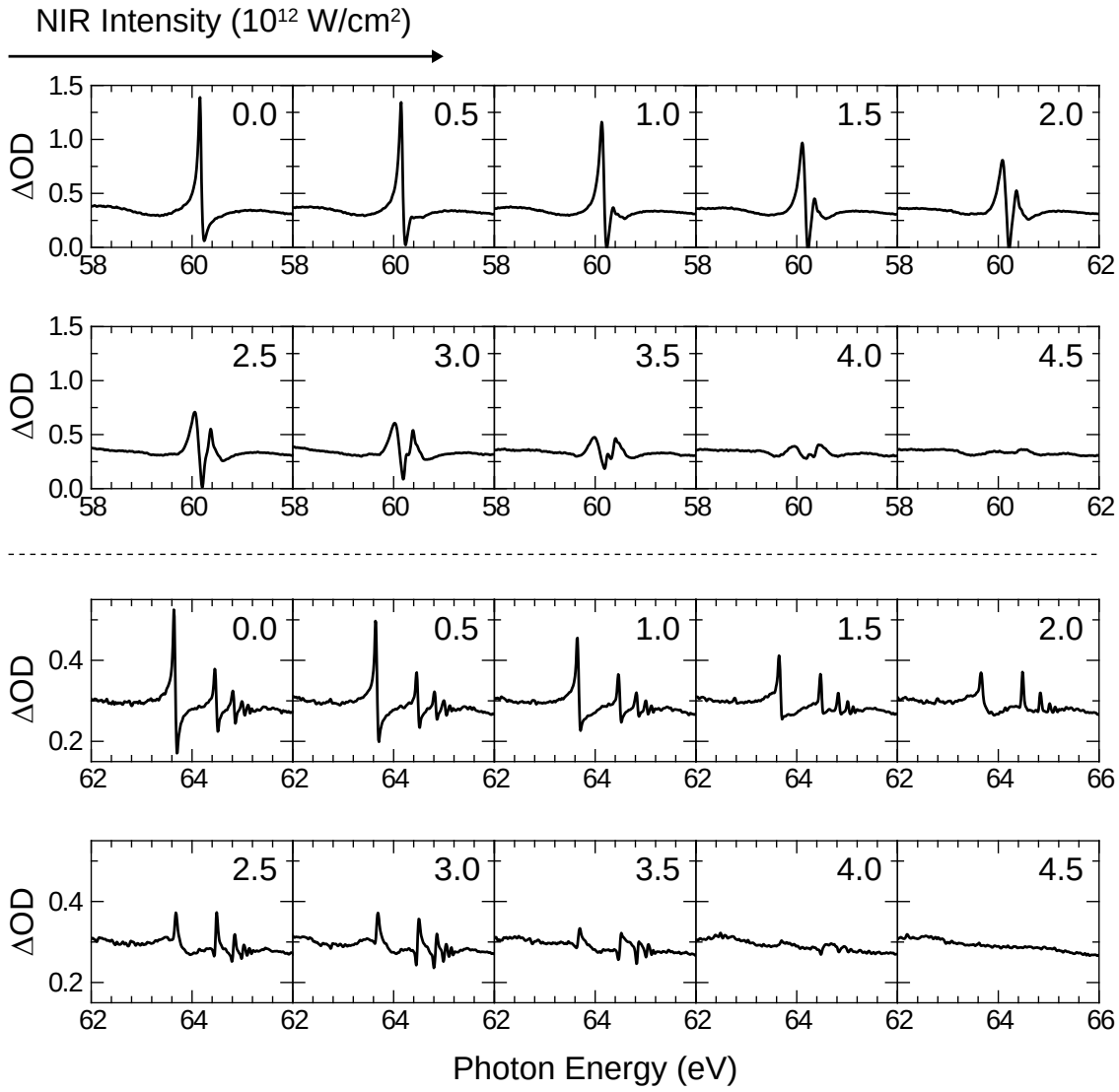

Figure 6.22: Experimentally measured absorption spectra for different NIR peak intensities. The measured spectra were averaged over two modulation periods ~ 2.4 fs, centered around $\tau \sim +5$ fs, where the Autler-Townes splitting as a function of time-delay is maximum (see Fig. 6.19 in section 6.7. The two topmost rows show the absorption line shape across the 2s2p state, where the formation of the Autler-Townes doublet can be followed. The calibrated NIR intensity is noted in each plot. The two lower sets of panels show measured absorption spectra across all higher states. A significant change in the line shape for the different NIR intensities can be observed from which state-resolved phase information can be extracted.

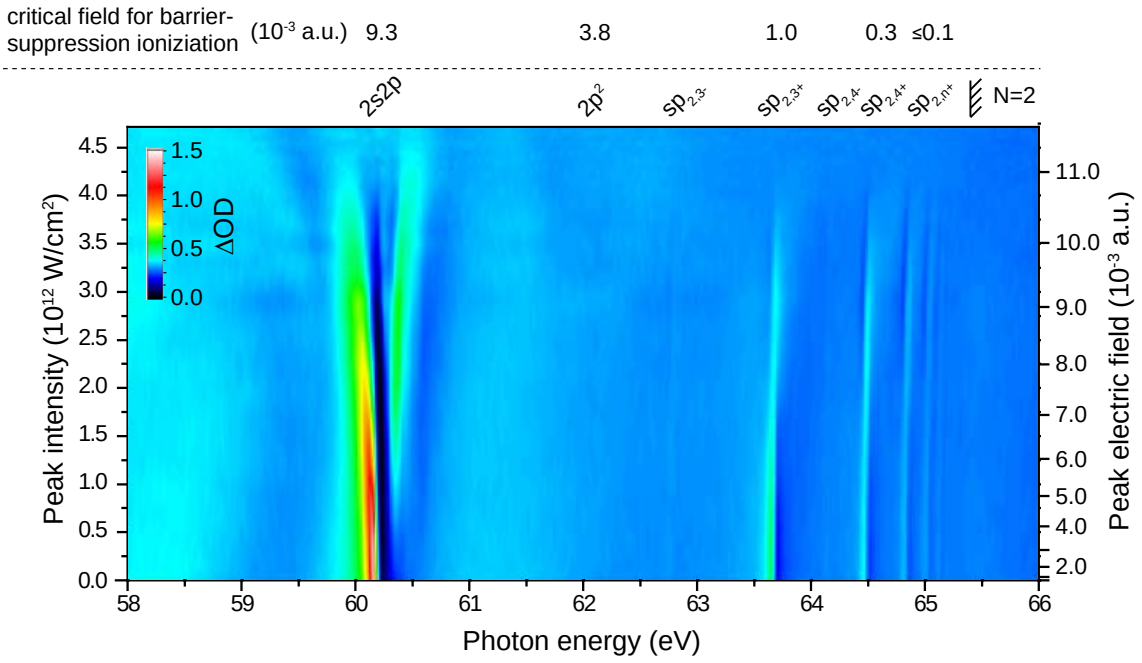

Figure 6.23: Absorption line shape across all observed doubly-excited states plotted vs. the NIR intensity. The time-delay configuration is as noted in Fig. 6.22. In total, absorption spectra for 33 different NIR intensities were experimentally recorded, calibrated as described in section 6.6, where a spline interpolation between these values is shown. A continuous transition from the perturbative (close to zero NIR field strength) to the strong-coupling regime is shown. The critical field strength for barrier-suppression ionization into the $N = 2$ continuum is indicated for various states. All states resist ionization but do change their line shape. All $\mathrm{sp}_{2,n+}$ ($n \geq 3$) states disappear almost simultaneously for NIR intensity $\gtrsim 4.0 \cdot 10^{12}$ W/cm^2.

intensity 2.5 and $3.5{\cdot}10^{12}$ W/cm^2, the profile of all states reverses in shape as compared with the zero intensity case. For $2.0{\cdot}10^{12}$ W/cm^2 Lorentzian absorption peaks are apparent while for $4.0{\cdot}10^{12}$ W/cm^2, window resonances can be attributed, just before disappearing at $4.5{\cdot}10^{12}$ W/cm^2. This behaviour is also revealed in a continuous two-dimensional plot in Fig. 6.23.

Fig. 6.23 shows the continuous transition from the perturbative (close to zero) to the strong-coupling regime (as confirmed by the observed Autler-Townes splitting). All states are observed to resist barrier suppression ionization (BSI, see section 2.2.1) into the $N = 2$ continuum, as they are clearly observed as stable and sharp resonance lines significantly above the corresponding critical field strengths. These were calculated using Eq. (2.36) of section 2.2.1. For the ionization potential, the respective energy distance of the states to the $N = 2$ continuum at 65.40 eV was considered. In addition, all states seem to abruptly disappear for NIR intensities $\gtrsim 4.0 \cdot 10^{12}$ W/cm^2. This resistance to laser-induced ionization seems particularly counterintuitive considering the autoionizing nature of all states. In [179], the experimental data could only be explained after taking the tunnel ionization of the $2p^2$ into the $N = 2$ continuum into account. This was also confirmed in subsequent theoretical analysis [183, 198] (see also section 6.1). At first glance this seems in contradiction to the results presented here, as tunneling-ionization (or multi-photon ionization

which would be more suitable for the here described scenario) even happens for field strengths below the BSI limits (see section 2.2.1). An explanation for this discrepancy is most likely the pulse duration, as in [179] a much longer 42 fs FWHM duration NIR pulse was used. The longer interaction thus has a more severe influence on the states in terms of ionization.

In addition to this resilience against ionization the asymmetric absorption line shape is again observed to change as previously discussed in Fig. 6.22. The explanation for this behaviour must again be a change in the phase of the decaying states, as the NIR is interacting just for a brief time, shortly after their excitation ($\tau \sim +5$ fs). It is postulated here that this phase results from the coherent coupling of all these states with the $N = 2$ continuum. This can be explained as follows: Within single electron models, states close to the ionization threshold can be treated as quasi-free particles. A free electron does not absorb energy from an interacting laser field. However, it interacts with the electric field and transiently acquires additional kinetic energy, the so-called ponderomotive energy (or potential) U_p (see Eq. (2.28) in section 2.2). After the laser pulse is over, the electron again is at rest (no energy is absorbed from the laser field), however, due to the transient interaction, the electron undergoes a phase-shift $\Delta\phi$, the so-called ponderomotive phase which is given by

$$\Delta\phi = \frac{1}{\hbar}\int_{-\infty}^{+\infty}\frac{1}{2}m_e v^2\left(t'\right)\mathrm{d}t' \tag{6.12}$$

with $v(t) = -\frac{e}{m_e}\int_{-\infty}^{t} E\left(t'\right)\mathrm{d}t'$, the velocity of the electrons. Now it should be recalled that all $sp_{2,n+}$ ($n \geq 3$) are of course two-electron states, classified with an inner electron in $N = 2$ and an outer electron occupying the state n (see section 2.9). It is thus assumed that only one, the outer electron, is experiencing this ponderomotive phase-shift $\Delta\phi$ given by Eq. (6.12). However, as the line shape is still resolved, the correlation between the two electrons is not destroyed during this interaction, the phase is then imprinted onto the whole entangled (in a superposition of s and p orbitals) two-electron state.

Considering a 7 fs FWHM Gaussian pulse duration, Eq. (6.12) yields $\Delta\phi = \pi$ for a peak intensity $\sim 5{\cdot}10^{12}$ W/cm^2. This is in agreement with the experimental observation, as above $\sim 3{\cdot}10^{12}$ W/cm^2 a characteristic inversion of the line shape can be observed. A more detailed comparison however also here is in need of a direct analytical connection of the absorption line shape and the imprinted phase as discussed above for the sub-cycle time-delay-dependent variation of the line shape in Fig. 6.21. Nevertheless, the model of an imprinted ponderomotive phase predicts the observed characteristic phase-(i.e. line shape)-changes in the observed intensity regime.

It can be seen in Figs. 6.22 and 6.23 that the line shape of the different states changes differently as a function of intensity. The state-resolved access can therefore be utilized to test different (and also more advanced) theoretical descriptions. Such theories will involve the careful investigation of the transition between effective single-electron to fully-correlated two-electron dynamics. Different approaches can be analyzed and tested, involving quasi-classical descriptions for the highest states, where a large phase-space of different states is available, as well as fully-correlated quantum-mechanical descriptions for the lowest states. With simultaneous access to both such types of states, and espe-

cially a mixing of both scenarios across the $sp_{2,3+}$ state, the very interesting transition regime between these two theoretical approaches is accessible. From Fig. 6.23 it can even be noted that the very faintly visible $sp_{2,3-}$ of the weaker series at 62.76 eV is also observed changing its shape. Thus a whole set of even different (correlated) series of excited two-electron states can be accessed in comparison for this scheme.

To finally give a numerical evidence that the above considered model of a ponderomotive phase is a reasonable assumption, the numerical simulation (see section 6.4) was employed, where, by contrast, only one of the three autoionizing states, the $sp_{2,3+}$ state, was considered. To mimic the ponderomotive coupling to the $N = 2$ continuum, the instantaneous ponderomotive phase $\Delta\phi \cdot dt$ was multiplied onto the state coefficient for each time step. As a result, the simulated absorption line shape (shown in the middle panels of Fig. 6.24) can be compared to the experimental data for a similar intensity (shown in the left panels of Fig. 6.24). The agreement is remarkable, as now the slower dynamical modifications underlying the ~ 1.2 fs modulation in the experimental data are in good agreement to the simulated data. With this simulated coupling, also the Raman-like contributions can be reproduced, which are additionally observed for all higher ($n \geq 4$) states. This provides further evidence that coherent coupling to the $N = 2$ continuum indeed occurs.

Coming back to the above mentioned discrepancy in the average modulation energy $\hbar\Delta\omega_c$ of the $sp_{2,3+}$ it can finally be argued that the additional coupling to the $N = 2$ continuum imprints an additional phase $\Delta\phi$ which effectively delays the response which is induced by $\Delta\Phi$ (see Eq. (6.7)) where the latter is proportional to τ. In other words, the ponderomotively shifted $sp_{2,3+}$ state appears closer in energy to the 2s2p state, which effectively lowers the modulation frequency. This is indeed confirmed for measured data at lower NIR intensities (e.g. $1.5 \cdot 10^{12}$ W/cm^2, shown in the right panel Fig. 6.24). A weaker contribution of the ponderomotive phase $\Delta\phi$ (or alternatively a weaker ponderomotive shift in energy) of the sp_{23+} state is expected for a lower NIR intensity. As a consequence, the corresponding modulation peak in the Fourier spectrum moves up in energy, closer to the diagonal of slope 1. This is quantified to

$$\hbar\Delta\omega_c^{\text{L.Int.}} = (3.47 \pm 0.09)\ \text{eV} \tag{6.13}$$

for the NIR intensity $1.5 \cdot 10^{12}$ W/cm^2. The error again denotes the standard deviation of the Gaussian fit. Comparing this result with the above result (Eq. (6.11)) for a higher NIR intensity ($3.3 \cdot 10^{12}$ W/cm^2), a systematic increase towards the theoretical $\Delta E = 3.51$ eV value is observed. This corresponds to a systematic decrease of the modulation from $\tau_{\text{H.Int.}} = 1.23$ fs for higher intensities down to $\tau_{\text{L.Int.}} = 1.19$ fs for lower intensities, i.e. a wave-packet cycle-period change corresponding to only 40 attoseconds could be quantified. The direct quantification of the induced quantum-state-phase modification for all measured NIR intensities is subject of ongoing analysis.

6.9 Conclusion on time-resolved autoionization

In this work, the experimental access to intrinsically correlated—as opposed to induced correlations e.g. by laser-driven recollision [63]—two-electron dynamics was demon-

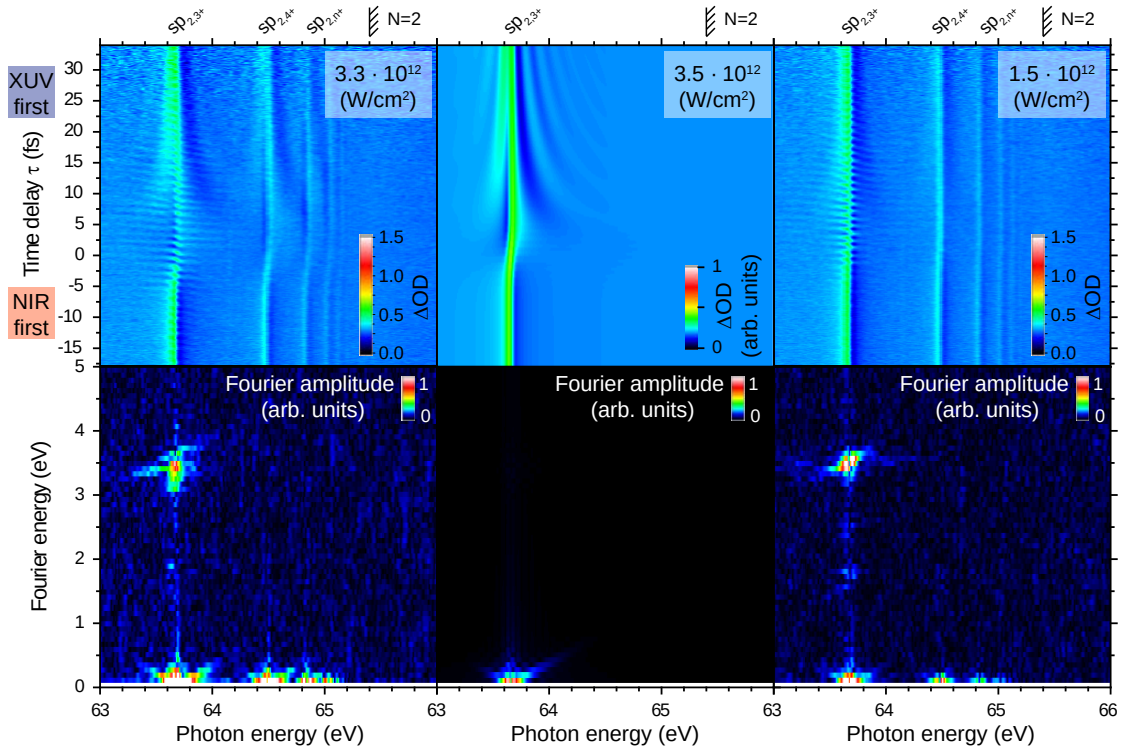

Figure 6.24: Comparison of the experimental absorption spectra as a function of time delay (for NIR intensity $3.3{\cdot}10^{12}$ W/cm^2) for the higher $\mathrm{sp}_{2,n+}$ ($n \geq 3$) states (left panels) with a numerical simulation of a single state ponderomotively coupled to the $N = 2$ continuum. (middle panels, the NIR intensity was $3.5 \cdot 10^{12}$ W/cm^2, see text for details). A qualitatively good agreement can be observed in comparison with the experimental data for a similar intensity. For a lower NIR intensity ($1.5 \cdot 10^{12}$ W/cm^2, right panels), the ponderomotive coupling is less pronounced. As a consequence, the Fourier analyzed modulation peak (shown in the bottom panels) moves up in energy as compared for higher intensities. See text for further details.

strated. A range of doubly excited states was observed below the $N = 2$ ionization threshold in helium. The availability of high spectral resolution (47 meV FWHM), realized with a home-built flat-field spectrograph based on a variable-line-space grating, allowed to distinguish between several excited states in the measured photo-absorption spectra. With observed $\mathrm{sp}_{2,n+}$ ($2 \leq n \leq 8$) and $\mathrm{sp}_{2,n}$ ($3 \leq n \leq 5$) states, in total 10 different correlated and entangled (consisting of s and p orbitals) two-electron states could be experimentally detected. These bound states (but of autoionizing nature) were accessed with XUV attosecond pulses. The NIR laser-induced coupling of these states to another bound state—the $2\mathrm{p}^2$—as well as to a continuum of states with effectively one single electron—the $N = 2$ continuum—was experimentally observed, quantified and discussed.

To investigate the couplings of these short-lived two-electron states (with life times ranging between 17 and $\gtrsim 100$ fs), a fully time-resolved transient-coupling scheme was developed and employed. Both the excitation with attosecond-pulsed XUV light and the coupling with a few-cycle ~ 7 fs duration NIR laser pulse is (much) shorter than the natural life time of the states. With a detector resolution on the order of their natural life-time width, state-resolved changes in their dynamics (initiated by the time-resolved coupling)

could be quantified in the transiently generated absorption spectra. Both the time-delayed position and the intensity of the NIR pulse was continuously changed, exploiting two dynamical parameters, to create a fully correlated three-dimensional spectroscopic data set.

To reveal the couplings, motivated by two-dimensional spectroscopy approaches previously developed in nonlinear optics, a Fourier analysis was employed which transfers the time-delay parameter into the energy domain. Doing so allowed to carefully distinguish and interpret different features in the transiently coupled absorption line shapes. As a result, so far unexplained features, which appeared in a recent theoretical treatment on a similar system [198], could be explained as Raman-like transition pathways. The analysis of the experimental data lead to the following main scientific results:

1. The experimental observation of a fully-correlated two-electron wave packet.
2. The coherent ponderomotive coupling of doubly-excited states to a single-ionization continuum was postulated and supported by experimental data.
3. The experimental observation of the strong coupling of three autoionizing states.

The two-electron wave packet was observed with a resonantly-enhanced (via the $2p^2$ state) coherent two-photon coupling between the lowest states of the $sp_{2,n+}$ ($^1P^o$) series, namely the 2s2p and the $sp_{2,3+}$. The modulation period of 1.18 fs was experimentally confirmed and observed as periodic changes (as a function of the NIR time delay) of the absorption signal across the 2s2p line shape. An Autler-Townes splitting between the 2s2p and the $2p^2$ states was observed, in agreement with earlier experiments [179]. In addition, the coupling of all three states (involving the $sp_{2,3+}$) could be verified. Thus, a strong coupling of in total three autoionizing states is experimentally observed. In contradiction to earlier findings [179, 183, 193, 198], ionization into the $N = 2$ continuum is not found to be significant for most of the considered NIR intensities, allowing to observe coupling up to relatively high intensities. An answer to this contradiction possibly includes the much shorter NIR pulse duration used in the presented experiments. A small hint for electromagnetically induced transparency in connection to the 2s2p–$2p^2$ Autler-Townes doublet was also given, as observed in [179].

The relevance of the single-electron $N = 2$ continuum in terms of a coherent coupling was not yet fully recognized in theory before. Only ionization was thus far considered, i.e. an incoherent loss mechanism. Within this work it could be demonstrated that coherent coupling with the $N = 2$ continuum plays a key role in order to explain the experimental data. The identification of this mechanism was possible with the spectrally-resolved and state-resolved detection of asymmetric Fano absorption profiles, which change both in dependence of time-delay and NIR intensity. The coupling, for the highest-excited $sp_{2,n+}$ states, was explained with a relatively simple model of a quasi-free single active electron: The outermost electron of the correlated two-electron state acquires a ponderomotive phase in the NIR laser field. This selective (only one electron) coupling interestingly does not destroy the correlation of the entangled two-electron states.

A very interesting mixture of couplings both to bound (autoionizing) states as well as to a single-electron continuum (of excited $N = 2$ ions) was observed for the $sp_{2,3+}$ state. As a

result, the continuum coupling imposes an additional phase $\Delta\phi$ on the $sp_{2,3+}$ state, on top of the phase $\Delta\Phi$ which is due to the coupling with the bound 2s2p state. Being observed as a function of the NIR time delay, this resulted in a slightly longer periodicity in the change of the absorption line shape of this state (by 50 attoseconds, 1.23 fs relative to the "theoretically expected" 1.18 fs). It was further demonstrated, that a lower NIR intensity, with less significant coupling to the $N = 2$ continuum, implies a retardation of only 10 attoseconds in periodicity (1.19 fs relative to the theoretical 1.18 fs wave-packet beating period), confirming the high interferometric stability in the built experimental apparatus. The two-dimensional analysis leading to this result is very similar (though qualitatively different) to the analysis of different energy pathways within two-dimensional spectroscopy techniques. These above obtained numbers also imply a high sensitivity on the detection of the ponderomotively induced phase, i.e. $2\pi \times 0.01/1.18 \approx 50$ mrad.

All experimental findings were confirmed with simultaneously performed home-built numerical simulations. Fully implemented in the time domain, including the autoionization process, they allow an intuitive access to the temporal evolution of the states.

To sum up, the demonstrated experimental observation of coherently-coupled two-electron states with access to their relative phases allows to carefully investigate their instantaneous response to laser electric fields, with tunably controlled peak field strengths all the way from the perturbative to the strong-coupling regime. This is realized most importantly *within a fraction* of the natural life time of the states, implying a deeper insight into correlated two-electron dynamics, which also play a key role in covalent bonds of molecular orbitals. In addition, the simultaneous access to a broad range of states was demonstrated, ranging from deeply-bound, to be treated fully quantum-mechanical, up to closely-lying higher-excited states, which are better understood from a quasi-classical perspective. Combined theoretical treatments which especially involve the transition regime between these two scenarios, to describe fully-correlated two-electron dynamics for the lower-lying states and single active electrons for the high-lying states, can be tested against the experimentally obtained data.

Chapter 7

Conclusion

The general theme throughout this thesis is the interferometric observation, understanding and control of ultrafast electron quantum dynamics. It was proposed how the sub-cycle nature of strong laser fields can be used to investigate the couplings between different electron quantum states, not being limited in access by selection rules. Electron quantum paths driven by strong laser fields were directly retrieved and understood from experimentally obtained data on a sub-cycle attosecond time scale. Coupling dynamics across correlated two-electron states in helium were experimentally measured and modeled, enabled by phase-resolved interferometric access.

From a technical point of view, it was the multi-dimensional interferometric measurement and data analysis in the temporal (attosecond) and spectral (meV) domain which enabled this experimental advance, made possible with a home-built apparatus of both high interferometric stability (10 as) and high spectral resolution (47 meV FWHM). The interferometric approach was motivated from successfully applied multi-dimensional spectroscopy techniques in the femtosecond domain, involving the Fourier analysis to create two-dimensional maps of corresponding energy or time domains. It was shown how these interferometric measurement schemes are understood as time-resolved experiments taking data as a function of several dynamical parameters of ultrashort laser pulses. These are their temporal delay to an interferometrically linked additional pulse, the carrier-envelope phase and the intensity. Driven by the success of the demonstrated techniques, further combinations of these parameters are conceivable in the future.

Across all investigated topics, the phase-resolved interference of electron quantum states of different nature was analyzed. This thesis involved the intrinsic interference of quasi-bound states, i.e. with degenerate bound and continuum parts, the process of autoionization, here fully accessed in the time-domain. It also covered the laser-induced interference between the bound parts of different such autoionizing states. Coupling these states to a single-electron continuum yielded an interference of two-electron states with single-electron continua. Finally also the interference of solely free electron states was investigated, driven with sub-cycle resolution in strong laser fields. This involved both the numerical simulation of their direct interference in the photoelectron spectra, as well as the experimentally-obtained indirect interference encoded in HHG spectra. All these processes naturally give access to the relative phase between the interfering states, thus

directly encoding the dynamics which are involved in a superposition of these states.

Scientifically, the results in chapter 4 propose how phase-resolved access to different electron quantum states can be gained in strong fields. Without influencing the observation by the strong fields, their field-free evolution can be accessed. In principle any state can be optically accessed, both dipole-allowed *and* non dipole-allowed from the ground state, and the excitation is not limited to the bandwidth of the laser pulses, both owing to the highly-nonlinear interaction. The results in chapter 5 demonstrate how experimentally observed and understood sub-cycle dynamics of free single-electron trajectories can be controlled with sub-100-as temporal resolution due to CEP stable (200 mrad) few-cycle laser pulses. The analysis was performed in the spirit of two-dimensional spectroscopy which allowed to disentangle temporally overlapping contributions and yielded an intuitive model of a temporal-triple-slit experiment. Across two-electron states in helium in chapter 6, qualitatively different couplings—both to another two-electron bound state, as well as to an effective single-electron continuum of states—could be disentangled. Both the multi-dimensional analysis technique as well as the home-built numerical simulation helped in this understanding.

All these examples, both numerical and experimental, involved different aspects of strong-field physics. Limits of weak perturbative and strong laser fields were involved, ranging between below 10^{12} W/cm^2 to above 10^{14} W/cm^2 of peak intensities. The underlying observed electron dynamics ranged from a deeply-correlated fully quantum-mechanical regime (coupling of discrete states), involving two electrons, up to a quasi-classical description of effectively one electron (involving quasi-classical phase shifts). For instance it was the transition from weak to strong laser fields which allowed the identification of a mixture of couplings across the $sp_{2,3+}$ state in helium in chapter 6. All these different regimes (laser fields and electron dynamics) were combined in home-built numerical simulations to uncover the mechanisms.

Looking out into the future, these results can be considered a starting point for the investigation and control of covalent bonds in molecular orbitals on an electronic level. These bonds also consist of two correlated electrons. Within the course of any chemical reaction, the correlated motion of these electrons is the most fundamental ingredient which eventually may determine the respective outcome. In such cases, the process can be described with—possibly short lived—transition states. Using the results from above, if such states are interrogated with a very short laser pulse (much shorter than their respective life time), a precise phase-control, governing the orbital shape of superpositions of these states could be achieved, with negligible destructive influence such as ionization. This may steer the subsequent—possibly much longer—natural time evolution, which eventually would determine the outcome of a chemical reaction at $t \to +\infty$. These would be decisive steps to fundamentally control chemistry from the bottom up, by spatio-temporally directing the electrons in molecules.

To sum up, using ultrashort laser pulses and fully employing their respective control knobs, such as the CEP, the intensity or an interferometrically stable temporal delay to another pulse in a multidimensional manner, and combining all this with the intrinsic (natural) spectral or temporal features of the investigated system, a deeper insight into small yet complex quantum systems has been and will continue to be gained along with

demonstrated and promising schemes of their control.

Appendix A

Atomic units

Atomic units are used in this thesis. Especially when numerical simulations are performed, these units are very useful to decrease the amount of complexity within the numerical treatment and reduce the involved formulas to only relevant quantities. In addition, these units allow for an easy comparison of different quantities. Using atomic units, Planck's reduced constant $\hbar$, the electron mass m_e, the elementary charge e, and Coulomb's constant $(4\pi\varepsilon_0)^{-1}$ of the electric force are all set to unity[1] ($\hbar = m_\mathrm{e} = e = (4\pi\varepsilon_0)^{-1} = 1$). With this convention, for instance the energy and frequency of a photon are related via $E = \omega$, or the energy and momentum of an electron are connected via $E = p^2/2$. A selected list of conversion factors between atomic units and conventional SI units is given in the table below.

Table A.1: Physical quantities expressed in atomic units, with data taken from [206] which was updated in 2010.

atomic unit of	SI value
energy	$(27.211\,385\,05 \pm 0.000\,000\,60)$ eV
time	$(24.188\,843\,265\,02 \pm 0.000\,000\,000\,12) \cdot 10^{-18}$ s
length	$(0.529\,177\,210\,92 \pm 0.000\,000\,000\,17)$ Å
electric field strength	$(5.142\,206\,52 \pm 0.000\,000\,11) \cdot 10^{9}$ V/cm
intensity	$(3.509\,445\,21 \pm 0.000\,000\,15) \cdot 10^{16}$ W/cm^2

It should be noted here, that the atomic unit of intensity is *not* defined as the atomic unit of energy per unit time and area, but is more straightforwardly related to the atomic unit of the electric field strength via $I_\mathrm{a.u.} = 1/2 \cdot \varepsilon_0 c \mathscr{E}^2_\mathrm{a.u.}$. This allows for an easy conversion between atomic units of the electric field strength naturally used in computational treatments and SI units of the laser intensity which is more straightforwardly connected to experimental measurements. For example $\mathscr{E} = 0.1$ a.u. then leads to $I = 0.1^2 \times I_\mathrm{a.u.} = 3.509... \cdot 10^{14}$ W/cm^2. The speed of light in atomic units is just the inverse of the fine structure constant $c = \alpha^{-1}$, where

$$\alpha^{-1} = 137.035999074 \pm 0.000000044.$$

[1] It should be noted that not the electron charge but the elementary charge is set to unity. Thus in atomic units the electron charge is -1.

Bibliography

[1] J. B. J. Fourier.
Théorie analytique de la chaleur.
Firmin Didot, Paris (1822).

[2] J.-C. Diels and W. Rudolph.
Ultrashort Laser Pulse Phenomena.
Second edition. Academic Press (2006).

[3] http://refractiveindex.info/.

[4] P. E. Ciddor.
Refractive index of air: new equations for the visible and near infrared.
Appl. Opt. **35**, 1566–1573 (1996).

[5] F. Lindner, G. G. Paulus, H. Walther, A. Baltuška, E. Goulielmakis, M. Lezius, and F. Krausz.
Gouy Phase Shift for Few-Cycle Laser Pulses.
Phys. Rev. Lett. **92**, 113001 (2004).

[6] A. E. Siegman.
Lasers.
University Science Books, Sausalito (1986).

[7] R. Szipöcs, K. Ferencz, C. Spielmann, and F. Krausz.
Chirped multilayer coatings for broadband dispersion control in femtosecond lasers.
Opt. Lett. **19**, 201–203 (1994).

[8] T. Brabec (Ed.).
Strong field laser physics.
Springer series in optical sciences. Springer (2008).

[9] http://www.nist.gov/pml/data/periodic.cfm.

[10] J. Javanainen, J. H. Eberly, and Q. Su.
Numerical simulations of multiphoton ionization and above-threshold electron spectra.
Phys. Rev. A **38**, 3430–3446 (1988).

[11] L. V. Keldysh.
Ionization in field of a strong electromagnetic wave.
Sov. Phys. JETP **20**, 1307–& (1965).

[12] A. M. Perelomov, V. S. Popov, and M. V. Terent'ev.
Ionization of atoms in an alternating electric field.
Sov. Phys. JETP **23**, 924–& (1966).

[13] V. S. Popov.
Tunnel and multiphoton ionization of atoms and ions in a strong laser field (Keldysh theory).
Phys. Usp. **47**, 855 (2004).

[14] M. V. Ammosov, N. B. Delone, and V. P. Krainov.
Tunnel ionization of complex atoms and of atomic ions in an alternating electromagnetic field.
Sov. Phys. JETP **64**, 1191–1194 (1986).

[15] S. Augst, D. D. Meyerhofer, D. Strickland, and S. L. Chint.
Laser ionization of noble gases by Coulomb-barrier suppression.
J. Opt. Soc. Am. B **8**, 858–867 (1991).

[16] G. L. Yudin and M. Y. Ivanov.
Nonadiabatic tunnel ionization: Looking inside a laser cycle.
Phys. Rev. A **64**, 013409 (2001).

[17] P. Agostini and L. F. DiMauro.
The physics of attosecond light pulses.
Rep. Prog. Phys. **67**, 813 (2004).

[18] F. Krausz and M. Ivanov.
Attosecond physics.
Rev. Mod. Phys. **81**, 163–234 (2009).

[19] P. B. Corkum.
Plasma perspective on strong field multiphoton ionization.
Phys. Rev. Lett. **71**, 1994–1997 (1993).

[20] A. Mcpherson, G. Gibson, H. Jara, U. Johann, T. S. Luk, I. A. Mcintyre, K. Boyer, and C. K. Rhodes.
Studies of Multiphoton Production of Vacuum Ultraviolet-Radiation in the Rare-Gases.
J. Opt. Soc. Am. B **4**, 595–601 (1987).

[21] M. Lewenstein, P. Balcou, M. Y. Ivanov, A. L'Huillier, and P. B. Corkum.
Theory of High-Harmonic Generation by Low-Frequency Laser Fields.
Phys. Rev. A **49**, 2117–2132 (1994).

[22] M. C. Kohler, C. Ott, P. Raith, R. Heck, I. Schlegel, C. H. Keitel, and T. Pfeifer.
High Harmonic Generation Via Continuum Wave-Packet Interference.
Phys. Rev. Lett. **105**, 203902 (2010).

[23] M. Kohler.
Frontiers of High-Harmonic Generation.
PhD Thesis, Universität Heidelberg (2011).

[24] P. Salières, B. Carré, L. Le Déroff, F. Grasbon, G. G. Paulus, H. Walther, R. Kopold, W. Becker, D. B. Milošević, A. Sanpera, and M. Lewenstein.
Feynman's Path-Integral Approach for Intense-Laser-Atom Interactions.
Science **292**, 902–905 (2001).

[25] G. Sansone, C. Vozzi, S. Stagira, and M. Nisoli.
Nonadiabatic quantum path analysis of high-order harmonic generation: Role of the carrier-envelope phase on short and long paths.
Phys. Rev. A **70**, 013411 (2004).

[26] V. Wong and I. A. Walmsley.
Linear filter analysis of methods for ultrashort-pulse-shape measurements.
J. Opt. Soc. Am. B **12**, 1491–1499 (1995).

[27] C. Iaconis and I. Walmsley.
Spectral phase interferometry for direct electric-field reconstruction of ultrashort optical pulses.
Opt. Lett. **23**, 792–794 (1998).

[28] L. Lepetit, G. Chériaux, and M. Joffre.
Linear techniques of phase measurement by femtosecond spectral interferometry for applications in spectroscopy.
J. Opt. Soc. Am. B **12**, 2467–2474 (1995).

[29] E. Tokunaga, A. Terasaki, and T. Kobayashi.
Frequency-domain interferometer for femtosecond time-resolved phase spectroscopy.
Opt. Lett. **17**, 1131–1133 (1992).

[30] J. P. Geindre, P. Audebert, A. Rousse, F. Falliès, J. C. Gauthier, A. Mysyrowicz, A. D. Santos, G. Hamoniaux, and A. Antonetti.
Frequency-domain interferometer for measuring the phase and amplitude of a femtosecond pulse probing a laser-produced plasma.
Opt. Lett. **19**, 1997–1999 (1994).

[31] V. May, O. Kuehn, and M. Schreiber.
Density matrix description of ultrafast dissipative wave packet dynamics.
J. Phys. Chem. **97**, 12591–12595 (1993).

[32] J. J. Sakurai.
Modern Quantum Mechanics.
revised edition. Addison Wesley (1994).

[33] C. Cohen-Tannoudji, B. Diu, and F. Laloe.
Quantum Mechanics.
Second edition. Wiley-Interscience (2006).

[34] B. Bransden and C. Joachain.
Physics of Atoms and Molecules.
Pearson Education, second edition. Prentice Hall (2003).

[35] I. I. Rabi.
Space Quantization in a Gyrating Magnetic Field.
Phys. Rev. **51**, 652–654 (1937).

[36] S. H. Autler and C. H. Townes.
Stark Effect in Rapidly Varying Fields.
Phys. Rev. **100**, 703–722 (1955).

[37] P. Lambropoulos and P. Zoller.
Autoionizing states in strong laser fields.
Phys. Rev. A **24**, 379–397 (1981).

[38] U. Fano.
Effects of Configuration Interaction on Intensities and Phase Shifts.
Phys. Rev. **124**, 1866–1878 (1961).

[39] H. Bachau, P. Lambropoulos, and R. Shakeshaft.
Theory of laser-induced transitions between autoionizing states of He.
Phys. Rev. A **34**, 4785–4792 (1986).

[40] L. B. Madsen, P. Schlagheck, and P. Lambropoulos.
Laser-Induced Transitions between Triply Excited Hollow States.
Phys. Rev. Lett. **85**, 42–45 (2000).

[41] L. B. Madsen, P. Schlagheck, and P. Lambropoulos.
Laser-induced transitions between triply excited hollow states.
Phys. Rev. A **62**, 062719 (2000).

[42] L. B. Madsen and P. Lambropoulos.
Line shapes in photoexcitation of triply excited hollow states.
J. Phys. B **34**, 1855 (2001).

[43] S. I. Themelis, P. Lambropoulos, and M. Meyer.
Ionization dynamics in double resonance involving autoionizing states in helium: the effect of pulse shapes.
J. Phys. B **37**, 4281 (2004).

[44] P. Lambropoulos, P. Maragakis, and J. Zhang.
Two-electron atoms in strong fields.
Phys. Rep. **305**, 203 – 293 (1998).

[45] R. W. Boyd.
Nonlinear Optics.
Second edition. Academic Press, San Diego (2003).

[46] C. Rullière (Ed.).
Femtosecond Laser Pulses: Principles and Experiments.
Second edition. Springer, New York (2005).

[47] U. Fano.
Correlations of two excited electrons.
Rep. Prog. Phys. **46**, 97 (1983).

[48] H. Klar.
Correlation in single- and multiphoton processes.
In F. Ehlotzky (Ed.), *Fundamentals of Laser Interactions*, volume 229 of *Lecture Notes in Physics*, pp. 149–160. Springer Berlin / Heidelberg (1985).
10.1007/3-540-15640-2_43.

[49] R. P. Madden and K. Codling.
New Autoionizing Atomic Energy Levels in He, Ne, and Ar.
Phys. Rev. Lett. **10**, 516–518 (1963).

[50] J. W. Cooper, U. Fano, and F. Prats.
Classification of Two-Electron Excitation Levels of Helium.
Phys. Rev. Lett. **10**, 518–521 (1963).

[51] K. Schulz, G. Kaindl, M. Domke, J. D. Bozek, P. A. Heimann, A. S. Schlachter, and J. M. Rost.
Observation of New Rydberg Series and Resonances in Doubly Excited Helium at Ultrahigh Resolution.
Phys. Rev. Lett. **77**, 3086–3089 (1996).

[52] M. Domke, K. Schulz, G. Remmers, G. Kaindl, and D. Wintgen.
High-resolution study of $^1P^o$ double-excitation states in helium.
Phys. Rev. A **53**, 1424–1438 (1996).

[53] D. R. Herrick and O. Sinanoğlu.
Comparison of doubly-excited helium energy levels, isoelectronic series, autoionization lifetimes, and group-theoretical configuration-mixing predictions with large-configuration-interaction calculations and experimental spectra.
Phys. Rev. A **11**, 97–110 (1975).

[54] C. D. Lin.
Classification of Doubly Excited States of Two-Electron Atoms.
Phys. Rev. Lett. **51**, 1348–1351 (1983).

[55] D. R. Herrick.
New Symmetry Properties of Atoms and Molecules, volume 52, pp. 1–115.
John Wiley & Sons, Inc. (1983).

[56] C. D. Lin.
Hyperspherical coordinate approach to atomic and other Coulombic three-body systems.
Phys. Rep. **257**, 1 – 83 (1995).

[57] G. Tanner, K. Richter, and J.-M. Rost.
The theory of two-electron atoms: between ground state and complete fragmentation.
Rev. Mod. Phys. **72**, 497–544 (2000).

[58] J. Madroñero and A. Buchleitner.
Ab initio quantum approach to planar helium under periodic driving.
Phys. Rev. A **77**, 053402 (2008).

[59] J. Eiglsperger, B. Piraux, and J. Madroñero.
Spectral representation of the three-body Coulomb problem: Perspectives for highly doubly excited states of helium.

Phys. Rev. A **80**, 022511 (2009).

[60] J. E. Thoma and R. R. Jones.
Nonexponential Decay of Autoionizing Shock Wave Packets.
Phys. Rev. Lett. **83**, 516–519 (1999).

[61] S. N. Pisharody and R. R. Jones.
Probing Two-Electron Dynamics of an Atom.
Science **303**, 813–815 (2004).

[62] D. N. Fittinghoff, P. R. Bolton, B. Chang, and K. C. Kulander.
Observation of nonsequential double ionization of helium with optical tunneling.
Phys. Rev. Lett. **69**, 2642–2645 (1992).

[63] B. Walker, B. Sheehy, L. F. DiMauro, P. Agostini, K. J. Schafer, and K. C. Kulander.
Precision Measurement of Strong Field Double Ionization of Helium.
Phys. Rev. Lett. **73**, 1227–1230 (1994).

[64] J. B. Watson, A. Sanpera, D. G. Lappas, P. L. Knight, and K. Burnett.
Nonsequential Double Ionization of Helium.
Phys. Rev. Lett. **78**, 1884–1887 (1997).

[65] R. Moshammer, B. Feuerstein, W. Schmitt, A. Dorn, C. D. Schröter, J. Ullrich, H. Rottke, C. Trump, M. Wittmann, G. Korn, K. Hoffmann, and W. Sandner.
Momentum Distributions of Ne^{n+} *Ions Created by an Intense Ultrashort Laser Pulse*.
Phys. Rev. Lett. **84**, 447–450 (2000).

[66] U. Eichmann, M. Dörr, H. Maeda, W. Becker, and W. Sandner.
Collective Multielectron Tunneling Ionization in Strong Fields.
Phys. Rev. Lett. **84**, 3550–3553 (2000).

[67] A. N. Pfeiffer, C. Cirelli, M. Smolarski, X. Wang, J. H. Eberly, R. Dörner, and U. Keller.
Breakdown of the independent electron approximation in sequential double ionization.
New J. Phys. **13**, 093008 (2011).

[68] K. Meyer, C. Ott, P. Raith, A. Kaldun, Y. Jiang, A. Senftleben, M. Kurka, R. Moshammer, J. Ullrich, and T. Pfeifer.
Noisy Optical Pulses Enhance the Temporal Resolution of Pump-Probe Spectroscopy.
Phys. Rev. Lett. **108**, 098302 (2012).

[69] M. Marques and E. Gross.
TIME-DEPENDENT DENSITY FUNCTIONAL THEORY.
Annu. Rev. Phys. Chem. **55**, 427–455 (2004).

[70] A. L. Schawlow and C. H. Townes.
Infrared and Optical Masers.
Phys. Rev. **112**, 1940–1949 (1958).

[71] T. H. Maiman.
Stimulated Optical Radiation in Ruby.
Nature **187**, 493–494 (1960).

[72] http://www.femtolasers.com/.

[73] D. Strickland and G. Mourou.
Compression of amplified chirped optical pulses.
Opt. Commun. **56**, 219 – 221 (1985).

[74] M. Nisoli, S. Stagira, S. De Silvestri, O. Svelto, S. Sartania, Z. Cheng, M. Lenzner, C. Spielmann, and F. Krausz.
A novel-high energy pulse compression system: generation of multigigawatt sub-5-fs pulses.
Appl. Phys. B **65**, 189–196 (1997).

[75] S. C. Rae and K. Burnett.
Detailed simulations of plasma-induced spectral blueshifting.
Phys. Rev. A **46**, 1084–1090 (1992).

[76] A. Wirth, M. T. Hassan, I. GrguraŽ, J. Gagnon, A. Moulet, T. T. Luu, S. Pabst, R. Santra, Z. A. Alahmed, A. M. Azzeer, V. S. Yakovlev, V. Pervak, F. Krausz, and E. Goulielmakis.
Synthesized Light Transients.
Science **334**, 195–200 (2011).

[77] A. M. Marschar.
Messung und Kontrolle der Träger-Einhüllenden-Phase von ultrakurzen Laserpulsen.
BSc Thesis, Universität Heidelberg (2010).

[78] J. Ye and S. T. Cundiff.
Femtosecond Optical Frequency Comb: Principle, Operation, and Applications.
Springer US (2005).

[79] T. Udem, J. Reichert, R. Holzwarth, and T. W. Hänsch.
Accurate measurement of large optical frequency differences with a mode-locked laser.
Opt. Lett. **24**, 881–883 (1999).

[80] H. Telle, G. Steinmeyer, A. Dunlop, J. Stenger, D. Sutter, and U. Keller.
Carrier-envelope offset phase control: A novel concept for absolute optical frequency measurement and ultrashort pulse generation.
Appl. Phys. B **69**, 327–332 (1999).

[81] T. Fuji, J. Rauschenberger, A. Apolonski, V. S. Yakovlev, G. Tempea, T. Udem, C. Gohle, T. W. Hänsch, W. Lehnert, M. Scherer, and F. Krausz.
Monolithic carrier-envelope phase-stabilization scheme.
Opt. Lett. **30**, 332–334 (2005).

[82] http://www.menlosystems.com/.

[83] T. Wittmann, B. Horvath, W. Helml, M. G. Schatzel, X. Gu, A. L. Cavalieri, G. G. Paulus, and R. Kienberger.
Single-shot carrier-envelope phase measurement of few-cycle laser pulses.
Nature Phys. **5**, 357–362 (2009).

[84] A. M. Sayler, T. Rathje, W. Müller, K. Rühle, R. Kienberger, and G. G. Paulus.
Precise, real-time, every-single-shot, carrier-envelope phase measurement of ultrashort laser pulses.
Opt. Lett. **36**, 1–3 (2011).

[85] M. Schönwald.
Phase-matched few-cycle high-harmonic generation: ionisation gating and half-cycle cutoffs.
Diploma Thesis, Universität Heidelberg (2010).

[86] http://henke.lbl.gov/optical_constants/.

[87] http://www.qioptiq-shop.com/en/Precision Optics/Mirrors/Plane-Mirrors/Silver-Circular-Plane-Mirrors-Laser-Quality.html.

[88] https://www.cvimellesgriot.com/Products/Protected Silver-Flat-Mirrors.aspx.

[89] J. H. Moore, C. C. Davis, M. A. Coplan, and S. C. Greer.
Building Scientific Apparatus.
Fourth edition. Cambridge University Press, Cambridge (2009).

[90] http://www.newfocus.com/.

[91] R. Heck.
Erzeugung hoher Harmonischer durch Interferenz freier Elektronenwellenpakete / Charakterisierung und Einrichtung eines Toroidalspiegels.
BSc Thesis, Universität Heidelberg (2010).

[92] C. Ott.
Erzeugung, Fokussierung und Charakterisierung Hoher Harmonischer.
Diploma Thesis, Universität Würzburg (2008).

[93] M. Schultze, A. Wirth, I. Grguras, M. Uiberacker, T. Uphues, A. Verhoef, J. Gagnon, M. Hofstetter, U. Kleineberg, E. Goulielmakis, and F. Krausz.
State-of-the-art attosecond metrology.
J. Electron. Spectrosc. Relat. Phenom. **184**, 68 – 77 (2011).

[94] M. Suman, G. Monaco, M.-G. Pelizzo, D. L. Windt, and P. Nicolosi.
Realization and characterization of an XUVmultilayer coating for attosecond pulses.
Opt. Express **17**, 7922–7932 (2009).

[95] F. Calegari, M. Lucchini, M. Negro, C. Vozzi, L. Poletto, O. Svelto, S. D. Silvestri, G. Sansone, S. Stagira, and M. Nisoli.
Temporal gating methods for the generation of isolated attosecond pulses.
J. Phys. B **45**, 074002 (2012).

[96] L. Poletto, S. Bonora, M. Pascolini, and P. Villoresi.
Instrumentation for analysis and utilization of extreme-ultraviolet and soft x-ray high-order harmonics.
Rev. Sci. Instrum. **75**, 4413–4418 (2004).

[97] H. Mashiko, A. Suda, and K. Midorikawa.
Focusing multiple high-order harmonics in the extreme-ultraviolet and soft-x-ray regions by a platinum-coated ellipsoidal mirror.
Appl. Opt. **45**, 573–577 (2006).

[98] C. Bourassin-Bouchet, S. de Rossi, F. Delmotte, and P. Chavel.
Spatiotemporal distortions of attosecond pulses.
J. Opt. Soc. Am. A **27**, 1395–1403 (2010).

[99] J. Ullrich, R. Moshammer, A. Dorn, R. Dörner, L. P. H. Schmidt, and H. Schmidt-Böcking.
Recoil-ion and electron momentum spectroscopy: reaction-microscopes.
Rep. Prog. Phys. **66**, 1463 (2003).

[100] http://www.edmundoptics.com/images/articles/curve.gif.

[101] http://www.physikinstrumente.com/.

[102] http://www.lebowcompany.com/.

[103] N. Nakano, H. Kuroda, T. Kita, and T. Harada.
Development of a flat-field grazing-incidence XUV spectrometer and its application in picosecond XUV spectroscopy.
Appl. Opt. **23**, 2386–2392 (1984).

[104] T. Kita, T. Harada, N. Nakano, and H. Kuroda.
Mechanically ruled aberration-corrected concave gratings for a flat-field grazing-incidence spectrograph.
Appl. Opt. **22**, 512–513 (1983).

[105] H. A. Rowland.
XXIX. On concave gratings for optical purposes.
Philos. Mag. Ser. 5 **16**, 197–210 (1883).

[106] H. G. Beutler.
The Theory of the Concave Grating.
J. Opt. Soc. Am. **35**, 311–350 (1945).

[107] http://www.lambda-at.com/pdf/ConcaveGrating Spectrograph-Grazing(1)%5B1%5D.pdf.

[108] http://www.princetoninstruments.com/.

[109] A. Baltuška, T. Udem, M. Uiberacker, M. Hentschel, E. Goulielmakis, C. Gohle, R. Holzwarth, V. S. Yakovlev, A. Scrinzi, T. W. Hänsch, and F. Krausz.
Attosecond control of electronic processes by intense light fields.
Nature **421**, 611–615 (2003).

[110] C. Ott, P. Raith, and T. Pfeifer.
Sub-cycle strong-field interferometry.
Opt. Express **18**, 24307–24315 (2010).

[111] L. R. Khundkar and A. H. Zewail.
Ultrafast Molecular Reaction Dynamics in Real-Time: Progress Over a Decade.
Annu. Rev. Phys. Chem. **41**, 15–60 (1990).

[112] N. F. Scherer, R. J. Carlson, A. Matro, M. Du, A. J. Ruggiero, V. Romero-Rochin, J. A. Cina, G. R. Fleming, and S. A. Rice.
Fluorescence-detected wave packet interferometry: Time resolved molecular spectroscopy with sequences of femtosecond phase-locked pulses.
J. Chem. Phys. **95**, 1487–1511 (1991).

[113] T. Ergler, A. Rudenko, B. Feuerstein, K. Zrost, C. D. Schröter, R. Moshammer, and J. Ullrich.
Spatiotemporal Imaging of Ultrafast Molecular Motion: Collapse and Revival of the D_2^+ *Nuclear Wave Packet*.
Phys. Rev. Lett. **97**, 193001 (2006).

[114] B. Feuerstein, T. Ergler, A. Rudenko, K. Zrost, C. D. Schröter, R. Moshammer, J. Ullrich, T. Niederhausen, and U. Thumm.
Complete Characterization of Molecular Dynamics in Ultrashort Laser Fields.
Phys. Rev. Lett. **99**, 153002 (2007).

[115] M. Winter, R. Schmidt, and U. Thumm.
Multidimensional quantum-beat spectroscopy: Towards the complete temporal and spatial resolution of the nuclear dynamics in small molecules.
Phys. Rev. A **80**, 031401 (2009).

[116] F. Kelkensberg, C. Lefebvre, W. Siu, O. Ghafur, T. T. Nguyen-Dang, O. Atabek, A. Keller, V. Serov, P. Johnsson, M. Swoboda, T. Remetter, A. L'Huillier, S. Zherebtsov, G. Sansone, E. Benedetti, F. Ferrari, M. Nisoli, F. Lépine, M. F. Kling, and M. J. J. Vrakking.
Molecular Dissociative Ionization and Wave-Packet Dynamics Studied Using Two-Color XUV and IR Pump-Probe Spectroscopy.
Phys. Rev. Lett. **103**, 123005 (2009).

[117] G. Sansone, F. Kelkensberg, J. F. Perez-Torres, F. Morales, M. F. Kling, W. Siu, O. Ghafur, P. Johnsson, M. Swoboda, E. Benedetti, F. Ferrari, F. Lepine, J. L. Sanz-Vicario, S. Zherebtsov, I. Znakovskaya, A. L'Huillier, M. Y. Ivanov, M. Nisoli, F. Martin, and M. J. J. Vrakking.
Electron localization following attosecond molecular photoionization.
Nature **465**, 763–766 (2010).

[118] R. R. Jones, C. S. Raman, D. W. Schumacher, and P. H. Bucksbaum.
Ramsey interference in strongly driven Rydberg systems.
Phys. Rev. Lett. **71**, 2575–2578 (1993).

[119] M. Wollenhaupt, A. Assion, D. Liese, C. Sarpe-Tudoran, T. Baumert, S. Zamith, M. A. Bouchene, B. Girard, A. Flettner, U. Weichmann, and G. Gerber.
Interferences of Ultrashort Free Electron Wave Packets.
Phys. Rev. Lett. **89**, 173001 (2002).

[120] J. Mauritsson, T. Remetter, M. Swoboda, K. Klünder, A. L'Huillier, K. J. Schafer, O. Ghafur, F. Kelkensberg, W. Siu, P. Johnsson, M. J. J. Vrakking, I. Znakovskaya, T. Uphues, S. Zherebtsov, M. F. Kling, F. Lépine, E. Benedetti, F. Ferrari, G. Sansone, and M. Nisoli.
Attosecond Electron Spectroscopy Using a Novel Interferometric Pump-Probe Technique.
Phys. Rev. Lett. **105**, 053001 (2010).

[121] T. Nubbemeyer, K. Gorling, A. Saenz, U. Eichmann, and W. Sandner.
Strong-Field Tunneling without Ionization.
Phys. Rev. Lett. **101**, 233001 (2008).

[122] I. Schlegel.

Ultra-short time scale physics (simulations and experimental methods) / Technical implementation of a laser monitoring and beam shutting system.
BSc Thesis, Universität Heidelberg (2010).

[123] M. Y. Ivanov.
Trapping of Population at Rydberg States during Strong-Field Multiphoton Ionization.
Laser Phys. **3**, 640–643 (1993).

[124] M. Y. Ivanov.
Suppression of resonant multiphoton ionization via Rydberg states.
Phys. Rev. A **49**, 1165–1170 (1994).

[125] J. Fleck, J. Morris, and M. Feit.
Time-dependent propagation of high energy laser beams through the atmosphere.
Appl. Phys. A **10**, 129–160 (1976).

[126] M. Feit, J. F. Jr., and A. Steiger.
Solution of the Schrödinger equation by a spectral method.
J. Comput. Phys. **47**, 412 – 433 (1982).

[127] T. Pfeifer, D. Walter, G. Gerber, M. Y. Emelin, M. Y. Ryabikin, M. D. Chernobrovtseva, and A. M. Sergeev.
Transient enhancement of high-order harmonic generation in expanding molecules.
Phys. Rev. A **70**, 013805 (2004).

[128] D. B. Milošević, G. G. Paulus, D. Bauer, and W. Becker.
Above-threshold ionization by few-cycle pulses.
J. Phys. B **39**, R203 (2006).

[129] D. B. Milošević, G. G. Paulus, and W. Becker.
Ionization by few-cycle pulses: Tracing the electron orbits.
Phys. Rev. A **71**, 061404 (2005).

[130] F. Lindner, M. G. Schätzel, H. Walther, A. Baltuška, E. Goulielmakis, F. Krausz, D. B. Milošević, D. Bauer, W. Becker, and G. G. Paulus.
Attosecond Double-Slit Experiment.
Phys. Rev. Lett. **95**, 040401 (2005).

[131] T. Brixner, N. H. Damrauer, G. Krampert, P. Niklaus, and G. Gerber.
Adaptive shaping of femtosecond polarization profiles.
J. Opt. Soc. Am. B **20**, 878–881 (2003).

[132] A. T. J. B. Eppink and D. H. Parker.
Velocity map imaging of ions and electrons using electrostatic lenses: Application in photoelectron and photofragment ion imaging of molecular oxygen.
Rev. Sci. Instrum. **68**, 3477–3484 (1997).

[133] A. I. Kuleff and L. S. Cederbaum.
Charge migration in different conformers of glycine: The role of nuclear geometry.
Chem. Phys. **338**, 320 – 328 (2007).

[134] S. Mukamel.
MULTIDIMENSIONAL FEMTOSECOND CORRELATION SPECTROSCOPIES OF ELECTRONIC AND VIBRATIONAL EXCITATIONS.
Annu. Rev. Phys. Chem. **51**, 691–729 (2000).

[135] D. M. Jonas.
TWO-DIMENSIONAL FEMTOSECOND SPECTROSCOPY.
Annu. Rev. Phys. Chem. **54**, 425–463 (2003).

[136] R. Ernst, G. Bodenhausen, and A. Wokaun.
Principles of Nuclear Magnetic Resonance in One and Two Dimensions.
International series of monographs on chemistry. Clarendon Press (1990).

[137] Y. Tanimura and S. Mukamel.
2-Dimensional Femtosecond Vibrational Spectroscopy of Liquids.
J. Chem. Phys. **99**, 9496–9511 (1993).

[138] S. Mukamel.
Principles of nonlinear optical spectroscopy.
Oxford series on optical sciences. Oxford University Press (1999).

[139] M. C. Asplund, M. T. Zanni, and R. M. Hochstrasser.
Two-Dimensional Infrared Spectroscopy of Peptides by Phase-Controlled Femtosecond Vibrational Photon Echoes.
Proc. Natl. Acad. Sci. USA **97**, 8219–8224 (2000).

[140] P. Tian, D. Keusters, Y. Suzaki, and W. S. Warren.
Femtosecond Phase-Coherent Two-Dimensional Spectroscopy.
Science **300**, 1553–1555 (2003).

[141] T. Brixner, J. Stenger, H. M. Vaswani, M. Cho, R. E. Blankenship, and G. R. Fleming.
Two-dimensional spectroscopy of electronic couplings in photosynthesis.
Nature **434**, 625–628 (2005).

[142] G. S. Engel, T. R. Calhoun, E. L. Read, T. K. Ahn, T. Mancal, Y. C. Cheng, R. E. Blankenship, and G. R. Fleming.
Evidence for wavelike energy transfer through quantum coherence in photosynthetic systems.
Nature **446**, 782–786 (2007).

[143] I. V. Schweigert and S. Mukamel.
Coherent Ultrafast Core-Hole Correlation Spectroscopy: X-Ray Analogues of Multidimensional NMR.
Phys. Rev. Lett. **99**, 163001 (2007).

[144] P. Antoine, A. L'Huillier, and M. Lewenstein.
Attosecond Pulse Trains Using High–Order Harmonics.
Phys. Rev. Lett. **77**, 1234–1237 (1996).

[145] P. M. Paul, E. S. Toma, P. Breger, G. Mullot, F. AugÃl', P. Balcou, H. G. Muller, and P. Agostini.
Observation of a Train of Attosecond Pulses from High Harmonic Generation.
Science **292**, 1689–1692 (2001).

[146] T. Pfeifer, A. Jullien, M. J. Abel, P. M. Nagel, L. Gallmann, D. M. Neumark, and S. R. Leone.
Generating coherent broadbandcontinuum soft-x-ray radiation byattosecond ionization gating.
Opt. Express **15**, 17120–17128 (2007).

[147] E. Mansten, J. M. Dahlström, J. Mauritsson, T. Ruchon, A. L'Huillier, J. Tate, M. B. Gaarde, P. Eckle, A. Guandalini, M. Holler, F. Schapper, L. Gallmann, and U. Keller.
Spectral Signature of Short Attosecond Pulse Trains.
Phys. Rev. Lett. **102**, 083002 (2009).

[148] A. Gazibegović-Busuladžić, E. Hasović, M. Busuladžić, D. B. D B Milošević, F. Kelkensberg, W. K. Siu, M. J. J. Vrakking, F. Lépine, G. Sansone, M. Nisoli, I. Znakovskaya, and M. F. Kling.
Above-threshold ionization of diatomic molecules by few-cycle laser pulses.
Phys. Rev. A **84**, 043426 (2011).

[149] M. Krüger, M. Schenk, and P. Hommelhoff.
Attosecond control of electrons emitted from a nanoscale metal tip.
Nature **475**, 78–81 (2011).

[150] A. Borot, A. Malvache, X. Chen, A. Jullien, J.-P. Geindre, P. Audebert, G. Mourou, F. Quere, and R. Lopez-Martens.
Attosecond control of collective electron motion in plasmas.
Nature Phys. **advance online publication**, – (2012).

[151] G. Sansone, C. Vozzi, S. Stagira, M. Pascolini, L. Poletto, P. Villoresi, G. Tondello, S. De Silvestri, and M. Nisoli.

Observation of Carrier-Envelope Phase Phenomena in the Multi-Optical-Cycle Regime.
Phys. Rev. Lett. **92**, 113904 (2004).

[152] G. Farkas and C. Tóth.
Proposal for attosecond light pulse generation using laser induced multiple-harmonic conversion processes in rare gases.
Phys. Lett. A **168**, 447 – 450 (1992).

[153] S. Harris, J. Macklin, and T. Hänsch.
Atomic scale temporal structure inherent to high-order harmonic generation.
Opt. Commun. **100**, 487 – 490 (1993).

[154] J. L. Krause, K. J. Schafer, and K. C. Kulander.
Calculation of photoemission from atoms subject to intense laser fields.
Phys. Rev. A **45**, 4998–5010 (1992).

[155] H. G. Muller.
Reconstruction of attosecond harmonic beating by interference of two-photon transitions.
Appl. Phys. B **74**, 17–21 (2002).

[156] P. Salières, A. L'Huillier, and M. Lewenstein.
Coherence Control of High-Order Harmonics.
Phys. Rev. Lett. **74**, 3776–3779 (1995).

[157] K. Varjú, Y. Mairesse, P. Agostini, P. Breger, B. Carré, L. J. Frasinski, E. Gustafsson, P. Johnsson, J. Mauritsson, H. Merdji, P. Monchicourt, A. L'Huillier, and P. Salières.
Reconstruction of Attosecond Pulse Trains Using an Adiabatic Phase Expansion.
Phys. Rev. Lett. **95**, 243901 (2005).

[158] Y. Mairesse, A. de Bohan, L. J. Frasinski, H. Merdji, L. C. Dinu, P. Monchicourt, P. Breger, M. Kovačev, R. Taïeb, B. Carré, H. G. Muller, P. Agostini, and P. Salières.
Attosecond Synchronization of High-Harmonic Soft X-rays.
Science **302**, 1540–1543 (2003).

[159] M. B. Gaarde, F. Salin, E. Constant, P. Balcou, K. J. Schafer, K. C. Kulander, and A. L'Huillier.
Spatiotemporal separation of high harmonic radiation into two quantum path components.
Phys. Rev. A **59**, 1367–1373 (1999).

[160] P. Salières, P. Antoine, A. de Bohan, and M. Lewenstein.
Temporal and Spectral Tailoring of High-Order Harmonics.
Phys. Rev. Lett. **81**, 5544–5547 (1998).

[161] M. Nisoli, G. Sansone, S. Stagira, S. De Silvestri, C. Vozzi, M. Pascolini, L. Poletto, P. Villoresi, and G. Tondello.
Effects of Carrier-Envelope Phase Differences of Few-Optical-Cycle Light Pulses in Single-Shot High-Order-Harmonic Spectra.
Phys. Rev. Lett. **91**, 213905 (2003).

[162] Y. Mairesse and F. Quéré.
Frequency-resolved optical gating for complete reconstruction of attosecond bursts.
Phys. Rev. A **71**, 011401 (2005).

[163] G. Sansone, E. Benedetti, F. Calegari, C. Vozzi, L. Avaldi, R. Flammini, L. Poletto, P. Villoresi, C. Altucci, R. Velotta, S. Stagira, S. De Silvestri, and M. Nisoli.
Isolated Single-Cycle Attosecond Pulses.
Science **314**, 443–446 (2006).

[164] E. Goulielmakis, M. Schultze, M. Hofstetter, V. S. Yakovlev, J. Gagnon, M. Uiberacker, A. L. Aquila, E. M. Gullikson, D. T. Attwood, R. Kienberger, F. Krausz, and U. Kleineberg.
Single-Cycle Nonlinear Optics.
Science **320**, 1614–1617 (2008).

[165] A. D. Bandrauk, S. Chelkowski, and N. H. Shon.
Measuring the Electric Field of Few-Cycle Laser Pulses by Attosecond Cross Correlation.

Phys. Rev. Lett. **89**, 283903 (2002).

[166] M. Kitzler, N. Milosevic, A. Scrinzi, F. Krausz, and T. Brabec.
Quantum Theory of Attosecond XUV Pulse Measurement by Laser Dressed Photoionization.
Phys. Rev. Lett. **88**, 173904 (2002).

[167] R. Kienberger, E. Goulielmakis, M. Uiberacker, A. Baltuška, V. Yakovlev, F. Bammer, A. Scrinzi, T. Westerwalbesloh, U. Kleineberg, U. Heinzmann, M. Drescher, and F. Krausz.
Atomic transient recorder.
Nature **427**, 817–821 (2004).

[168] K. T. Kim, D. H. Ko, J. Park, V. Tosa, and C. H. Nam.
Complete temporal reconstruction of attosecond high-harmonic pulse trains.
New J. Phys. **12**, 083019 (2010).

[169] L. Chipperfield, J. Robinson, P. Knight, J. Marangos, and J. Tisch.
The generation and utilisation of half-cycle cut-offs in high harmonic spectra.
Laser & Photon. Rev. **4**, 697–719 (2010).

[170] C. A. Haworth, L. E. Chipperfield, J. S. Robinson, P. L. Knight, J. P. Marangos, and J. W. G. Tisch.
Half-cycle cutoffs in harmonic spectra and robust carrier-envelope phase retrieval.
Nature Phys. **3**, 52–57 (2007).

[171] G. Sansone.
Calculation of quantum paths using the non-adiabatic saddle point approximation.
private communications (2012).

[172] T. Pfeifer, M. J. Abel, P. M. Nagel, A. Jullien, Z.-H. Loh, M. J. Bell, D. M. Neumark, and S. R. Leone.
Time-resolved spectroscopy of attosecond quantum dynamics.
Chem. Phys. Lett. **463**, 11 – 24 (2008).

[173] W. Heitler and F. London.
Wechselwirkung neutraler Atome und homöopolare Bindung nach der Quantenmechanik.
Z. Phys. A **44**, 455–472 (1927).

[174] F. Remacle and R. D. Levine.
An electronic time scale in chemistry.
Proc. Natl. Acad. Sci. USA **103**, 6793–6798 (2006).

[175] W. Vanroose, F. Martín, T. N. Rescigno, and C. W. McCurdy.
Complete Photo-Induced Breakup of the H2 Molecule as a Probe of Molecular Electron Correlation.
Science **310**, 1787–1789 (2005).

[176] M. Born and R. Oppenheimer.
Zur Quantentheorie der Molekeln.
Ann. Phys. (Leipzig) **389**, 457–484 (1927).

[177] G. A. Worth and L. S. Cederbaum.
BEYOND BORN-OPPENHEIMER: Molecular Dynamics Through a Conical Intersection.
Annu. Rev. Phys. Chem. **55**, 127–158 (2004).

[178] X. Zhou, P. Ranitovic, C. W. Hogle, J. H. D. Eland, H. C. Kapteyn, and M. M. Murnane.
Probing and controlling non-Born-Oppenheimer dynamics in highly excited molecular ions.
Nature Phys. **8**, 232–237 (2012).

[179] Z.-H. Loh, C. H. Greene, and S. R. Leone.
Femtosecond induced transparency and absorption in the extreme ultraviolet by coherent coupling of the He 2s2p (1Po) and 2p2 (1Se) double excitation states with 800 nm light.
Chem. Phys. **350**, 7 – 13 (2008).

[180] M. Fleischhauer, A. Imamoglu, and J. P. Marangos.
Electromagnetically induced transparency: Optics in coherent media.
Rev. Mod. Phys. **77**, 633–673 (2005).

[181] P. J. Hicks and J. Comer.
Ejected electron spectroscopy of autoionizing states excited by low energy electron impact.
J. Phys. B **8**, 1866 (1975).

[182] A. Bürgers, D. Wintgen, and J.-M. Rost.
Highly doubly excited S states of the helium atom.
J. Phys. B **28**, 3163 (1995).

[183] M. Tarana and C. H. Greene.
Femtosecond transparency in the extreme-ultraviolet region.
Phys. Rev. A **85**, 013411 (2012).

[184] S. Gilbertson, M. Chini, X. Feng, S. Khan, Y. Wu, and Z. Chang.
Monitoring and Controlling the Electron Dynamics in Helium with Isolated Attosecond Pulses.
Phys. Rev. Lett. **105**, 263003 (2010).

[185] Z. X. Zhao and C. D. Lin.
Theory of laser-assisted autoionization by attosecond light pulses.
Phys. Rev. A **71**, 060702 (2005).

[186] M. Wickenhauser, J. Burgdörfer, F. Krausz, and M. Drescher.
Time Resolved Fano Resonances.
Phys. Rev. Lett. **94**, 023002 (2005).

[187] M. Wickenhauser and J. Burgdörfer.
Theoretical Aspects of Time-Resolved Autoionization.
Laser Phys. **14**, 492–496 (2004).

[188] X. M. Tong and C. D. Lin.
Double photoexcitation of He atoms by attosecond xuv pulses in the presence of intense few-cycle infrared lasers.
Phys. Rev. A **71**, 033406 (2005).

[189] M. Drescher, M. Hentschel, R. Kienberger, M. Uiberacker, V. Yakovlev, A. Scrinzi, T. Westerwalbesloh, U. Kleineberg, U. Heinzmann, and F. Krausz.
Time-resolved atomic inner-shell spectroscopy.
Nature **419**, 803–807 (2002).

[190] O. Smirnova, V. S. Yakovlev, and A. Scrinzi.
Quantum Coherence in the Time-Resolved Auger Measurement.
Phys. Rev. Lett. **91**, 253001 (2003).

[191] T. Mercouris, Y. Komninos, and C. A. Nicolaides.
Time-dependent formation of the profile of the He $2s2p\,^1P^o$ *state excited by a short laser pulse*.
Phys. Rev. A **75**, 013407 (2007).

[192] W.-C. Chu and C. D. Lin.
Theory of ultrafast autoionization dynamics of Fano resonances.
Phys. Rev. A **82**, 053415 (2010).

[193] W.-C. Chu, S.-F. Zhao, and C. D. Lin.
Laser-assisted-autoionization dynamics of helium resonances with single attosecond pulses.
Phys. Rev. A **84**, 033426 (2011).

[194] Z.-H. Loh, M. Khalil, R. E. Correa, R. Santra, C. Buth, and S. R. Leone.
Quantum State-Resolved Probing of Strong-Field-Ionized Xenon Atoms Using Femtosecond High-Order Harmonic Transient Absorption Spectroscopy.
Phys. Rev. Lett. **98**, 143601 (2007).

[195] E. Goulielmakis, Z.-H. Loh, A. Wirth, R. Santra, N. Rohringer, V. S. Yakovlev, S. Zherebtsov, T. Pfeifer, A. M. Azzeer, M. F. Kling, S. R. Leone, and F. Krausz.
Real-time observation of valence electron motion.
Nature **466**, 739–743 (2010).

[196] R. Santra, V. S. Yakovlev, T. Pfeifer, and Z.-H. Loh.
Theory of attosecond transient absorption spectroscopy of strong-field-generated ions.
Phys. Rev. A **83**, 033405 (2011).

[197] H. Wang, M. Chini, S. Chen, C.-H. Zhang, F. He, Y. Cheng, Y. Wu, U. Thumm, and Z. Chang.
Attosecond Time-Resolved Autoionization of Argon.
Phys. Rev. Lett. **105**, 143002 (2010).

[198] W.-C. Chu and C. D. Lin.
Photoabsorption of attosecond XUV light pulses by two strongly laser-coupled autoionizing states.
Phys. Rev. A **85**, 013409 (2012).

[199] M. Holler, F. Schapper, L. Gallmann, and U. Keller.
Attosecond Electron Wave-Packet Interference Observed by Transient Absorption.
Phys. Rev. Lett. **106**, 123601 (2011).

[200] M. B. Gaarde, C. Buth, J. L. Tate, and K. J. Schafer.
Transient absorption and reshaping of ultrafast XUV light by laser-dressed helium.
Phys. Rev. A **83**, 013419 (2011).

[201] L. Argenti and E. Lindroth.
Ionization Branching Ratio Control with a Resonance Attosecond Clock.
Phys. Rev. Lett. **105**, 053002 (2010).

[202] J. A. R. Samson, Z. X. He, L. Yin, and G. N. Haddad.
Precision measurements of the absolute photoionization cross sections of He.
J. Phys. B **27**, 887 (1994).

[203] S. Hagstotz.
Simulation von Elektronendynamik in autoionisierenden Heliumniveaus unter dem Einfluss ultrakurzer Laserpulse.
BSc Thesis, Universität Heidelberg (2011).

[204] C. Ott, A. Kaldun, P. Raith, K. Meyer, M. Laux, Y. Zhang, S. Hagstotz, T. Ding, R. Heck, and T. Pfeifer.
Quantum Interferometry and Correlated Two-Electron Wave-Packet Observation in Helium.
submitted (2012).

[205] E. Lindroth.
Calculation of the $2s2p - 2p^2$ dipole matrix element.
private communications (2012).

[206] http://physics.nist.gov/cuu/Constants/.

Danksagung

Zu guter Letzt möchte ich die Gelegenheit nutzen all jenen zu danken, die diese Arbeit überhaupt erst möglich gemacht haben:

- Mit Abstand am meisten Dank gebührt meinem Betreuer und Mentor **Thomas Pfeifer**. Nicht nur daß er mir die Gelegenheit bot, von Beginn an in seiner Gruppe mitzuwirken, sondern vor allem für die außerordentlich gute Betreuung und sein ständig offenes Ohr für alle möglichen Probleme. In unzähligen Diskussionen habe ich durch sein intuitives physikalisches Verständnis sehr viel gelernt.

- Ich danke **Marcus Motzkus** für die Übernahme des Zweitgutachtens meiner Arbeit.

- **Andreas Kaldun** möchte ich für die tatkräftige Unterstützung rund um den Aufbau und der Durchführung der Experimente bedanken, sowie den teilweise zähen aber abwechslungsreichen Justagearbeiten am Lasersystem. Die anregenden physikalischen Diskussionen mit ihm und auch mit **Steffen Hagstotz** haben mir sehr viel geholfen. Auch danken möchte ich **Martin Laux** für den unermüdlichen Einsatz im Labor und **Markus Kohler** für die Unterstützung in theoretischen Fragen.

- Ein Dankeschön gilt auch all jenen die tatkräfig an der Aufbauarbeit im Labor beteiligt waren, allen voran **Philipp Raith**, **Michael Schönwald**, **Anja Marschar** und **Robert Heck** für die Hilfe von Beginn an, insbesonders Michael für die unterstützende Hilfe beim Anfertigen des Designs und Philipp für die Unterstützung bei der Arbeit im Labor.

- **Giuseppe Sansone** möchte ich danken für die inhaltliche Unterstützung zu dieser Arbeit sowie für die Freundschaft im Büro und auch darüber hinaus. Auch möchte ich **Robert Mooshammer** danken für die physikalischen Diskussionen und das Durchlesen meiner Arbeit.

- Ein großes Dankeschön geht an dieser Stelle auch an **Helga Krieger**, **Bernd Knape** und **Christian Kaiser**, die durch ihre technische Unterstützung maßgeblich zu einer erfolgreichen Laborarbeit beigetragen haben, genauso wie allen Mitarbeitern der technischen Werkstätten und der Konstruktion.

- Ich danke auch **Kristina Meyer**, **Alexander Sperl**, **Peter Caradonna**, **Rima Schüssler** und allen weiteren schon genannten Personen für das Korrekturlesen meiner Arbeit.

- Auch ein Dankeschön gilt allen weiteren aktuellen und ehemaligen Mitgliedern unseres *Interatto*-Teams, nämlich **Veit Stooß**, **Yizhu Zhang**, **Thomas Ding**, **Yogesh Patil**, **Iris Schlegel** und **Christoph Bogda**.

- Ich danke auch allen hier namentlich nicht erwähnten Freunden und Kollegen am MPIK die zu einer schönen und unvergesslichen Zeit beigetragen haben, inbesonders auch allen aus der Gruppe um **Joachim Ullrich**.

- Besonders möchte ich meinen Mitdoktoranden und Freunden **Katharina Schneider** und **Michael Schuricke** danken, nicht nur für das zuletzt gemeinsame Ausharren in der Bibliothek.

- Allen oben genannnten Personen gilt vor allem natürlich für die gute und entspannte Arbeitsatmosphäre ein großes Dankeschön. Die Sommerschulen, die spontanen Grillaktionen, die Gruppenausflüge und auch alle sonstigen gemeinsamen Feierlichkeiten und Freizeitaktivitäten außerhalb der Arbeit bleiben unvergesslich.

- Ich möchte all meinen Freunden aus nah und fern danken für ihre Unterstützung, ganz besonders auch meiner WG. Ohne all die Unterstützung und Freundschaft wäre diese Arbeit sicherlich nicht möglich gewesen.

- Zuletzt möchte ich auch meiner Familie und allen Verwandten ein großes Dankeschön sagen. Durch ihre ständige und bedingungslose Unterstützung ist eine solche Arbeit überhaupt erst möglich. Danke.

Erklärung

Diese Arbeit ist von mir selbstständig verfasst worden. Ich habe keine anderen als die von mir angegebenen Quellen und Hilfsmittel benutzt.

Heidelberg, 18.05.2012 .....

Christian Ott